

**PERFORMANCE EVALUATION OF CONNECTIONS IN  
CONCRETE STRUCTURES USING 3D-RBSM**

**MUHAMMAD SHOAIB KARAM**

**PERFORMANCE EVALUATION OF CONNECTIONS IN  
CONCRETE STRUCTURES USING 3D-RBSM**

By

MUHAMMAD SHOAIB KARAM

A Dissertation Submitted to Nagoya University  
In Partial Fulfillment of the Requirements for  
The Degree of Doctor of Engineering

Department of Civil Engineering  
Graduate School of Engineering, Nagoya University  
Nagoya, Japan



# ABSTRACT

Currently, the utilization and application of the precast concrete structure and concrete-steel composite structure have increased in association with the increment of social demands for enhancement of the structural performance, productivity, and the renewal of existing structures. Therefore, the detailed evaluation of mechanical behaviors of connection in concrete structures especially the crack and stress propagation process inside the connection is desired to verify for improving the structural performance as well as for developing the new structural members.

Specifically, in terms of the connections of concrete structure, the modeling of connection of members and the boundary between different materials are very important because the mechanical and deformation performance are dominant at the region of connection. The precast construction method is one of the efficient and suitable approaches for the maintenance and the rehabilitation of the degraded infrastructures .e.g. renewal projects of the deteriorated reinforced concrete deck slabs in bridges etc. Furthermore, in recent years, the use of the concrete-steel composite construction has been adopted widely and extensively for contributing towards the superior structural response.

The performance evaluation of the connection in concrete structure and the interaction of concrete with deformed rebar in cast in-situ RC joint and with the steel connector in concrete-steel composite should be determined. However, it is difficult to investigate the detailed internal failure process comprehensively from experiments. The numerical simulations are helpful as they can assess not only the capacity and deformation performance but also the detailed internal failure process and the mechanism of the connections, quantitatively. To evaluate the complex interaction between concrete and deformed rebar comprehensively, the mesoscale modeling is regarded as the most efficient numerical approach by including the actual geometrical features of the deformed rebar.

In order to evaluate the interaction of concrete and deformed rebar and the detailed internal failure process of the connections, the numerical simulations based on the 3D-RBSM can be an effective approach. The 3D-RBSM highlights its advantage in capturing the nonlinear mechanical behavior of concrete. Considering the previously stated discussion the study mainly focused on the performance evaluation of loop joints in precast construction, the bond behavior between concrete and deformed rebar, and the Perfobond shear connector in concrete-steel composite construction.

Initially, the internal failure mechanism of the horizontal type loop joints was evaluated using 3D-RBSM and it was determined that the failure of the loop joint without inner reinforcing rebars inside the loop was characterized by the occurrence of diagonal cracks at the region of tensile loop rebars. The presence and the bond strength of the inner reinforcing bars inside the loop joint played the vital role in suppressing the diagonal crack propagation and reproduced the compression failure behavior.

Furthermore, the limitation of the conventional 3D-RBSM and the beam element model and the need of proposing a new analytical model i.e. coupled RBSM and solid FEM were highlighted. The coupled RBSM and solid FEM was applied to evaluate the macroscopic bond behavior of deformed rebar and concrete in RC specimens using mesoscale simulation. The complex interaction of the concrete and deformed rebar was investigated under the influence of the varying concrete cover thicknesses, rebar diameters, externally applied lateral pressures, and for investigating the detailed internal failure mechanism of concrete etc. The bond characteristics, failure behaviors (splitting and pull-out) along with detailed internal failure process were revealed, comprehensively.

Finally, the numerical evaluation of shear resistance of the PBL shear connector using the coupled RBSM and solid FEM Model was performed under the effect of varying amounts of the lateral pressures and connection parameters. It was confirmed that the shear capacity of the PBL increased and the failure mode changed from shear failure to splitting failure of the side concrete blocks of PBL with the increased amounts of lateral pressures and the parameters of the transverse rebar. It was also determined that the increased amounts of lateral pressures and the parameters of the transverse rebar caused the enhancement of shear capacity of the PBL against the vertically applied shear load in simple push-out test.

# ACKNOWLEDGEMENTS

First and foremost, I would like to express my sincerest gratitude to my supervisor, Professor Hikaru Nakamura who supported and motivated me so much during the completion of the Ph.D program. I am also thankful to my former supervisor Associate Professor Yoshihito Yamamoto who provided me valuable support and ideas in the numerical simulations. I am honoured to be student of the two most prestigious and renowned teachers in civil engineering discipline of Japan. I appreciate all their patience, guidance, ideas, and motivations which they provided during these three years.

My professors taught me how to make critical thinking and how to do research. The dedication and enthusiasm of my supervisor inspired me always, especially during the tough moments in my doctoral course. Most importantly, he encouraged me in my most difficult time near the completion of the Ph.D. degree. I am deeply thankful to sincere gratitude of the other members in my examination committee: Professor Yasuhiko Sato from Waseda University, Professor Kazuo Tateishi, and Professor Takeshi Hanji for their time and effort and valuable recommendations for this dissertation.

I am deeply thankful to all my laboratory members who have contributed to both personal and professional life during my Ph.D. pursuit. I also gratefully acknowledge the support of Associate Professor Taito Miura. I am extremely thankful to my seniors; Dr. Mac Mendoza, Dr. Roy Sushanta, and Dr. Yizhou Yang who provided valuable knowledge and wonderful ideas to improve my research skills.

I would like to also thank my former and current lab mates; Mr. Usman Farooq my country fellow, Ikuma san, Kitagawa san, Oshima san, Watanabe san, Kiyama san, Mr. Shunyuan Chi, Mitsutani san, Sato san, Takemura san, Mr. Champ Puttipong, Mr. Attik, and Mr. Ardhi Natino, etc. for all their kind supports during doctoral program.

All blessings in life are by the grace of Almighty Allah. God blessed me with the opportunity to study abroad. Special thanks to my mother (Mrs. Azra Parveen), father (Mr. Karam Khan), sister and brother who always encouraged me during hard times in my life. To my special one, Fatima Mushtaq, I am also thankful to her who always prays for my success and happiness being a true partner in my life.

# Table of Contents

<b>ABSTRACT .....</b>	<b>I</b>
<b>ACKNOWLEDGEMENTS.....</b>	<b>III</b>
<b>Table of Contents .....</b>	<b>IV</b>
<b>List of Tables.....</b>	<b>VIII</b>
<b>List of Figures .....</b>	<b>IX</b>
<b>1 General Introduction .....</b>	<b>1</b>
1.1 Background.....	1
1.2 Literature review .....	5
1.2.1 RC Joints.....	5
1.2.2 Bond Behavior between concrete and steel.....	7
1.2.3 The shear resistance of the Perfobond (PBL) shear connector.....	8
1.3 The purpose and objectives .....	10
1.4 Organization of dissertation contents .....	12
<b>2 Analytical Method: Conventional 3D-RBSM and the Beam Element Model .....</b>	<b>15</b>
2.1 Introduction .....	15
2.2 Modeling of the concrete using 3D-RBSM.....	15

2.2.1	General description of 3D-RBSM .....	15
2.2.2	Constitutive models and model parameters of concrete in 3D-RBSM.....	17
2.2.3	Verification for mesh size dependency of the numerical model .....	21
2.3	Modeling of steel reinforcement using the beam element model.....	24
2.4	Summary.....	25
<b>3</b>	<b>Performance Evaluation of the Horizontal Loop Joints in Precast Concrete Beams Using 3D-RBSM and the Beam Element Model .....</b>	<b>26</b>
3.1	Introduction .....	26
3.2	Test overview and numerical modeling .....	27
3.3	Results and Discussion .....	32
3.3.1	Case 1 (Ordinary RC beam) .....	32
3.3.2	Case 2 (Precast beams with loop joints) .....	34
3.3.3	Case 3 (Precast beams with increased loop interval and varying steel amount of inner reinforcing steel) .....	38
3.4	Summary.....	42
<b>4</b>	<b>Limitation of Conventional 3D-RBSM and Beam Element Model and Introduction of New Model .....</b>	<b>44</b>
4.1	Introduction .....	44
4.2	Limitation of existing numerical model and proposal of new model.....	44
4.3	Coupled RBSM and solid FEM model.....	45
4.3.1	Modeling of concrete and steel.....	47
4.3.2	Modeling of the concrete-steel interface .....	47
4.4	Summary.....	52

## **5 Numerical Evaluation of the Bond Behavior of Deformed Rebar Using Coupled RBSM and Solid FEM Model ..... 53**

5.1 Introduction .....	53
5.2 Evaluation of macroscopic bond behavior in two ends pull-out test.....	54
5.2.1 Test overview and numerical modeling.....	54
5.2.2 Evaluation of the bond behavior in two ends pull-out test .....	57
5.2.3 Investigation of internal failure process and mechanism .....	61
5.3 Evaluation of macroscopic bond behavior in one end pull-out test subjected to lateral pressures .....	67
5.3.1 Test overview and numerical modeling.....	67
5.3.2 Results and discussion for numerical evaluation in one end pull-out test.....	70
5.4 Evaluation of detailed failure behavior in axially loaded RC prisms under direct tension .....	78
5.4.1 Test overview and numerical modeling.....	78
5.4.2 Results and discussion against evaluation of the detailed failure behaviors.....	81
5.5 Summary.....	87

## **6 Numerical Evaluation of Shear Resistance of Perfobond (PBL) Shear Connector Using the Coupled RBSM and Solid FEM Model..... 89**

6.1 Introduction .....	89
6.2 Numerical evaluation of PBL shear connector under the influence of varying amounts of lateral pressures .....	91
6.2.1 Test overview and numerical modeling.....	91
6.2.2 Results and discussions .....	95
6.2.3 Investigation of the failure process and the mechanism.....	97

6.3 Evaluation of combined effects for the lateral pressure and hole diameter ...	103
6.4 Numerical evaluation of transverse effect rebar inside the hole of the PBL shear connector.....	107
6.4.1 Contribution of the transverse rebar .....	108
6.4.2 Effect of the rebar diameter .....	123
6.4.3 Effect of the rebar position inside hole.....	131
6.4.4 Effect of the yield strength ( $f_y$ ) of the rebar.....	139
6.5 Summary.....	147
<b>7 Conclusions .....</b>	<b>150</b>
7.1 Conclusions .....	150
7.2 Recommendations for future study .....	153
<b>References .....</b>	<b>155</b>

## List of Tables

Table 2.1 Calibrated model parameters of normal spring.....	20
Table 2.2 Calibrated model parameters of shear spring.....	20
Table 3.1 Detail of the specimens.....	30
Table 3.2 Summary of deformed behaviors of Case 3.....	41
Table 5.1 Geometrical details and the mechanical properties of the deformed rebars.....	55
Table 6.1 Numerical evaluation for the transverse rebar effects.....	107

# List of Figures

Figure 1.1 Congestion of the rebars at the RC joint due to seismic detailing (Matsumoto et al. 2016).....	4
Figure 1.2 Existing mesoscale model using RBSM (Hayashi et al. 2013) .....	4
Figure 1.3 Organization of the dissertation.....	14
Figure 2.1 Description of the 3D-RBSM element.....	16
Figure 2.2 Constitutive models of normal and shear springs in 3D-RBSM.....	17
Figure 2.3 Geometrical dimensions of the beam for three-point loading test.....	22
Figure 2.4 Analytical models for the verification of mesh size dependency.....	22
Figure 2.5 Analytical results for mesh size dependency of 3D-RBSM.....	23
Figure 2.6 Model of steel reinforcement using beam elements (Yamamoto et al. 2014).....	24
Figure 2.7 Bond stress-slip relationship (Yamamoto et al. 2014).....	24
Figure 3.1 Loop (vertical and horizontal) joints in precast beams.....	27

Figure 3.2 Horizontal loop joint with and without inner reinforcing bars.....	28
Figure 3.3 Geometrical details of the ordinary RC beam (Case 1) .....	29
Figure 3.4 Geometrical details of precast beams with loop joint (Case 2) .....	29
Figure 3.5 Analytical models of ordinary RC beam and precast beams with loop joints.....	31
Figure 3.6 Experimental and analytical load displacement relationship of ordinary RC beam (case 1) .....	33
Figure 3.7 Experimental and analytical deformed behaviors of ordinary RC beam.....	33
Figure 3.8 Experimental and analytical load displacement relationships of precast beams with loop joints (case 2) .....	35
Figure 3.9 Comparison of the experimental and the analytical results for case 2-1 (2NBS) .....	37
Figure 3.10 Comparison of the experimental and the analytical results for case 2-2.....	38
Figure 3.11 Load displacement relations case 3.....	39
Figure 3.12 Diagonal crack propagation behavior between the loops rebars in case 2 and case 3.....	40
Figure 3.13 Steel ratio in horizontal loop joints.....	40
Figure 4.1 Coupled RBSM and Solid FEM model.....	46

Figure 4.2 3D-model of the deformed reinforcement .....	47
Figure 4.3 RBSM and solid FEM boundary interface.....	48
Figure 4.4 Representation of the concrete and the steel elements.....	51
Figure 5.1 Representation of the geometrical features of the deformed rebar.....	54
Figure 5.2 Representation of the geometrical dimensions of the specimens and the test set up.....	55
Figure 5.3 Numerical models embedded with rebar D19.....	56
Figure 5.4 Numerical models embedded with rebar D25.....	57
Figure 5.5 Bond stress slip relations under varying concrete cover thicknesses.....	58
Figure 5.6 Illustration of the regions with reduced strength of concrete around the rebar.....	59
Figure 5.7 Revised bond stress slip relations with reduced strength of the concrete around the rebar.....	60
Figure 5.8 Comparison of the original and the revised model.....	61
Figure 5.9 Deformation response of c10 with rebar of D25.....	62
Figure 5.10 Deformation response of c25 with rebar of D25.....	63
Figure 5.11 Deformation response of c50 with rebar of D25.....	64
Figure 5.12 Deformation response of c100 with rebar of D25.....	65

Figure 5.13 Representation of the test set up in one end pull-out.....	68
Figure 5.14 3D model of the steel reinforcement.....	69
Figure 5.15 Numerical models for one end pull-out test.....	69
Figure 5.16 Stress slip relations of unconfined specimen embedded with rebar D19.....	71
Figure 5.17 Deformed behaviors of unconfined specimen embedded with rebar D19.....	72
Figure 5.18 Stress slip relations of confined specimen embedded with rebar D19.....	73
Figure 5.19 Deformed behaviors of confined specimen with $\varphi = 20$ degrees .....	74
Figure 5.20 Deformed behaviors of confined specimen with $\varphi = 30$ degrees .....	75
Figure 5.21 Stress slip relations of unconfined specimen embedded with rebar D29.....	77
Figure 5.22 Deformed behaviors of unconfined specimen embedded with rebar D29. ....	77
Figure 5.23 Details of the test specimens embedded with rebar D32 . ....	79
Figure 5.24 Details of the specimens used for the sensitivity analysis of rebar lug spacing. ....	80
Figure 5.25 Numerical models for evaluating the detailed failure behaviors in axially loaded RC prisms. ....	81

Figure 5.26 Internal crack formation with rebar D32. ....	82
Figure 5.27 Longitudinal crack formation with rebar D32. ....	84
Figure 5.28 Deformed behaviors with lug spacing of 30 mm.....	85
Figure 5.29 Deformed behaviors with lug spacing of 15 mm. ....	86
Figure 6.1 Representation of force resisting components of typical PBL shear connector.....	90
Figure 6.2 Geometrical details of the test specimen. ....	92
Figure 6.3 3D model of perforated steel plate using eight-noded nonlinear solid FEM.....	93
Figure 6.4 Analytical model of the test specimen. ....	94
Figure 6.5 Influence of lateral pressures on the shear capacity of PBL. ....	95
Figure 6.6 Comparison of test and analytical failure mode.....	96
Figure 6.7 Representation of various stages for shear response evaluation. ....	98
Figure 6.8 Detailed failure process and mechanism for low lateral pressure case. ....	99
Figure 6.9 Detailed failure process and mechanism for high lateral pressure case. ....	101
Figure 6.10 Analytical model of the specimen for evaluation of combined effects for the lateral pressure and hole diameter. ....	104

Figure 6.11 Illustration of the combined effects of the lateral pressures and the diameters of the holes on analytical shear capacities. ....	105
Figure 6.12 Comparison of the failure behaviors for low and high lateral pressures against 75-mm and 50-mm diameters of the holes at the peak stage.....	106
Figure 6.13 Geometrical details of the specimens for the transverse rebar effect. ....	108
Figure 6.14 Analytical models for the transverse rebar effect. ....	109
Figure 6.15 Representation of CEB-Shima hybrid bond model. ....	109
Figure 6.16 Comparison of shear capacities of specimen with and without rebar. ....	110
Figure 6.17 Comparison of the analytical and the empirical shear capacities. ....	113
Figure 6.18 Representation of various stages for shear response of transverse rebar effect.....	114
Figure 6.19 Failure process of the specimen without transverse rebar. ....	115
Figure 6.20 Failure process of the specimen with transverse rebar of fixed ends. ....	117
Figure 6.21 Failure process of the specimen with transverse rebar of free ends. ....	118
Figure 6.22 Comparison of strain distribution of transverse rebar for fixed and free ends cases. ....	121
Figure 6.23 Comparison of curvature distribution of transverse rebar for fixed and free ends cases. ....	122

Figure 6.24 Effect of the rebar diameter on the shear capacity. ....	123
Figure 6.25 Comparison of the analytical and the empirical shear capacities for rebar diameter effect. ....	124
Figure 6.26 Failure process of the specimen embedded with transverse rebar of D10.....	125
Figure 6.27 Failure process of the specimen embedded with transverse rebar of D13.....	126
Figure 6.28 Failure process of the specimen embedded with transverse rebar of D16.....	127
Figure 6.29 Comparison of strain distribution for different diameters of the transverse rebars.....	129
Figure 6.30 Comparison of curvature distribution for different diameters of the transverse rebars. ....	130
Figure 6.31 Analytical models with different rebar positions inside hole. ....	132
Figure 6.32 Load-displacement relationships with different rebar positions inside hole. ....	132
Figure 6.33 Failure process of the specimen with transverse rebar at a top position.....	133

Figure 6.34 Failure process of the specimen with transverse rebar at a middle position.....	134
Figure 6.35 Failure process of the specimen with transverse rebar at a bottom position.....	135
Figure 6.36 Comparison of strain distribution for the different positions of the transverse rebars inside hole. ....	138
Figure 6.37 Comparison of curvature distribution for the different positions of the transverse rebars inside hole. ....	139
Figure 6.38 Load-displacement relationships with different yield strengths of the transverse rebar. ....	140
Figure 6.39 Failure process of the specimen with transverse rebar of yield strength 295 MPa. ....	141
Figure 6.40 Failure process of the specimen with transverse rebar of yield strength 345 MPa. ....	142
Figure 6.41 Failure process of the specimen with transverse rebar of yield strength 490 MPa. ....	143
Figure 6.42 Comparison of the strain distribution with different yield strengths of the transverse rebar. ....	145
Figure 6.43 Comparison of the curvature distribution with different yield strengths of the transverse rebar.....	146

# 1 General Introduction

## 1.1 Background

Currently, the utilization and application of the precast concrete structure and concrete-steel composite structure have been increased in association with the increment of social demands of enhancement of the structural performance and productivity and the renewal of existing structures. Therefore, the detailed evaluation of mechanical behaviors of such kind of structures and the crack and stress propagation process inside the structure is desired to verify and improve the structural performance and to develop the new members. Especially, in terms of connections of precast concrete structures and concrete-steel composite structure, the modeling of the joint of members and boundary between different materials are very important because the mechanical and deformation performance at this local area is dominant factor of the whole structural performance. In particular, for precast concrete structures, the connection between the precast segments and the boundary surface between the precast segment and the cast in-situ concrete are dominant. For the joints, since the deformed rebar is usually used for connection and stress transmission, the detailed verification including the bond and anchorage of deformed rebar is required. On the other hand, for concrete-steel composite members, stress transmission between steel and concrete is that the dowel effect is utilized in shear and bond effect is utilized in tension. The deformed rebar is often arranged to support dowel effect of rebar and bond effect with concrete. The detailed verification including shear stress transfer of concrete as well as shear transfer and bond stress transfer of deformed rebar are also required.

The precast construction method not only have merit for rapid and high productivity of concrete structures but also regarded as one of the efficient and suitable

approaches for the maintenance and rehabilitation of the degraded infrastructures. Specifically, in RC bridges, the deteriorated deck slabs have been reported as serious issues. The cumulative damages have been observed in 40% of the bridges in Japanese expressway as most of the bridges are aged 30 years or more. The rehabilitation or the renewal projects of the deteriorated RC deck slabs in bridges are usually carried out using the precast segment construction method and this construction method provides the advantages related to the improvement of productivity, better-quality control and the shortening the construction duration. The precast segments are connected using the cast in-situ RC joints. The structural performance of the precast structures mainly depends on the mechanical performance and permeability of the cast in-situ RC joints. The various types of the cast in-situ RC joints and anchoring methods have been proposed in the past. Nowadays, several types of the cast in-situ RC joints have been applied in precast concrete segments suggested by CEB, 1993; BSI, 1997b & ACI, 2001 are; loop joints (horizontal and vertical types), headed rebar connections, lapping of bars with straight ends or with U-hook or with L-hook, and prestressing, etc). Furthermore, in recent years, the use of the concrete-steel composite construction has been adopted widely and extensively for contributing towards the superior structural response (strength, stiffness, resistance against seismic and monotonic loadings, and provision of reduced member sizes, etc.). In the concrete-steel composite construction, the shear connectors (head stud and Perfobond shear connector etc.) are employed to transfer the load between concrete and steel.

The critical aspect of the precast construction and the concrete-steel composite structures involves the existence of the connection region; cast in-situ RC joint between precast concrete segments and the load transferring element (shear connector). Furthermore, the cast in-situ RC joint in precast structures and the shear connector in the concrete-steel composite structures have the prime importance to fulfill the safety and serviceability throughout its designed service life.

To investigate the performance evaluation of the connection in concrete structure; cast in-situ RC joint and the shear connector, the interaction of concrete with deformed rebar in cast in-situ RC joint and with the steel connector in concrete-steel composite should be determined. However, it is difficult to investigate the detailed internal failure process comprehensively from experiments. The empirical observations

can provide the bearing capacity and the surface damage progress without the detailed internal failure process of the joints in precast and concrete-steel composite structures. Furthermore, the efficient design procedures of connections can be developed based on the comprehensive understanding of the internal bearing mechanism provided by the interaction of the constituent materials. The numerical simulations are helpful as they can assess not only the capacity and deformation performance but also the detailed internal failure process and the mechanism of the joints in precast and concrete-steel composite structures, quantitatively. The interaction of concrete and steel contributing towards the mechanical behavior of the joints is dependent on the macroscopic bond between deformed rebar and concrete. To evaluate the complex interaction between concrete and steel comprehensively, the mesoscale modeling is regarded as the most efficient numerical approach. Because, they enable to express the local response of the RC member with the actual geometrical features of reinforcement (e.g. rib height, shape and lug spacing, etc.). It has capability to reproduce the conical shaped cracks around the deformed rebar originating from the ribs.

In order to evaluate the interaction of concrete and steel and the detailed internal failure process of the connections; cast in-situ RC joint and the shear connector, the numerical simulation based on the Rigid Body Spring Model (RBSM) could be an effective approach. The 3D-RBSM highlights its advantage in capturing the heterogeneity of material, making it a suited numerical tool for capturing the nonlinear mechanical behavior of concrete. Additionally, the 3D-RBSM tends to simulate the detailed cracking information in reinforced concrete elements effectively such as crack spacing, crack width, and the direction of the crack propagation. Thus, it has potential to adequately assess the complicated mechanical interaction between concrete and steel at the cast in-situ RC joints in precast segments.

Considering the adequacy and suitability of the 3D-RBSM for simulating the nonlinear mechanical response of the concrete, the past researchers like Matsumoto et al. 2016, Eddy et al. 2016, Nagai et al. 2016 and Hayashi et al. 2017 etc. employed the RBSM based mesoscale numerical simulations for the performance evaluation of the beam column knee joints with mechanical anchorages (Figure 1.1). Their numerical approach successfully simulated the internal cracks patterns and surface deformed behaviors of the concrete. Similarly, they achieved to directly model the shape of the

ribs of deformed rebar for simulating the bond behavior of deformed rebar. The proposed model successfully performed the evaluation for the crack propagation mechanism and the bearing mechanism of the congestion of rebar arrangement (Figure 1.2). But the application was limited in the bond mechanism of deformed rebar and the modeling of rebar was same model with concrete, in which plasticity behavior of steel based on continuum mechanics did not considered.

The knowledge gained through the internal failure mechanism using 3D-RBSM possibly conduces the rationalization of the joint or interface behavior of not only reinforced concrete members but also steel concrete composite members and leads to develop the rational design procedures of such kind of elements in member.



**Figure 1.1 Congestion of the rebars at the RC joint due to seismic detailing (Matsumoto et al. 2016)**

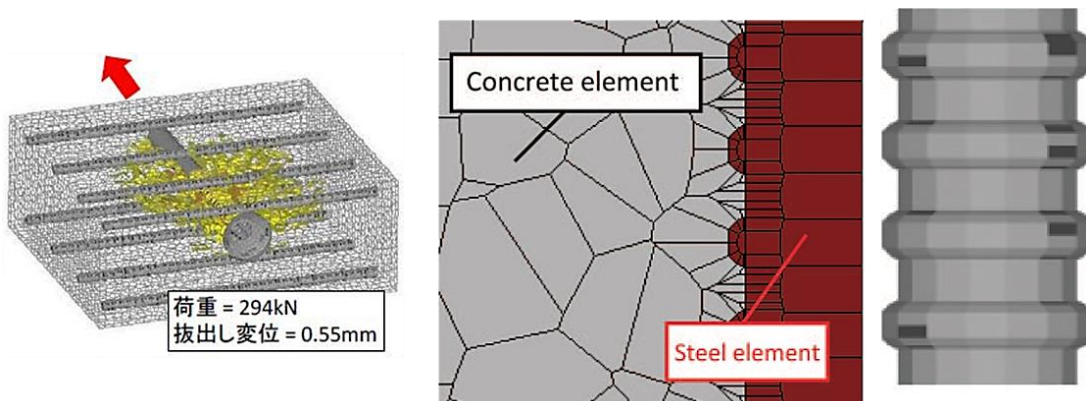


**Figure 1.2 Existing mesoscale model using RBSM (Hayashi et al. 2013)**

## **1.2 Literature review**

Considering the previously stated discussion regarding the cast in-situ RC joint in precast construction, the shear connector, and the interaction between concrete and steel at the joint interface, the literature review has been carried. In this study, the author had been mainly focused on three topics for the literature review to extract the historical information and the current issues. The targets of the literature review are about the loop joints in precast concrete, the bond behavior between concrete and deformed rebar, and the Perfobond shear connector in concrete-steel composite construction.

### ***1.2.1 RC Joints***

Various types of the cast in-situ RC joints and the anchoring methods have been proposed in precast concrete design. The main purpose of the cast in situ RC joints is to transfer the forces between the precast segments in order to fulfill the intended structural interaction and the mechanical response when the structure is being loaded. Therefore, the efforts are always devised and proposed for the structural improvement of the cast in-situ reinforced concrete joints in the precast construction. As stated earlier, the most commonly used the reinforced cast in situ joints are; loop joints (horizontal and vertical types), headed rebar connections, lapping of bars; with straight ends, U-hook and with L-hook, and the pre-stressed joints. The focus is specifically made for the RC loop joints here. The performance evaluation has been investigated in past studies considering various test parameters and the loading types.

Daniel et al. 2014, investigated the loop connections with the cast in situ fiber reinforced concrete. The effect of the addition of the steel fibers to the cast in situ concrete for reducing the width was performed and reported that the reduction of the cast in situ joint was observed by adding the steel fibers. The expression was also proposed to evaluate the capacity of the loop joint. Ryu et al. 2007, experimentally investigated the static and the fatigue strength of the loop joints under static and the fatigue loading. The main varying parameters were the diameters of the loop rebars and the width of the joints. The mechanical behaviors of the beams connected with loop joints were compared with the ordinary beam without loop joints. It was investigated that the overlapping region between the beams has similar or rather good mechanical

characteristics compared to the RC beam having no loop joints. Ong et al. 2006, investigated the flexural behavior of the precast joints connected through the horizontal loop joints. The precast specimens were connected using one to one loop joints. The varying parameters in the test were different overlapping longitudinal lengths, internal diameters of the mandrel of the loop, the overlapping transverse spacings, percentage of the penetrating bars, and the roughness of the interface. It was reported that the flexural strength was increased with the increased overlapping longitudinal lengths. Similarly, the decreased overlapping transverse spacings also increased the deformation capacity of the joint. Based on the experimentation, an empirical equation was also proposed to calculate the capacity of the specimens.

Joergensen et al. 2013 examined the limit analysis of the loop joints between precast concrete elements loaded in tensile loading. The varying parameters in the test were the overlapping length of the loop rebars, the spacing between the loop rebars and the amount of transverse reinforcement inside the loop joints. The mechanical behavior of the loop joint was investigated. These parameters were found to influence the capacity of the loop joint. The influence of these parameters was investigated to reduce the failure of the loop joint. Similarly, Yamamoto et al 2010 numerically simulate the quantitative failure behavior of the vertical type loop joints loaded under flexure loading using Rigid Body Spring Model and highlighted the internal failure mechanism in vertical type loop joints. Based on the numerical evaluation, the role of the penetrating rebars inside the loop joints was revealed. The failure mechanism for loop joints with and without the presence of the penetrating rebars inside the loop joints was discussed. Furthermore Junbao 2004, investigated the structural behavior of the loop connections in the precast beams connected through horizontal and vertical type loop joints.

Based on the literature review of the RC joints specifically the loop joints in precast concrete segments, it was observed that most of the studies were experimentally based and reported the influence of various test parameters on the bearing capacity of the joint. On the other hand, the performance evaluation and internal failure mechanism of the vertical type loop joint have already been investigated numerically, however, the detailed internal failure mechanism for horizontal type loop joints is unknown yet and therefore the comprehensive knowledge of internal failure process for horizontal type loop joints is required.

### ***1.2.2 Bond Behavior between concrete and steel***

The bond between steel and concrete is an important parameter that influences the overall structural performance when the system is loaded. The satisfactory and safe use of the reinforced concrete elements depends on the adequate bond strength characteristics of the deformed steel to concrete. The transfer of the stresses from the steel to adjoining concrete depends on the bond characteristics between steel and adjacent concrete.

The bond resistance mechanism of the steel and the concrete was investigated experimentally by many researchers under various test parameters and boundary conditions. The satisfactory bond performance between steel and concrete ensures adequate ductile behavior of the reinforced concrete (Rao et al. 2007). There was a wide range of variables that altered the effectiveness of the bond strength properties between steel and concrete .e.g. the concrete type and mechanical properties, the embedment length, geometrical features (rib height, shape and lug spacing, etc.) of the reinforcing steel, the diameter of the steel reinforcement, the concrete cover thickness and the amount of confinement (active and passive) applied, etc. (Metelli et al. 2014, Lemnitzer et al. 2009, Kankam et al. 1997).

The mode of failures (splitting and pull-out etc.) were also influenced by the amount of confinement applied. The studies revealed that the bond strength and ultimate slip for deformed rebars increased as the active confinement increased while other parameters were kept constant. The peak bond strength was more for the large diameter of the bar when the normal pressure was applied (Torre-Casanova et al. 2013, Raymond et al. 1965). Similarly, the bond strength was also found to be increased for reinforced concrete specimens embedded with round bars. The value of the end slip got increased as the externally applied lateral pressure was increased (Robins et al. 1982). The effects of confinement by transverse reinforcement and the concrete compressive strength were also analyzed in reinforced concrete joint conditions.

The confinement by transverse reinforcement had little influence on local bond behavior of deformed bars at the joint while ultimate bond strength increased proportionally as the square root of concrete compressive strength (Soroushian et al. 1991). The bond strength was found to be increased as the passive confinement through

concrete cover thickness increased (Iizuka et al. 2011). The investigations on the bond behavior of plain round bars in concrete subjected to complex lateral pressure showed that the ultimate and residual bond strengths got increased as the average lateral pressure was increased and the slip at ultimate bond strength reduced initially and then increased remarkably with the increased lateral pressure (Xu et al. 2014).

The confinement provided by the concrete cover and lateral reinforcing bars affected the bond splitting stress and cracking for reinforced concrete plates under uniaxial and biaxial tension (Dawood et al. 2012). Similarly, the effect of stress distribution variation inside the concrete and uneven contact pressure and friction between the concrete block and steel plate interface also affected the bond strength of the reinforced concrete block in the pull-out test (Chu et al. 2014).

The experimental investigations in the axially loaded reinforced concrete prisms in tension evaluating the detailed internal cracking mechanism were also conducted by Goto 1971, 1980. The formation and the orientation of the internal cracks, and the propagation of the internal and surface cracks were also investigated. Similarly, the effect of the rebar geometrical features on the bond behavior and the cracking pattern was also examined.

### ***1.2.3 The shear resistance of the Perfobond (PBL) shear connector***

In recent years, the use of concrete-steel composite construction has been adopted widely and extensively, contributing towards the superior structural response (strength, stiffness, resistance against seismic and monotonic loadings, and provision of reduced member sizes, etc.) and the ease of construction.

The critical aspect of the concrete-steel composite structures involves the existence of a load transferring element (shear connector) between steel and concrete. The composite action between concrete-steel in the composite construction heavily depends on the mechanical behavior of the shear connectors. Therefore, the efforts are always devised and proposed for the structural improvement of the shear connectors in concrete-steel composite construction.

The perfobond rib shear connector [Perfobond Leiste in German (PBL)], firstly introduced and developed by the German consultants, was being practiced in concrete-steel composite structures (hybrid girder joints, hybrid truss joints, the hybrid pylon

joints and the anchorage joints between the suspenders and the girders) (Kim et al. 2011, He et al. 2013, Liu et al. 2013, He et al. 2016, Li et al. 2018, Liu et al. 2018). It behaved like a key, and transferred the large internal forces between concrete and steel; and provided advantages related to ease of installation, economic reliability, ductility, and the excellent bearing capacity and the anti-fatigue behavior, etc. (Veldanda et al. 1992, Machacek et al. 2002, Yang et al. 2018).

Over the years, the researchers performed numerous studies to investigate the shear resistance of the PBL shear connector under the influence of various connection parameters and structural conditions. It was mentioned that the shear resistance of the PBL shear connector was dependent on the diameter of transverse reinforcement inside the hole of the PBL, the diameter of the hole, the thickness of the perforated steel plate, and the stress state in the vicinity of the concrete of the PBL (Wang et al. 2018). The experimental investigation (Taira et al. 2013), revealed that the shear resistance was influenced by the laterally applied varying amounts of pressures to surrounding concrete blocks of the PBL in the simple push-out test and the shear capacity was increased with the increased amounts of the applied lateral pressures. Similarly, the influence of the lateral constraints, concrete compressive strength, the diameter of transverse steel in the rib hole, and the bond between concrete-steel plate interfaces on the bearing mechanism of the PBL in push-out tests were also investigated, experimentally (Zhao et al. 2018).

Furthermore, an experimental study was performed to evaluate the shear resistance capacity and the failure behavior of the PBL under the effect of mechanical properties of concrete and the different rib arrangements and a shear capacity equation was proposed that took into account the influence of the rib height, the rib spacing, and the rib arrangement (Ahn et al. 2010). Similarly, experimental and parametric based studies were also carried out to observe the effect of different types of rib patterns, rib hole configurations including the varying number of drilled holes in rib and the transverse rebar effect inside rib hole, etc. on the shear response, the modes of failure and the slip response of the PBL (Vianna et al. 2013, Zheng et al. 2016).

Furthermore, it was reported that the shear resistance and the failure modes (local shear failure and splitting failure) of the PBL shear connector were also dependent on the concrete sizes of the adjoining concrete blocks of the PBL in the simple push-out test (Nakajima et al. 2018). Considering the PBL shear connector

relatively more effective concerning the structural integrity compared with the conventional shear connectors (head studs and group studs etc.), the shear resistance of the PBL was also studied in various concrete-steel composite structural elements e.g. slab, slim floor steel beams, and the diaphragm walls, etc. (Jeong et al. 2009, Chen et al. 2016, Hosseinpour et al. 2018).

There existed two major investigation techniques or approaches for the shear response evaluation of the PBL, firstly through the experimental studies by conducting model tests and secondly through the numerical analyses using the finite-element method (FEM). On the one hand, most of the past studies were experimental based which evaluated the structural performance of the PBL. On the other hand, the past numerical simulation studies utilized the finite element analyses mainly focused on capturing the test shear strength and the macroscopic load-displacement response under the influence of several test parameters that affected the shear capacity of the PBL and mostly addressed the shear resistance (deformation, stress contours and strain distributions) of the steel plate (Al-Darzi et al. 2007, Yu et al. 2012, Fan et al. 2014, Liu et al. 2019, Li et al. 2019, Liu et al. 2020). In contrast to focus on steel plate, few simulation studies (Munemoto et al. 2014) were conducted aimed at verifying the reproducibility of crack propagation behaviors and the failure modes of concrete.

The investigation and understanding regarding the detailed internal failure mechanism are important and essential for establishing rational design methods and reinforcement details. Therefore, it is required to analyze the internal failure behavior of concrete comprehensively using numerical simulation analyses. Therefore, in the current research focus is made to investigate the shear strength of the PBL shear connector and to highlight the detailed failure process of concrete, especially the internal crack propagation behavior and stress distributions, through simulation analyses, which has not been discussed efficiently in past researches.

### **1.3 The purpose and objectives**

Based on introduction and literature review of the previous studies, it can be assessed that the information regarding the detailed internal failure process and mechanism of the connections is insufficient. The comprehensive evaluation can be

achieved using 3D-RBSM, as it has potential to evaluate the nonlinear mechanical response of RC, effectively. The complex bond behavior between concrete and the deformed rebar of the RC joints can be efficiently evaluated through mesoscale analyses using 3D-RBSM. The past researches performed the mesoscale analyses, as discussed in section 1.1 and employed the rigid body model for the deformed rebar considering the geometrical features of the rebar. However, the steel is a continuous material and the reproducibility of the elastoplasticity of the steel in numerical simulation was the limitation in those models, as the 3D-RBSM is suitable for capturing the mechanical behavior of heterogeneous material like concrete.

Considering the limitations of the existing mesoscale models based on 3D-RBSM, the coupled RBSM and solid FEM model has been adopted for the numerical evaluations (Ikuma et al. 2017, Karam et al. 2019). In coupled RBSM and solid FEM model the concrete is modeled using 3D-RBSM, and the steel is modeled using eight-noded nonlinear solid finite elements and has capability to simulate the nonlinear behavior of concrete and the elastoplasticity of the steel simultaneously. In concrete-steel composite structures, the shear resistance is mainly contributed by the steel shear connectors and is of major concern. In this regard, coupled RBSM and solid FEM model is an adequate numerical tool as the steel shear connector is modeled using nonlinear 3D finite elements.

Based on the discussion stated earlier, the purpose and objective of this study is explained as follows:

The numerical evaluations to investigate the internal cracking behavior specifically the normal stress distribution of the concrete for various structural behaviors (the macroscopic bond behavior between the concrete and the deformed rebar) using the mesoscale numerical investigations through coupled RBSM and solid FEM model as the comprehensive understanding of the internal failure mechanism is still insufficient.

The evaluation of the connection (loop joints in precast beams and the Perfobond shear connector in steel-concrete composite construction) in concrete structures as there are no numerical investigations yet, to simulate the internal failure mechanism and to demonstrate the reasons behind the occurrence of any particular failure behaviors of concrete, comprehensively. These failure mechanisms are beneficial

to have knowledge about the resistance mechanism of the joints and for establishing the design procedures.

## **1.4 Organization of dissertation contents**

The flow chart of this study is given in Figure 1.3. The dissertation overall consists of seven chapters. The contents of this dissertation are briefly explained as follows.

Chapter 1 is the introduction of this study, including the research background, a general review of related references, the study objectives and the organization of the dissertation.

Chapter 2 includes the analytical approach based on 3D-RBSM and the beam element model to simulate the mechanical behavior of the RC under various structural conditions. The basic characterizations regarding the modeling of the concrete by employing the 3D-RBSM (constitutive models, the material parameters and verification of mesh size dependency) and the modeling of the steel reinforcement by using the beam element are highlighted. The applicability of the 3D-RBSM and beam element model is highlighted in next chapter by determining the performance evaluation of loop joints in precast construction.

Chapter 3 presents the performance evaluation especially the failure mechanism of the precast beams using the horizontal type loop joints. The comparison of the loop joints with and without penetrating rebars inside the loop is also evaluated. Moreover, the influence of the loop interval and amount of steel of penetrating rebars inside the loop joint are investigated numerically.

Chapter 4 discusses limitation of the conventional 3D-RBSM and the beam element model to simulate the mechanical behavior of the reinforced concrete (RC). Furthermore, the need of proposing a new analytical model is also explained and introduction to the new numerical model; coupled RBSM and the nonlinear solid Finite Element Method (FEM) is presented. The basic characterizations regarding the modeling of the concrete, the steel, and the concrete-steel interface in coupled RBSM and solid FEM model are demonstrated. The utilization of the coupled RBSM and solid FEM model is discussed in next chapters in order to evaluate the complex interaction

between concrete and deformed rebar and to investigate the shear resistance of the PBL shear connector.

Chapter 5 illustrates the numerical evaluation of the Macroscopic bond behavior of deformed rebar using coupled RBSM and solid FEM model and also presents the internal failure mechanism of the concrete in axially loaded RC specimens in two ends pull-out test, RC specimens in one end pull-out test and detailed failure behavior in axially loaded RC prisms under direct tension.

Chapter 6 presents the numerical evaluation of shear resistance of the Perfobond (PBL) shear connector using the coupled RBSM and solid FEM Model. The shear resistance evaluation of the PBL is performed for detailed internal crack propagation process and the failure mechanism of the concrete influenced by the varying amounts of the lateral pressures. Similarly, the combined effects of the lateral pressures and the hole diameters are evaluated. Furthermore, the numerical evaluations of the PBL are also performed for the various effects of the transverse rebar inside the hole of the PBL.

Chapter 7 includes the conclusions derived from this study and recommendations for future study.

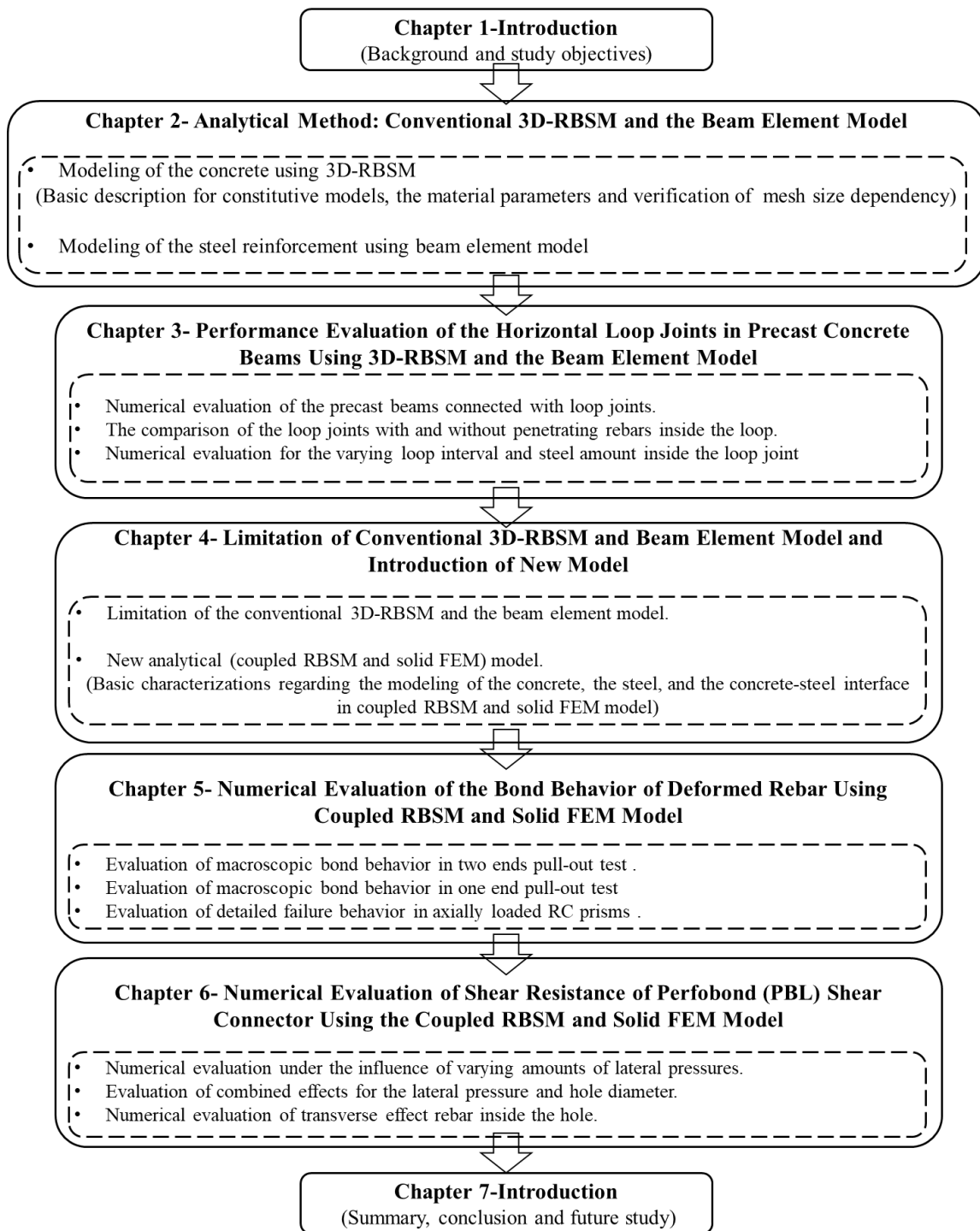


**Figure 1.3 Organization of the dissertation**

## **2 Analytical Method: Conventional 3D-RBSM and the Beam Element Model**

### **2.1 Introduction**

In this chapter, the analytical approach based on the Rigid Body Spring Model (3D-RBSM) and the beam element model to simulate the mechanical behavior of the reinforced concrete (RC) are explained. The basic characterizations regarding the modeling of concrete by employing the 3D-RBSM and the modeling of steel reinforcement by using the beam element are reviewed. Firstly, the brief description for the 3D-RBSM is presented. Furthermore, the discussion is also made for the constitutive models and the calibrated model parameters of the springs (normal and shear) in 3D-RBSM. The verification of the mesh size dependency of the model parameters is also investigated by numerical analyses for uniaxial compression, uniaxial tension and three-point loading tests.

After highlighting the description of the 3D-RBSM, the analytical method for the modeling of the steel reinforcement using the beam element is illustrated.

### **2.2 Modeling of the concrete using 3D-RBSM**

#### ***2.2.1 General description of 3D-RBSM***

The concrete is modeled using 3D-RBSM. The 3D-RBSM is comprised of an assemblage of rigid elements. The rigid elements are interconnected by employing the normal and the tangential springs along with their interfaces of boundaries. The 3D-RBSM has been proved to be an effective and efficient numerical approach for the

quantitative evaluation of the nonlinear mechanical response of the concrete, such as crack propagation behavior, the shear transfer behavior of the cracked surfaces and the compression failure assessment inclusive of localization and the constraint pressure dependence (Yamamoto et al. 2008). The cracks initiate and propagate through the interfaces of boundaries of the rigid elements and are strongly influenced by the mesh design of the concrete in numerical analyses. In order to overcome this fact, the random geometry of rigid particles has been adopted by using the Voronoi diagram as shown in Figure 2.1, and the elements in 3D-RBSM are discretized using random geometry mesh Bolander et al. (2011). The Figure 2.1 illustrates; (1) discretization of the concrete using Voronoi diagram; (2) representation of the integration points on the boundary interface of rigid particles; and (3) representation of the normal and the shear springs.

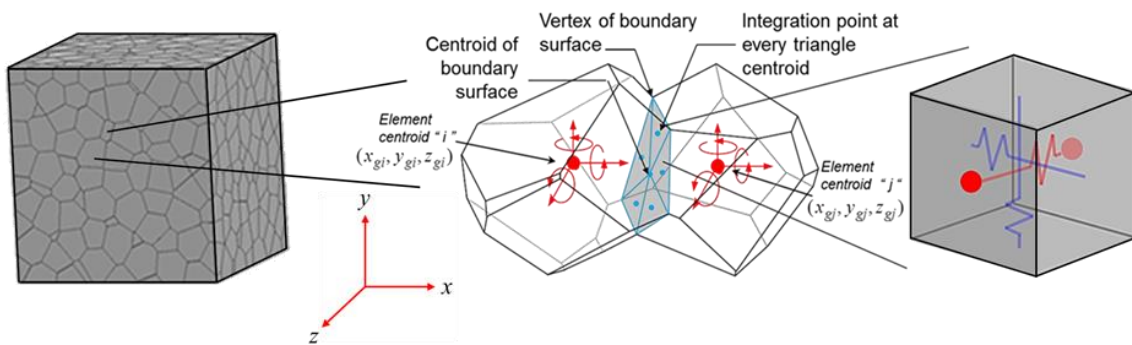


**Figure 2.1 Description of the 3D-RBSM element**

The complete detail regarding the element formulation of 3D-RBSM as well as the calibrated parameters of the springs for concrete materials is available in the previous research by Yamamoto et al. (2008). Here solely the basic description of 3D-RBSM has been discussed, briefly. A two-element assembly of 3D-RBSM as shown in Figure 2.1, is employed to derive the system equilibrium equations in 3D-RBSM. The response of the spring model represents an insight into the interaction between the rigid particles. Each rigid particle involves the three rotational and the three translational degrees of freedom assigned at the geometric centroid that characterize the particles according to the Voronoi diagram as illustrated in Figure 2.1.

The springs are defined on the integration points as depicted in Figure 2.1. The integration points are produced through the division of the surface of rigid particles into

sets of triangles as shown in Figure 2.1, the geometric centroid of each triangle is corresponding to one integration point. Furthermore, the induction and arrangement of integration points and springs in such manner as shown in Figure 2.1, automatically develops the effects of flexural and torsional behavior without the need to introduce any additional rotational springs. The integration point of each element consists of one normal and two tangential springs (Yamamoto et al. 2014).

### 2.2.2 Constitutive models and model parameters of concrete in 3D-RBSM

The numerical simulation analyses for the nonlinear behavior of concrete in 3D-RBSM greatly depends on the constitutive models assigned to the springs. The combination of the constitutive models as well as the distribution of the springs over the boundary surfaces together facilitates the reproduction of the nonlinear mechanical response of concrete. The formation of cracks in concrete is expressed by the failure of these springs. The models that can capture the localization and softening behavior under various stress states are proposed and applied to the constitutive models of the springs.

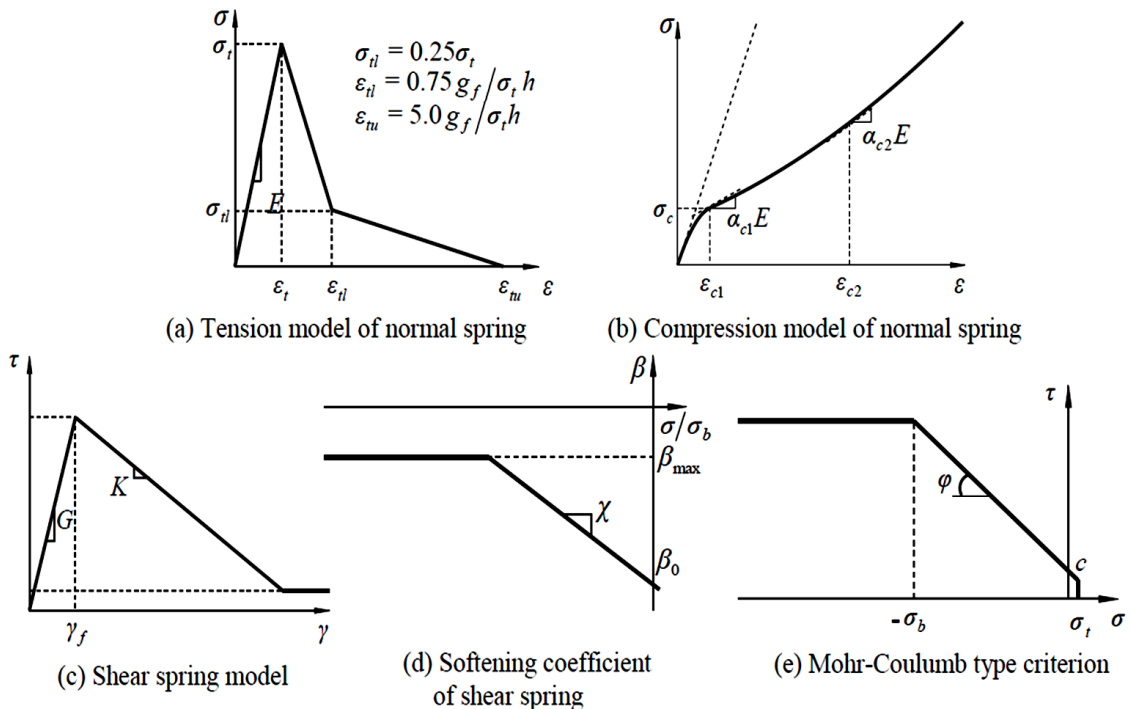


**Figure 2.2 Constitutive models of normal and shear springs in 3D-RBSM**

The material constitutive models for tension, compression, and shear behaviors of concrete are presented in Figure 2.2. The tensile model for normal springs is shown in Figure 2.2 (a). The tensile behavior is modeled as linear elastic up to the tensile strength ( $\sigma_t$ ) and then changes to a bilinear softening branch. After the occurrence of the cracking, the quarter (1/4) model is assumed. The strain parameters  $\varepsilon_{tu}$  and  $\varepsilon_{tl}$  are the functions of tensile fracture energy, tensile strength, and the distance between the nuclei represented by  $g_f$ ,  $\sigma_t$ , and  $h$ , respectively. The compressive stress-strain relation for the normal springs has also been shown in Figure 2.2 (b), modeled as S-shape curve considering the combination of two quadratic functions using the parameters defined in the following equations; from Equation ((2.1) and to Equation (2.2). The parameters  $\sigma_c$  and  $\varepsilon_{c1}$  are the compressive strength and the corresponding compressive strain of the normal spring, as shown in Equation ((2.1) and Equation (2.2), respectively. The values of  $\sigma_c$ , as well as  $E$ , are related to the macroscopic material parameters of the concrete,  $f_c^*$  and  $E^*$ , by the factors. The nonlinearity of the compression behavior of the normal spring is controlled by the parameters  $\sigma_c$ ,  $\varepsilon_{c2}$ ,  $\alpha_{c1}$  and  $\alpha_{c2}$ .

$$\sigma = \begin{cases} a_0\varepsilon^2 + b_0\varepsilon & (\varepsilon > \varepsilon_{c1}) \\ a_1\varepsilon^2 + b_1\varepsilon + c_1 & (\varepsilon \leq \varepsilon_{c1}) \end{cases} \quad (2.1)$$

$$\varepsilon_{c1} = -\frac{2\sigma_c}{E(1 + \alpha_{c1})} \quad (2.2)$$

$$a_0 = -\frac{E(1 - \alpha_{c1})}{2\varepsilon_{c1}} \quad (2.3)$$

$$b_0 = E \quad (2.4)$$

$$a_1 = \frac{E(\alpha_{c2} - \alpha_{c1})}{2(\varepsilon_{c2} - \varepsilon_{c1})} \quad (2.5)$$

$$b_1 = \frac{E(\alpha_{c1}\varepsilon_{c2} - \alpha_{c2}\varepsilon_{c1})}{\varepsilon_{c2} - \varepsilon_{c1}} \quad (2.6)$$

$$c_1 = -a_1 \varepsilon_{c1}^2 - b_1 \varepsilon_{c1} - \sigma_c \quad (2.7)$$

The combination of two shear springs controls the shear behaviors in 3D-RBSM, as shown in Figure 2.2 (c). The combined shear strain has been shown in Equation (2.8), where  $\gamma_l$  and  $\gamma_m$  represent the strains of the springs in each direction shear to the boundary surface and similarly the combined shear stress ( $\tau$ ) can be calculated in each direction ( $\tau_l$  and  $\tau_m$ ) from the shear stress–strain relation as shown in Equation (2.9).

$$\gamma = \sqrt{\gamma_l^2 + \gamma_m^2} \quad (2.8)$$

$$\tau_l = \tau \frac{\gamma_l}{\gamma}, \tau_m = \tau \frac{\gamma_m}{\gamma} \quad (2.9)$$

$$\tau = \begin{cases} G\gamma & (\gamma < \tau_{f,soft} / G) \\ \tau_{f,soft} & (\gamma \geq \tau_{f,soft} / G) \end{cases} \quad (2.10)$$

$$\tau_{f,soft} = \max(\tau_f + K \langle \gamma_{max} - \gamma_f \rangle, 0.1\tau_f) \quad (2.11)$$

$$K = \beta G \quad (2.12)$$

$$\beta = \min(\beta_0 + \chi(\sigma / \sigma_b), \beta_{max}) \quad (2.13)$$

$$\tau_f = \begin{cases} c - \sigma \tan \varphi & (\sigma > -\sigma_b) \\ c + \sigma_b \tan \varphi & (\sigma \leq -\sigma_b) \end{cases} \quad (2.14)$$

$$\beta_{cr} = \frac{\varepsilon_t}{\varepsilon} \exp \left\{ \frac{\kappa}{\varepsilon_{tu}} (\varepsilon - \varepsilon_{tu}) \right\} \quad (2.15)$$

The stress–strain relationship envelope for the shear behavior is shown in Figure 2.2 (d) and from Equation (2.10) to Equation (2.13). The parameter  $\gamma_{max}$  describes the maximum shear strain in the loading history whereas the parameters  $G$  and  $K$  refer to the elastic shear modulus and the shear softening coefficient, respectively. The shear

softening coefficient ( $K$ ) depends on the magnitude of normal stress of the normal spring and the parameters  $\beta_0$ ,  $\beta_{max}$  and  $\chi$ . The Mohr-Coulomb criterion is selected as the failure envelope for the shear springs as shown in Figure 2.2 (e) and Equation (2.14), where  $c$  and  $\varphi$  represent the cohesion and the angle of internal friction, respectively. Moreover, when a crack forms, it is considered that the shear stress decreases with an increase in crack width at the cracked surface, and the tensile softening (Figure 2.2 (a)) occurs in the normal spring. The shear stress calculated using Equation (2.9) is then revised using a shear deterioration coefficient ( $\beta_{cr}$ ), as shown in Equation (2.15), to represent the decrease in shear stress due to increased crack width. The shear deterioration coefficient ( $\beta_{cr}$ ) is found to be dependent on the cracking and the strains  $\varepsilon_i$  and  $\varepsilon_{iu}$  of the normal spring, respectively.

**Table 2.1 Calibrated model parameters of normal spring**

Elastic Modulus	Tensile Response		Compressive Response			
	$\sigma_t$ (N/mm <sup>2</sup> )	$g_f$ (N/mm)	$\sigma_c$ (N/mm <sup>2</sup> )	$\varepsilon_{c2}$	$\alpha_{c1}$	$\alpha_{c2}$
$1.4E^*$	$0.65f_t^*$	$0.5G_F^*$	$1.5f_c'^*$	-0.015	0.15	0.25

**Table 2.2 Calibrated model parameters of shear spring**

Shear stiffness	Fracture Criterion			Softening Behavior			
	$c$ (N/mm <sup>2</sup> )	$\varphi$ (degree)	$\sigma_b$ (N/mm <sup>2</sup> )	$\beta_0$	$\beta_{max}$	$\chi$	$\kappa$
$0.35E$	$0.14f_c'^*$	37	$1.00f_c'^*$	-0.05	-0.025	-0.01	-0.3

\* The macroscopic material parameters obtained from the experimental results

$E^*$ : Elastic Modulus,  $f_t^*$ : Tensile Strength,  $g_f^*$ : Fracture Energy,  $f_c'^*$ : Compressive Strength

The calibrated material parameters of the constitutive models for normal and shear springs are shown in Table 2.1 and Table 2.2, respectively. The calibration of material parameters of the constitutive models has been conducted through the parametric analyses (specimen size, shape, mesh size and compressive strength of concrete) comparing with the macro stress-strain test relationships including the

softening part subjected to uniaxial compression, hydrostatic compression, triaxial compression and uniaxial tension (Yamamoto et al. 2008, Gedik et al. 2011, Yamamoto et al. 2014). The above-mentioned model parameters are valid for the normal strength concrete having mesh size ranging between 10 to 30 mm. It has been also been confirmed that the 3D-RBSM incorporating these calibrated material parameters effectively reveals the initiation and propagation of visible cracks in concrete. The compression model of the normal spring does not include the softening behavior and the failure of the normal spring. However, the compressive failure response including confinement effect and localized failure behavior can be reproduced by means of the combination of normal and shear spring in 3D-RBSM.

### ***2.2.3 Verification for mesh size dependency of the numerical model***

As discussed earlier in section 2.2.2, Table 2.1 and Table 2.2, the material parameters of the constitutive models of concrete in 3D-RBSM have been calibrated by conducting parametric analyses comparing with the test results of normal strength concrete considering the average mesh size of approximately 10 mm. Whereas, the proper numerical modeling of concrete under various investigations (evaluation of the macroscopic bond behavior around the deformed rebar utilizing mesoscale simulations) which will be discussed in next chapters of the current study, often require to select the average mesh size less than average mesh size (10 mm) for which the material parameters of the constitutive models have been originally calibrated in 3D-RBSM.

Therefore, it is an important aspect to investigate the mesh size dependency of the 3D-RBSM employing for the modeling of concrete. The mesh size dependency of the 3D-RBSM is investigated numerically through the sensitivity analysis of mesh size considering mesh size less than 10 mm under uniaxial compression and uniaxial tension and three-point loading tests. In a sensitivity analysis of mesh size, the diameter and height of the cylinder for direct compression and tension cases are 100 mm and 200 mm, respectively with the concrete compressive strength around 45.2 MPa. The dimensions of the beam for the three-point loading test are 400 x 100 x 100 mm<sup>3</sup> with a loading span of 300 mm. The height and width of the notch are 20 mm and 5mm, respectively as shown in Figure 2.3. The average mesh sizes considered in the sensitivity analysis of

mesh size are 3 mm and 10 mm. The analytical models in this regard are shown in Figure 2.4.

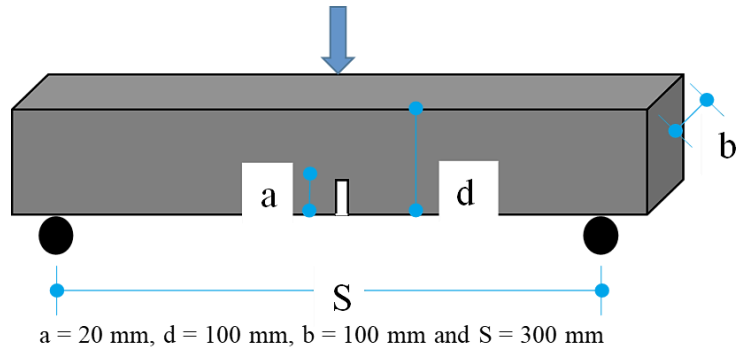


**Figure 2.3 Geometrical dimensions of the beam for three-point loading test**

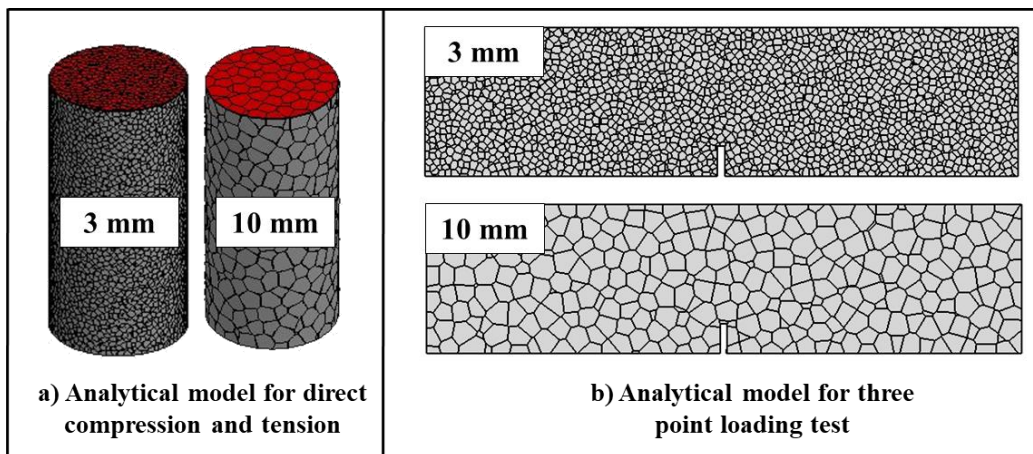
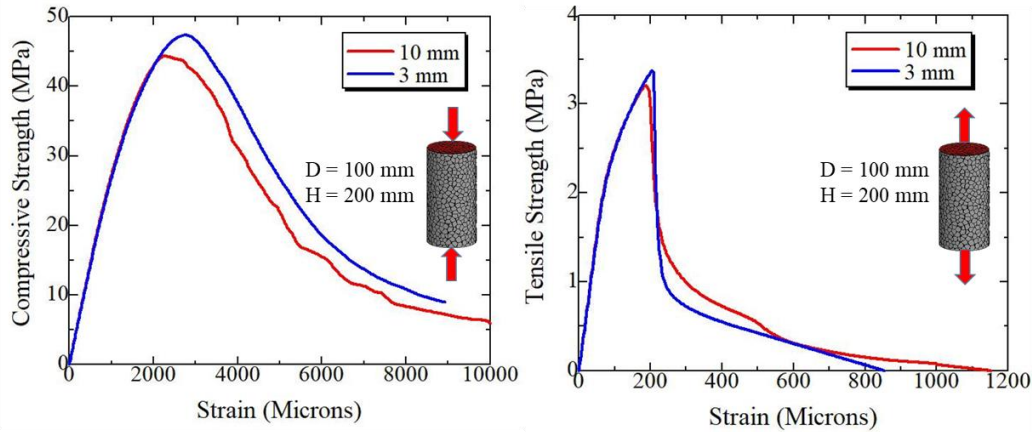


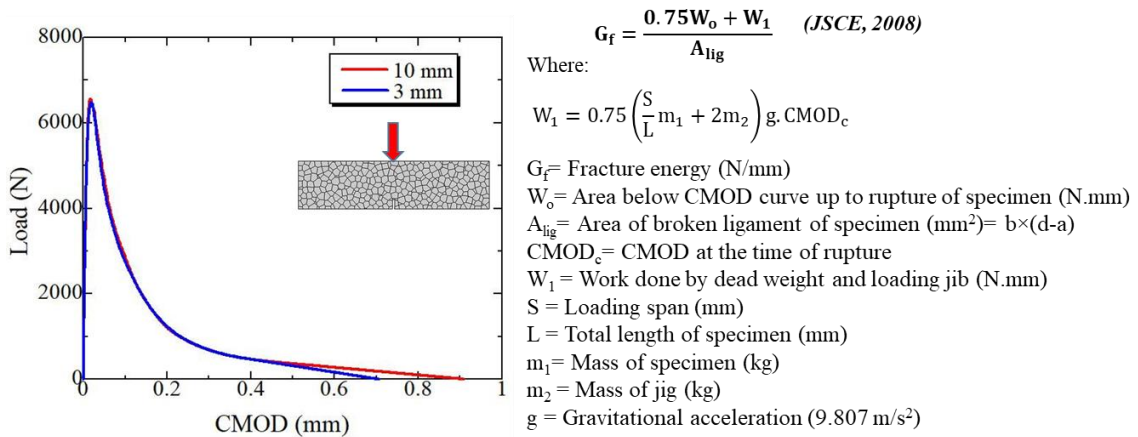
**Figure 2.4 Analytical models for the verification of mesh size dependency**

The stress-strain relationships corresponding to direct compression case, direct tension case, and three-point loading test are discussed here. The stress-strain relationships against direct compression and direct tension are shown in Figure 2.5 (a). The load and crack mouth opening (CMOD) relationship in three-point loading is also shown in Figure 2.5 (b) to evaluate the tensile fracture energy as model parameter required in Table 2.1 using the relationship proposed by the standard specification of Japan Society of Civil Engineers (JSCE, 2008) for concrete structures. Figure 2.5 (a); stress-strain relationships in direct compression and direct tension and Figure 2.5 (b); the relationship for three-point loading against 3 mm and 10 mm mesh sizes show that

the analytical results are very close to each other and the difference is minimal for 3 mm and 10 mm mesh sizes and do not influence the tensile fracture energy and the difference can be ignored here.



a) Analytical results for direct compression and tension



b) Analytical results for three point loading

**Figure 2.5 Analytical results for mesh size dependency of 3D-RBSM**

The results for mesh sensitivity analysis show that the numerical model does not have mesh size dependency and can be employed for the numerical analyses in this study without requiring any modification based on mesh size dependency.

### 2.3 Modeling of steel reinforcement using the beam element model

The steel reinforcement embedded in concrete is modeled as series of regular beam elements that can be freely located within the structure, regardless of the concrete mesh design. The beam element has capability to simulate the bending effects of the steel reinforcement. The two translation and one rotational degree of freedoms are defined on each beam node using the springs. The beam elements are attached to the concrete particles utilizing zero-size link elements as shown in Figure 2.6.

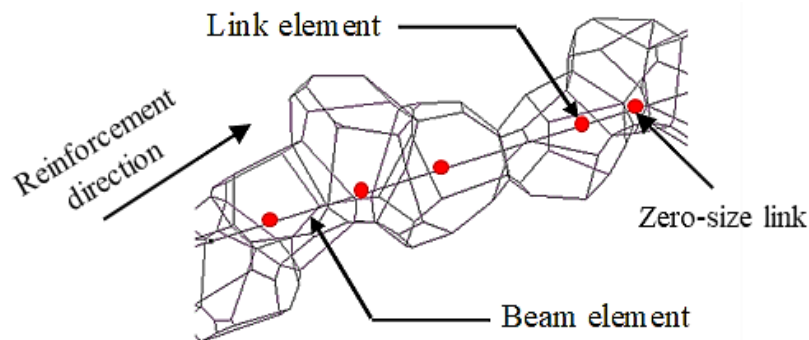


**Figure 2.6 Model of steel reinforcement using beam elements (Yamamoto et al. 2014)**

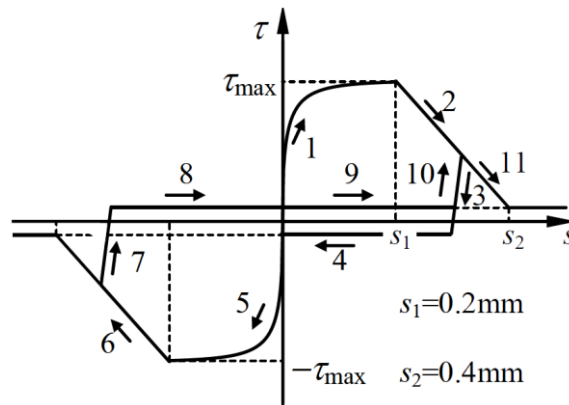


**Figure 2.7 Bond stress-slip relationship (Yamamoto et al. 2014)**

For the stress-strain relationship of the steel reinforcement, the bilinear kinematic hardening model is applied (Yamamoto et al. 2014) as shown in Figure 2.7. The bond stress-slip relationship as shown in Figure 2.7 contains the two parts; (1) up to the shear strength, the relationship proposed by Suga et al., (2001) governs, (2) in the post-peak region the relation proposed by the CEB-FIB is adopted, (CEB, 1990). The

bond stress-slip relationship has been provided in the spring parallel to the reinforcement of the link element. The springs parallel to reinforcement are responsible for the bonding characteristics and the stress transfer mechanism between the steel reinforcement and the concrete.

The springs in the direction perpendicular to the reinforcing steel axis are linear elastic and are given sufficiently large stiffness. The relative displacement between the 3D-RBSM element and the reinforcing steel is neglected in the perpendicular direction of the steel.

## **2.4 Summary**

In this chapter, the analytical methodology including modeling of concrete utilizing the 3D-RBSM and the modeling of steel reinforcement by using the beam element to simulate the mechanical behavior of reinforced concrete (RC) were explained. The verification of the mesh size dependency of the model parameters was also investigated numerically through the sensitivity analysis of the mesh size under uniaxial compression and uniaxial tension and three-point loading tests and revealed that the 3D-RBSM can be employed without the need to consider mesh size dependency in numerical analyses for the element sizes ranging between 3 mm to 10 mm. The basic description regarding the 3D-RBSM and the beam element model were reviewed

After presenting the relevant description of the 3D-RBSM and the beam element model, the applicability of the conventional 3D-RBSM and the beam element model will be confirmed in the next chapter through the performance evaluation of the horizontal loop joints in precast beams.

# **3 Performance Evaluation of the Horizontal Loop Joints in Precast Concrete Beams Using 3D-RBSM and the Beam Element Model**

## **3.1 Introduction**

Attempts to use precast concrete elements have been increasing widely in recent years for improving the productivity, better-quality control and the effective completion of the reinforced concrete structures. Nowadays, Several types of the reinforced cast in situ joints are being applied in precast concrete members based on the specifications proposed by the various design codes for loop joints (horizontal and vertical types), headed rebar connections, lapping of bars; with straight ends, U-hook and with L-hook, and the pre-stressed joints (Junbao et al. 2004).

Specifically mentioning about the loop joints, they have more significance and the advantages in the loop rebar joints, the bond stress of straight parts and the bearing pressure of the curved parts can be utilized effectively. Thus, there is a possibility that the joint length can be shortened or minimized compared with the conventional lap joint. The loop joints are divided into two categories; (1) Vertical loop joints and (2) Horizontal loop joints, as shown in Figure 3.1.

The vertical type loop joints are the most commonly used in precast elements arranged vertically to beams or slab members. The vertical type loop joints have been investigated experimentally by many researchers subjected to various structural conditions of the site. Furthermore, the horizontal loop joints are also useful depending on the construction conditions (e.g. shear key in vertical joints of precast wall panels subjected to shear loading, and so on). Due to the limited use of the horizontal loop

joints as shown in Figure 3.1, the horizontal loop joints have not been investigated sufficiently yet and the detailed internal failure process and mechanism are unknown.

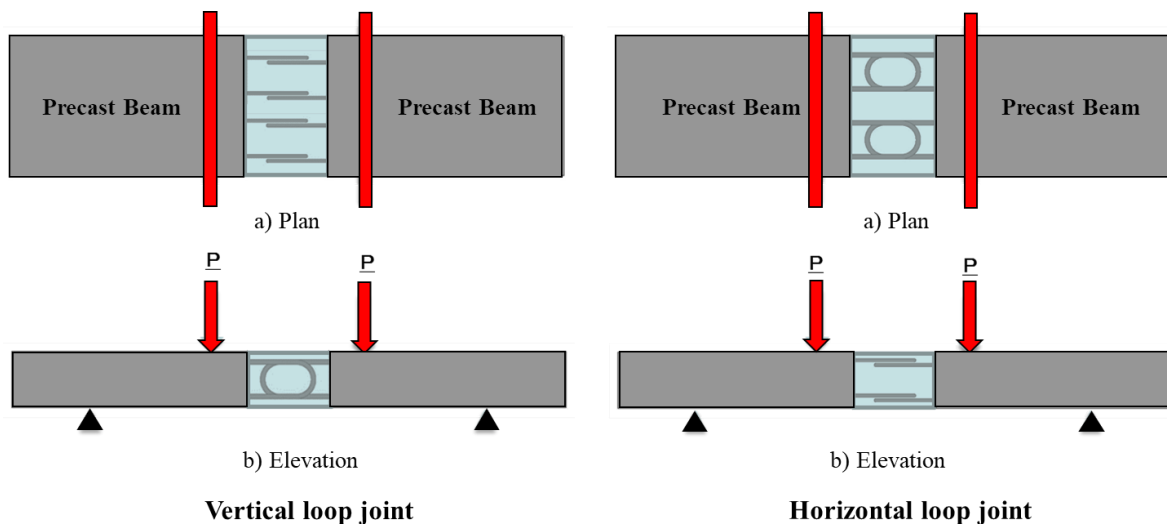


**Figure 3.1 Loop (vertical and horizontal) joints in precast beams**

This chapter mainly deals with the performance evaluation especially the failure mechanism of the precast beams using the horizontal type loop joints. Moreover, the influence of the inner reinforcing rebars inside the loop joints on the mechanical response of the loop joint is also investigated using numerical approaches based on the experimental results. In the current research, the author solely focused on the numerical evaluation to highlight the internal fracture mechanism of the already designed and experimentally investigated loop joints performed by other researcher.

### **3.2 Test overview and numerical modeling**

In this chapter, two different types of test specimens are discussed, the ordinary reinforced concrete (RC) beam and the precast beams joined through cast in situ horizontal loop joints, represented by case 1 and case 2, respectively. The case 1 represents the ordinary RC beam without the presence of the loop joint. The case 2 is further subdivided into two parts; case 2-1 and case 2-2. The case 2-1 and case 2-2 represent the horizontal loop joints with and without inner reinforcing bars inside the loop joint, respectively as shown in Figure 3.2.

The experiment was performed to investigate the mechanical behavior of the horizontal type loop joints between the precast concrete beams. The role of the inner reinforcing rebars against deformation capacity and the failure behavior also examined. The comparison for load carrying capacity was also made for the loop joints with and without the presence of the inner reinforcing rebars inside the loop joint.

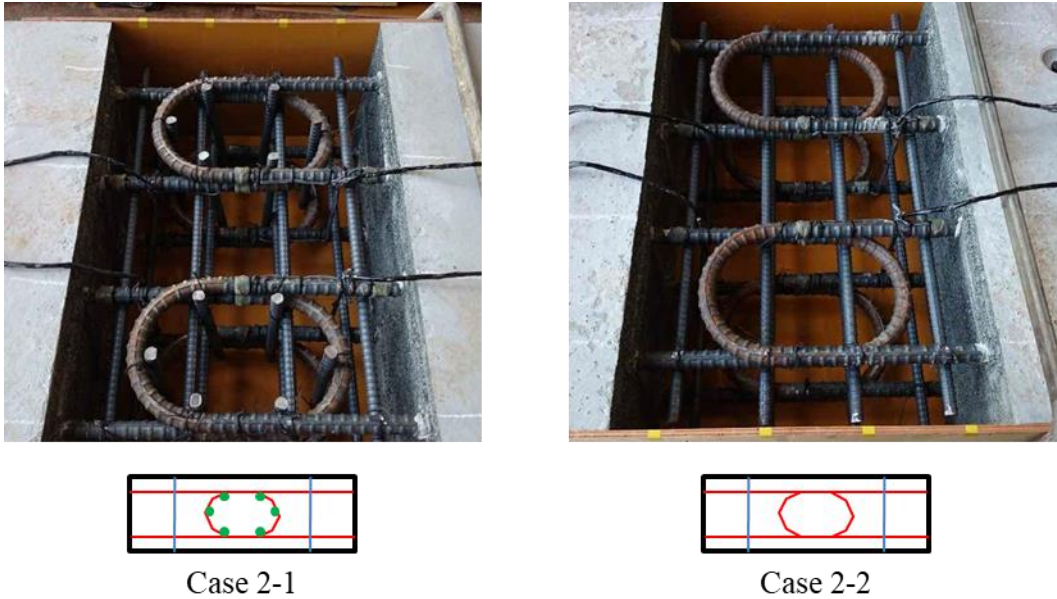


**Figure 3.2 Horizontal loop joint with and without inner reinforcing bars**

The geometrical dimensions (all are in mm) of the test specimens (case 1 and case 2) are shown in Figure 3.3 and Figure 3.4, respectively. The RC beam has dimensions of  $4000 \times 1000 \times 400 \text{ mm}^3$  while the loading span is 3600 mm. The main reinforcement of D32 and the distribution rebars of D22 and D16 were used. The specimen with loop joints as shown in Figure 3.4 has the same dimensions as that of the ordinary RC beam. The specimen with loop joints has two adjoining precast concrete beams, each beam has a dimension of  $1700 \times 1000 \times 400 \text{ mm}^3$ .

The broken lines in Figure 3.4 represent the cast in situ reinforced loop joint with a joint length of 600 mm. The concrete compressive strength of the adjacent precast beams and the cast in situ loop joint was 56.8 and 43.4 MPa, respectively. The specimen with loop joints had loop reinforcement of D32 and the inner reinforcing rebars inside the loop were of D22. The yield strength ( $f_y$ ) of the all steel reinforcement (D32, D22, and D16) was 388 MPa.

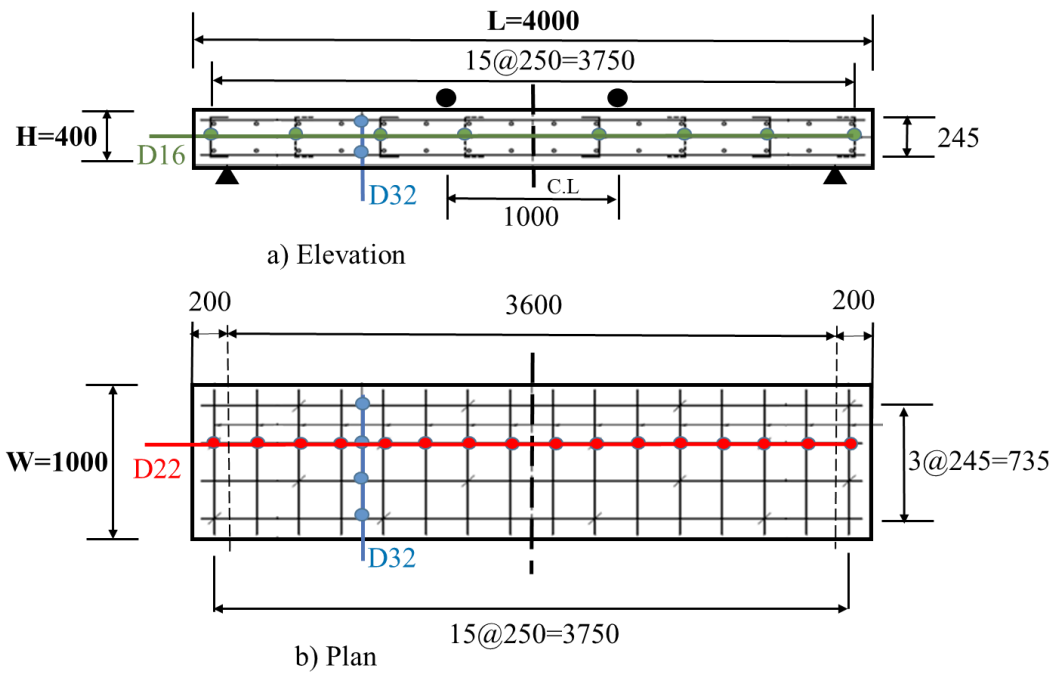


**Figure 3.3 Geometrical details of the ordinary RC beam (Case 1)**

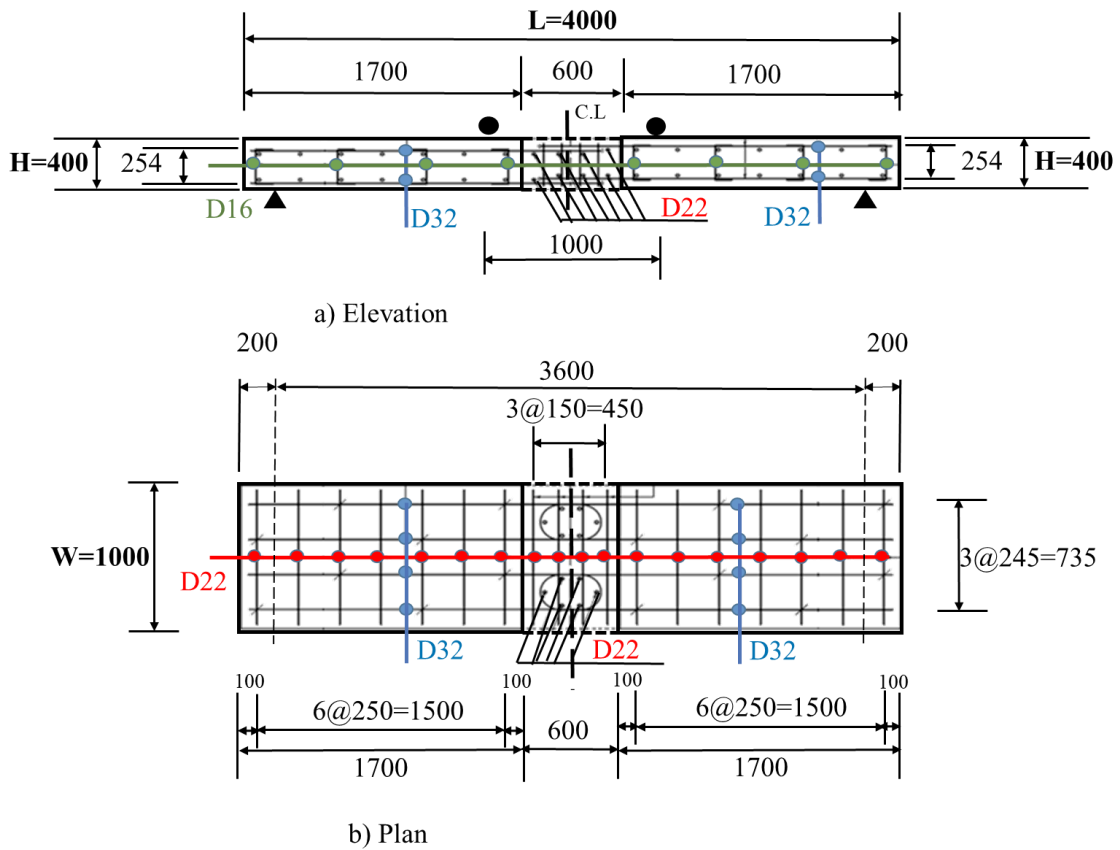


**Figure 3.4 Geometrical details of precast beams with loop joint (Case 2)**

**Table 3.1 Detail of the specimens**

Series	Type	Distribution Rebar in Loop	Specimen Detail	Remarks
1	Case 1	None		Ordinary RC beam
2	Case 2-1	D22 × 6		Loop with inner reinforcing bar
	Case 2-2	None		Loop without inner reinforcing bar
3	Case 3-0	None		Distance between main loops has been increased by 10 mm.  10 mm increment
	Case 3-1	D22 × 6		
	Case 3-2	D22 × 2		
	Case 3-3	D32 × 2		
	Case 3-4	D22 × 8		
	Case 3-5	D22 × 4 and D32 × 2		

The present evaluation is initiated with the investigation of case 1 (the ordinary RC) beam and case 2 (loop joints with and without inner reinforcing bars inside the loop). After numerical analyses of the case 1 and case 2, the new series (case 3) was considered.

The case 3 was introduced by increasing the vertical distance between the loops rebar of case 2 by 10 mm (34 mm to 44 mm). Firstly, the main objective of that 10 mm increment between loops rebar was to provide the construction ease at the site during placement of precast beams with horizontal loop joints and thus reducing the erection time. Secondly, to investigate the influence of the varying amount of the steel of inner reinforcing rebars inside the loop on the mechanical behavior of the cast in situ loop joint. In this regard, the complete detail of all the test series has been shown in Table 3.1. Table 3.1 shows, the main varying parameters in case 3 are; the 10 mm vertical increment in main loop rebars and the variation of the steel amount inside the loop for the inner reinforcing rebars. Therefore, it was important to investigate the effect of the above-mentioned parameters on the load-carrying capacity and the deformed behavior of the loop joint. In numerical simulations, the half model is being analyzed. The numerical models corresponding to all the cases have been shown in Figure 3.5.

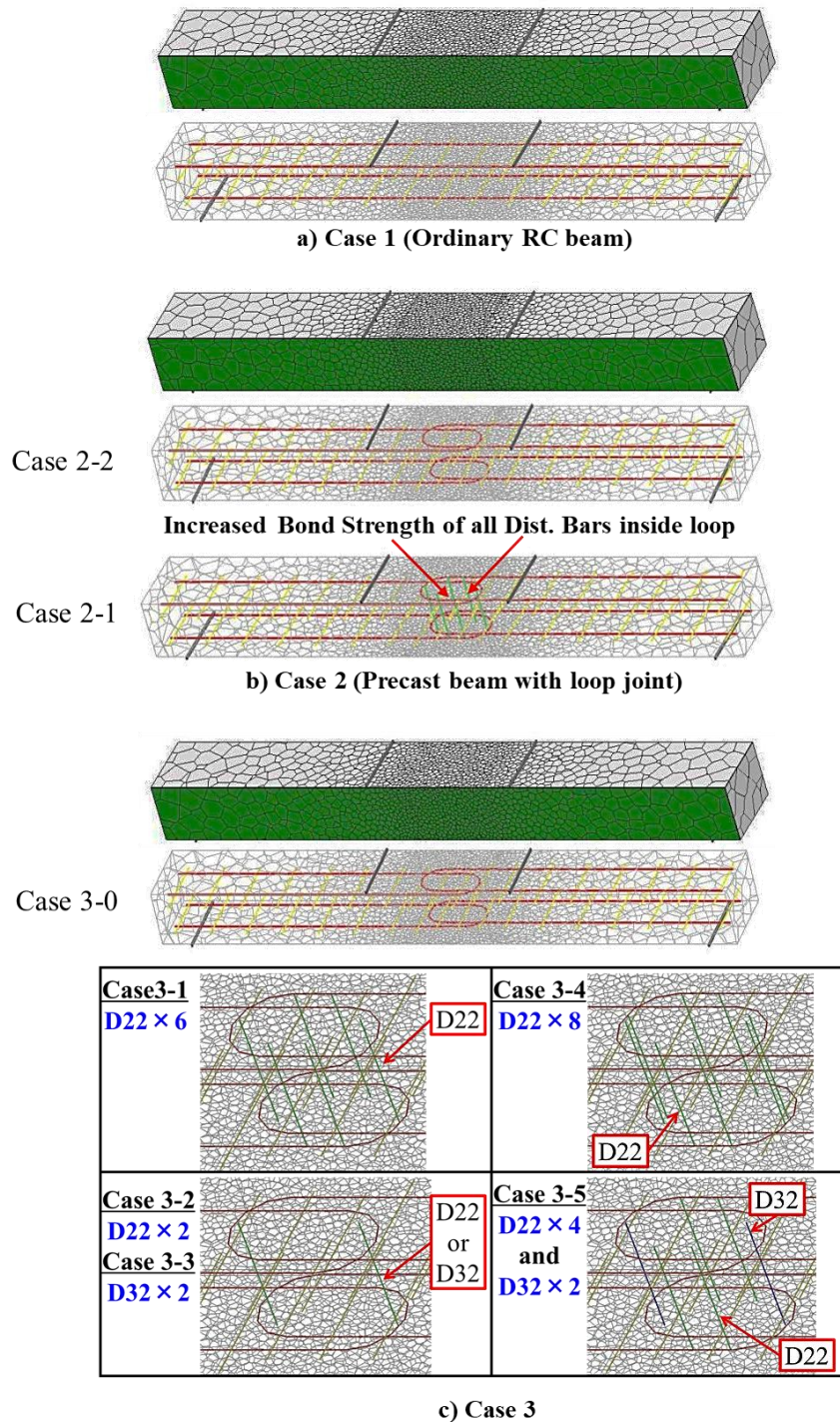


**Figure 3.5 Analytical models of ordinary RC beam and precast beams with loop joints**

An axis of symmetry has been considered along with the depth (1000 mm) of the specimens. The green surface here represents the symmetrical face of the analytical

model. The fine mesh with an average mesh size around 10 mm has been selected at the joint region considering the area of more interest. The selected mesh size at the joint region is less than the vertical distance between main loops rebars and then the mesh size has been gradually increased from the loop joint region to side of the precast beams in order to reduce the analytical computational cost. In this regard, the average mesh size in the numerical simulations incorporated for the numerical modeling of concrete joint and side precast beams approximately ranges between 10 to 30 mm as the model parameters as shown in Table 2.1 and Table 2.2 are required to use an element size ranging between 10 to 30 mm.

Concrete is modeled using 3D-RBSM based on the formulation of Yamamoto et al. (2008) and the steel rebar is modeled employing the beam element model as described earlier in the second chapter. After analytical modeling of the test specimens, the results are discussed.

### **3.3 Results and Discussion**

#### **3.3.1 Case 1 (Ordinary RC beam)**

The ordinary RC beam has been analyzed by both approaches; experimentally and numerically. Figure 3.6 shows the comparison of the experimental and the numerical results (load displacement). Figure 3.6 shows that the numerical and test load carrying capacities are found to be in good agreement. Figure 3.6 shows that the numerical simulations slightly overestimated the experimental results. The reasons for overestimation of yield strength and ultimate load may be due to simplification of rebar or boundary condition details in analysis. The test and the analytical deformed behaviors are shown in Figure 3.7. In the test the compression failure has been observed. The numerical simulation also captured the compression failure in the post peak region, effectively same as that of experimentation as shown in Figure 3.7.

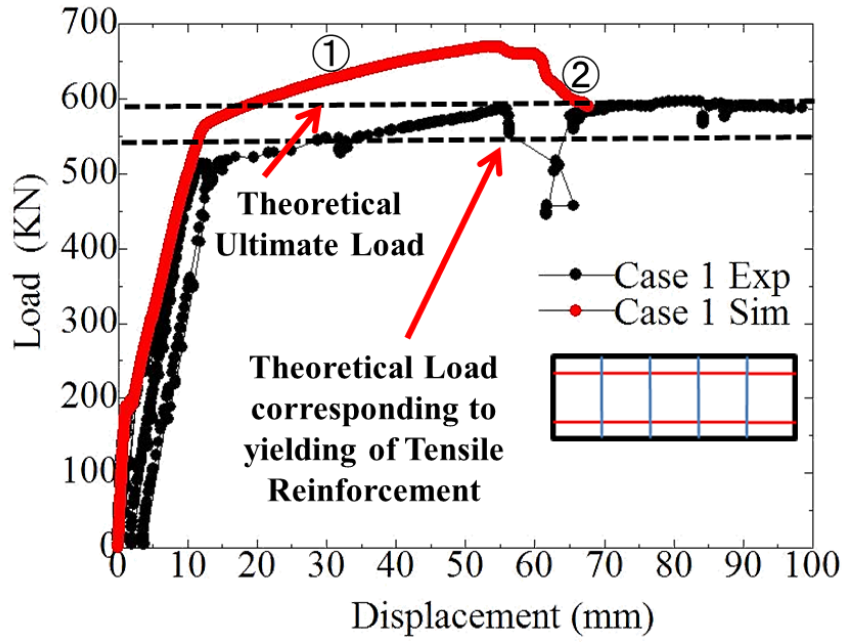


Figure 3.6 Experimental and analytical load displacement relationship of ordinary RC beam (case 1)

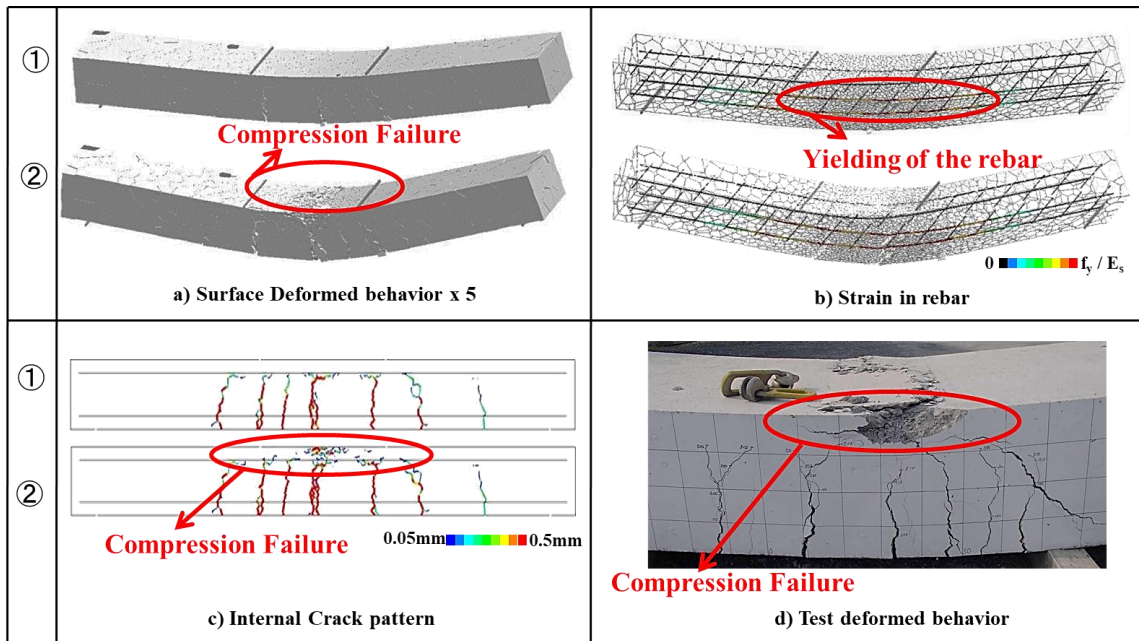


Figure 3.7 Experimental and analytical deformed behaviors of ordinary RC beam

### 3.3.2 Case 2 (*Precast beams with loop joints*)

Figure 3.8 shows the experimental and the analytical load displacement relationships of the precast beams joined by using cast in situ horizontal loop joints. The load displacement relationships for the horizontal loop joints with (case 2-1) and without (case 2-2) the inner reinforcing rebars within the loop has been presented in Figure 3.8.

Firstly, the discussion is made for case 2-2; loop without inner reinforcing rebars within the loop. Figure 3.8 (b) shows that brittle failure behavior has been observed in the test. In the same manner, the numerical model also captures the brittle behavior (case 2-2) before yielding of the loop reinforcing bar in the absence of the inner reinforcing bar, although the numerical simulation results tend to evaluate slight overestimation of the ultimate load compared to the experimental results.

Figure 3.8 (a) shows that the loop with inner reinforcing rebars within the loop (case 2-1) produced the ductile failure behavior in the test, and the numerical model also reproduces the same behavior. The numerical investigation in case 2-1 was initiated by considering the normal bond strength (NBS) of the inner reinforcing rebars and the analytical results reproduced the underestimation of the load carrying capacity and the ductility. In case 2-1, loop with normal bond strength (NBS) of the inner reinforcing rebars, although it has not been shown here, it was observed that the loop reinforcing bars yielded, before the occurrence of the compression failure at the upper side of the beam and produced the same failure mode as that of the case 2-2.

In the loop with inner reinforcing rebars within the loop, it was observed that the cover thickness of the inner reinforcing bars within the loop was much larger than that of the main loop reinforcing bars. It is well known that the bond strength depends on the concrete cover thickness provided to the steel reinforcement (Iizuka et al. 2011). In the numerical simulation for case 2-1, the bond strength evaluated as being doubled of normal bond strength, (case 2-1 2NBS), calculated by using the empirical relation proposed by Iizuka et al. 2011 for the bond strength evaluation under the influence of varied concrete cover thickness, has been considered only for the inner reinforcing rebars within the loop as shown in Figure 3.8 (a). After incorporating the doubled of normal bond strength, (case 2-1 2NBS) only for the inner reinforcing rebars within the

loop the numerical effectively reproduced the load-carrying capacity and ductile failure behavior which was consistent as observed in the test.

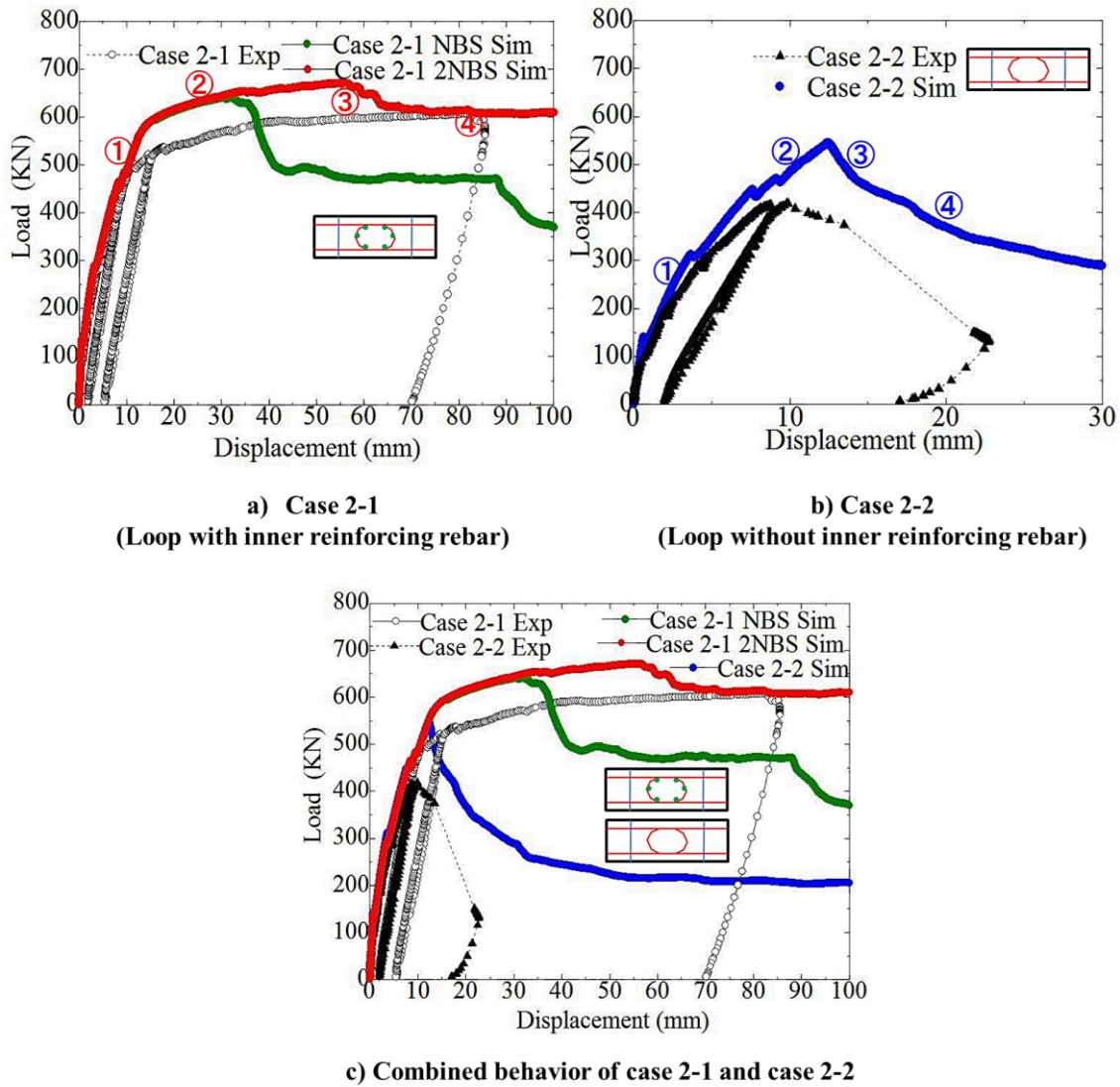
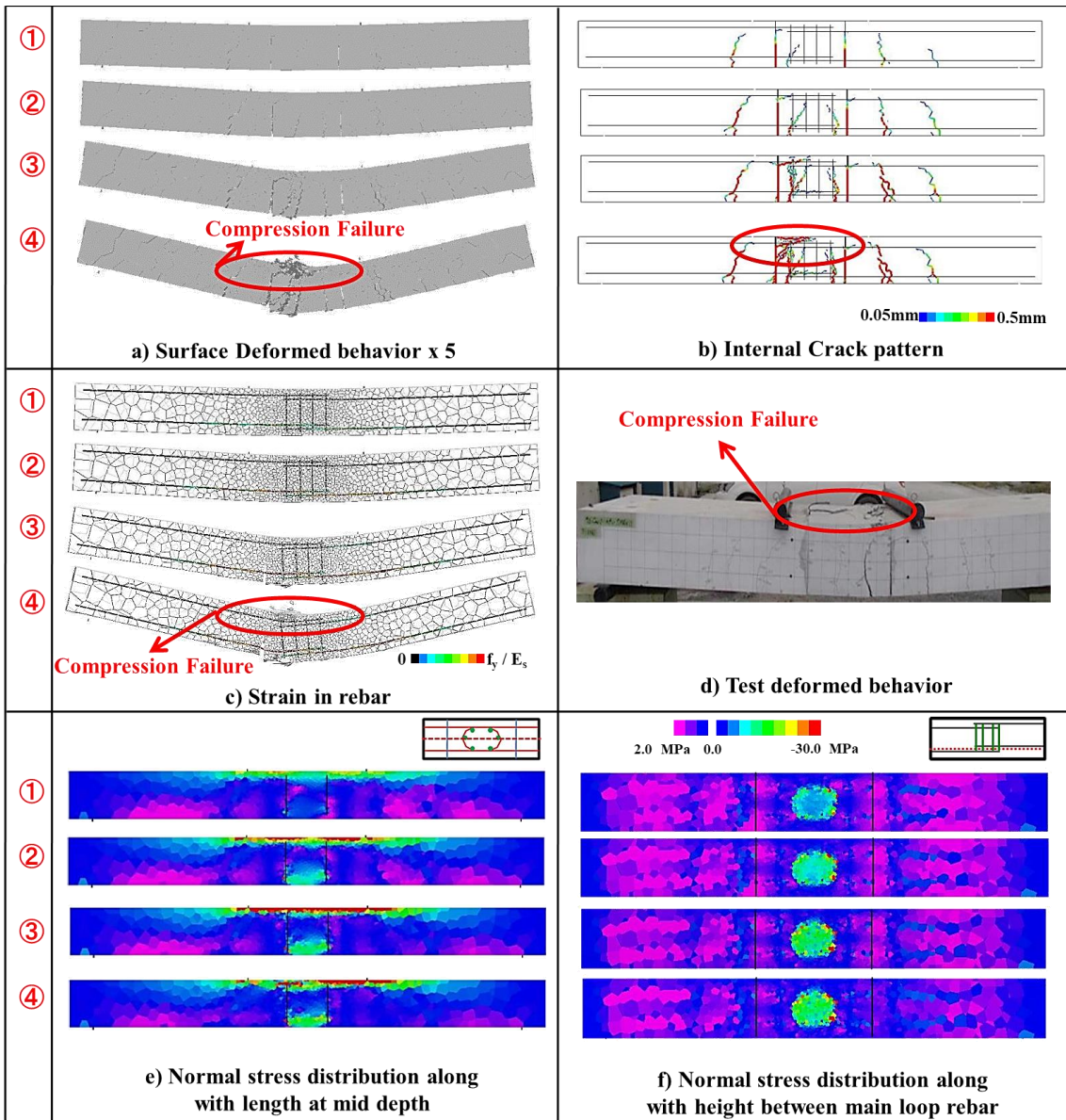


**Figure 3.8 Experimental and analytical load displacement relationships of precast beams with loop joints (case 2)**

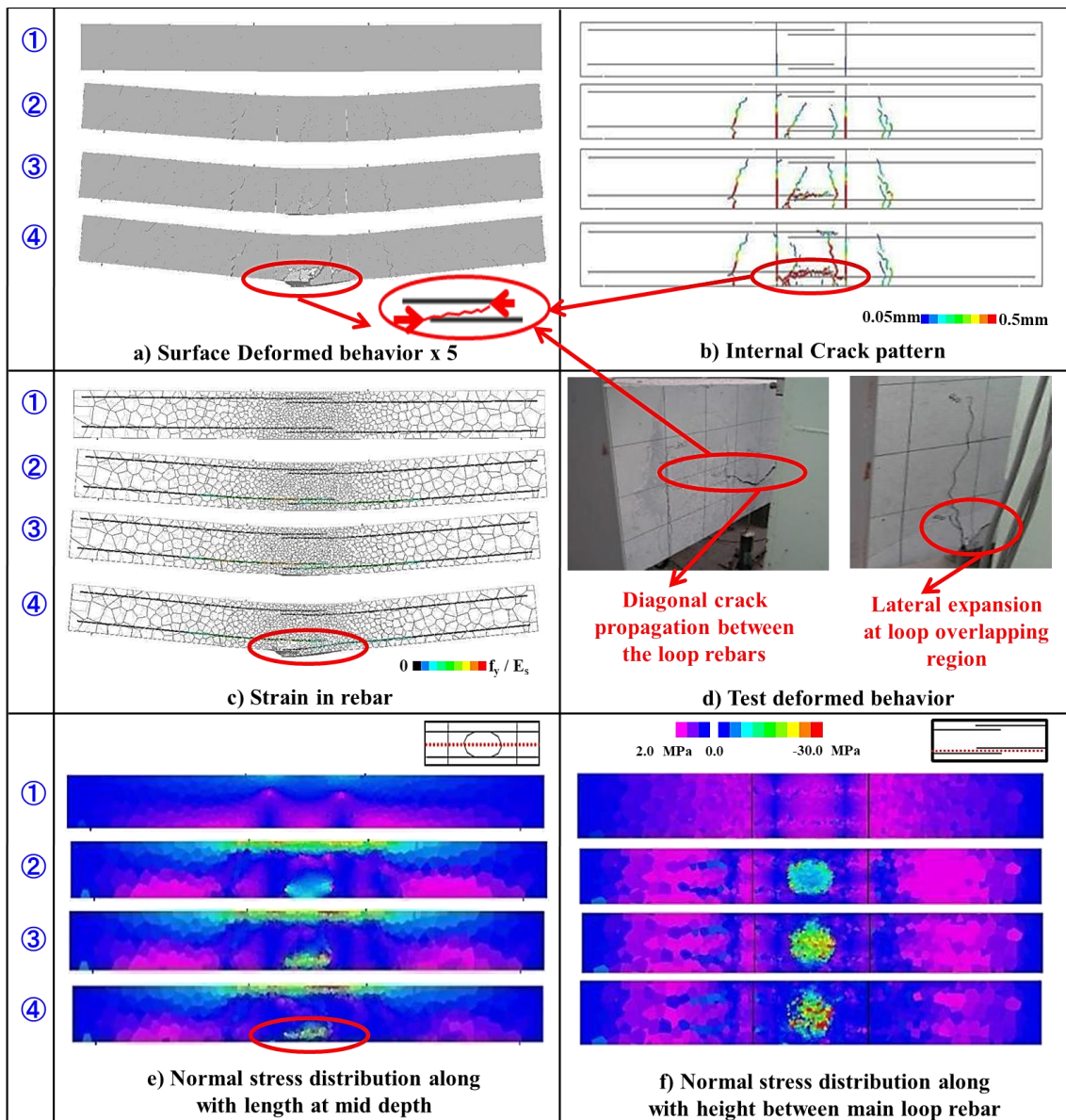
The deformation behavior, internal crack pattern and the normal stress distribution along with length and height of case 2-1 2NBS and case 2-2 have been shown in Figure 3.9 and Figure 3.10, respectively. The various stages moving from peak to post peak regions are selected on the load displacement relationship to highlight the internal failure mechanism as marked in Figure 3.8 from (1) to (4).

Figure 3.9 and Figure 3.10 shows that the numerical model captures the cracking patterns, deformation, and failure modes, effectively. Firstly, the failure mechanism of loop without inner reinforcing rebars inside the loop (case 2-2) is being discussed. Furthermore, it can also be investigated from the internal crack diagram and normal stress distributions in Figure 3.10, the failure of the loop joint without inner reinforcing rebars (case 2-2) was determined by the propagation of the diagonal crack due to the shear stress occurred between the loop reinforcing bars as highlighted by red circles in Figure 3.10.

However, the deformed behaviors shown in Figure 3.9 highlights the significance of the inner reinforcing rebars and reveals that inner reinforcing rebars play a vital role in suppressing the occurrence and the propagation of the diagonal cracks between the rebars of tensile loops. As a result of the restraining effect against diagonal crack propagation due to inner reinforcing rebars in case 2-1, the load-carrying capacity and the failure behaviors are strongly influenced and enhanced by the presence of the inner reinforcing rebars. Figure 3.9 shows that the loop with inner reinforcing rebars reproduced the compression failure instead of loop type failure as observed in case 2-2. From the analytical results of case 2-1 2NBS as shown in Figure 3.8 (a) and Figure 3.9, it can be observed, by increasing the bond strength only for the inner reinforcing bars, the model captured the deformation capacity and the ductile failure mode same as observed in the experiment of case 2-1.



**Figure 3.9 Comparison of the experimental and the analytical results for case 2-1 (2NBS)**



**Figure 3.10 Comparison of the experimental and the analytical results for case 2-2**

### 3.3.3 Case 3 (Precast beams with increased loop interval and varying steel amount of inner reinforcing steel)

After the numerical validation of case 1 and case 2, the numerical simulation was extended for case 3. The bond strength only for the inner reinforcing rebars which had large cover thickness within the loop than the main tensile loop rebars evaluated as being doubled of normal bond strength (2NBS) was also adopted for the numerical

simulation of case 3. The numerical simulation results of case 3 are shown in Figure 3.11.

Figure 3.11 shows that the vertical increment of 10 mm distance between the main loop reinforcement reduced the peak load of case 3-0 and case 3-1 compared with case 2-2 and case 2-1, respectively. The mechanism of the peak load reduction is explained here. The peak load reduced as the diagonal crack propagated easily between tensile loops in case 3 compared with case 2 as shown in Figure 3.12. Figure 3.11 also shows that varied (increased) steel amount of inner reinforcing rebars inside the loop caused the increased peak load. The peak load increased in case 3-2 and case 3-3 compared with case 3-0 but showed the loop type failure. The loop failure can be described as the propagation of the diagonal crack between the tensile loop rebar at the joint region as shown in Figure 3.12, causing the concrete between the loop rebar to lose the stress transfer mechanism and hence tensile stress at the lower edge of the beam could not be transferred, leading to failure before the yielding of the tensile reinforcement.

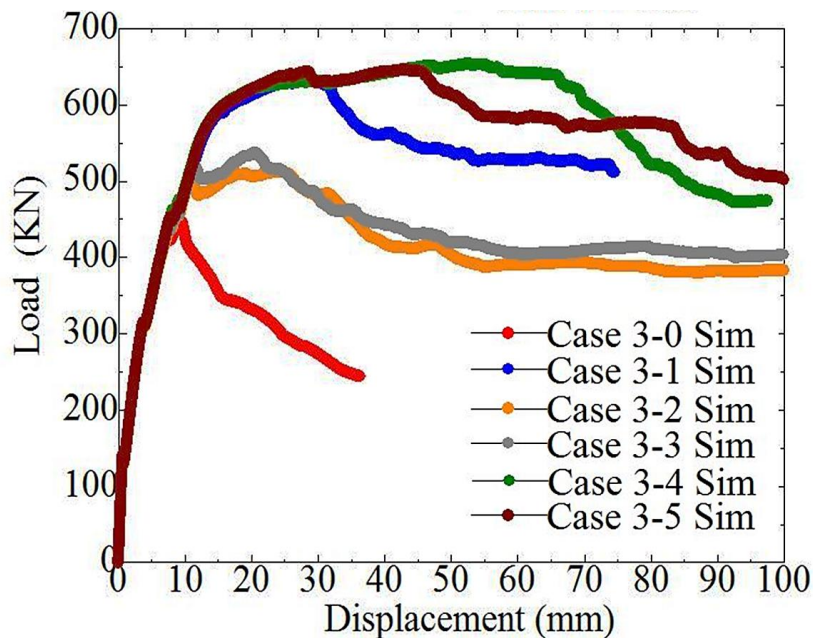


**Figure 3.11 Load displacement relations case 3**

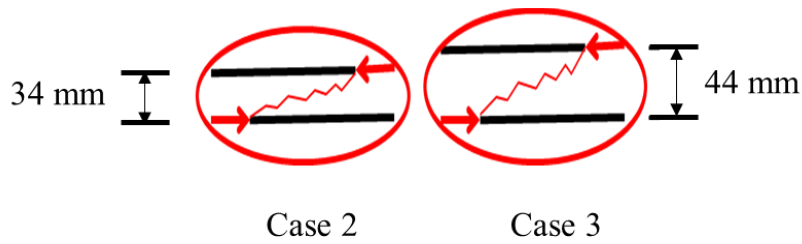


**Figure 3.12 Diagonal crack propagation behavior between the loops rebars in case 2 and case 3**

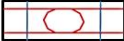
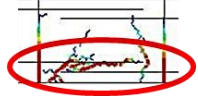
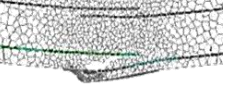
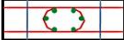
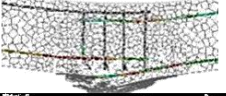
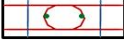
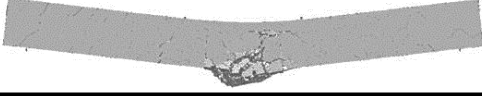
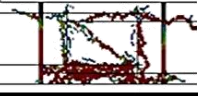
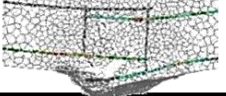
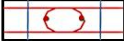
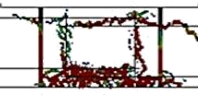
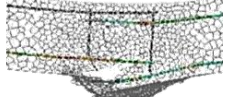
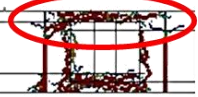
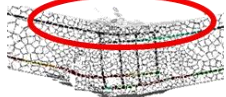
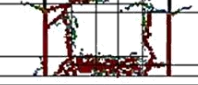
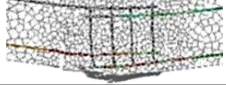
Moreover, the influence of varied amount of steel reinforcement of inner reinforcing steel is also highlighted in Table 3.2. In Table 3.2, the cases are arranged with an ascending order of the steel amount of inner reinforcing rebar inside the loop.

Table 3.2 shows the surface deformed behaviors, internal crack patterns, and the strain in the loop rebars. The characteristic post-peak failure mode against each case is also presented in Table 3.2. Figure 3.11 shows that the case 3-5 showed slightly better performance among all cases except case 3-4, case 3-5 reproduced the loop type failure after yielding of the rebar. Table 3.2 also shows that case 3-5 has the maximum steel amount (3.74 %) inside the loop, while case 3-4 reproduced the compression failure at the top side of the beam and case 3-4 also showed more ductility compared with case 3-5 as shown in Figure 3.11. The failure can be described as in case 3-5, due to the progress of the softening of the bond-slip model (Figure 2.3) between inner reinforcing rebars and the concrete, the diagonal crack propagated between the tensile loop reinforcement and thus caused the loop type failure. All the cases showed the loop type failure except case 3-4 as shown in Table 3.2. Furthermore, the case 3-4 showed the maximum peak load among all the cases as shown in Figure 3.11.

$$\text{Steel Ratio} = \frac{\text{Total area of inner reinforcing steel inside the loop}}{\text{Total area of concrete inside the loop}}$$

**Figure 3.13 Steel ratio in horizontal loop joints**

Table 3.2 Summary of deformed behaviors of Case 3

Type	Deformed Behaviors at Post Peak Stage Deformed behavior x 5      0.05mm  0.5mm      0  $f_y / E_s$			Mode of Failure	Steel ratio within Loop	Summation of the Circumferential Length of Distribution rebar within loop
<b>Case 3-0</b> 				<i>Loop failure</i> before yielding of rebar	Nil	Nil
<b>Case 3-1</b> 				<i>Loop failure</i> after yielding of rebar	2.76 %	420 mm
<b>Case 3-2</b> 				<i>Loop failure</i> before yielding of rebar	0.92 %	140 mm
<b>Case 3-3</b> 				<i>Loop failure</i> before yielding of rebar	1.89 %	200 mm
<b>Case 3-4</b> 				<i>Compression failure</i>	3.69 %	<b>560 mm</b>
<b>Case 3-5</b> 				<i>Loop failure</i> after yielding of rebar	<b>3.74 %</b>	480 mm

The steel ratio for the horizontal loop joints can be defined as; the total area of steel reinforcement of inner reinforcing inside the loop/ total area of concrete inside the loop as shown in Figure 3.13. It can be seen from Table 3.2, although the case 3-5 has the maximum steel ratio within loop compared with the case 3-4, the structural performance in case 3-4 was superior compared with case 3-5. It can be explained as the case 3-4 has more summation of the circumferential length (560 mm) of the inner reinforcing rebar than case 3-5 (480 mm). More the summation of the circumferential length of the inner reinforcing rebar within the loop provided the more bond resistance capacity and hence produced more confinement to the concrete inside the loop due to bond behavior and thus prevented the occurrence and propagation of the diagonal crack between the tensile loops and reproduced the compression failure behavior on the top side of the beam.

### **3.4 Summary**

In this chapter, the failure mechanism of the horizontal loop joints and the role of the inner reinforcing bars inside the loop joints are highlighted by experimental and numerical analyses.

- 1) The failure of the loop joint without inner reinforcing rebars inside the loop was by the occurrence of diagonal cracks in the tensile loop region and showed brittle failure behavior. The presence and the bond strength of the inner reinforcing bars inside the loop joint played the vital role in suppressing the diagonal crack occurrence and propagation, thus restrained the loop type failure and reproduced the compression failure having ductile failure characteristics.
- 2) The numerical analyses also revealed that for simulations with higher precision, it is necessary to adequately evaluate the bond characteristics of the inner reinforcing bars which have relatively large cover thickness.
- 3) The numerical investigation against increased the loop interval between loop rebars also highlighted that the deformation capacity of the loop. The peak decreased with the increased of loop interval due to increase in diagonal crack propagation between two tensile loop rebars at the joint region.

- 4) The varying steel amount of the inner reinforcing rebars inside the loop did not show any significant change in the loop failure mode. However, the surface area of the inner reinforcing rebars inside the loop showed more influence on the deformation performance and the failure modes of the loop joint. It was observed that more surface of the inner reinforcing rebar inside the loop provided the more bond resistance capacity and hence produced more confinement to the concrete inside the loop due to bond behavior and thus prevented diagonal crack propagation and reproduced the compression failure mode rather than loop type failure.

# **4 Limitation of Conventional 3D-RBSM and Beam Element Model and Introduction of New Model**

## **4.1 Introduction**

In this chapter, firstly the limitation of the conventional 3D-RBSM and the beam element model to simulate the mechanical behavior of reinforced concrete (RC) as discussed in chapter 2 is highlighted. Similarly, the need of proposing a new analytical model is also explained. After mentioning the limitation of 3D-RBSM and the beam element model, the brief introduction to the new numerical model; coupled Rigid Body Spring Model (RBSM) and the nonlinear solid Finite Element Method (FEM) is presented.

The basic characterizations regarding the modeling of concrete, steel, and concrete-steel interface in coupled RBSM and solid FEM model are described.

## **4.2 Limitation of existing numerical model and proposal of new model**

3D-RBSM has been referred as an effective numerical approach for the evaluation of nonlinear fracture behavior of concrete (internal crack initiation, propagation, and orientation), quantitatively, Yamamoto et al. (2008). The applicability of 3D-RBSM and the beam element has also been confirmed in chapter 3.

The limitation of the numerical model using 3D-RBSM for modeling of the concrete and the beam element for the modeling of the steel as well as the background regarding the development of new numerical are explained here. In recent years, many

studies have been conducted and attempts have been employed to evaluate and to investigate the complex variations in bond characteristics between the concrete and the steel under various test parameters and boundary conditions through mesoscale simulations using RBSM.

The researchers like Hayashi et al. 2013, Matsumoto et al. 2016, Eddy et al. 2016, Nagai et al. 2017, utilized RBSM based mesoscale models, directly modeled the shape of the reinforcing steel including ribs and size of deformed rebar, successfully performed the simulation for the crack propagation mechanism and structural performance of RC members. The previous models were found to be effective to express the complex bond characteristics. However, those models modeled reinforcing bars by RBSM using a regular mesh. RBSM is a kind of discrete type model proposed by Kawai, (1978). It is well confirmed that cracking behavior and failure localization behavior can only be developed using random polyhedral mesh through the Voronoi diagram, while the Poisson's effect cannot be expressed through regular mesh generation. Therefore, the existing mesoscale models using RBSM have limitations in simulating the elastic behavior of the reinforcing bar when regular mesh generation is applied. Moreover, the Poisson's effect can be captured by RBSM with a random polyhedron. However, in that case, it is difficult to simulate the macroscopic elasto-plastic response of the reinforcing bar. Therefore, the existing RBSM based mesoscale models are unable to reproduce the elasto-plasticity response of steel. This limitation refers to the development of a new numerical model; coupled RBSM and nonlinear solid FEM.

### **4.3 Coupled RBSM and solid FEM model**

Considering the limitation of the existing model, the mesoscale numerical model; coupled RBSM and nonlinear solid FEM model, has been proposed by Ikuma et al. 2018 to upgrade and overcome the previously stated limitations of the existing mesoscale models employing RBSM for the modeling of concrete and steel as shown in Figure 4.1. The complete detail regarding the formulation of the coupled RBSM and nonlinear solid FEM model has been explained in the research work of Ikuma et al. 2018. The brief description is highlighted in this study.

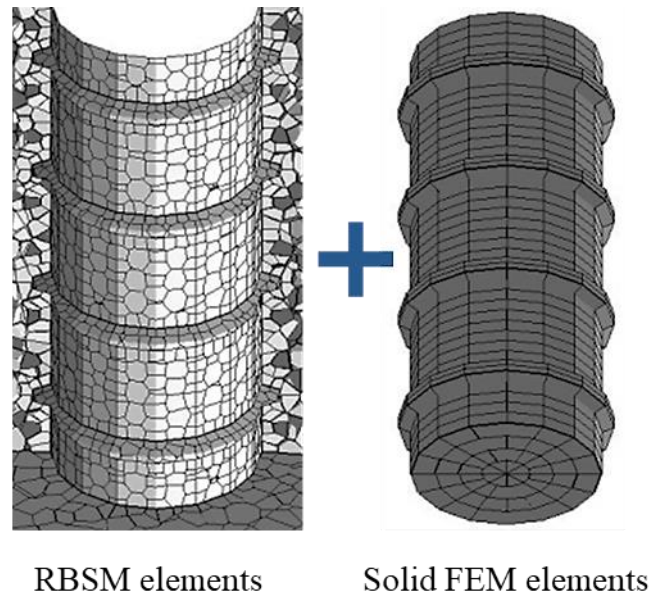


**Figure 4.1 Coupled RBSM and Solid FEM model**

The coupled RBSM and nonlinear solid FEM model has the capability to simulate the nonlinear fracture behavior of concrete as well as the elasto-plastic response of steel reinforcement. The numerical analyses using mesoscale coupled RBSM and solid FEM is an efficient approach for simulating the mechanical response of reinforced concrete. It is well understood the bond strength of concrete is strongly affected by the bearing of the ribs of deformed rebar and the complex stress state occurs around them. The mesoscale modeling using coupled RBSM and solid FEM is useful in this regard as it has the tendency to reproduce the local response of steel, concrete and their interaction with the cracking. Furthermore, it has the potential to simulate the detailed internal failure mechanism, produces the local response (stress state and cracking in concrete around the rebar), and also includes the geometrical details (rib height, shape, and lug spacing, etc.) of steel reinforcement, etc.

In the coupled RBSM and solid FEM model, the reinforcing steel is modeled using eight-nodes nonlinear solid finite elements and the adjoining concrete is modeled by using 3D-RBSM as shown in Figure 4.1.

### ***4.3.1 Modeling of concrete and steel***

In the coupled RBSM and solid FEM, concrete is modeled using 3D-RBSM considering the same constitutive models and the calibrated material parameters as discussed in chapter 2, while the reinforcing steel bar embedded in concrete is modeled using eight-nodes nonlinear solid FEM elements considering the actual geometrical features e.g., rib height, shape and lug spacing, etc. account for the proper interlocking with the surrounding concrete. The 3D-models for the deformed rebars (D19 and D32) using the actual geometrical details mentioned by the steel manufactures have been shown in Figure 4.2. A Von Mises plasticity model with strain hardening is used for the constitutive model of steel.

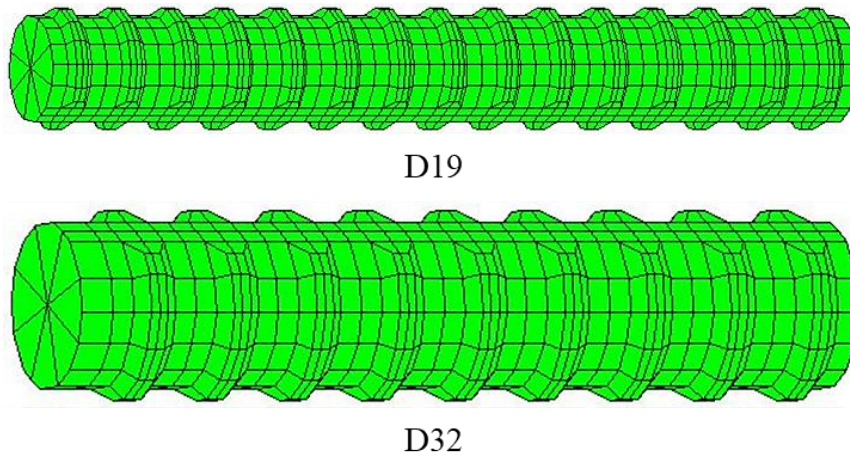


**Figure 4.2 3D-model of the deformed reinforcement**

### ***4.3.2 Modeling of the concrete-steel interface***

The concrete elements (3D-RBSM) and the steel elements (solid FEM) have been connected through the coupling of boundary interfaces of concrete and steel elements utilizing link elements. In the coupled RBSM and solid FEM model, each link element on the interface between RBSM element and nonlinear solid FEM element consists of two shear springs and one normal spring as shown in Figure 4.3.

The deformation of each spring of the link element is obtained by the relative displacement between the surfaces of the RBSM element and nonlinear solid FEM element and subsequently converting it to the local coordinate system.

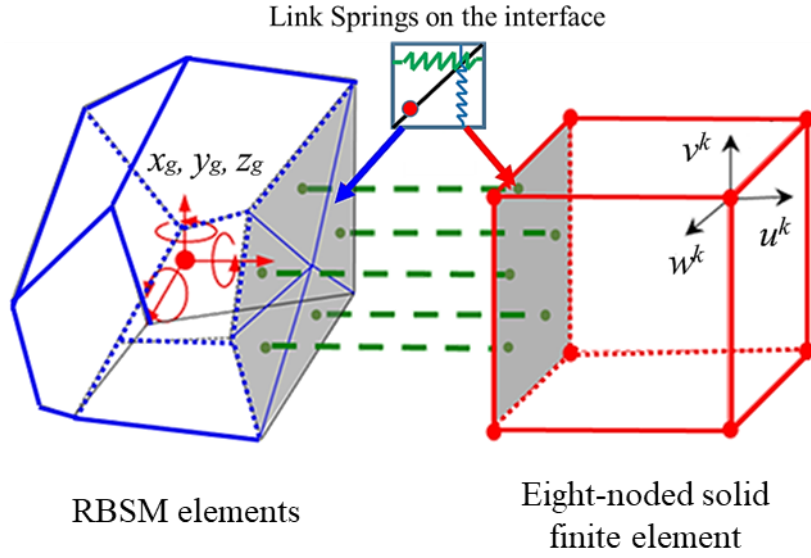


**Figure 4.3 RBSM and solid FEM boundary interface**

The brief description regarding formulation of link element between RBSM element and eight-noded nonlinear finite elements is described here. Firstly, displacements are defined in  $x, y, z$  direction ( $u_{solid}, v_{solid}, w_{solid}$ ) at link element on boundary of solid element, an arbitrary point in each element is described using shape function  $N_i$  and displacement of each node ( $u^i, v^i, w^i$ ), ( $i = 1, 2, \dots, 8$ ) using Equation (4.1).

$$u_{FEM} = \begin{pmatrix} u_{solid} \\ v_{solid} \\ w_{solid} \end{pmatrix} = \begin{bmatrix} N_1 & 0 & 0 & N_2 & 0 & 0 & \dots & N_8 & 0 & 0 \\ 0 & N_1 & 0 & 0 & N_2 & 0 & \dots & 0 & N_8 & 0 \\ 0 & 0 & N_1 & 0 & 0 & N_2 & \dots & 0 & 0 & N_8 \end{bmatrix} \begin{pmatrix} u^1 \\ v^1 \\ w^1 \\ u^2 \\ v^2 \\ w^2 \\ \vdots \\ u^8 \\ v^8 \\ w^8 \end{pmatrix} \quad (4.1)$$

On the other hand, shape functions of each node of eight-nodes solid element are expressed in Equation (4.2). The displacement at integration points of link element on boundary of RBSM element ( $u_{RBSM}, v_{RBSM}, w_{RBSM}$ ) can be calculated as shown in Equation (4.3), mentioned in the work by Yamamoto et al. (2008). Then the relative displacement between RBSM and FEM  $d_g$  can be defined by  $u_{FEM}$  and  $u_{RBSM}$

respectively, using Equation (4.4) and the deformation  $d_l$  of each spring in link element is calculated using Equation (4.5).

$$\begin{aligned}
N_1(r, s, t) &= \frac{1}{8}(1-r)(1-s)(1-t) & N_2(r, s, t) &= \frac{1}{8}(1+r)(1-s)(1-t) \\
N_3(r, s, t) &= \frac{1}{8}(1+r)(1+s)(1-t) & N_4(r, s, t) &= \frac{1}{8}(1-r)(1+s)(1-t) \\
N_5(r, s, t) &= \frac{1}{8}(1-r)(1-s)(1+t) & N_6(r, s, t) &= \frac{1}{8}(1+r)(1-s)(1+t) \\
N_7(r, s, t) &= \frac{1}{8}(1+r)(1+s)(1+t) & N_8(r, s, t) &= \frac{1}{8}(1-r)(1+s)(1+t)
\end{aligned} \tag{4.2}$$

$$u_{RBSM} = \begin{pmatrix} u_{RBSM} \\ v_{RBSM} \\ w_{RBSM} \end{pmatrix} = \begin{bmatrix} 1 & 0 & 0 & 0 & (z_i - z_g) & -(y_i - y_g) \\ 0 & 1 & 0 & -(z_i - z_g) & 0 & (x_i - x_g) \\ 0 & 0 & 1 & (y_i - y_g) & -(x_i - x_g) & 0 \end{bmatrix} \begin{pmatrix} u \\ v \\ w \\ \theta_x \\ \theta_y \\ \theta_z \end{pmatrix} \tag{4.3}$$

$$d_g = u_{RBSM} - u_{FEM} \tag{4.4}$$

$$d_l = Bu, \quad u = \begin{pmatrix} u_{RBSM} \\ u_{FEM} \end{pmatrix} \tag{4.5}$$

Where,  $B$  can be described as

$$B = MQR^* \tag{4.6}$$

$$M = \begin{bmatrix} -1 & 0 & 0 & 1 & 0 & 0 \\ 0 & -1 & 0 & 0 & 1 & 0 \\ 0 & 0 & -1 & 0 & 0 & 1 \end{bmatrix} \tag{4.7}$$

$$Q = \begin{bmatrix} Q_{RBSM} & 0 \\ 0 & Q_{FEM} \end{bmatrix} \quad (4.8)$$

Then,  $Q_{RBSM}$  and  $Q_{FEM}$  will be expressed as,

$$Q_{RBSM} = \begin{bmatrix} 1 & 0 & 0 & 0 & (z_i - z_g) & -(y_i - y_g) \\ 0 & 1 & 0 & -(z_i - z_g) & 0 & (x_i - x_g) \\ 0 & 0 & 1 & (y_i - y_g) & -(x_i - x_g) & 0 \end{bmatrix} \quad (4.9)$$

$$Q_{FEM} = \begin{bmatrix} N_1 & 0 & 0 & N_2 & 0 & 0 & \dots & N_8 & 0 & 0 \\ 0 & N_1 & 0 & 0 & N_2 & 0 & \dots & 0 & N_8 & 0 \\ 0 & 0 & N_1 & 0 & 0 & N_2 & \dots & 0 & 0 & N_8 \end{bmatrix} \quad (4.10)$$

$$R = \begin{bmatrix} l & m & n \\ -m & l & 0 \\ \frac{l}{\sqrt{l^2 + m^2}} & \frac{m}{\sqrt{l^2 + m^2}} & 0 \\ -lm & -mn & \sqrt{l^2 + m^2} \\ \frac{-lm}{\sqrt{l^2 + m^2}} & \frac{-mn}{\sqrt{l^2 + m^2}} & \sqrt{l^2 + m^2} \end{bmatrix} \quad (4.11)$$

In addition,  $R$  is coordinate transformation matrix which converts relative displacement of RBSM and FEM  $\mathbf{d}_g$  in global coordinates into spring deformation  $\mathbf{d}_l$  in local coordinates. Each component of the matrix is shown in Equation (4.11). Here,  $l, m, n$  is direction cosine which indicates the direction of normal spring of link element. If small deformation is supposed, it is equal to the direction cosine of boundary surface of RBSM element. When  $l$  and  $m$  are equal to 0, it is described as below.

$$R = \begin{bmatrix} 0 & 0 & -1 \\ 0 & 1 & 0 \\ 1 & 0 & 0 \end{bmatrix} \quad (4.12)$$

Furthermore, the constitutive models of normal and shear springs on the boundary interface are assumed to be the same as that for modeling of the concrete in 3D-RBSM (Figure 2.2, Table 2.1 and Table 2.2). However, the model parameters of constitutive models for normal and shear springs on the boundary interface have been

changed considering the friction between steel and concrete on the boundary interface, Hayashi et al. 2013. In specimens with 3D modeling of the steel rebar, the constitutive model of the normal and the shear springs on the boundary interface are same as that of concrete model (Figure 2.2), however, the tensile strength of the normal spring on the boundary interface has been reduced to half as that of concrete considering the weakness of the boundary interface.

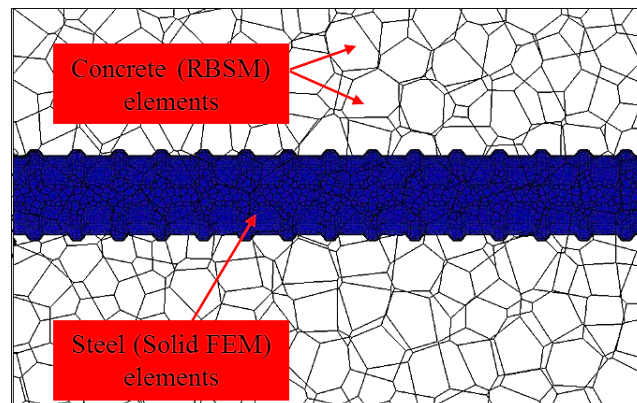


**Figure 4.4 Representation of the concrete and the steel elements**

The numerical model couples the RBSM elements and the solid FEM elements regardless the position of nodes of the FEM elements, additionally the numerical model has the capability to reproduce the link elements arbitrarily on the boundary interface between concrete and steel elements and consequently reduces the analytical computational cost. The numerical model employs the same coupling technique for combining the RBSM elements and the solid FEM elements as applied by the past researcher for coupling of the RBSM elements and the shell FEM elements Mendoza et al. 2018, based on the Inverse-Mapping algorithm using Taylor expansion.

Furthermore, it is pertinent to mention that the selection of the average mesh size near to the boundary interface of the concrete element (3D-RBSM) and steel element (solid FEM) is an important aspect and should be selected less than the rib height of the steel reinforcement for the proper representation of the geometrical features of the steel reinforcement in numerical modeling as shown in Figure. 4.4. The average mesh size adopted for the mesoscale simulations in current research generally ranges 70 to 80 % of the rib height of the deformed rebar.

## **4.4 Summary**

In this chapter, the limitation of the conventional 3D-RBSM and the beam element model and the need of proposing a new numerical model were explained. After mentioning the limitations of 3D-RBSM and the beam element, the brief introduction to the new numerical model; coupled RBSM and solid FEM was presented. Similarly, the basic characterizations regarding the modeling of the concrete, the steel, and the concrete-steel interface in coupled RBSM and solid FEM model were described.

The validation and numerical evaluations through the coupled RBSM and solid FEM model are discussed in the next chapter for reinforced concrete (RC) elements under various test parameters and the loading types.

# **5 Numerical Evaluation of the Bond Behavior of Deformed Rebar Using Coupled RBSM and Solid FEM Model**

## **5.1 Introduction**

As discussed in chapter 1, the bond behavior between concrete and deformed rebar is an important parameter that defines the structural behavior of reinforced concrete. This chapter includes the numerical evaluation of the macroscopic bond behavior of deformed rebar using the coupled RBSM and solid FEM model considering mesoscale simulation analysis. The numerical evaluation of the coupled RBSM and solid FEM model have been carried for;

- 1) Macroscopic bond behavior in axially loaded RC specimens in two ends pull-out test.
- 2) Bond characteristics of the RC cubical specimens in one end pull-out test subjected to lateral pressures applied to the concrete surface.
- 3) Detailed failure behavior in axially loaded RC prisms under direct tension.

The discussion is presented for the evaluation of the bond behavior of the 3D rebar corresponding to the above-mentioned mechanical behaviors and the internal failure process and mechanism are also simultaneously highlighted through the mesoscale numerical analyses using coupled RBSM and solid FEM model.

## 5.2 Evaluation of macroscopic bond behavior in two ends pull-out test

The initial evaluation of the numerical model is adopted for determining the macroscopic bond characteristics between reinforcing steel bars and the concrete including the effect of varying concrete cover thicknesses and the rebar diameters by using the test investigations of Iizuka et al. 2011, loaded under two ends pull-out test.

### 5.2.1 Test overview and numerical modeling

In test the varying parameters were the rebar diameters and the concrete cover thicknesses. The specimens were embedded with deformed rebars of D19 and D25 in the middle of the specimen. The geometrical details and the mechanical properties of the steel reinforcement are shown in Figure 5.1 and Table 5.1.

The specimens embedded with deformed rebar D19 have cover thickness ( $c$ ) of 10 mm, 30 mm, 38 mm, and 50 mm while the specimens with deformed rebar D25 have cover of 10 mm, 25 mm, 30 mm, 50 mm, and 100 mm, respectively. All the specimens were of cubical geometry with a size of 150 mm x 150 mm x 150 mm except the specimen embedded with rebar of D25 with a concrete cover thickness of 100 mm and that had a size of 250 mm x 250 mm x 150 mm. The concrete compressive strength of the specimens was approximately 30.0 MPa. The embedded length of the reinforcing bar was 150 mm for all the specimens, provided the ultimate bond strength, and post-peak softening behavior within the linear elastic range of the steel. The strain gauge was applied in the middle of the specimen. The dimensions (all dimensions are in mm) of the specimens and the test set up are shown in Figure 5.2.

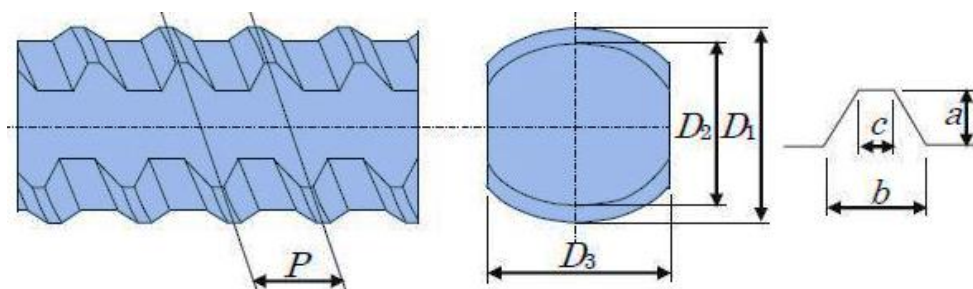
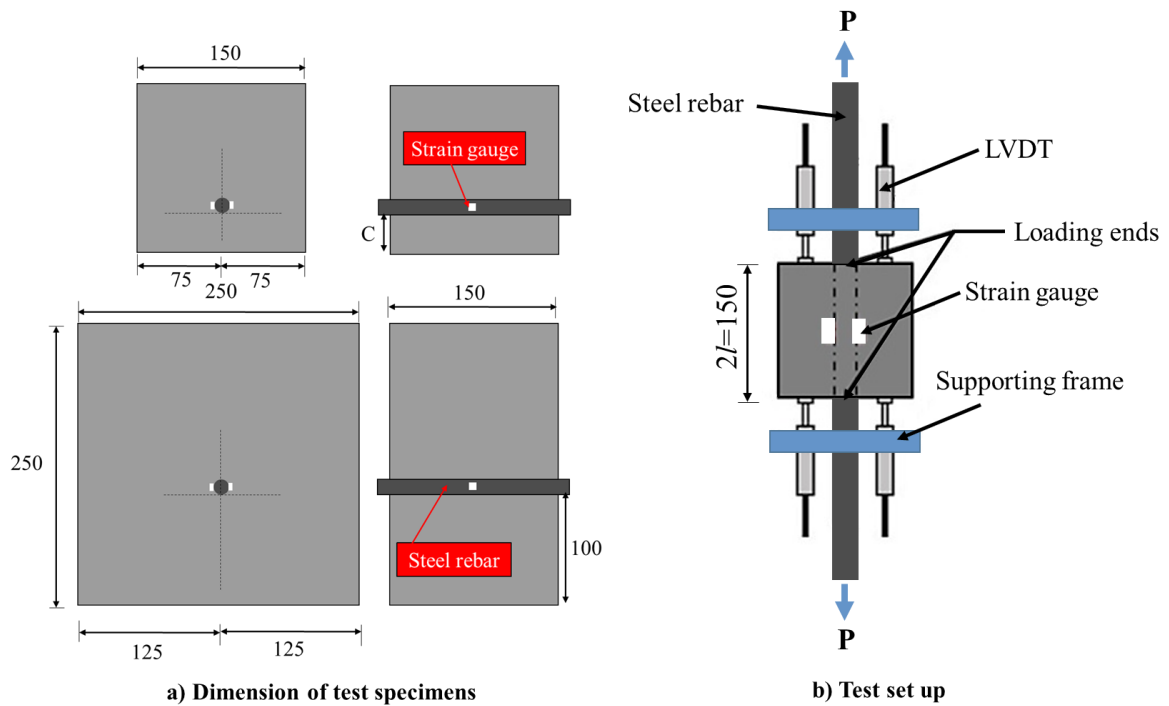


Figure 5.1 Representation of the geometrical features of the deformed rebar

**Table 5.1 Geometrical details and the mechanical properties of the deformed rebars**

Sr. No	Nominal diameter	Nominal area	External diameter	Core diameter	Rib spacing	Rib details			Yield strength	Young's modulus
	D <sub>2</sub> mm	A <sub>s</sub> mm <sup>2</sup>	D <sub>1</sub> mm	D <sub>3</sub> mm	P mm	a mm	b mm	c mm	f <sub>y</sub> MPa	E <sub>s</sub> MPa
<b>D19</b>	18.4	286.5	21.2	17.7	10.0	1.8	4.4	2.1	1039	1.87 x 10 <sup>5</sup>
<b>D25</b>	24.4	506.7	28.4	23.6	13.0	2.0	6.4	2.4	1013	1.89 x 10 <sup>5</sup>
<b>D32</b>	30.4	794.2	35.2	29.4	16.0	2.4	8.1	3.3	994	1.83 x 10 <sup>5</sup>



**Figure 5.2 Representation of the geometrical dimensions of the specimens and the test set up**

The tensile loading was applied to the both ends of rebar; the slip of rebar was measured by linear differential transducers (LVDTs) whereas the average bond stress of concrete based on the stress of the steel was measured by using the Equation (5.1).

$$\tau = A_s (\sigma_{s1} - \sigma_{s0}) / ul \quad (5.1)$$

Where,

A<sub>s</sub> = Nominal cross-sectional area of steel reinforcement

$\sigma_{s1}$  = Steel stress at the loading end

$\sigma_{s0}$  = Steel stress at the center of the rebar

$u$  = Nominal rebar perimeter

$l$  = Embedded length of the half specimen i.e. 75 mm, in this investigation

In this regard, the numerical models for RC specimens embedded with rebars D19 and D25 with varying concrete cover thickness are shown in Figure 5.3 and Figure 5.4, respectively. Concrete is modeled using 3D-RBSM based on the formulation of Yamamoto et al. (2008) and the steel rebar is modeled employing the eight noded nonlinear solid finite elements using the actual geometrical features (rib height, shape, and lug spacing, etc.) as shown in Table 5.1. The average mesh size around the rebar is 1.5 mm which is less than rib height of the steel reinforcement (Table 5.1), whereas relatively large mesh size is selected at the ends to reduce the analytical computational cost. The attention is made to avoid to the sudden variation of the mesh size from small to large mesh size as it may suppress and affect the internal crack pattern. The main objective of the investigation is to highlight the variation of bond macroscopic bond characteristics of deformed bars subjected to the varying concrete cover thickness and to validate the coupled RBSM and solid FEM model utilizing the test results considering the previously stated test parameters.

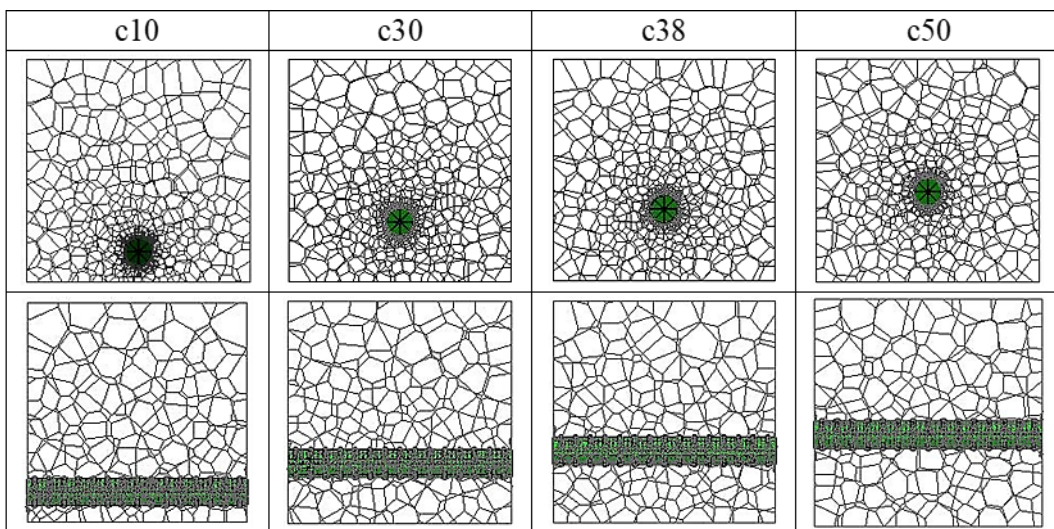


**Figure 5.3 Numerical models embedded with rebar D19**

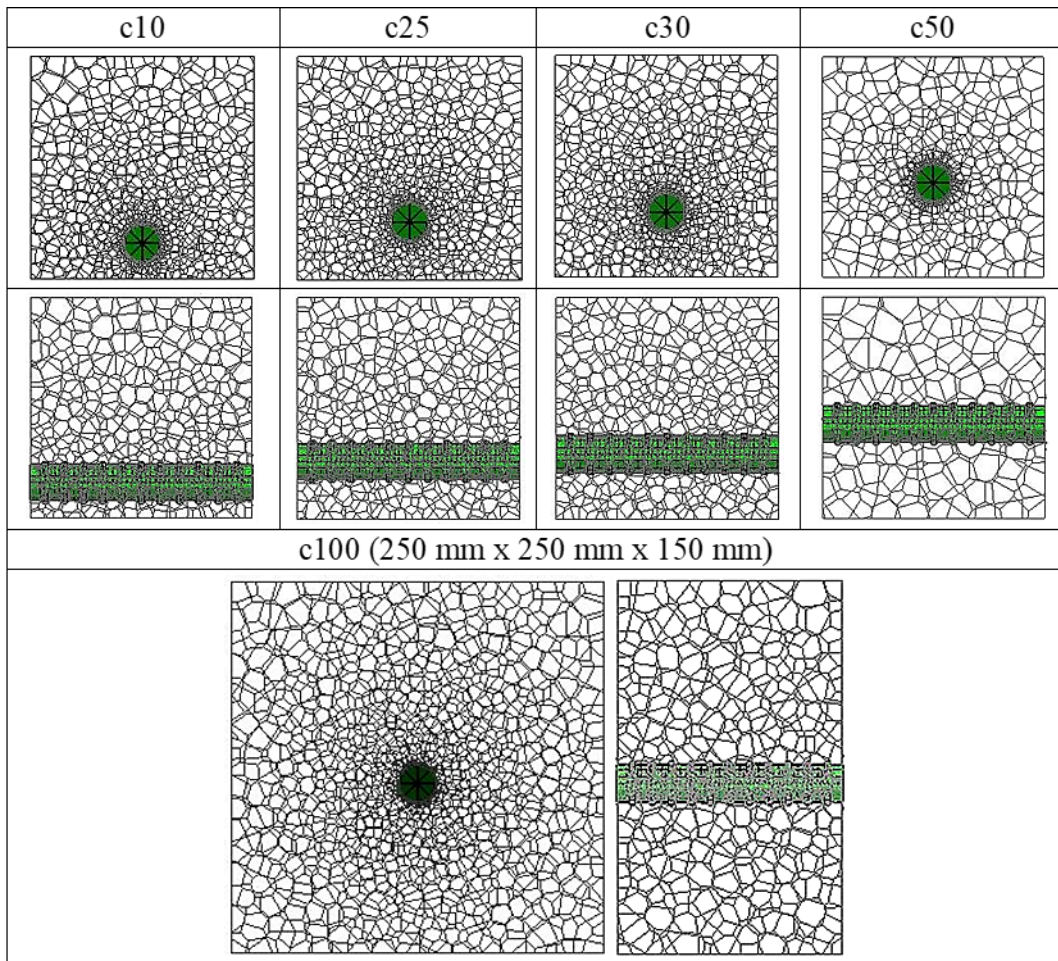


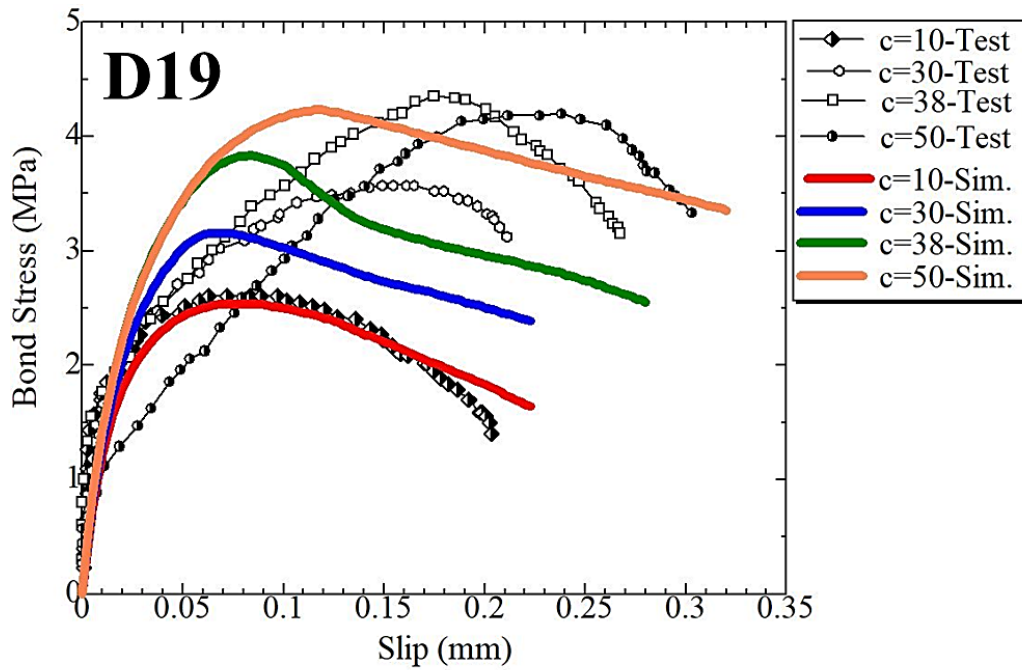
**Figure 5.4 Numerical models embedded with rebar D25**

### ***5.2.2 Evaluation of the bond behavior in two ends pull-out test***

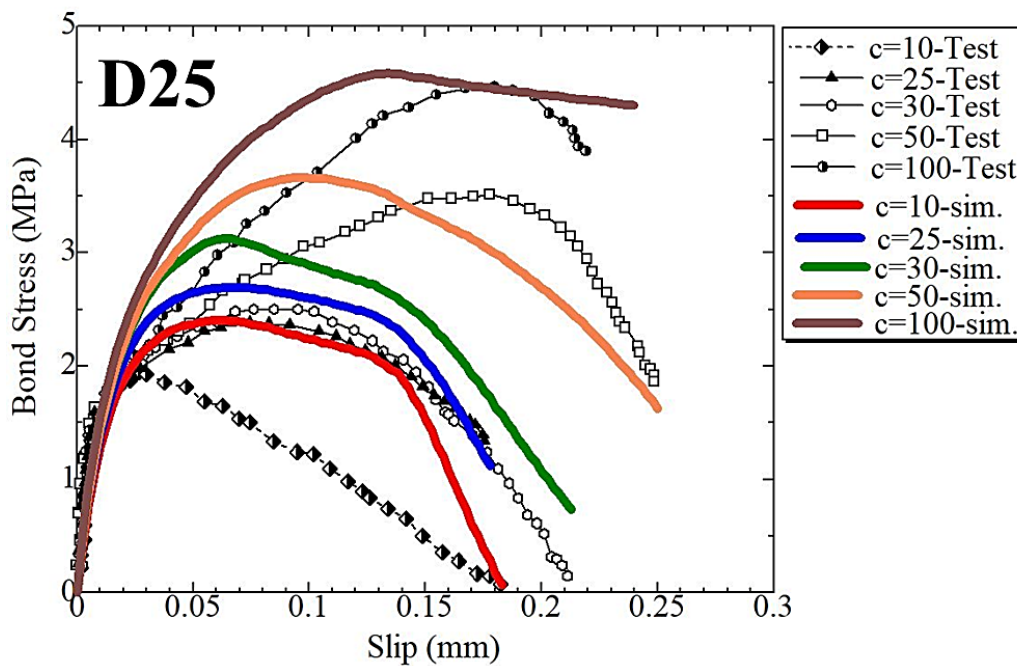
The validation and evaluation results of coupled RBSM and solid FEM model for macroscopic bond strength evaluation are discussed here for varying concrete cover thickness and rebar diameters loaded in two ends pull-out tests. The stress slip relationships for the deformed rebars D19 and D25 have been shown in Figure 5.5.

Figure 5.5 shows that in the test the bond stress increases against an increase in the concrete cover thicknesses for both rebars (D19 and D25). The numerical model also captures the same tendency of increasing bond stress with the increase in concrete cover thicknesses. The coupled RBSM and solid FEM model adequately reproduces the test results subjected to the varying concrete cover thicknesses and the rebar diameters.

The numerical model simulates the experimental peak bond stress reasonably but underestimates the test peak slip.



a) Bond stress-slip relationship for rebar D19



b) Bond stress-slip relationship for rebar D25

Figure 5.5 Bond stress slip relations under varying concrete cover thicknesses

The previous investigations revealed that the regions around rebar had a high water-cement ratio because of the wall effect (Maekawa et al. 2004) and aggregates did not exist around the rebar. These regions around the rebar should be simulated with reduced mechanical properties of concrete. In this regard, the concrete compressive strength should be reduced to half around the rebar and the influence region corresponding to this modification ranges equal to diameter ( $D$ ) of the rebar from its center (Hayashi et al. 2013) as shown in Figure 5.6.

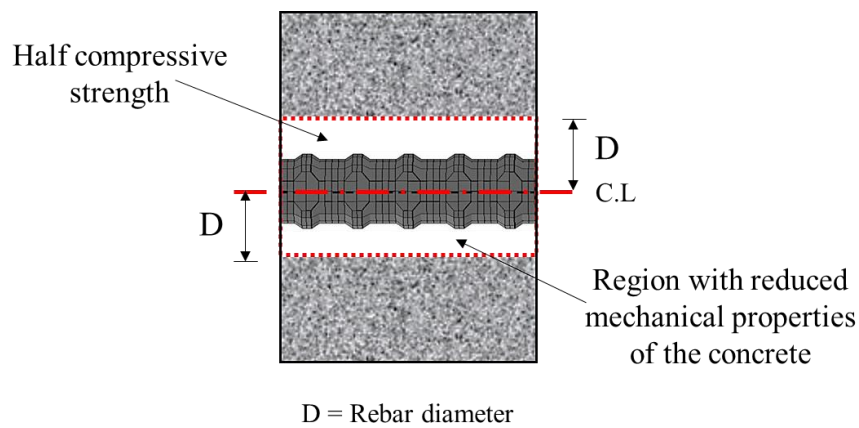
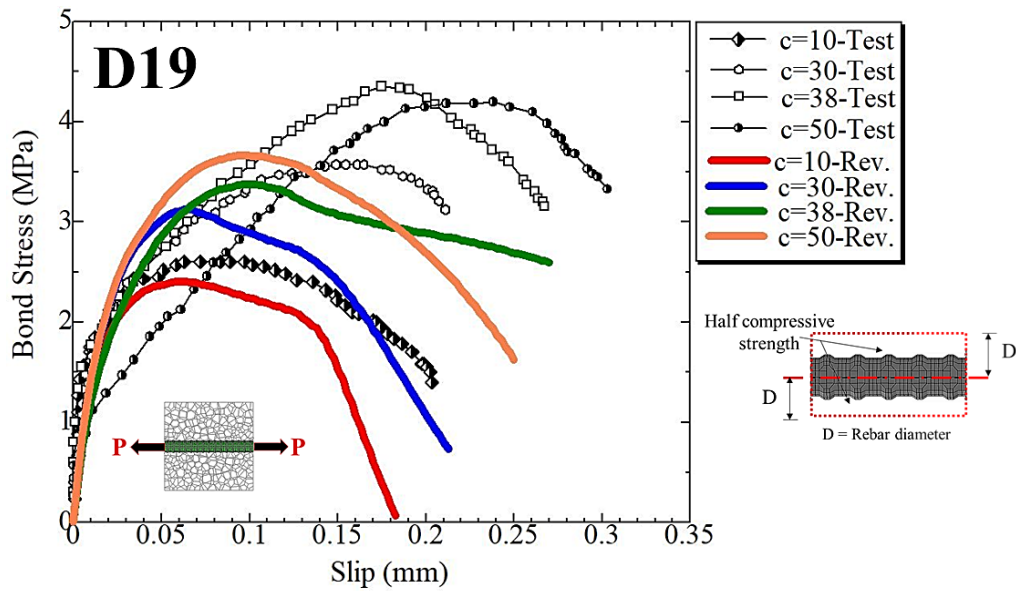


**Figure 5.6 Illustration of the regions with reduced strength of concrete around the rebar**

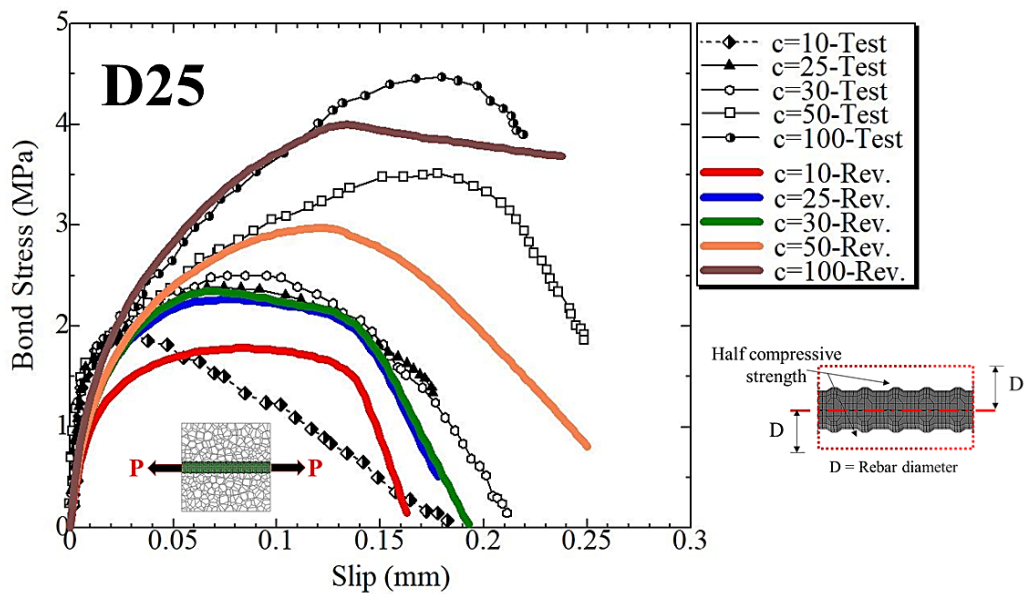
The original coupled RBSM and solid FEM model has been modified incorporating the recommendations of previous researchers. The revised numerical analyses have been performed including the reduction of the concrete mechanical properties around the rebar. The revised stress-slip relationships corresponding to revised numerical analyses are shown in Figure 5.7.

Figure 5.7 shows that the peak slip slightly improves but the peak stress decreases more compared with the results of the original model as shown in Figure 5.5. The numerically simulated peak stress and peak slip of the original and the revised models have been compared with the test results as shown in Figure 5.8. Figure 5.8 shows the improvement of the results (bond stress and slip) achieved by the revised model is negligible compared with the original model. Figure 5.8 also shows and that the original coupled RBSM and solid FEM model reasonably simulates the test peak

stress and peak slip without requiring any modification. Therefore, the original model is adopted for further analyses of the bond behavior.

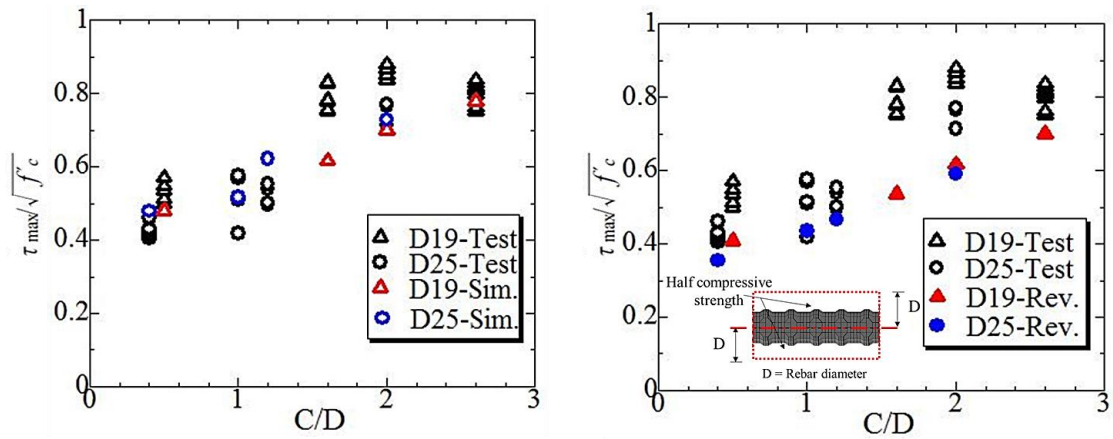


a) Revised bond stress-slip relationship for rebar D19

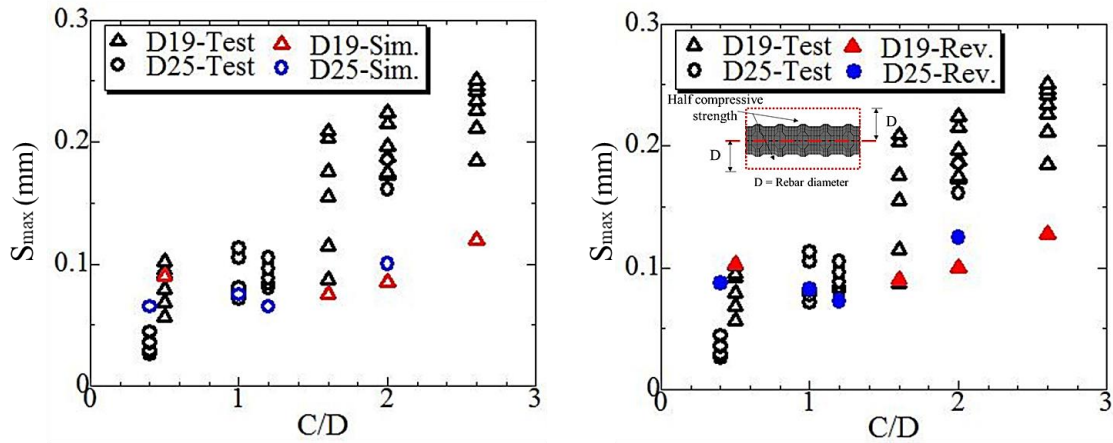


b) Revised bond stress-slip relationship for rebar D25

**Figure 5.7 Revised bond stress slip relations with reduced strength of the concrete around the rebar**



a) Comparison of peak stress for original and revised model



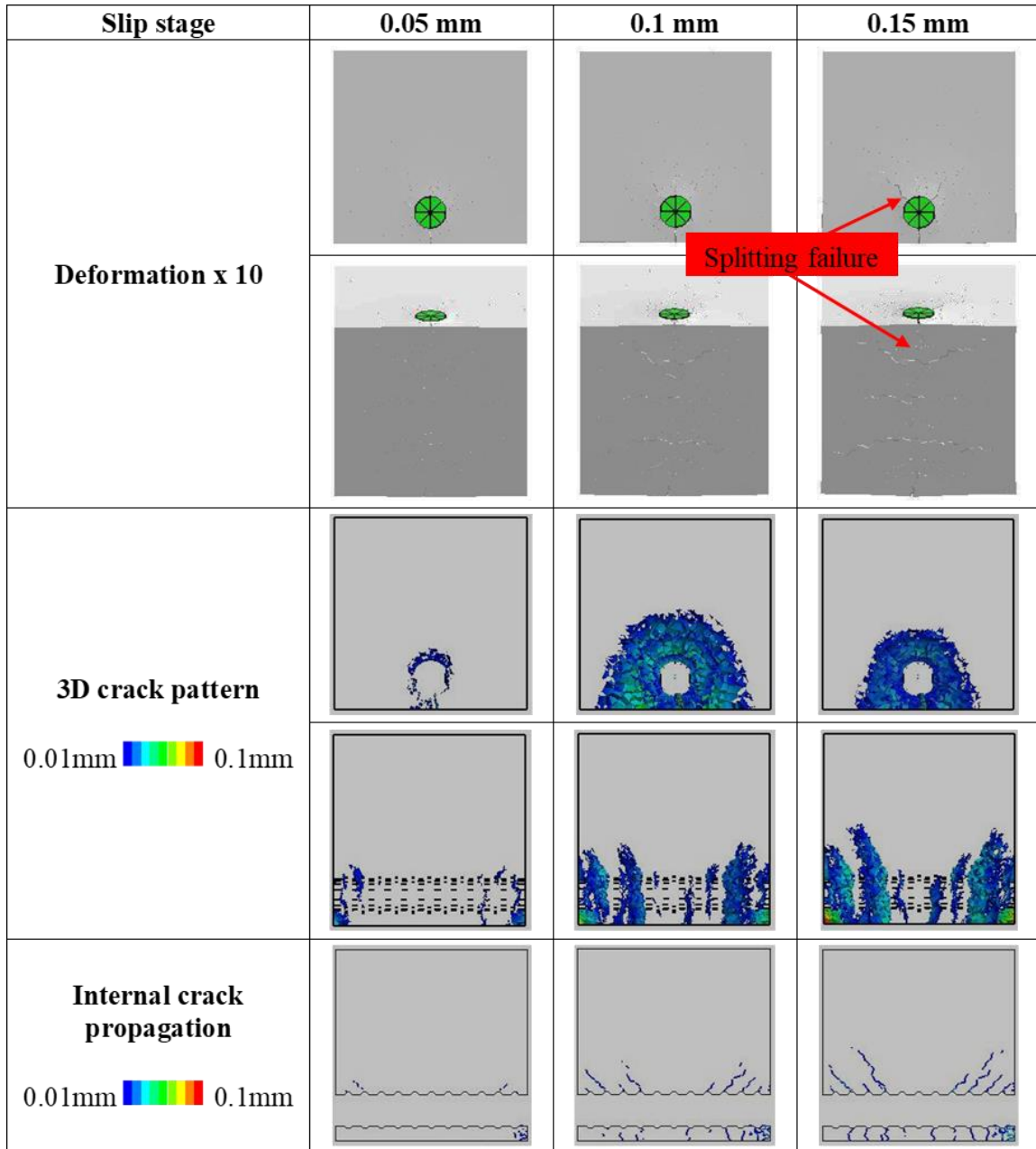
b) Comparison of peak slip for original and revised model

Figure 5.8 Comparison of the original and the revised model

### 5.2.3 Investigation of internal failure process and mechanism

After validation of the numerical model (Figure 5.8), as the numerical results lie between minimum and maximum test investigations, the internal failure process and mechanism are evaluated. The effect of concrete cover thickness on the deformation response of the specimens along with discussion regarding the detailed internal failure process have been explained here. The deformed behaviors based on the findings of the original numerical model corresponding to the concrete cover thickness ( $c$ ) of 10 mm, 25 mm, 50 mm, and 100 mm embedded with rebar D25 have been demonstrated in Figure 5.9, Figure 5.10, Figure 5.11 and Figure 5.12, respectively. The concrete cover thicknesses have been divided into three categories; small =  $c_{10}$  and  $c_{25}$ , medium =  $c_{50}$

and large = c100. The deformed behaviors (surface cracks, 3D and internal crack) have been presented against the slip stages of 0.05 mm, 0.1 mm and 0.15 mm on stress slip relationships.



**Figure 5.9 Deformation response of c10 with rebar of D25**

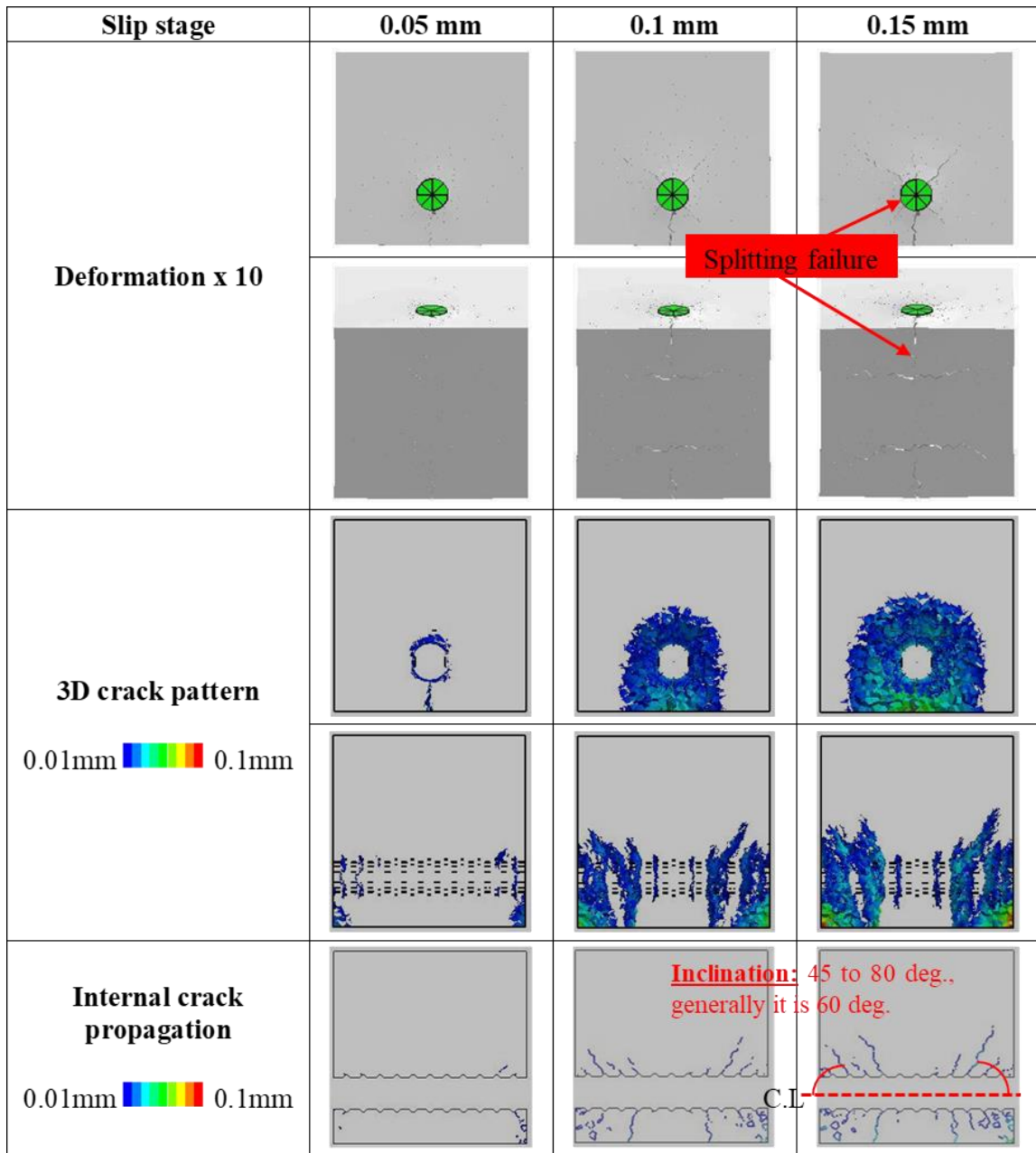
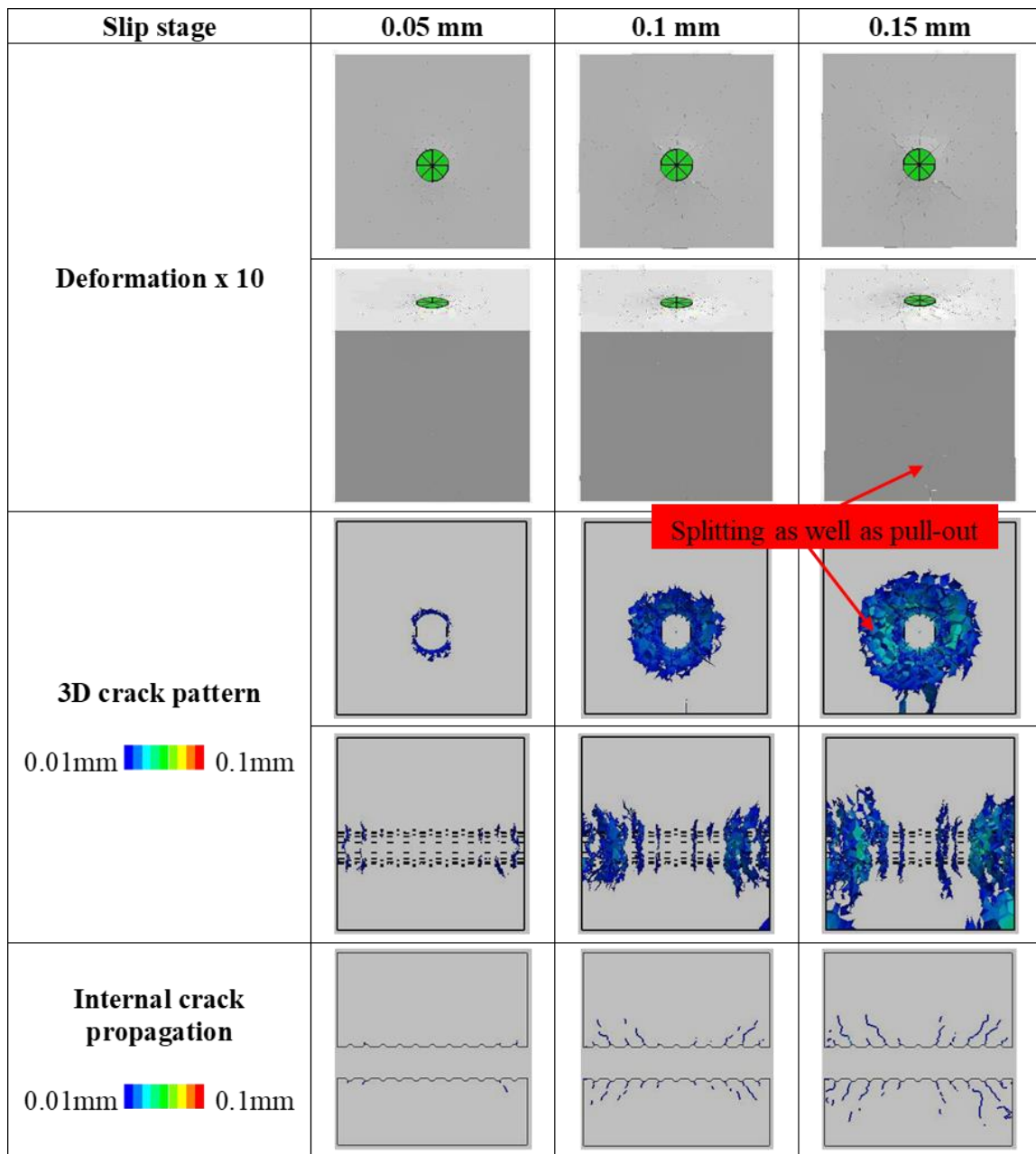
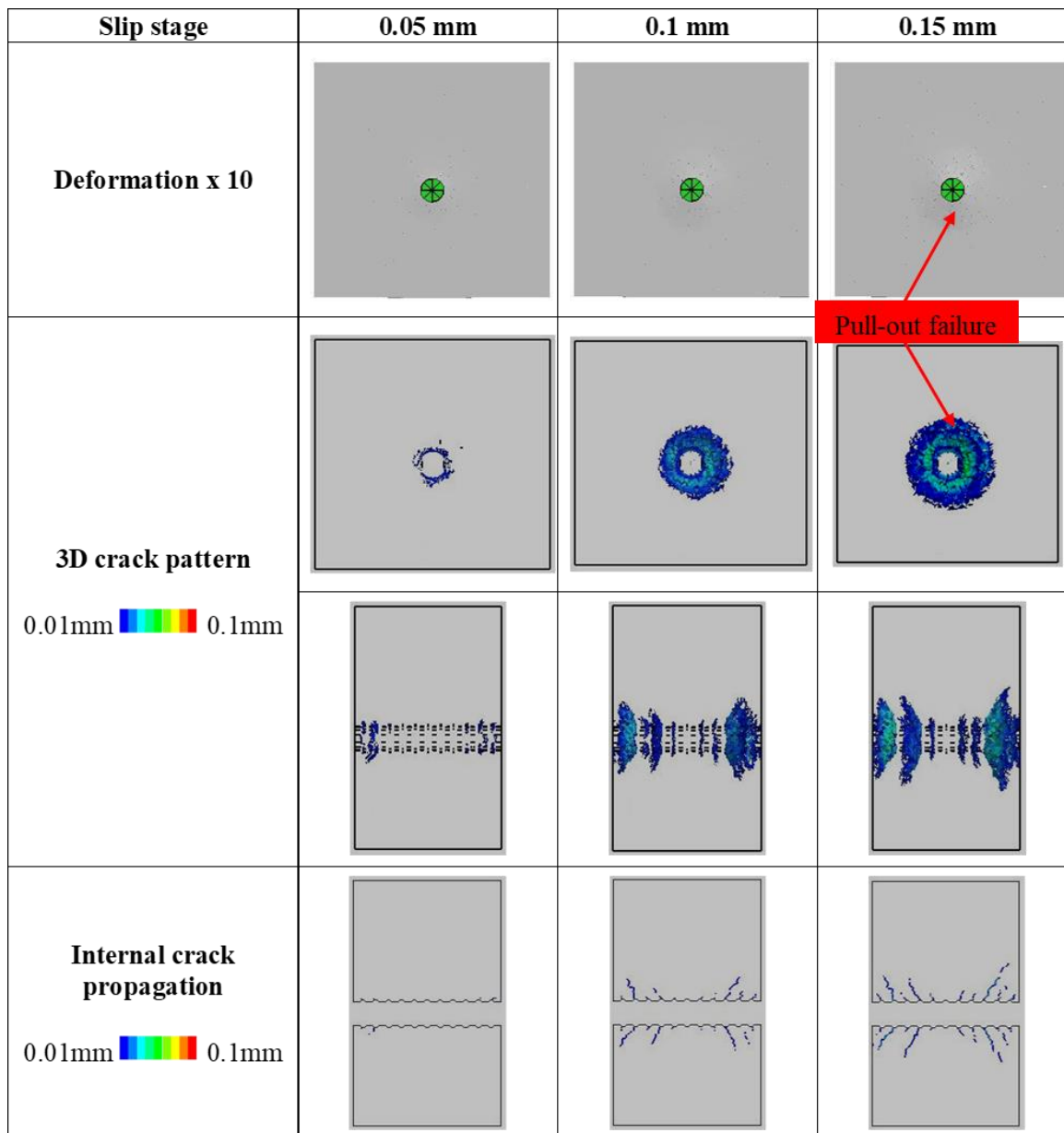


Figure 5.10 Deformation response of c25 with rebar of D25



**Figure 5.11 Deformation response of c50 with rebar of D25**



**Figure 5.12 Deformation response of c100 with rebar of D25**

The deformed behaviors in Figure 5.9 and Figure 5.10 highlight that in the case of the small cover thicknesses of 10 mm and 25 mm, specimens show longitudinal radial crack development initiating from the loading ends of the reinforcing bar at small slip stage of 0.05 mm before the peak. Then the progress of radial cracks happens from loading ends towards the middle of the specimens and thus consequently causes the splitting failure in post-peak as shown in Figure 5.9 and Figure 5.10. The inclination of the internal crack originating from the ribs of the deformed rebars ranges between 45

degrees to 80 degrees, which also correlates well with the test investigations of Goto, 1971).

Figure 5.11 illustrates the deformed behaviors in the specimen with the medium concrete cover thickness of 50 mm. The specimen shows relatively improved performance because of an increase in cover thickness (the passive confinement effect due to concrete cover). The numerical model efficiently responds to the passive confinement provided by the cover thickness. Figure 5.11 shows that at a slip stage of 0.05 mm there is no radial crack development in contrast with the small (c10 and c25) cover thickness case in Figure 5.9 and Figure 5.10. Similarly, at the slip stage of 0.1 mm in Figure 5.11, the crack propagation at the ends just starts while in small (c10 and c25) cover thickness case, it fully progresses to the full length of the specimen. Figure 5.11 shows that medium concrete cover thickness of 50 mm reproduces splitting cracking after the peak and exhibits mixed type failure i.e. splitting as well as pull-out.

Moreover, Figure 5.12 illustrates the deformed behaviors in the specimen with a large concrete cover thickness of 100 mm. Figure 5.12 reveals that there is no splitting crack propagation on the surface of the specimen. The crack propagation happens internally around the rebar. The large concrete cover thickness of the specimen restrains the initiation and propagation of splitting crack to surface of the specimen and reproduces the pull-out type failure.

The deformed behaviors highlight the difference in internal failure process and mechanism under the influence of varying degree of the passive confinement; generated due to variation in the concrete cover thicknesses. The numerical simulations clearly demonstrate that the deformed behaviors are found to be dependent on the degree of passive confinement. The deformation response transforms from splitting failure to the pull-out failure with the increase in concrete cover thickness while keeping the diameter of the rebar and the compressive strength of concrete constant. Moreover, the internal crack patterns reveal that the coupled RBSM and solid FEM model effectively simulates the crack initiation and the orientation, originating from the ribs of the rebar. The stress slip relations and deformed behavior reveal that the coupled RBSM and solid FEM model effectively simulates the effect of varying concrete cover thickness and rebar diameters on bond strength.

### **5.3 Evaluation of macroscopic bond behavior in one end pull-out test subjected to lateral pressures**

After the numerical evaluation of the macroscopic bond characteristics between the reinforcing steel bars and the concrete under two ends pull-out test, the numerical evaluation is also carried for the bond behavior evaluation in one end pull-out test under the influence of externally applied lateral pressures to the concrete surface using the test investigations of Raymond et al. 1965.

For numerical evaluation of the bond behavior in one end pull-out test, the reinforced concrete specimens under the effect of lateral pressure are simulated. The focus is specifically made on the effects of stress conditions and the boundary conditions on the bond characteristics, crack propagation behaviors, and the failure modes of specimens.

#### ***5.3.1 Test overview and numerical modeling***

In this numerical evaluation, the numerical simulations are carried out against the already published test results of RC specimens loaded under one end pull-out test with and without application of the lateral pressures.

All the test specimens were of cubical geometry with a size of 150 mm x 150 mm x 150 mm. The specimens were embedded with the deformed bars of D19 and D29. The yield strength ( $f_y$ ) of the steel reinforcement was around 632.30 MPa. The concrete compressive strength of the specimens was around 32.5 MPa. The embedment length of the reinforcing bar was 150 mm for all the specimens. The specimens were seated on a system of bearing plates and a spherically bearing block to ensure that the load would be of axial nature. A leather pad of around 1.5 mm thickness was placed between the concrete specimens and the bearing steel plates. The lateral pressure was applied to two parallel concrete faces of 150 mm cube specimens using a loading frame that enclosed the test specimens, hydraulic ram, and the spherically seated bearing blocks. A dial micrometer gage was used to determine the movement of the deformed bar to the concrete. The simple representation of the one end pull-out test is shown in Figure 5.13.

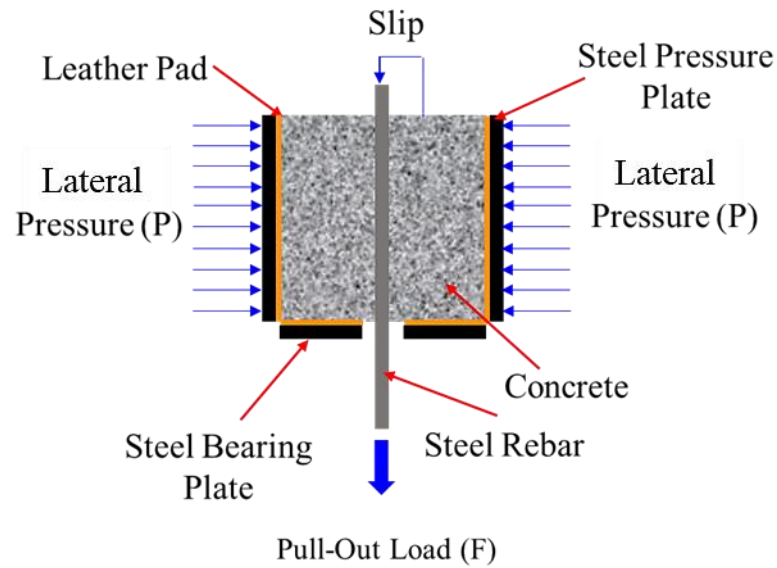


**Figure 5.13 Representation of the test set up in one end pull-out**

The pull-out load was applied to the one end of the rebar, and the bond stress of the concrete was measured by using the Equation (5.2).

$$\text{Bond Stress} = F / \pi dl \quad (5.2)$$

Where,

F = Pull – out Load

d = Rebar diameter

l = Embedded length of the rebar

The numerical simulations are mainly divided into three cases. The specimens embedded with deformed rebar D19, without and with the application of the lateral pressures and are recognized as case 1 and case 2 here, respectively. Similarly, the unconfined specimens embedded with deformed rebar D29 are considered as case 3. Initially, the numerical evaluation of case 1 and case 2 was performed. The numerical simulations were further extended for case 3 after numerical evaluations of case 1 and case 2. For the numerical modeling of the test specimens; concrete is modeled using 3D-RBSM based on the formulation of Yamamoto et al. (2008) and the steel rebars (D19 and D29) are modeled employing the eight noded nonlinear solid finite elements using the actual geometrical features (rib height, shape, and lug spacing, etc.) as shown in Figure 5.14.

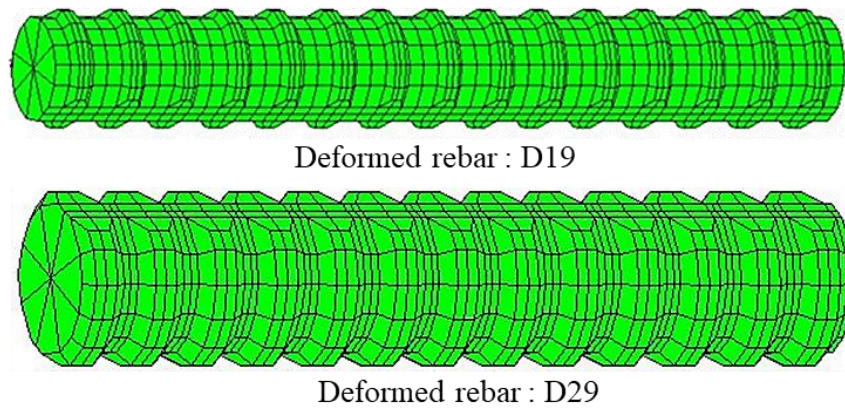


**Figure 5.14 3D model of the steel reinforcement**

The numerical models corresponding to all three cases have been illustrated in Figure 5.15 (all dimensions are in mm). The average mesh size for concrete in all cases is selected less than the rib height of steel reinforcement. The average mesh size selected near the boundary interface of concrete and steel is around 1.5 mm.

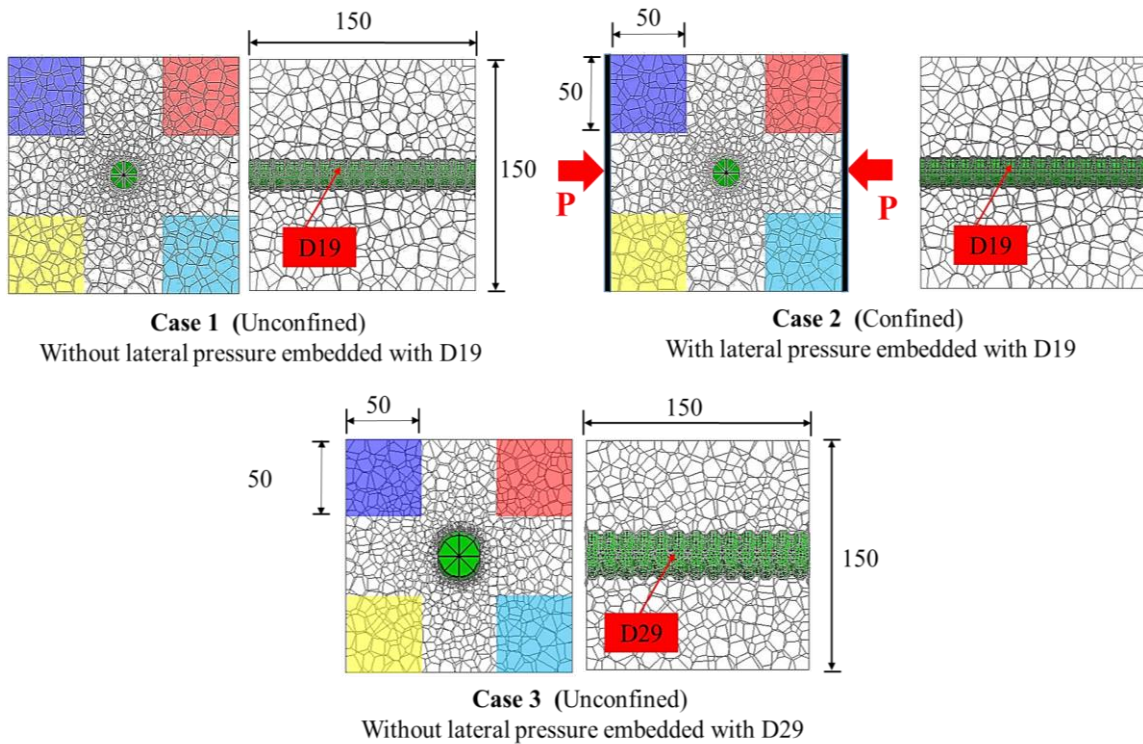


**Figure 5.15 Numerical models for one end pull-out test**

The relatively large mesh size of around is selected at the ends of the specimen to reduce the analytical computational cost. The preliminary numerical investigations suggested that the pull-out region of the concrete cones might be influenced by the reaction forces generated against the different sizes of the steel bearing plates, thus affected the overall deformed behaviors and the bond strengths. Since, the reference test did not provide the information of the test boundaries (numbers and size of the plates). Therefore, the limited details for the boundaries in the test necessitate to select the reasonable numbers and size of the loading plates in the numerical simulations which should not affect the pull off region of the concrete cone under the one end pull-out tests. Therefore, the four number of plates are used in the numerical modeling to address the above-mentioned facts. The size of each plate is 50 mm x 50 mm as shown in Figure 5.15.

### ***5.3.2 Results and discussion for numerical evaluation in one end pull-out test***

The numerical simulation results are presented for case 1 (unconfined specimen embedded with rebar D19), case 2 (confined specimen embedded with rebar D19) and case 3 (unconfined specimen embedded with rebar D29).

#### ***5.3.2.1 Case 1 (Unconfined specimen embedded with rebar D19)***

As discussed earlier, the boundary conditions for the plates in the experiment play a significant role in controlling the deformation capacity and deformed behaviors. Therefore, it is important to consider the boundary conditions of test adequately, for high precision numerical simulations. The leather pad between the concrete specimens and the bearing steel plates (section 5.3.1) may influence the level of friction and thus reaction force imparted on the concrete surface and ultimately may alter the bond strengths of the specimens in one end pull-out test. To address these test boundary conditions in numerical simulations, the different friction levels are investigated numerically between the concrete specimens and the steel plates through the sensitivity analysis of friction. The friction between the steel plates and the concrete elements is controlled by the parameters of Mohr-Coulomb criteria of the shear spring between the elements (Figure 2.2e), where  $c$  and  $\phi$  are the cohesion and the angle of internal friction, respectively. In sensitivity analysis of the friction, the different levels of frictions between the concrete specimens and the steel plates are incorporated by selecting the

different angles of internal friction ( $\varphi$ ) for the shear springs to lie between 0 degree and 37 degree. The numerical simulation results for case 1 considering the sensitivity analysis of friction has been illustrated in Figure 5.16.

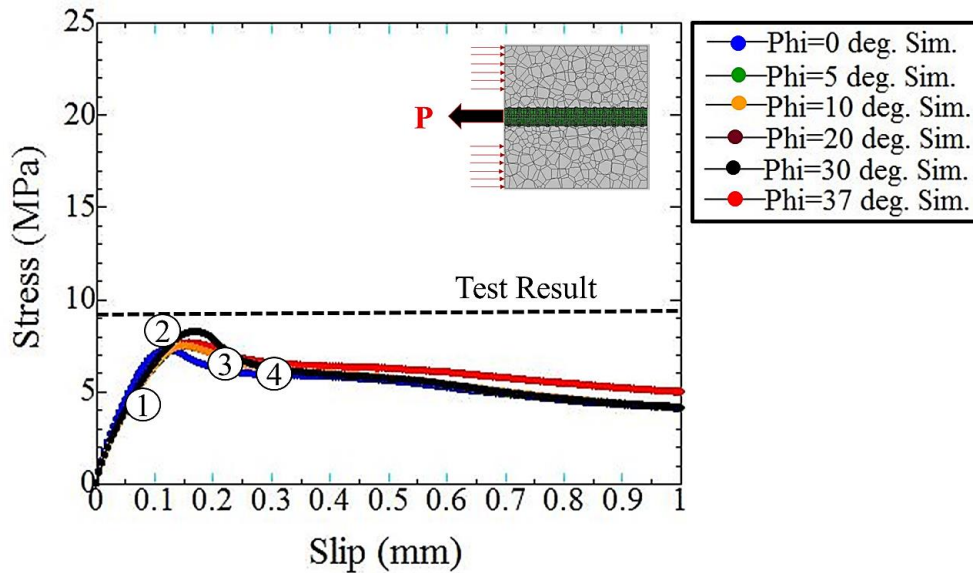


**Figure 5.16 Stress slip relations of unconfined specimen embedded with rebar D19**

It is evident from the Figure 5.16; the stress slip relationships are dependent on the friction between the concrete specimen and the bearing steel plates. The Figure 5.16 shows that for low friction levels ( $\varphi = 0, 5,$  and  $10$  degree), the simulations results are on the lower side compared with the other friction levels ( $\varphi = 20, 30$  and  $37$  degree). The cases corresponding to internal friction angle equal to  $20$  deg. and  $30$  deg. show almost the same behavior, and express the maximum bond stress close to the test value. On the other hand, the case where the internal friction angle is  $37$  degree, the maximum bond stress decreases a little. Based on the sensitivity analysis of the friction, the internal friction angle equal to  $20$  degree has been adopted.

Figure 5.17 shows that the deformation behaviors obtained by numerical simulation for case 1, corresponding to the internal friction angle of  $20$  degree. The internal failure process is explained here. Figure 5.17 shows that at a slip stage of  $0.075$  mm on stress slip curve, it can be confirmed that the cracks propagate conically from the surface of the reinforcing bar, starting from the loading end of the deformed rebar, as investigated by the Goto (1971). Furthermore, at slip stage corresponding to  $0.1$  mm,

splitting cracks occur. In post-peak, corresponding to slip of 0.3 mm, it can be seen that the cracks propagate to the ends of the specimen and cause the splitting failure of the specimen. In the test, the splitting of the specimen was observed and the specimen failed into four segments. In the same manner, the numerical analyses also reproduce the splitting failure mode and the failure of the specimen into four segments. Figure 5.17 shows that the numerical simulation failure mode is consistent with the experimental observations.

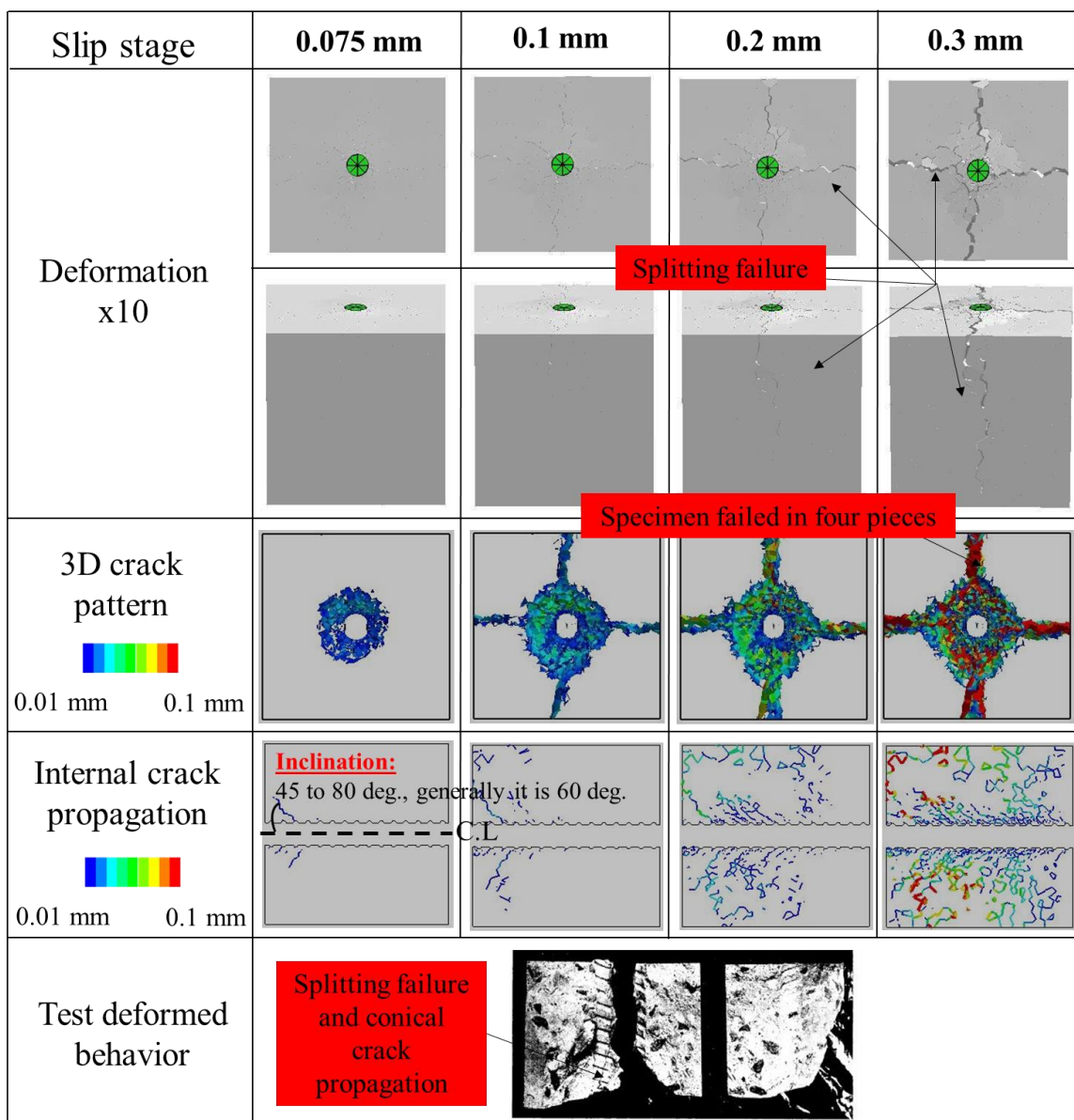


**Figure 5.17 Deformed behaviors of unconfined specimen embedded with rebar**

**D19**

### 5.3.2.2 Case 2 (Confined specimen embedded with rebar D19)

The numerical simulation results of the specimen confined by externally applied lateral pressure (50 % of  $f'_c$ ) is discussed here. The numerical simulation of case 2 is also based on the sensitivity analysis of friction between the concrete specimens and the bearing steel plates while externally applied lateral pressure is kept constant. The simulation results of case 2 are shown in Figure 5.18. Figure 5.18 shows that the applied lateral pressure causes the ultimate bond stress and ultimate slip to increase compared with the unconfined specimen (case 1) as shown in Figure 5.16.

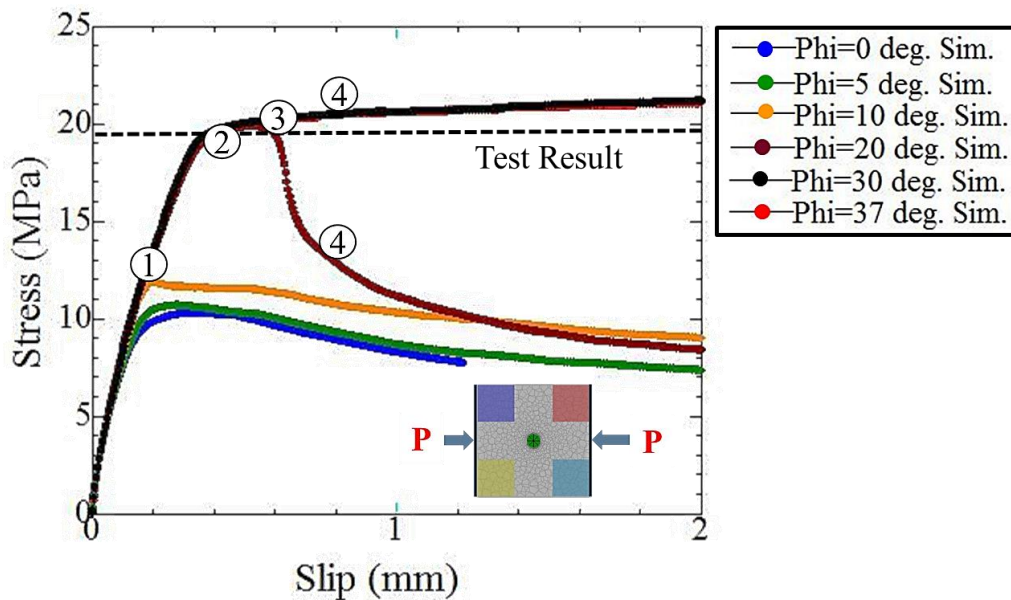
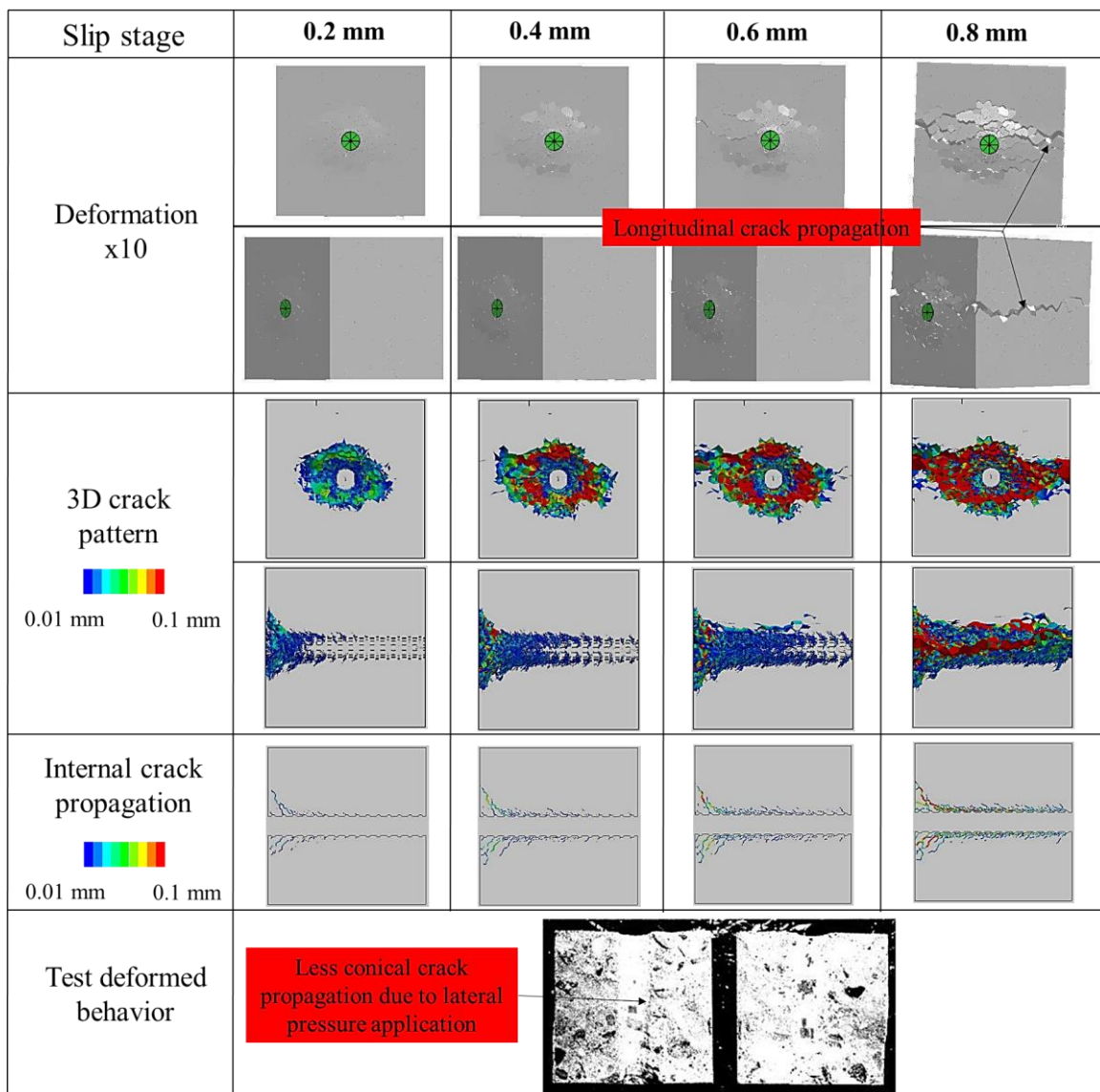


**Figure 5.18 Stress slip relations of confined specimen embedded with rebar D19**

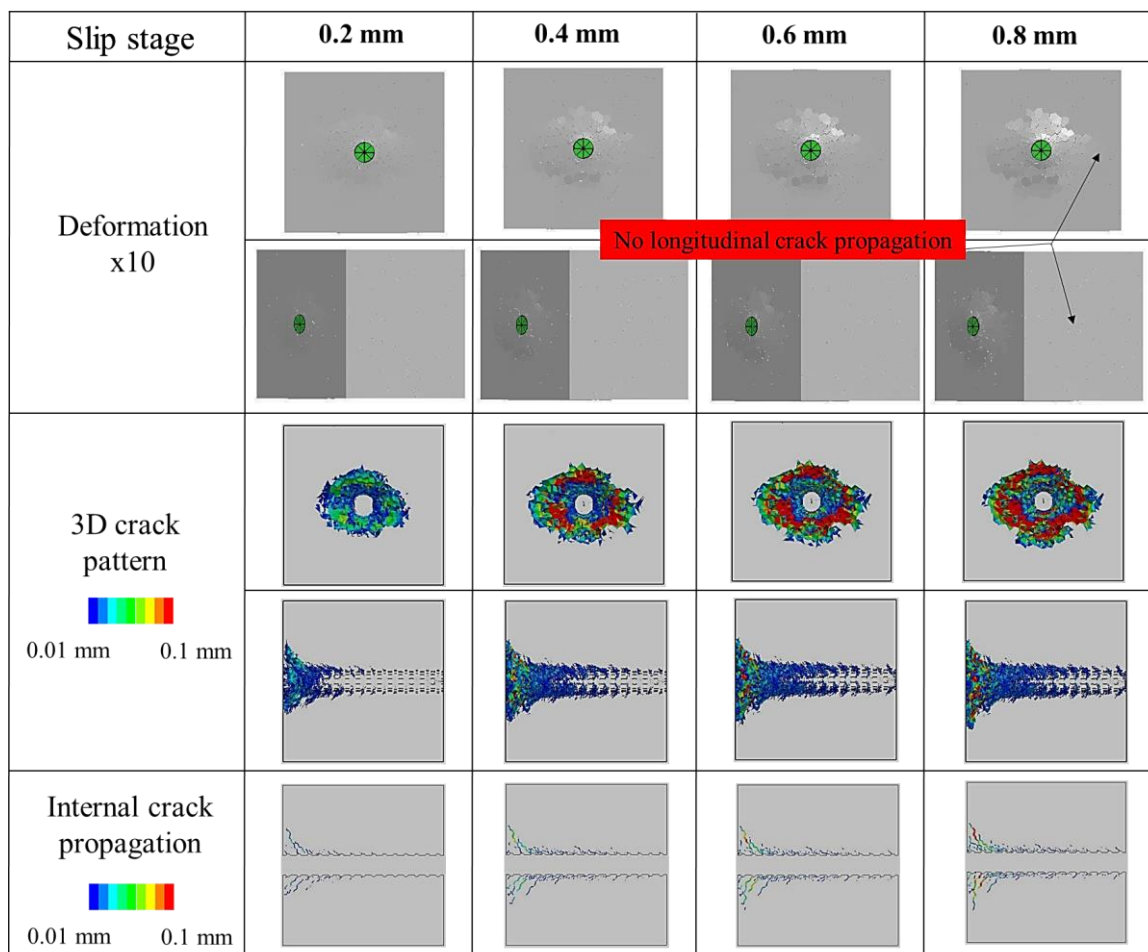
The stress slip relationships show that the numerical simulation results are also highly sensitive to the friction between concrete and steel bearing plates. Figure 5.18 shows that for low friction levels ( $\phi = 0, 5,$  and  $10$  degree), the simulation results are on the lower side. It is evident from the stress slip curves as shown in Figure 5.18, in the case where the internal friction angle is  $20$  deg., the simulated stress slip results are found to be in agreement with the experimental results and also express softening behavior. On the other hand, when the internal friction angle is increased beyond  $20$  degree, the corresponding friction generated between the concrete surface and the steel

plate is so high and the yielding of the rebar occurs in the pull-out test and consequently, no softening behavior appears. This behavior can be confirmed through stress slip relationships against  $\varphi = 30$  and  $37$  degree as shown in Figure 5.18.

The stress slip behaviors simulated in Figure 5.18 can be clarified through the deformed behaviors. The deformed behaviors for mild friction level ( $\varphi = 20$  degree) and high friction level ( $\varphi = 30$  degree) are shown in Figure 5.19 and Figure 5.20, respectively.



**Figure 5.19 Deformed behaviors of confined specimen with  $\varphi = 20$  degrees**



**Figure 5.20 Deformed behaviors of confined specimen with  $\phi = 30$  degrees**

In very low friction levels ( $\phi=0, 5,$  and  $10$  degree), although the deformed behaviors are not shown here, it is observed that the specimen shows the splitting type failure and as result of these splitting failures the peak stresses are less as shown in Figure 5.18. The comparison of internal crack patterns of unconfined and confined specimens is discussed here as shown in Figure 5.17 and Figure 5.19, respectively. Figure 5.19 clearly highlights that internal crack propagation around the rebar is less compared with unconfined specimens as shown in Figure 5.17. The lateral pressure restrains the crack propagation in confined specimens and as result of that behaviors the peak stress and peak slip get improved in confined specimens as shown in Figure 5.18, in contrast with unconfined specimens.

Figure 5.19 shows that in mild friction level ( $\phi = 20$  degree), at slip stages of  $0.2$  mm and  $0.4$  mm before the peak there is only the conical crack development around the

rebar and at slip stage 0.6 mm around the peak, the crack propagates from one pressure face to another pressure face. In post-peak, at a slip stage of 0.8 mm, along with crack propagation development from one pressure face to another pressure face and it also extends longitudinally. The specimen confined with mild friction level ( $\varphi = 20$  degree) produces the mixed type failure, i.e., the splitting as well as the pull-out as shown in Figure 5.19). In test, the crack propagation was observed from one pressure face to another pressure face and the cracks also intersected the embedded rebar. Figure 5.19 shows that the numerical simulation results correlate well with the test investigations against mild friction level ( $\varphi = 20$  degree).

Figure 5.20 shows the deformed behavior of confined specimens in high friction level ( $\varphi = 30$  degree). Figure 5.20 shows that at all the slip stages there is no longitudinal crack propagation. This behavior is reproduced because of high friction generated between the steel plates and the concrete surface against the internal friction angle ( $\varphi$ ) more than 20 degree as shown in Figure 5.17.

Based on the results of the sensitivity analysis of friction for simulating the test stress slip relationships and the failure modes in unconfined (case 1) and confined (case 2) specimens, the reasonable level of friction is considered corresponding to the  $\varphi = 20$  degree on the boundaries.

### **5.3.2.3 Case 3 (Unconfined specimen embedded with rebar D29)**

The numerical evaluation of the unconfined specimen embedded with rebar D29 also based on the mild friction level ( $\varphi = 20$  degree). The numerical simulation results are shown in Figure 5.21. Figure 5.21 shows that the original coupled RBSM and solid FEM model underestimates the peak stress and peak slip compared with the test results.

Therefore, the original numerical model has been revised considering the half compressive strength of concrete around the rebar as explained earlier in section 5.2.2 and Figure 5.16. The revised simulation result is illustrated by a blue solid line as shown in Figure 5.21. Figure 5.21 shows that the revised model effectively captures the ultimate stress but still slightly underestimates the experimental peak slip.

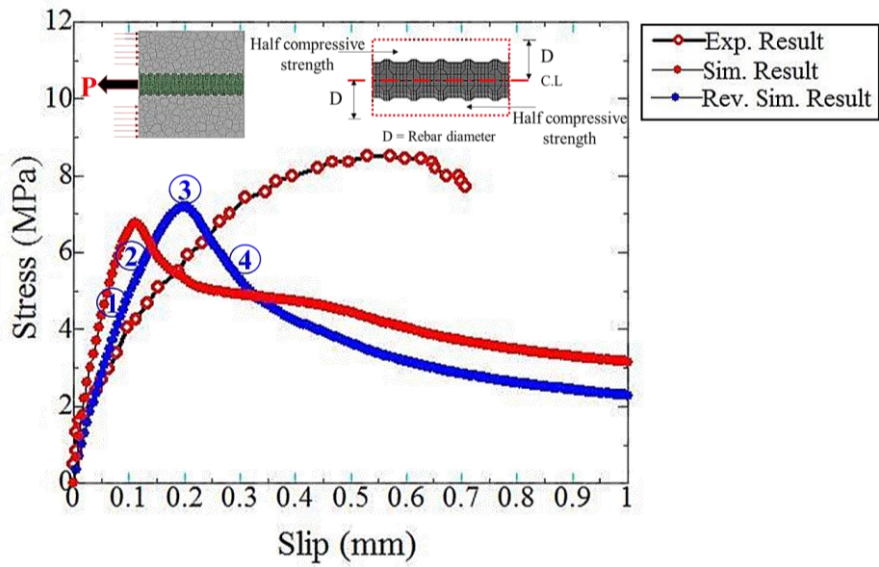


Figure 5.21 Stress slip relations of unconfined specimen embedded with rebar D29

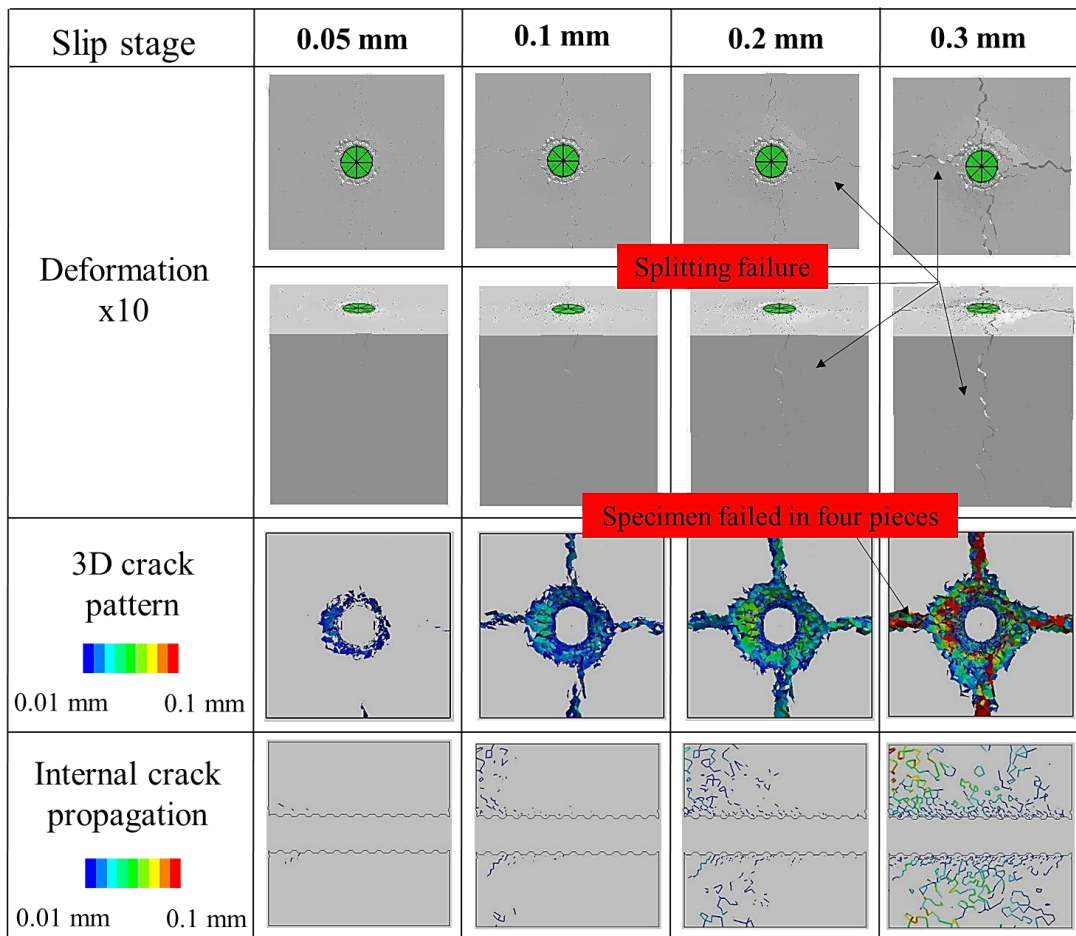


Figure 5.22 Deformed behaviors of unconfined specimen embedded with rebar

D29

The deformed behaviors of unconfined specimen embedded with rebar D29 have been shown in Figure 5.22. Figure 5.22 shows the same failure process as that of the unconfined specimen in case 1. The specimen in case 3 also shows the radial crack development originating from the reinforcing rebar and causes the specimen to be failed into four pieces. Figure 5.22 shows that the specimen in case 3 also reproduces the splitting failure behavior.

## **5.4 Evaluation of detailed failure behavior in axially loaded RC prisms under direct tension**

The numerical evaluation of the coupled RBSM and solid FEM model is also performed for the numerical evaluation against detailed failure behaviors (internal cracking mechanism) using the experimental investigations related to axially loaded reinforced concrete prisms in direct tension by Goto et al. 1971 and 1980.

### ***5.4.1 Test overview and numerical modeling***

The mesoscale simulations using the numerical model have been carried out for the axially loaded RC prisms in tension evaluating the detailed failure mechanism. In the test, the internal crack formation and pattern were investigated corresponding to the stress of the deformed rebar using axially loaded RC prism in tension.

The size of the specimen used for the observation of the internal crack pattern was 120 mm x 120 mm x 1000 mm, embedded concentrically with the deformed rebar of D32, whereas for the longitudinal crack (crack in the direction of bar axis and formed corresponding to the high stress of rebar), the size of the specimen was 120 mm x 120 mm x 880 mm. The yield strength ( $f_y$ ) of the steel reinforcement was around 390.0 MPa. The cylinder compressive strength and the tensile splitting strength of concrete were around 30.0 MPa and 2.8 MPa, respectively. The tensile loading was applied to exposed ends of the reinforcing steel. The internal crack formation was investigated by providing the narrow holes parallel to the reinforcing steel. The ink was injected during the application of the tensile loading, the internal cracks were dyed and afterward the specimens were cut in half along planes. In the test, three shallow notches were

introduced in the specimens before conducting the experiment such that the first crack would occur at the notches. The prescribed position of the notches in the specimens, splitting face and the cross-sectional details (all dimensions are in mm) of previously discussed specimens are shown in Figure 5.23.

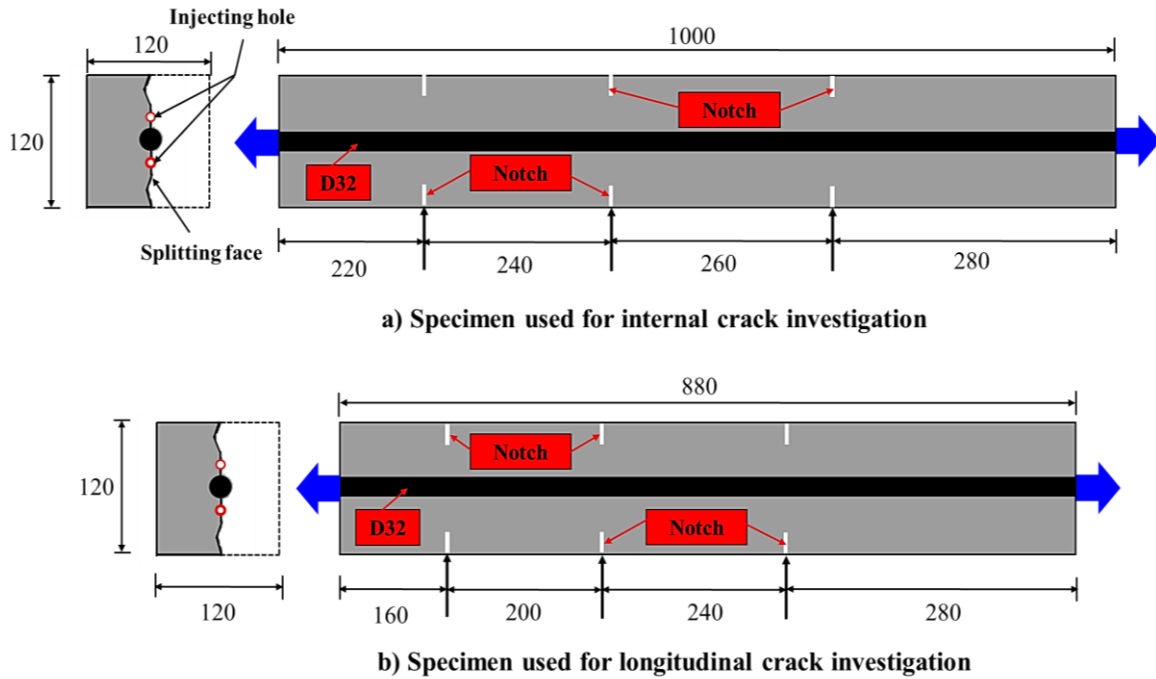


**Figure 5.23 Details of the test specimens embedded with rebar D32**

The objective of the experiment was to reveal the quantitative fracture process and mechanism of concrete around the tensile deformed rebar in axially loaded specimens.

After numerical evaluation of the numerical model for the internal and the longitudinal crack propagation behaviors, the sensitivity of the numerical model was also confirmed for the varying lug spacing of the rebar. The sensitivity analysis of lug spacing was carried out through the specimens with a size of 180 mm x 180 mm x 300 mm embedded with the deformed rebar of D51 having the varying lug spacing of 15 mm and 30 mm. In this regard, the lengths of specimens in numerical simulation analyses were selected between two experimental notches as shown in Figure 5.24.

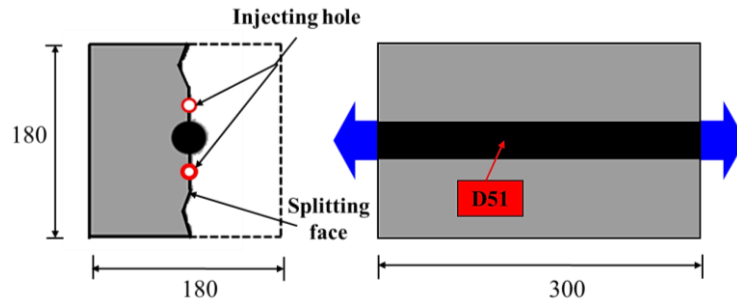
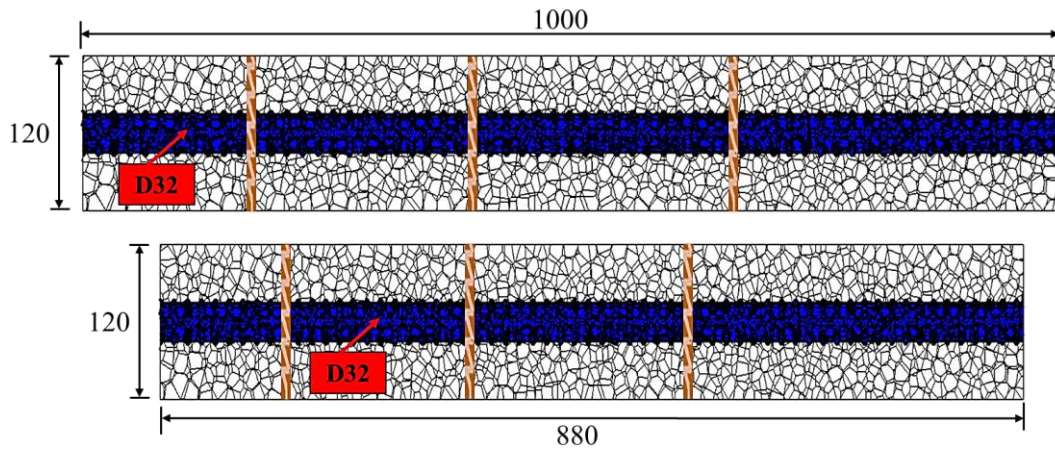


**Figure 5.24 Details of the specimens used for the sensitivity analysis of rebar lug spacing**

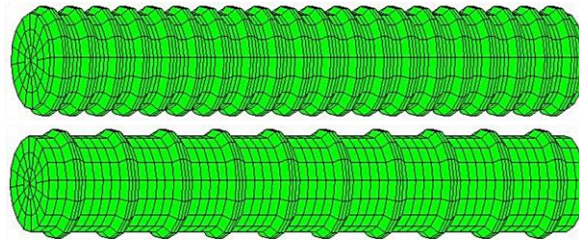
The purpose of sensitivity analysis for lug spacing was to highlight the variation of the internal crack pattern and the bond characteristics against varied lug spacing for the same diameter of the rebar.

The numerical models corresponding to all the specimens are shown in Figure 5.25. The average mesh size of concrete in numerical models ranges between 2 mm to 10 mm to reduce the computational cost. As mentioned earlier, the shallow notches were introduced in the test specimens such that first crack would occur there, these test shallow notches have also been incorporated in the numerical simulations. The numerical model includes the complete modeling of concrete region without making grooves for the test shallow notches as shown in Figure 5.25.

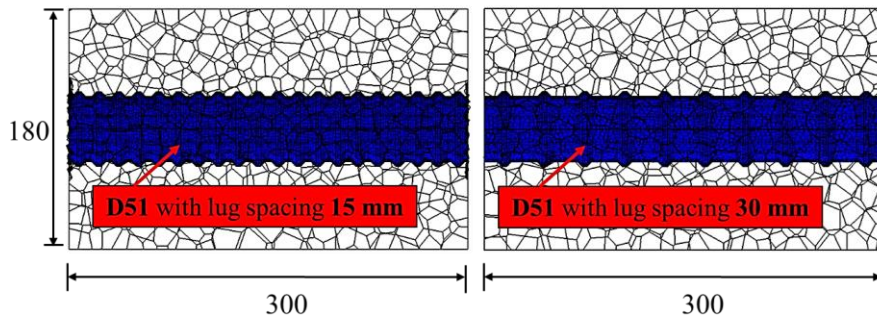
However, to incorporate the behavior of the test shallow notches, the material parameters (tensile strength ( $\sigma_t$ ), cohesion ( $c$ ) and fracture energy ( $g_f$ )) of the constitutive models for the normal and the shear springs of concrete on the locations of the notches have been reduced by 70 % over the full cross-section such that the crack initiation would first occur there.



a) Numerical models for internal and longitudinal crack investigation



b) 3D model of rebar D51  
(lug spacing: 15mm and 30 mm)



c) Numerical models for the sensitivity analysis of rebar lug spacing

**Figure 5.25 Numerical models for evaluating the detailed failure behaviors in axially loaded RC prisms**

#### 5.4.2 Results and discussion against evaluation of the detailed failure behaviors

The internal and the surface cracks formation using the deformed reinforcement through the mesoscale numerical analyses have been investigated numerically in axially loaded concrete prisms under direct tension. In the test, the internal cracks were comprised of primary and secondary cracks. The cracks formed firstly lateral to the

rebar axis were designated as primary cracks. After the formation of primary cracks, the new cracks also initiated and propagated near to primary cracks and joined the primary cracks when the rebar stress became fairly high. The internal cracks (primary and secondary) propagation around the deformed rebar in concrete have been shown in Figure 5.26 using the mesoscale numerical analyses.

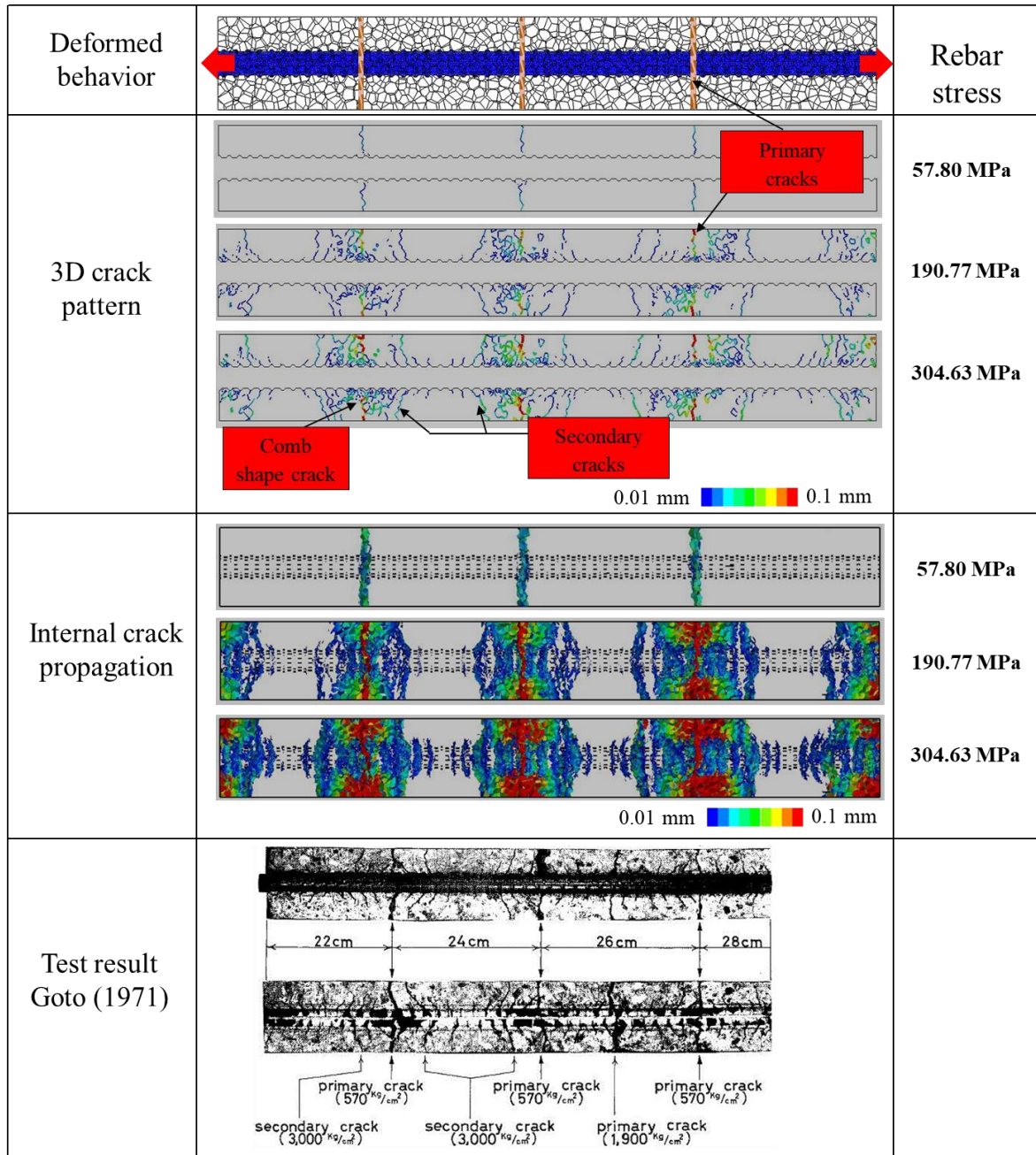


Figure 5.26 Internal crack formation with rebar D32

The mesoscale modeling reveals the internal fracture mechanism of the axially loaded tensile RC prisms. Figure 5.26 shows the occurrence of primary cracks at the location of the notches perpendicular to the rebar axis. Figure 5.26 shows, after the occurrence of the primary cracks, numerous conical shape lateral cracks also form around the deformed rebar with their apexes near to the rebar lugs and the bases directing towards the closet primary crack and join the formerly formed internal (primary) cracks against the increasing stress of rebar.

The discussion is made for the comparison regarding the inclination, the crack space and the number of cracks in the test and the numerical analyses. In the test, it was observed that the inclination of the internal cracks was within 45 to 80 degree to the bar axis and many of them were roughly 60 degree and the maximum crack spacing was around 25 cm. In the numerical simulations, the crack angle ranges between 60 to 80 degree and most of cracks incline around 65 degree and maximum crack spacing is approximately 26 cm as shown in Figure 5.26. Figure 5.26 shows the propagation of 3 secondary cracks to the surface of the prism in test at rebar stress of 300 MPa and the numerical simulation also captures the 3 secondary cracks and their propagation to the surface of the prism at rebar stress of 305 MPa. The coupled RBSM and solid FEM model effectively captured the internal failure pattern of the axially loaded test specimens same as observed in the test. Figure 5.26 also confirms the formation of primary and secondary cracks around the deformed rebar, these numerical observations are consistent with test investigations. Figure 5.26 shows that the formation of internal cracks in concrete resembles the comb shape deformed pattern as investigated in test.

The internal crack formation in concrete around the deformed rebar significantly affects the bonding characteristics and thus influences the overall bonding mechanism between concrete and steel compared with plain rebar. The formation of internal cracks in concrete resembles a comb like pattern as shown in Figure 5.26. The internal cracks usually occur at 60 degree to rebar axis, the deformation of concrete like comb shape causes the tightening of the concrete between the teeth of the comb as the steel tension is increased. The reaction of tightening force produces ring tension crack in concrete around the rebar and consequently the formation of longitudinal crack. The formation of longitudinal cracks principally occurs because of ring tension induced in concrete against high tensile stress of the rebar. The formation and the propagation of the

longitudinal cracks in the direction of the rebar axis have also been investigated numerically and shown in Figure 5.27.

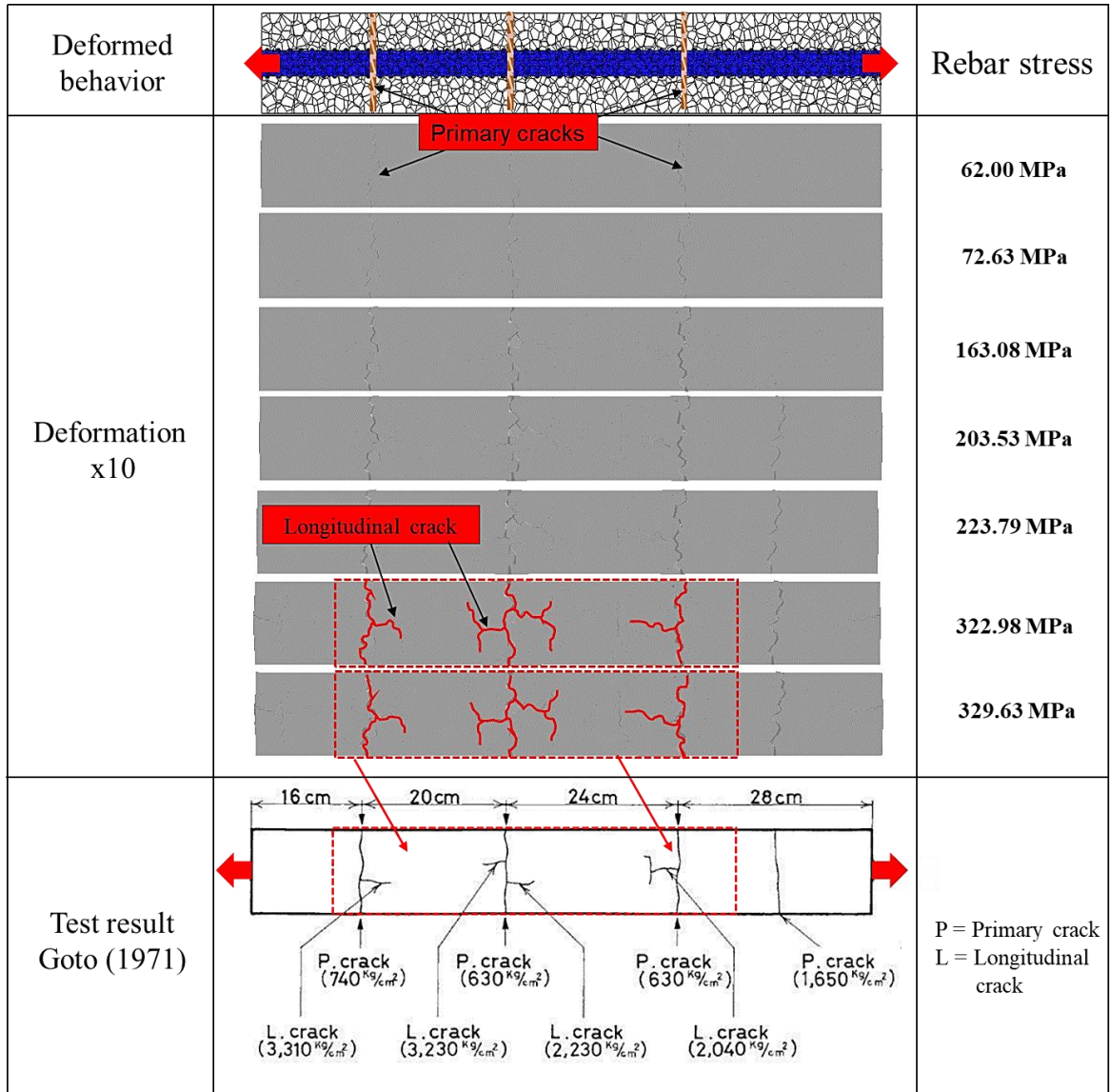


**Figure 5.27 Longitudinal crack formation with rebar D32**

Figure 5.27 highlights that firstly primary cracks initiate and propagate in concrete. Afterward, the longitudinal cracks parallel to rebar axis also propagate against the increased stress of the rebar as highlighted by red lines in Figure 5.27 due to ring tension around the deformed rebar. Figure 5.27 shows that in the test four primary cracks and three longitudinal cracks were observed and the numerical simulations also captures the same number of the primary and the longitudinal cracks corresponding to

comparable stress of the steel in the test. Figure 5.26 and Figure 5.27 show that the coupled RBSM and solid FEM model reasonably simulates the initiation and the propagation of the primary, the secondary, and the longitudinal cracks, quantitatively.

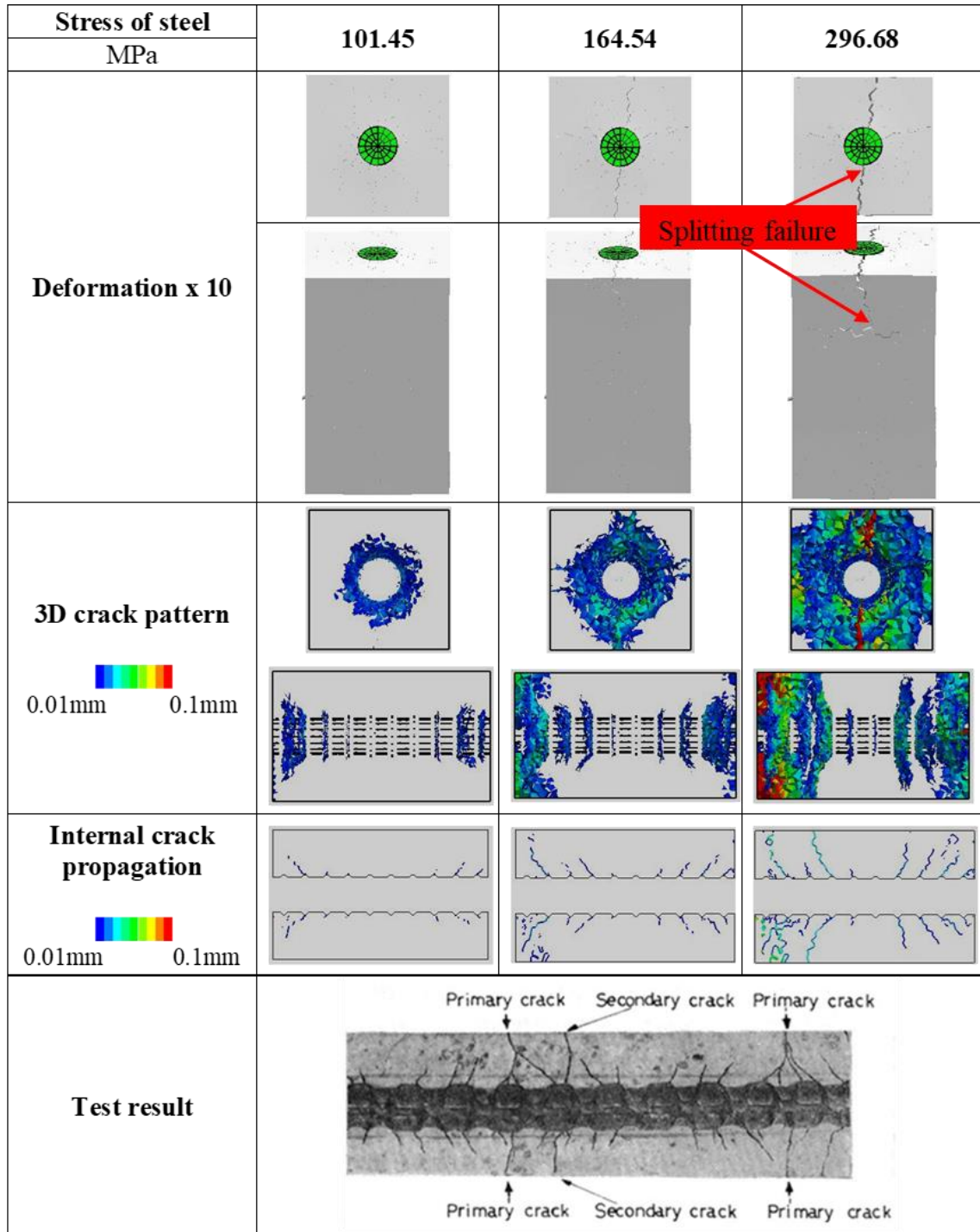
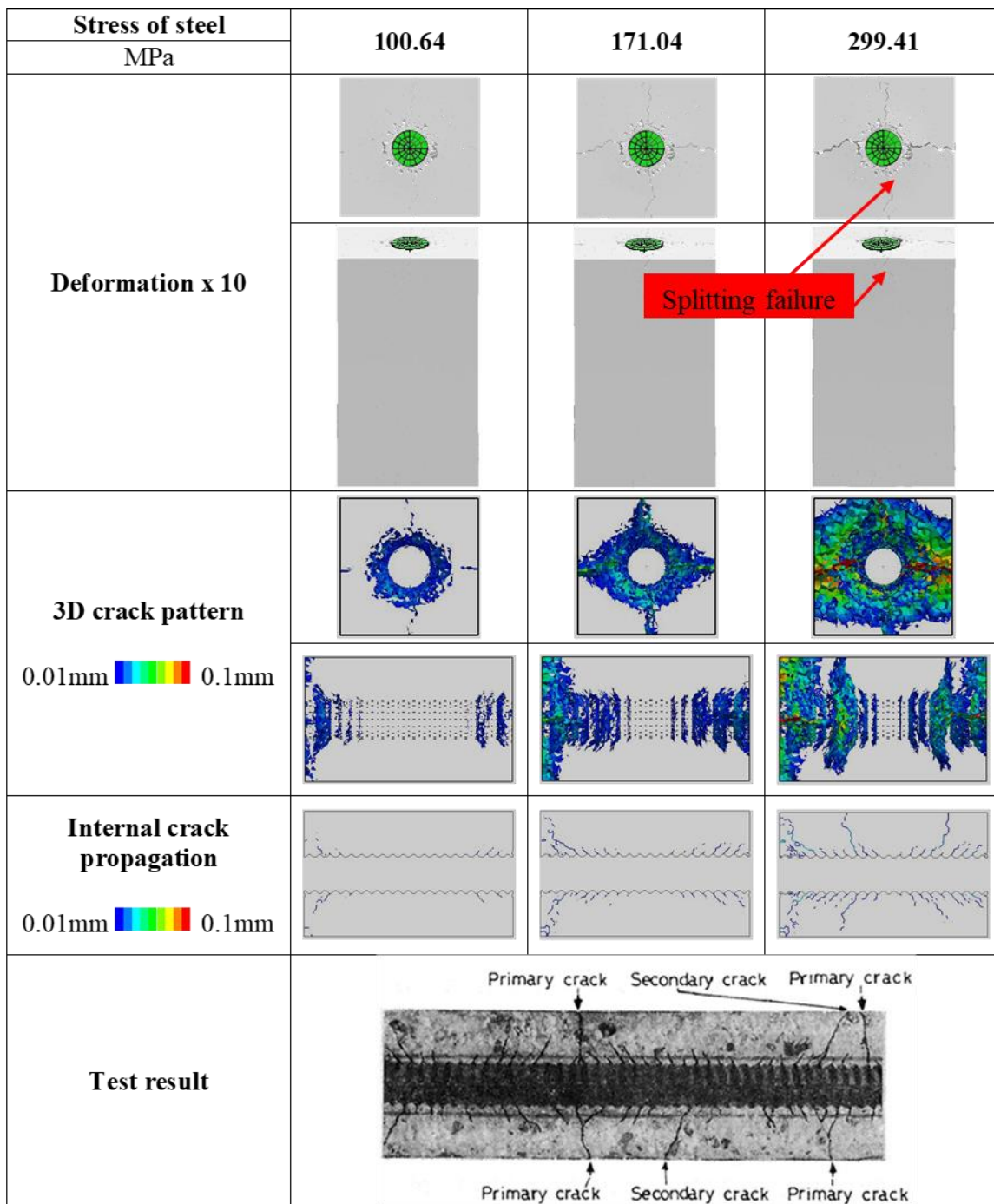


Figure 5.28 Deformed behaviors with lug spacing of 30 mm



**Figure 5.29 Deformed behaviors with lug spacing of 15 mm**

The internal crack pattern and surface deformed behaviors are different for both types of the specimens embedded with the rebar D51 of lug spacing 30 mm and 15 mm, although both specimens yield splitting type failure for the same level of the rebar stress. The specimen embedded with rebar having a lug spacing of 30 mm produces more

internal crack propagation in surrounding concrete compared with a lug spacing of 15 mm. Similarly, Figure 5.28 reveals, the internal cracks are more widely spaced and have more crack width formed around the rebar with the lug spacing of 30 mm compared with the lug spacing of 15 mm as shown in Figure 5.29. The internal crack patterns with varied lug spacing of the rebar as shown in Figure 5.28 and Figure 5.29 illustrate that the rebar geometrical details also influence the bonding behavior and the internal fracture mechanism in RC members.

## 5.5 Summary

The numerical evaluations for bond behavior using the coupled RBSM and solid FEM model are presented in this chapter. The numerical evaluations of the coupled RBSM and solid FEM model have been carried to simulate; (1) the macroscopic bond behavior in axially loaded RC specimens in two ends pull-out test, (2) the bond characteristics of the RC specimens in one end pull-out test subjected to lateral pressures and (3) the detailed failure behavior in axially loaded RC prisms under direct tension. The discussion regarding the validations of the numerical model corresponding to above-mentioned mechanical behaviors and the internal failure process are highlighted, simultaneously through mesoscale numerical analyses using coupled RBSM and solid FEM model. The results of the numerical evaluations are summarized:

- 5) In two ends pull-out test, the coupled RBSM and solid FEM model effectively simulates the macroscopic bond characteristics between steel rebars and concrete including the effect of the varying concrete cover thicknesses and the rebar diameters. The stress slip relationships highlighted that the concrete cover thickness reproduced relatively more influence on the macroscopic bond strength characteristics and the deformation capacity than the rebar diameter while keeping the compressive strength of concrete constant.

Moreover, the numerical model also adequately captured the deformed behaviors of the reinforced concrete specimens loaded in axial tension subjected to the varying concrete cover thicknesses and the rebar diameters. The transformation of the deformed behaviors from splitting failure to the pull-out failure showed the dependency as well as the correlation of the bond strength

with the degree of passive confinement i.e. through the concrete cover, while keeping the diameter of the steel rebar constant. The coupled RBSM and solid FEM model reasonably reveals the effect of passive confinement on the bond strength of concrete.

- 6) In one end pull-out test under the influence of the laterally applied pressures to the concrete, the unconfined RC specimens expressed lower bond strength compared with actively confined specimens, experimentally, and numerically. Whereas, the confined specimens showed the increased bond strength and slip at ultimate. It was also confirmed through simulation results that the confinement effect of lateral pressure was considered appropriately in numerical analysis.

The internal fracture mechanism was also revealed by the simulation results, the unconfined concrete specimens showed longitudinal radial crack development from reinforcing bar, caused the splitting type failure. Whereas, the confined concrete specimens demonstrate the splitting as well as the pull-out.

The coupled RBSM and solid FEM model not only validated the experimental investigations effectively but also simultaneously highlighted the importance and the influence of the test boundary conditions. It is evident from the numerical results, to obtain the deformation capacity and the deformed behaviors accurately in the numerical simulations, the test boundary conditions should be considered appropriately.

- 7) The internal fracture mechanism was highlighted by the numerical simulations using axially loaded tensile reinforced concrete prisms. The coupled RBSM and solid FEM model not only quantitatively demonstrated the formation and propagation of different types of cracks (primary, secondary and longitudinal) but also remarkably differentiated them against the increased stress stage of steel reinforcement. Moreover, the mesoscale numerical simulation also presented the effect of rebar geometrical features on the bonding behavior and the internal fracture process in the concrete. Furthermore, it was observed that the coupled RBSM and solid FEM model showed the capability to simulate the initiation, propagation, orientation and pattern of internal and surface cracks, appropriately.

# **6 Numerical Evaluation of Shear Resistance of Perfobond (PBL) Shear Connector Using the Coupled RBSM and Solid FEM Model**

## **6.1 Introduction**

The current chapter aims to highlight the shear resistance evaluation of the Perfobond (PBL) shear connector using the coupled RBSM and solid FEM model. The organization of the current chapter is as follows

- 1) Firstly, the numerical evaluation for PBL shear connector is carried out for the test shear capacities and the failure modes of the PBL shear connector specifically under the influence of the varying amounts of the lateral pressures applied to the surrounding concrete of the PBL. The detailed internal crack propagation process and the failure mechanism of the concrete influenced by the varying amounts of the lateral pressures are highlighted and discussed. After numerical evaluation under the influence of the varying amounts of the lateral pressures, the combined effects of the lateral pressures and the hole diameters are evaluated.
- 2) The numerical evaluations of the PBL are further extended for the effect of the transverse rebar inside the hole of the PBL.

The perfobond rib shear connector [Perfobond Leiste in German (PBL)], firstly introduced and developed by the German consultants, was being practiced in concrete-steel composite structures. It behaved like a shear key, and transferred the large internal forces between concrete and steel; and provided advantages related to ease of installation, economic reliability, ductility, and the excellent bearing capacity and the

anti-fatigue behavior, etc. (Veldanda et al. 1992, Machacek et al. 2002, Yang et al. 2018).

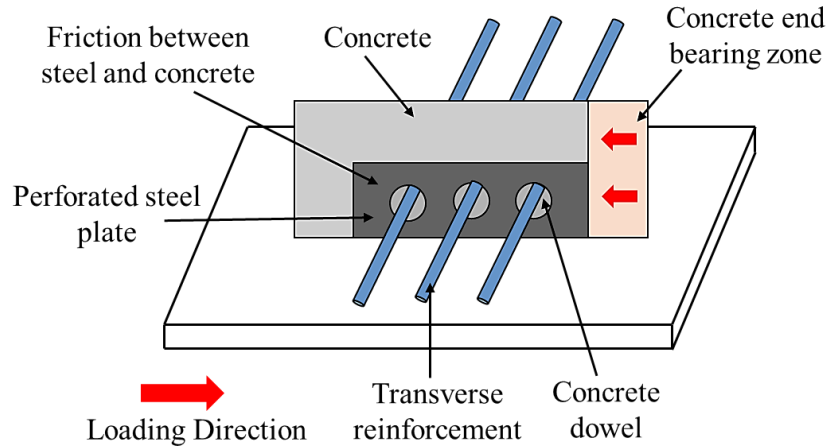


**Figure 6.1 Representation of force resisting components of typical PBL shear connector**

A typical PBL shear connector is composed of a perforated steel plate, attached with a steel section with transverse reinforcement within the rib perforations and the concrete passing through the rib perforations and forming the concrete dowels. The shear capacity of a typical PBL shear connector mainly comprised of: 1) the shear resistance of the concrete dowel, 2) the shear resistance of the transverse reinforcement, 3) the concrete end bearing resistance and 4) the frictional and the bond effects between concrete-steel interfaces (Zhang et al. 2018, Deng et al. 2019), as shown in Figure 6.1.

The investigation and understanding regarding the detailed internal failure mechanism are important and essential for establishing rational design methods and reinforcement details. Therefore, in this chapter, the detailed failure process of the concrete, especially the internal crack propagation behavior and the stress distributions, through the simulation analyses for the lateral pressures effect and for the transverse rebar effect inside the hole of the PBL, which has not been discussed efficiently in past researches are presented, using coupled RBSM and solid FEM model.

## **6.2 Numerical evaluation of PBL shear connector under the influence of varying amounts of lateral pressures**

In this section, the numerical evaluation is performed by utilizing the already published experimental investigations focusing on the shear resistance of the PBL under simple push-out test. For numerical evaluation, the test investigations corresponding to the most fundamental type PBL specimens with a single hole in the steel plate is selected so that the shear resistance, internal failure process, and mechanism of concrete can be discussed comprehensively and clearly. Specifically, the evaluation is performed for capturing the test shear capacities and the failure modes under the influence of the varying lateral pressures applied to surrounding concrete of the PBL, Taira et al. 2013.

### ***6.2.1 Test overview and numerical modeling***

The shear capacity of the PBL is influenced by the amounts of lateral pressures applied to the surrounding concrete of the PBL (Taira et al. 2013). In steel-concrete hybrid construction, the presence of transverse prestressing tendons in the concrete causes the generation of varied stress state around the PBL, and the concrete is loaded to varying levels of compressive forces. In the test, the mechanical response of a single PBL under simple push-out tests was investigated considering the influence of varying amounts of lateral pressures applied to surrounding concrete blocks. The main varying parameter in the test was the amount of the lateral pressures (1, 2, 3, 4, 6, 8, and 10 MPa) applied to two opposite faces of concrete blocks using mechanical jacks. The diameter of the hole and the thickness of the perforated steel plate were maintained constant. The test specimens were embedded with a perforated steel plate (230 x 150 x 12 mm) having a hole of 50 mm diameter between two side concrete blocks. All the test specimens had the rectangular geometry, with the size of 212 x 200 x 150 mm. The geometrical details (all dimensions are in mm) of the test specimens are presented in Figure 6.2.

The Teflon sheet was placed at the bottom of the test specimens between steel loading plates and concrete and the grease was used on the surface of the perforated steel plate in order to eliminate the frictional and bond effects between steel plates and surrounding concrete blocks. The simple push-out tests were performed by applying

vertical load on the top of the perforated steel plate loaded under the influence of the varying amounts of lateral pressures, applied to two opposite surfaces of the surrounding concrete blocks, simultaneously. The specimens subjected to lateral pressures: 1, 2, 3 and 4 MPa, had the concrete compressive strength around 42.2 MPa while the specimens with lateral pressures: 6, 8 and 10 MPa had the concrete compressive strength around 45.2 MPa.

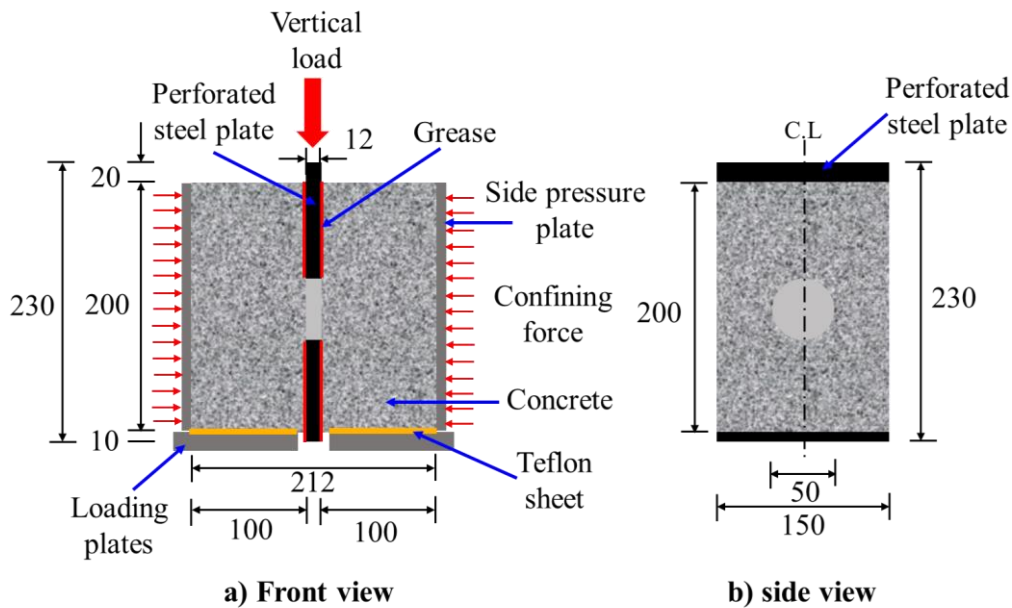


**Figure 6.2 Geometrical details of the test specimen**

In numerical model, the concrete is modeled using 3D-RBSM and the perforated steel plate of the PBL shear connector between side concrete blocks is modeled using eight-noded nonlinear solid finite elements. The 3D model for the perforated steel plate of the PBL used in the current study has been shown Figure 6.3. The numerical models corresponding to a single PBL shear connector, subjected to the varying amounts of lateral pressures are illustrated in Figure 6.4. The proper numerical modeling of concrete in the circular region (concrete dowel) between two side concrete blocks requires to adopt the average mesh size less than the thickness (12 mm) of perforated steel plate as the crack propagation behavior in the concrete dowel region depends on the selection of average mesh size. The crack propagation can occur inside the hole or along with the shear surface, therefore, the mesh size in the concrete dowel region is

selected in such a manner so that the internal failure process of the concrete dowel can be captured effectively in numerical simulations, whereas relatively large mesh size has been selected near the ends of concrete blocks to minimize the analytical computational cost as shown in Figure 6.4(a).

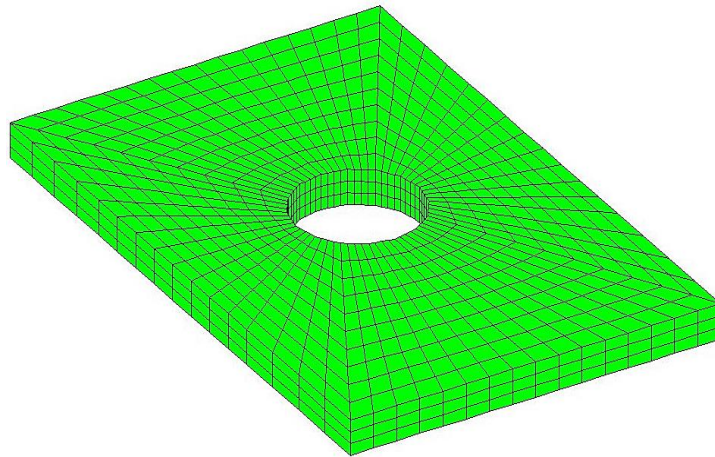


**Figure 6.3 3D model of perforated steel plate using eight-noded nonlinear solid FEM**

Therefore, the average mesh size in the circular region (concrete dowel) is set as 3 mm (lesser than the thickness of the perforated steel plate: 12 mm) and then the mesh size is gradually increased from the circular region to the side concrete blocks. In this regard, the average mesh size in numerical simulations incorporated for numerical modeling of the concrete approximately ranges between 3 to 13 mm. The mesh size dependency of the numerical model is also investigated numerically through the mesh sensitivity analysis ranging between the mesh sizes selected for the numerical modeling (section 2.2.3). The difference of results is found to be negligible and also confirms that the numerical model does not have mesh size dependency.

The numerical modeling of the test boundaries is elaborated here. It was reported that the shear capacity of the PBL shear connector was influenced by the friction between the concrete blocks and the test bed, loaded in the simple push-out test (Fuji et al. 2012). In the same manner, the preliminary numerical simulations also highlighted the dependency of shear response of PBL on the sensitivity of material

parameters; tensile strength ( $\sigma_t$ ), cohesion ( $c$ ), and angle of internal friction ( $\varphi$ ) selected for the modeling of test boundaries.

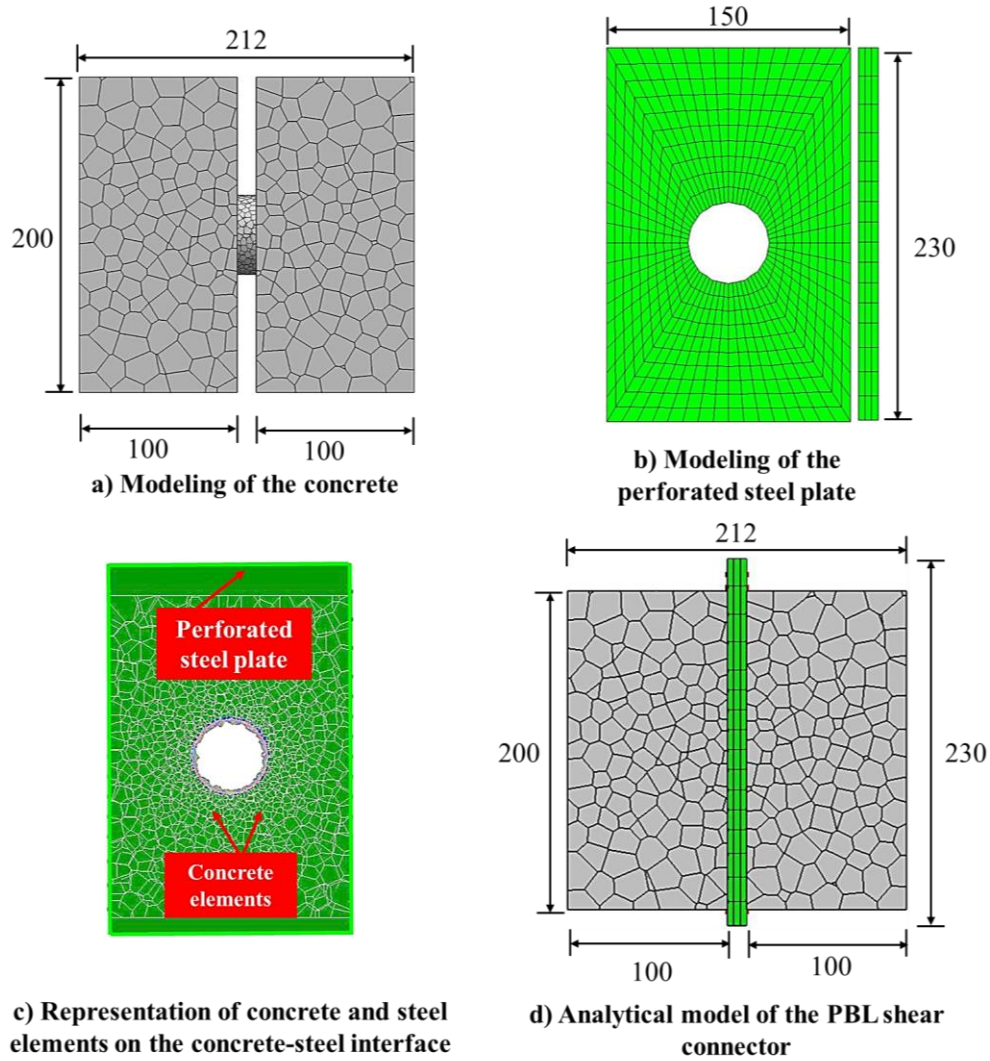


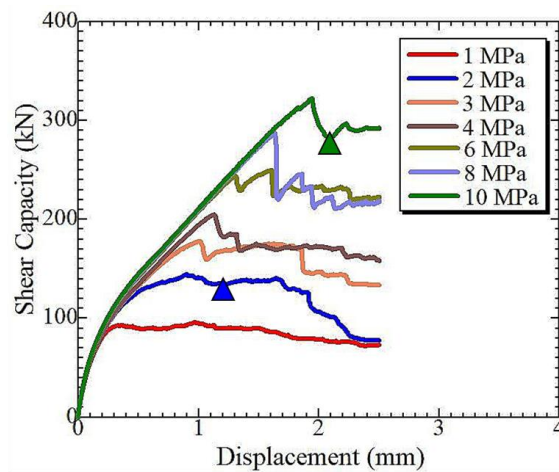
**Figure 6.4 Analytical model of the test specimen**

As mentioned earlier, the grease was applied on the surface of the perforated steel plate and Teflon sheet was placed between bottom loading plates and the concrete blocks in the test, in this regard, the test boundary conditions were modeled in simulation analyses of the PBL by adopting the minimal material parameters of the constitutive models ( $\sigma_t = 0.01$  MPa,  $c = 0.01$  MPa and  $\varphi = 2$  degrees) for the normal and shear springs (Table 2.1 and Table 2.2) between the steel plate and the concrete. The different amounts of lateral pressures to surrounding concrete blocks were applied by

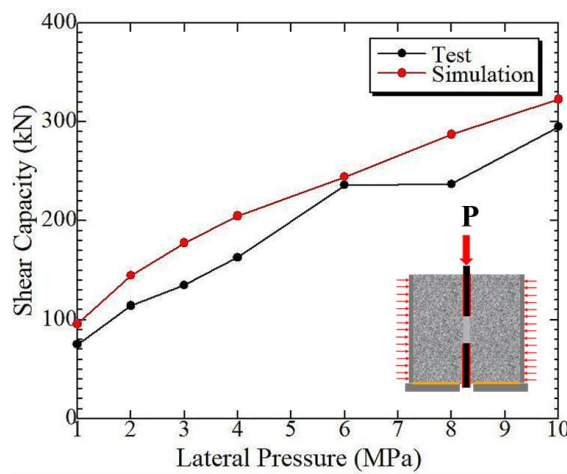
load control of a pressure plate consisting of one RBSM element. The vertical shear load was applied by displacement control of solid FEM nodes on top of the perforated steel plate.

### 6.2.2 Results and discussions

Since, the reference test (Taira et al. 2013), only provided the information about the concrete compressive strength ( $f_c$ ), and the tensile strength ( $\sigma_t$ ), elastic modulus ( $E$ ) and fracture energy ( $g_f$ ) as the model parameters required in Table 2.1 and Table 2.2 are assessed from the compressive strength of concrete using conversion formulae proposed in standard specifications of Japan Society of Civil Engineers for concrete structures (JSCE 2008).



a) Analytical load-displacement relations



b) Comparison of test and analytical shear capacities

**Figure 6.5 Influence of lateral pressures on the shear capacity of PBL**

The experimental investigations reported, however, the tensile strength of concrete was influenced by many factors (e.g. water-cement ratio, type and size of aggregates, curing and storage (moisture) conditions of the specimen, size of the specimen and conditions of testing (splitting test, uniaxial test, and flexural test), etc.) and tensile strength might be reduced. In this regard, approximately 30 % reduction only for the tensile strength ( $\sigma_t$ ) was incorporated in the numerical simulations while all other remaining material parameters (Table 2.1 and Table 2.2) were kept the same for modeling of concrete. Figure 6.5 illustrates the analytical load and relative displacement (between the bottom of the steel plate and mid height) relationships and the influence of lateral pressures on shear capacity of the PBL. In the test, it was observed that the shear capacity increased as the applied lateral pressure was increased as shown in Figure 6.5(b). In the same manner, the numerical simulation results also exhibit the increase in shear capacity with the increase in the lateral pressures applied to side concrete blocks. Figure 6.5(b) shows the slight deviation and overestimation of the numerical shear capacities compared with the test results, however, captures the tendency for an increase in shear capacity against increased lateral pressure, which is consistent with the test investigations.

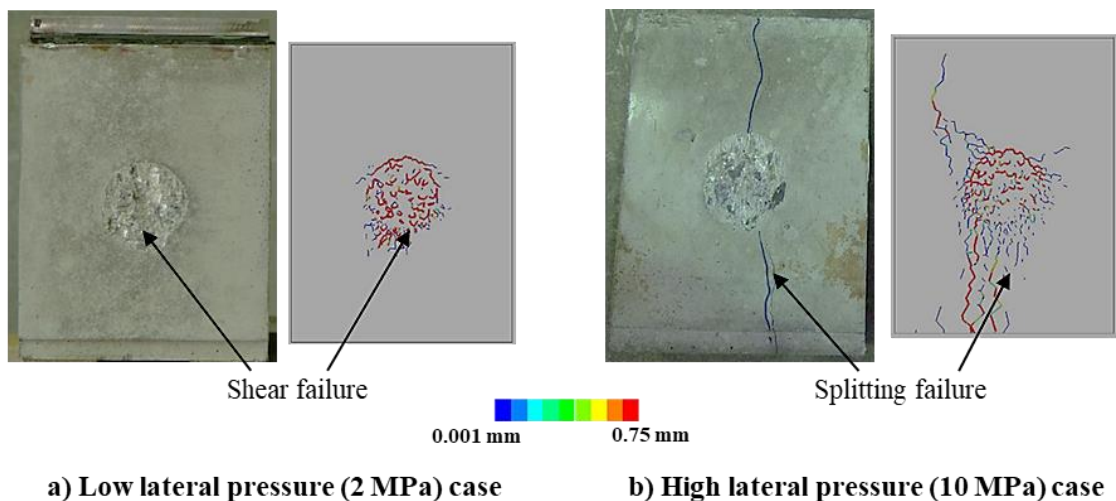


**Figure 6.6 Comparison of test and analytical failure modes**

In the test, mainly two types of failure modes were observed; (1) local shear failure along with the edge of the hole of the perforated steel plate and (2) splitting failure of side concrete blocks perpendicular to the thickness of the perforated steel plate as shown in Figure 6.6. The test photos show the damage and cracking at the steel-concrete contact surface, parallel to the thickness of the steel plate. Figure 6.6 also presents the analytical failure modes considering the cut section near the hole of steel plate parallel to the thickness of the plate, in post peak region for low (2 MPa) and high (10 MPa) lateral pressures applications corresponding to 1.2 mm and 2.1 mm displacements as marked in Figure 6.5(a), respectively. The comparison of the test and the analytical failure modes are found to be in good agreement.

The dominant failure mode corresponding to low lateral pressure applications (1 and 2 MPa) was shear failure while splitting failure mode was investigated for all remaining pressures applications (3, 4, 5, 6, 8, and 10 MPa) as it can be confirmed through the load-displacement relationships in Figure 6.5(a). The specimens subjected to low lateral pressure applications (1 and 2 MPa) exhibit the ductile failure behavior whereas all other specimens reproduce the splitting failure mode and load decreases after the peak due to the occurrence of splitting crack. The validation of the numerical model is confirmed and highlighted for the test shear capacities and the failure modes while the detailed failure process and mechanism are discussed in the next section.

### ***6.2.3 Investigation of the failure process and the mechanism***

After the evaluation of the failure modes and test shear capacities, the detailed failure process and mechanism are evaluated. The deformation response including internal crack patterns and normal stress distribution along with height and width (direction of lateral pressure application) for low (2 MPa) and high (10 MPa) lateral pressures with different failure modes as shown in Figure 6.6, are investigated. In order to highlight the discussion, the quantitative shear response in numerical simulations at various stages are selected on load displacement relationships as marked in Figure 6.7.

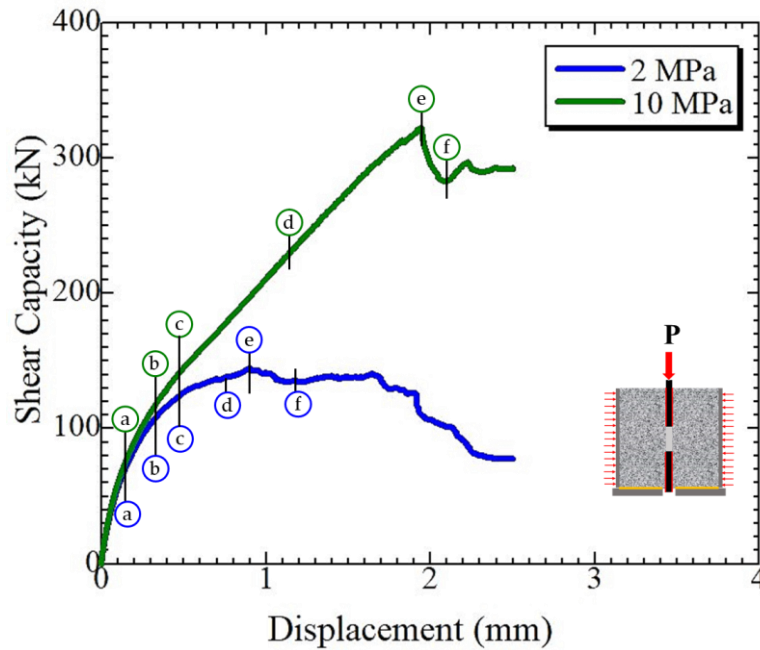


**Figure 6.7 Representation of various stages for shear response evaluation**

The detailed failure process in a specimen subjected to low lateral pressure (2 MPa) corresponding to various slip stages is shown in Figure 6.8. Figure 6.8 presents the surface deformed behaviors, internal crack patterns at the cut sections perpendicular and parallel to the thickness of steel plate and the normal stress distribution along with height (y-axis: direction corresponding to the application of push-out force) and width (z-axis: direction corresponding to the application of lateral pressure) at cut section perpendicular to the thickness of the steel plate. The crack widths indices for the internal cracks are highlighted through the variation of colors, from blue (0.001 mm) to red (0.75 mm). Similarly, the variation of normal stresses in concrete is shown by the indices, from 2 MPa (pink: tensile stress) to -50 MPa (red: compressive stress). From the internal crack pattern and the normal stress distribution at cut section defined near to mid depth perpendicular to the thickness of the steel plate at slip stage (a), it can be observed that firstly, the two horizontal cracks initiate near the top of the concrete dowel through the hole of the perforated steel plate and compressive stresses ( $\sigma_y$ ) occur on the top of the concrete dowel. Afterward, at slip stage (b), the horizontal cracks further propagate and the two vertical cracks also initiate and propagate around the shear surface against slightly increased shear force and the

compressive stresses ( $\sigma_y$ ) also transfer from top to almost mid height of the concrete dowel.

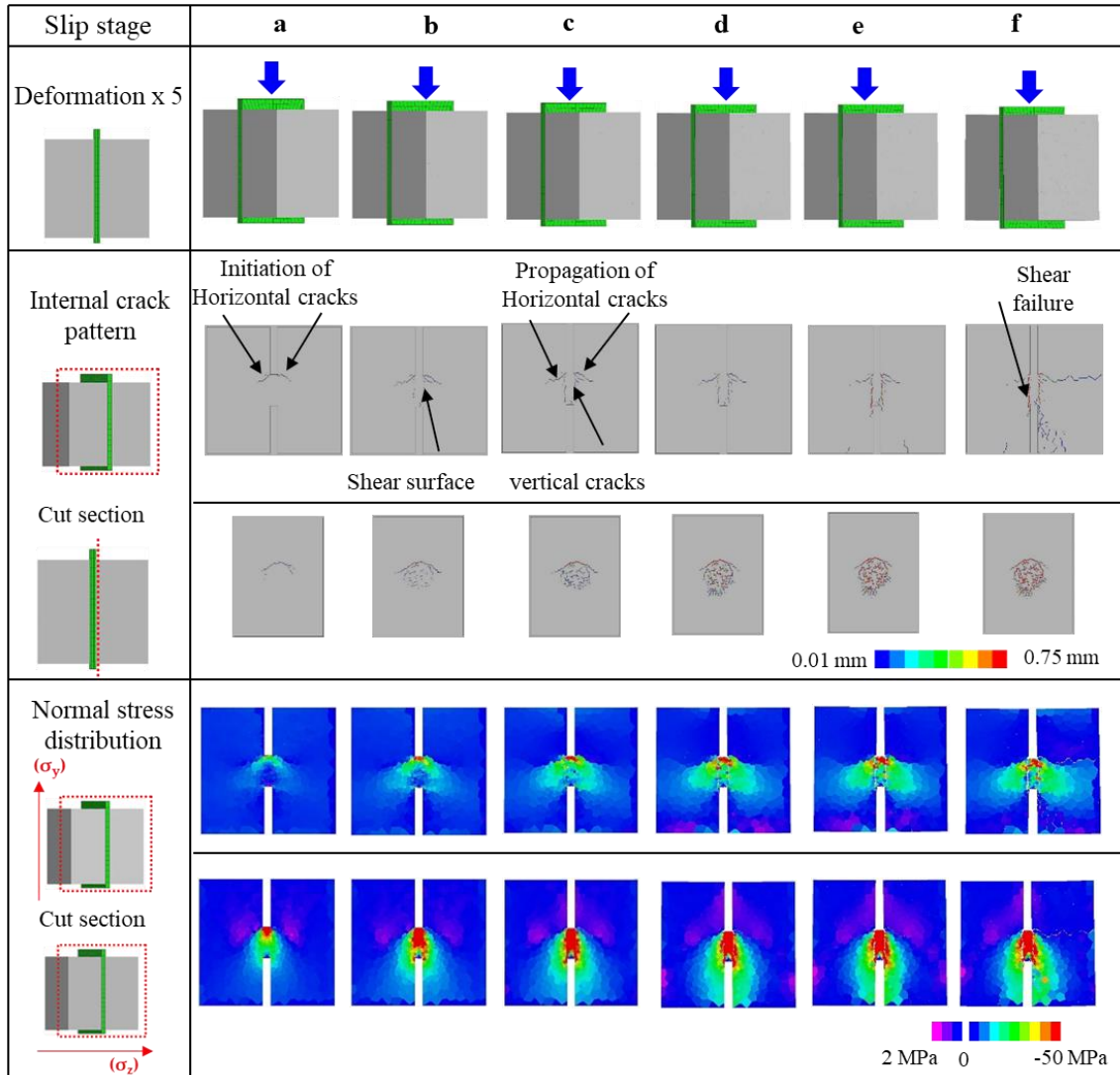


**Figure 6.8 Detailed failure process and mechanism for low lateral pressure case**

After slip stage (b), the slope of the load-displacement curve changes because of the propagation of the vertical crack along with shear surface and tends to become milder after slip stage (c). From internal crack patterns and the normal stress distribution along with the y-axis ( $\sigma_y$ ) at slip stages (c) and (d), it can be recognized that the vertical crack penetrates completely to the bottom of the hole and causes the shear slip on the

vertical cracked surface and the compressive stresses are concentrated in the concrete dowel region.

In the case of low lateral pressure application, the shear strength of the PBL is characterized by the shear failure of two cracked surfaces along with the edge of the hole in the steel plate consequently causing the failure of the concrete dowel, the same as observed in the test, illustrated in Figure 6.6. The distribution of the normal stress along with the y-axis ( $\sigma_y$ ) clearly depicts the transmission of large compressive stress (red color) from top to bottom of the concrete dowel with the increase of shear force, while along with the z-axis ( $\sigma_z$ ), the large compressive stresses are only concentrated on the top edge of the hole of steel plate. The surface crack patterns shown in Figure 6.8 also reveal that no splitting crack occur perpendicular to the thickness of the perforated steel in the surrounding concrete blocks in low lateral pressure application case and the concrete dowel mainly resist the vertical push-out force and the stresses along with y-axis and z-axis are mainly localized in the circular region between side concrete blocks.

Similarly, the detailed failure process and the mechanism for high lateral pressure (10 MPa) application captured by the numerical analyses is also discussed and presented in Figure 6.9. In high lateral pressure application, the initial internal crack propagation process near the steel plate hole follows the same failure mechanism as observed in low lateral pressure case .i.e. the occurrence of two horizontal cracks near the top of concrete dowels, afterward, initiation and propagation of vertical cracks around the shear surface causing the transformation of compressive stresses from top to bottom of the concrete dowel. However, the vertical crack propagation is restrained by the application of high lateral pressure as shown in Figure 6.9. It can be confirmed from the comparison of internal crack patterns for low and high pressures applications corresponding to slip stages (a), (b), and (c) as shown in Figure 6.8 and Figure 6.9, respectively.

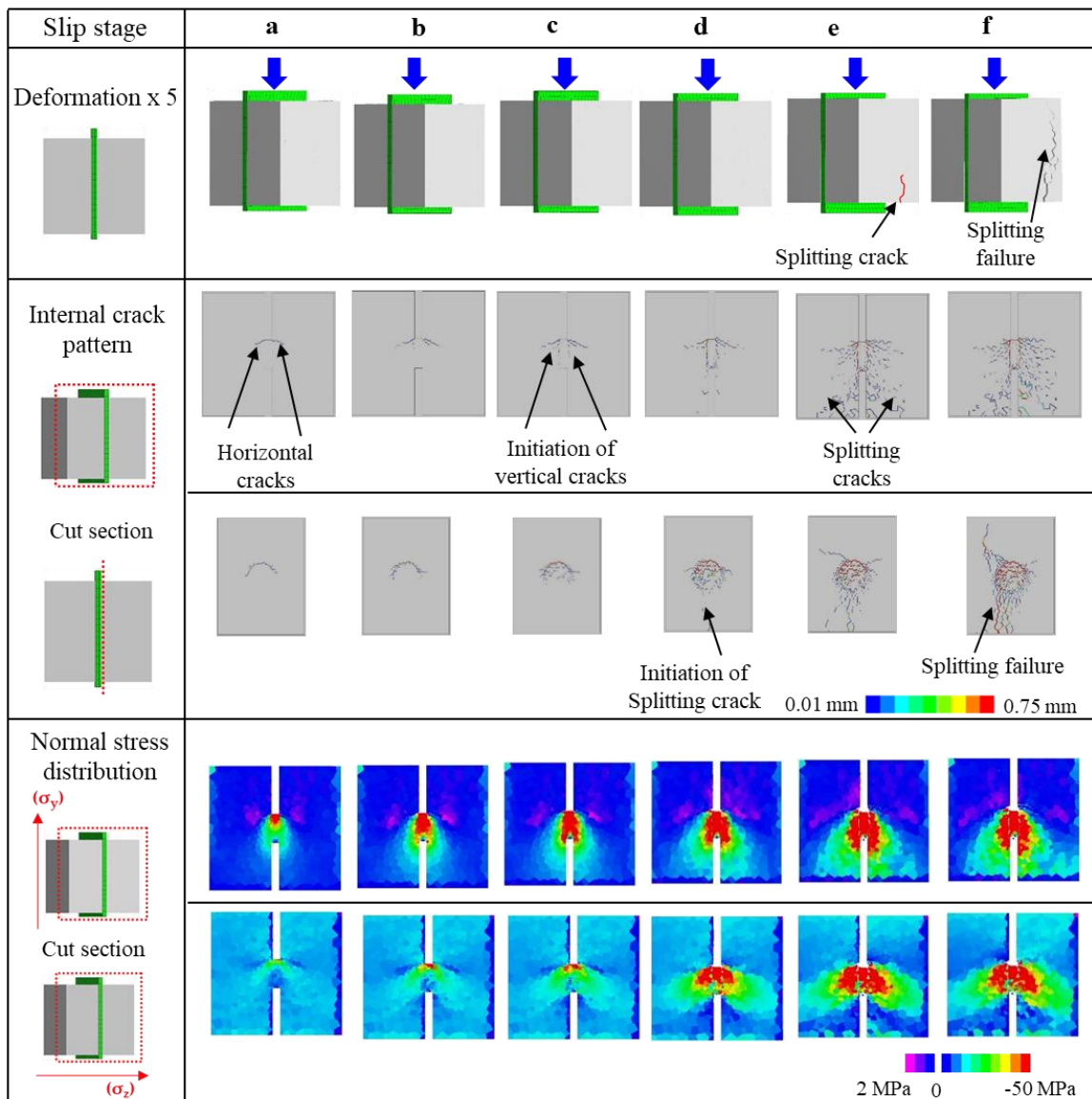


**Figure 6.9 Detailed failure process and mechanism for high lateral pressure case**

At slip stage (b) in Figure 6.8, the vertical crack initiates along with the shear surface while in Figure 6.9, there is no initiation of vertical crack. Similarly, the internal crack pattern corresponding to slip stage (c) in Figure 6.8 shows the vertical crack completely propagates along the shear surface, whereas in high pressure application, only the initiation of vertical crack occurs after the initiation of the horizontal cracks at the top of the concrete dowel. After the initiation of vertical crack at slip stage (c), the load tends to further increase (Figure 6.7) and exhibits an increasing slope of the load-displacement curve because of the restraining effect of shear dilatancy behavior by the

externally applied high lateral pressure, in contrast with the low lateral pressure application. Afterward, at slip stage (d) in Figure 6.9, the splitting cracks initiate under the concrete dowel, into the inner surfaces of the surrounding concrete blocks, in the perpendicular direction to the thickness of the perforated steel plate and the compressive stress along with y-axis ( $\sigma_y$ ) and z-axis ( $\sigma_z$ ) are induced in the side concrete blocks. Furthermore, the normal stresses along with height ( $\sigma_y$ ) and along with width ( $\sigma_z$ ) in the side concrete blocks almost have the same damage zone as that of splitting crack propagation region in the side concrete blocks in contrast with the low lateral pressure application case, where the normal stresses ( $\sigma_y$  and  $\sigma_z$ ) are only localized around the concrete dowel region as shown in Figure 6.8(c). At peak stage, the splitting cracks propagate the surface of the surrounding concrete blocks, and consequently cause the splitting failure behavior in the post peak, which is consistent as observed in the test. In high lateral pressure application, the shear strength of the PBL is determined by the occurrence of splitting failure behavior perpendicular to the thickness of the perforated steel plate in the surrounding concrete blocks.

It is pertinent to mention here, the distribution of normal stresses along with height ( $\sigma_y$ ) and width ( $\sigma_z$ ) in Figure 6.8 and Figure 6.9 clearly highlights the difference of internal resistance mechanism. The normal stresses along with height ( $\sigma_y$ ), in low lateral pressure application case, shows that the compressive stresses are concentrated around the concrete dowel region because of shear failure, whereas, in the high lateral pressure application case, the concrete in surrounding blocks and under the concrete dowels also undergoes the compressive stresses. Moreover, the normal stresses along with height ( $\sigma_y$ ) in Figure 6.8(c) and Figure 6.9(c) also highlight the difference of shear resistance behavior of concrete dowel concerning the varying amounts of lateral pressures applied. The damage zone of concrete dowel in low lateral pressure application case experiencing large compressive stresses as shown in Figure 6.8(c) is less as compared to the high lateral pressure application case as shown in Figure 6.9(c). The shear resistance of concrete dowel is enhanced because of high lateral pressure application and the damage zone of concrete dowel also extends in the side concrete blocks. Similarly, the normal stresses along with width ( $\sigma_z$ ) show that in low lateral pressure application case, the large compressive stresses only concentrate on the top edge of the hole, while in high lateral pressure application case, the compressive

stresses are observed in the complete concrete dowel region and further, the envelope of the compressive stresses induced in the side concrete blocks as shown in Figure 6.9(c) is more compared with the low lateral pressure application case as shown in Figure 6.8(c) because of splitting crack propagation. It is also observed that as the amount of lateral pressure applied to the side concrete blocks increases, consequently the envelope of the compressive stresses also expands more and the shear resistance of the PBL shear connector gets improved.

The detailed internal failure process and mechanism revealed in Figure 6.8 and Figure 6.9 captured by the numerical model efficiently highlights the difference of internal shear resistance mechanism of the PBL subjected to varying amounts of lateral pressures. The numerical model not only highlights the internal failure mechanism but also reproduces the transformation of failure modes (local shear failure in low lateral pressure and splitting failure in high lateral pressure) with respect to the amounts of lateral pressures applied to concrete surfaces, which is consistent as observed in the test.

### **6.3 Evaluation of combined effects for the lateral pressure and hole diameter**

After the validation of the numerical model and clarifying the detailed failure process and the mechanism in low and high lateral pressures as shown in Figure 6.8 and Figure 6.9 respectively, the numerical evaluation is performed to investigate the combined effects of the various lateral pressures and the holes' diameters on the shear capacity of the PBL shear connector. Although the diameter of the hole is one of the main connection parameters of the PBL shear connector, only the individual effect of each parameter on the shear capacity has been studied yet (Wang et al. 2018, Taira et al. 2013). For numerical evaluation in this regard, the specimen with the same geometrical dimensions as those in Section 6.2.1 (Figure 6.2) is simulated, where only the hole diameter is changed from 50-mm to 75-mm and the lateral pressures of 2 MPa, 6 MPa, and 10 MPa are also applied. The analytical model of the PBL shear connector with a hole of 75-mm diameter is shown in Figure 6.10.

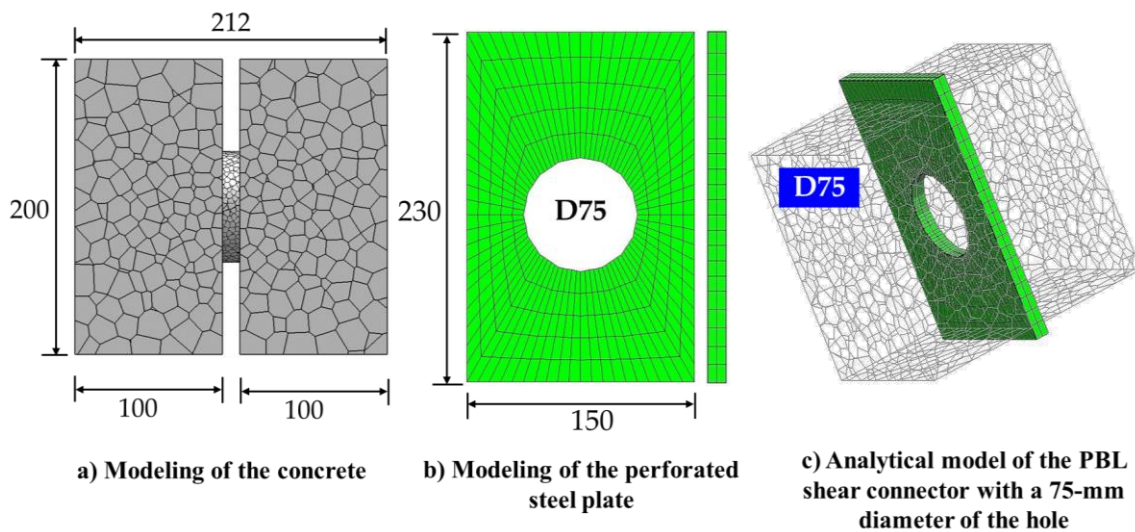


**Figure 6.10 Analytical model of the specimen for evaluation of combined effects for the lateral pressure and hole diameter**

The analytical relationships of the shear capacities corresponding to the combined effects of the lateral pressures and the holes' diameters are shown in Figure 6.11. It is noticed through the numerical investigations that the specimen with the hole of 75-mm diameter subjected to a lateral pressure of 2 MPa reproduces the shear failure mode, while the specimens with applied lateral pressures of 6 MPa and 10 MPa exhibit the splitting failure modes, which are found to be consistent as obtained for the 50-mm hole diameter specimen (section 6.2.3).

Figure 6.11 shows that the shear capacity increases with the increase in the lateral pressures and the holes' diameters, exhibiting the same trend against the individual effect of each parameter, as observed in the past research studies (Wang et al. 2018, Taira et al. 2013). However, it should be emphasized that there is a clear existence of the combined effects against the shear capacities, as the relationship for the 50-mm hole diameter and 75-mm hole diameter are not parallel to each other, as shown in Figure 6.11. Specifically, the increase in the shear capacity for a specimen with a hole of 75-mm diameter was found to be more in high lateral pressure compared with a lateral pressure of 2 MPa.

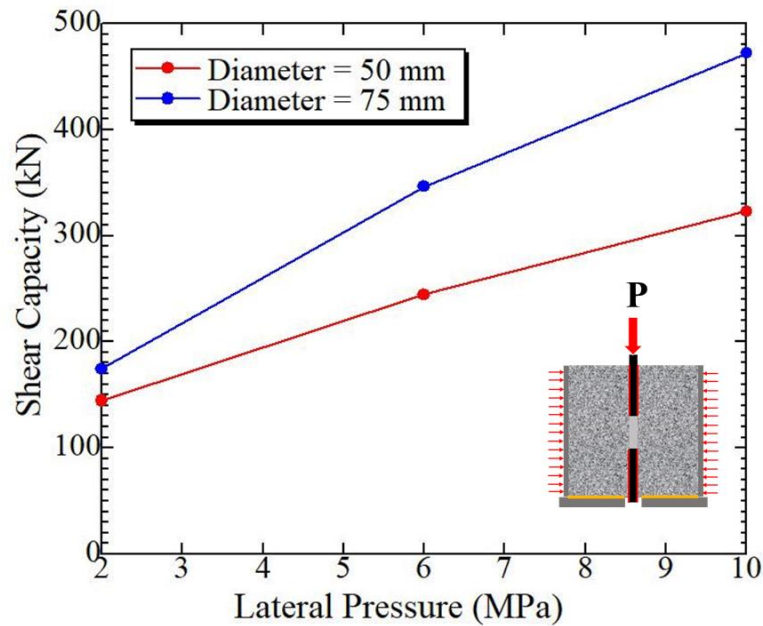


**Figure 6.11 Illustration of the combined effects of the lateral pressures and the diameters of the holes on analytical shear capacities**

The combined effects of the lateral pressures and the holes' diameters can also be efficiently examined through the internal cracking behavior and the normal stress distribution shown in Figure 6.12, considering the advantage of the reliable numerical approach. Figure 6.12 shows the internal crack patterns and the normal stress distribution along with height ( $\sigma_y$ ) for both diameters of the holes under lateral pressures of 2 MPa and 10 MPa at the peak stage. The normal stress distribution along with height ( $\sigma_y$ ) in Figure 6.12 shows that as the diameter of the hole is increased from 50-mm to 75-mm, the envelope of compressive stresses and the region of the large compressive stresses around the concrete dowel and in the side concrete blocks are also expanded more for both lateral pressures (2 and 10 MPa).

Figure 6.12 highlights that in a low lateral pressure case (2 MPa), the internal crack patterns are almost similar for both diameters, and the cracks propagate along the shear surfaces. In a 50-mm diameter case, the large compressive stresses surround the complete dowel region, whereas in the 75- mm diameter of the hole, the large compressive stresses have been observed on the upper region of the concrete dowel. However, since the region of the large compressive stresses exists almost up to the mid-height of the concrete dowel between the vertical cracks along the shear surfaces,

therefore, the increment in shear capacity is limited in a specimen subjected to a lateral pressure of 2 MPa.

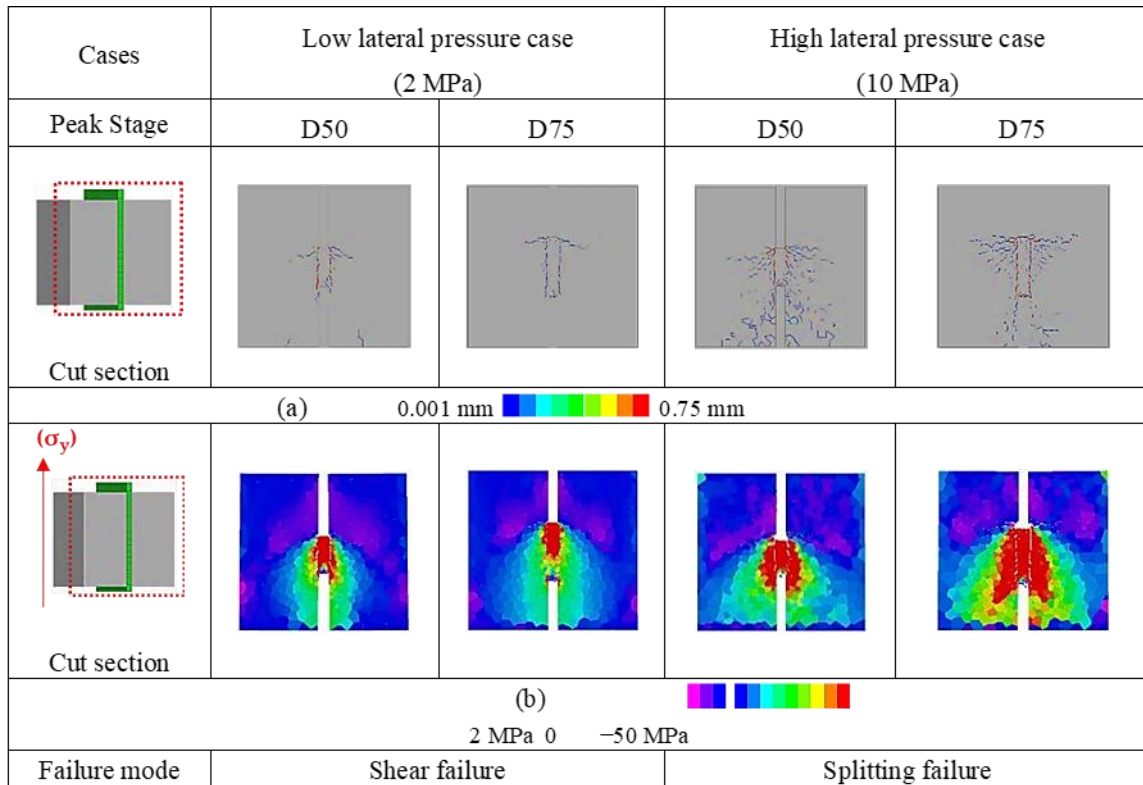


**Figure 6.12 Comparison of the failure behaviors for low and high lateral pressures against 75-mm and 50-mm diameters of the holes at the peak stage**

In high lateral pressure case (10 MPa), the internal crack propagation is less for the 75-mm diameter hole because of its greater shear resistance against the applied shear load compared with the 50-mm diameter. It is also evaluated that the region of the large compressive stresses in the 75-mm diameter case progresses more in the side concrete blocks compared with the 50-mm diameter case, and as a result, it contributes more toward the increase in shear capacity due to the wide regions of the large compressive stresses compared with the lateral pressure of 2 MPa and consequently produces the maximum shear capacity under the combined effects, as shown in Figure 6.11.

## 6.4 Numerical evaluation of transverse effect rebar inside the hole of the PBL shear connector

After the evaluation of the test shear capacities and the failure modes under the influence of the lateral pressures in section 6.2, the numerical investigations of the PBL shear connector are further extended for the transverse rebar effect inside the hole of the PBL shear connector. As mentioned earlier in section 6.1 and Figure 6.1, the transverse rebar inside the hole of the PBL shear connector plays an important role corresponding to the shear response and the deformation capacity of the PBL.

**Table 6.1 Numerical evaluation for the transverse rebar effects**

Serial No	Description	Rebar end condition	$f_y$ (MPa)	Rebar position inside hole	Rebar diameter (mm)	$f_c$ (MPa)
1	Contribution of transverse rebar	Fixed and free	345	Middle	D10	42.2
2	Effect of rebar diameter	Fixed	345	Middle	D10, D13, D16	42.2
3	Effect of rebar position inside hole	Fixed	345	Top, middle, bottom	D10	42.2
4	Effect of yield strength ( $f_y$ )	Fixed	290, 345, 490	Middle	D10	42.2

The numerical evaluation has been performed in this regard, considering the influential varying parameters of the transverse rebar, mentioned in the previous studies conducted by the past researchers to evaluate the shear capacity of the PBL shear connector. The varying parameters considered in this regard are; the end conditions (free and fixed), diameter of the rebar (D10, D13, and D16), the position of the transverse rebar inside hole (top, middle and bottom) and the yield strength (295 MPa, 345 MPa, and 490 MPa). The previously stated description has been summarized in Table 6.1.

The previous studies only mentioned about the increased behavior of the shear capacity with increased rebar diameter without highlighting the internal failure process of concrete. Therefore, the numerical simulation analyses are advantageous in this regard to illustrate the internal failure mechanism.

#### 6.4.1 Contribution of the transverse rebar

To investigate the contribution of the transverse rebar and to evaluate the effect of the varying parameters of the transverse rebar inside the hole of the PBL, the comparison is judged with the specimen without transverse rebar inside the hole as shown in Figure 6.13 (a). Figure 6.13 (all dimensions are in mm) shows that the numerical evaluation is carried out by adopting the same specimen as discussed in section 6.2.1 and Figure 6.2, however, the externally applied lateral pressure is eliminated here. The geometrical details of the specimen and the perforated steel plate, mechanical properties of the constituent materials and the boundary conditions are also kept same. The transverse rebar of diameter 10 mm with embedment length of 192 mm, providing 10 mm side concrete cover on both ends of the rebar is considered and placed in the middle of the hole as shown in Figure 6.13. The yield strength ( $f_y$ ) of the transverse rebar considered in current numerical simulation is 345 MPa.

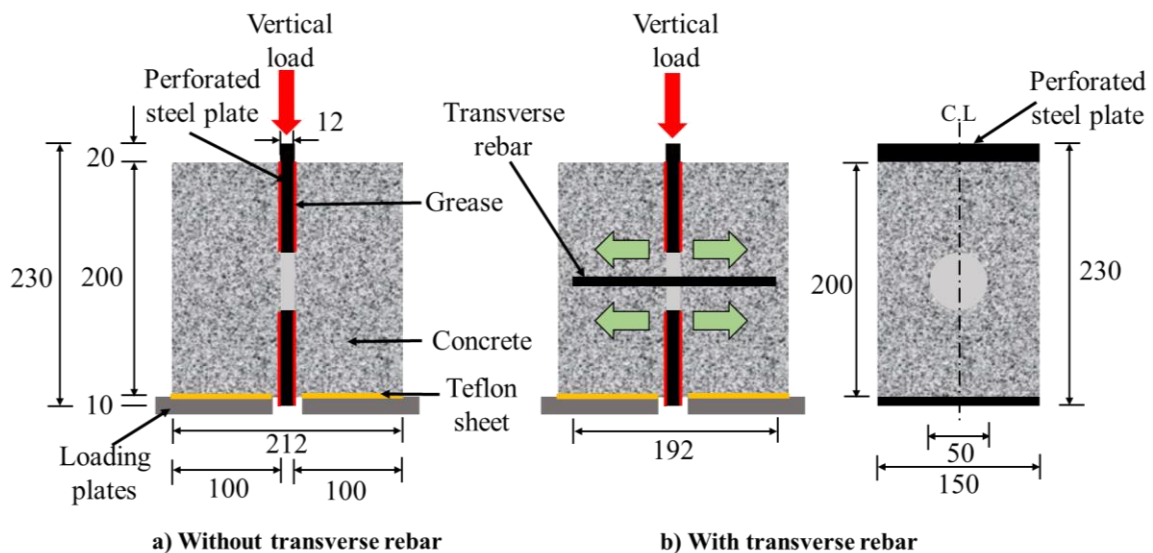


**Figure 6.13 Geometrical details of the specimens for the transverse rebar effect**

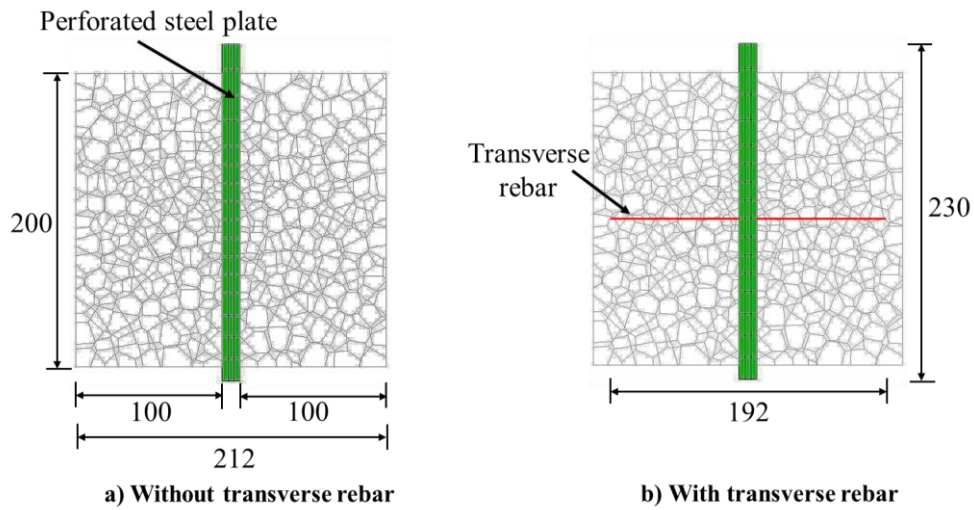


**Figure 6.14 Analytical models for the transverse rebar effect**

The analytical models of the specimens are shown in Figure 6.14. The analytical models have the average mesh size ranging between 3mm to 13mm same as used in section 6.2.1.

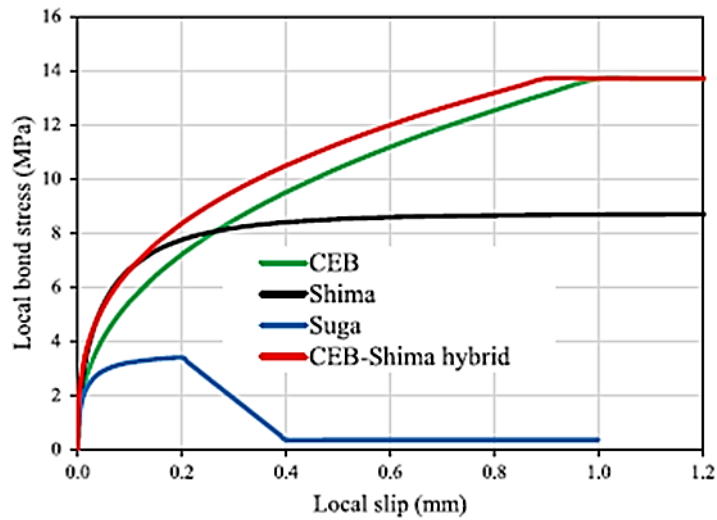


**Figure 6.15 Representation of CEB-Shima hybrid bond model**

The transverse rebar inside the hole is modeled by a fiber model in which the cross-section of the rebar is divided into several fibers and can simulate the bending behavior of the transverse rebar efficiently under the vertically applied shear load. The hybrid bond model proposed by Farooq et al. 2020 has been used for the transverse

rebar which has capability to simulate the internal cracking patterns and the stress distributions of concrete due to variation in the concrete cover thickness and also evaluates the bond behavior in 3D-RBSM, effectively. The local bond model proposed by Farooq et al. 2020 presented a new bond model based upon modification to the CEB-FIP model, termed as the “CEB-Shima hybrid” model. The objective of the model was to reasonably simulate the effect of various structural parameters on bond behaviors. The proposed model was represented by the red line in Figure 6.15. The initial loading stiffness of the model has a resemblance to the Shima model, being stiffer than the CEB-FIP model. In higher bond stress regions, ultimate bond stress and post-peak behavior are similar to the CEB-FIP model.

The objective of this investigation is to evaluate the shear resistance contributed by the transverse rebar in simple push-out test and also to highlight the detailed failure process and the internal mechanism. The failure process is also compared for PBL without transverse rebar as shown in Figure 6.14 (a).

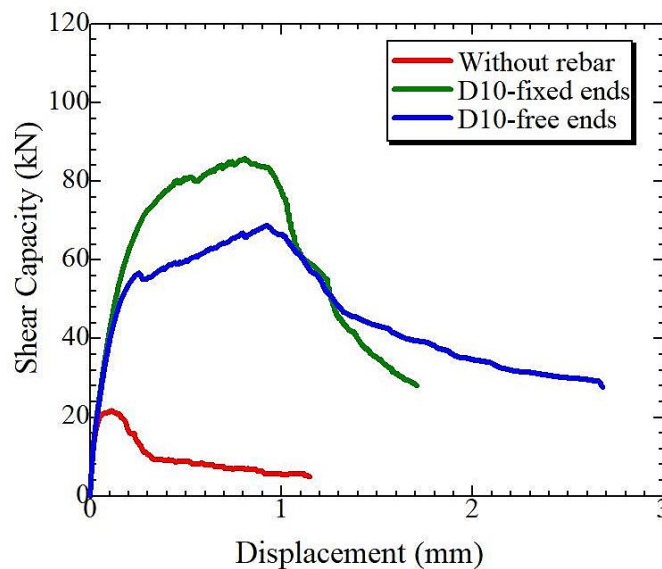


**Figure 6.16 Comparison of shear capacities of specimen with and without rebar**

Figure 6.16 shows the comparison of the shear capacities against specimens with and without the transverse rebar inside the hole of the PBL shear connector. The specimens with transverse rebar have been analyzed with free and fixed end conditions. Figure 6.16 shows the specimen with the transverse rebar having fixed end conditions

performs well compared with free ends and the specimen without transverse rebar in terms of the peak load and peak slip.

The numerically determined shear capacities are also compared with the shear capacities calculated through the empirical equations proposed by the past researchers. In this regard, Oguejiofor and Hosain et al. 1994, 1997, proposed two regression relations, equation 6.1 and equation 6.2, respectively for predicting the shear capacity of the PBL shear connector based on simple push-out tests and the numerical simulations. Both shear capacity equations mainly include the contribution of the concrete end-bearing resistance, shear resistance of the transverse reinforcement inside the hole and the shear resistance of the concrete dowel.

$$q_u = 0.59A_{cc} \sqrt{f_c} + 1.233A_{tr}f_y + 2.871nD^2 \sqrt{f_c} \quad (6.1)$$

$$q_u = 4.5h_{sc}t_{sc}f_c + 0.91A_{tr}f_y + 3.31nD^2 \sqrt{f_c} \quad (6.2)$$

Where,

$q_u$  = shear capacity (kN)

$A_{cc}$  = shear area of the concrete (mm<sup>2</sup>)

$A_{tr}$  = total area of the transverse reinforcement (mm<sup>2</sup>)

$f_c$  = concrete compressive strength (MPa)

$f_y$  = yield strength of the transverse reinforcement (MPa)

$n$  = number of rib holes

$D$  = diameter of the hole (mm)

$h_{sc}$  = height of the rib plate (mm)

$t_{sc}$  = thickness of the rib plate (mm)

Afterward, Yoshitaka et al. (2001) and Hosaka et al. (2000) proposed equations 6.3 and equation 6.4, to investigate the shear capacity of the PBL shear connectors without and with transverse reinforcement inside the hole, respectively. The Japan Society of Civil Engineers (JSCE) standard specifications for hybrid structures (JSCE 2009) also employed the same equations as proposed by Yoshitaka et al. and Hosaka et

al. to predict the shear capacity of the PBL at rib hole affected by the transverse reinforcement.

$$q_u = 3.38D^2 \left( t_{sc}/D \right)^{1/2} \times f_c - 39.0 \times 10^3 \quad (6.3)$$

$$\text{With } 22.0 \times 10^3 < \left[ D^2 \left( t_{sc}/D \right)^{1/2} \right] < 194.0 \times 10^3$$

$$q_u = 1.45 \times \left[ (D^2 - D_s^2) f_c + D_s^2 f_y \right] - 26.1 \times 10^3 \quad (6.4)$$

$$\text{With } 51.0 \times 10^3 < \left[ (D^2 - D_s^2) f_c + D_s^2 f_y \right] < 488.0 \times 10^3$$

Where,  $D_s$  = diameter of the transverse reinforcement (mm)

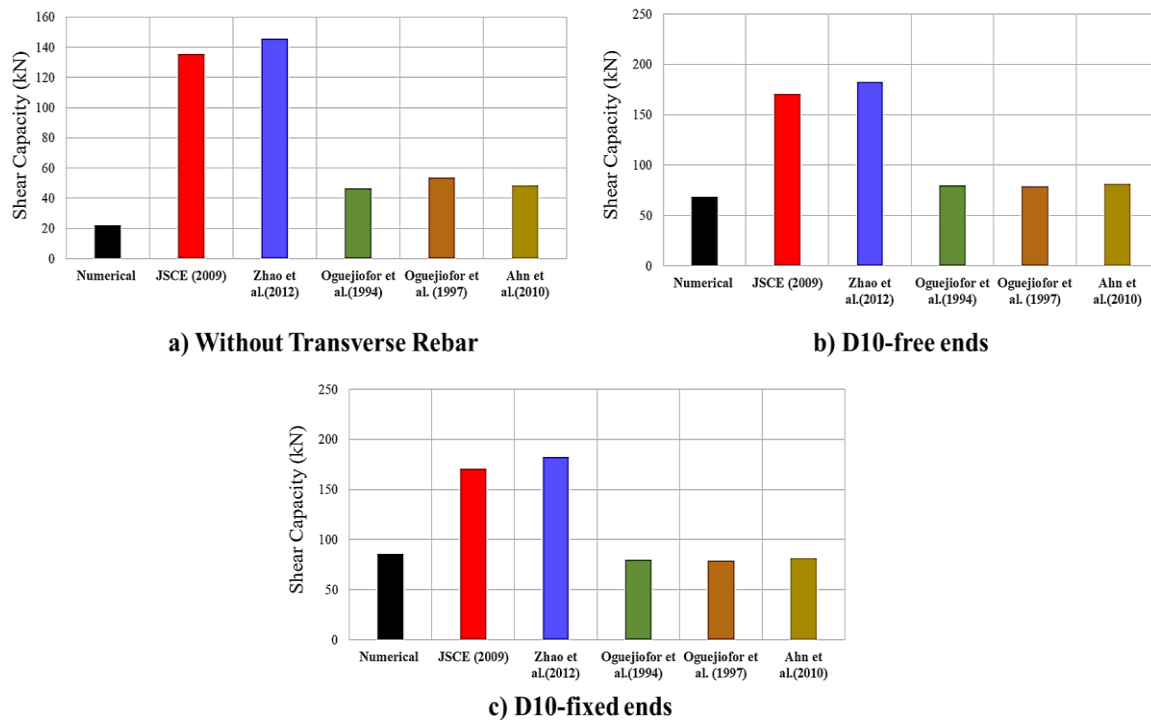
Ahn et al. (2010) proposed the shear capacity equation 6.5, based on the modification of equation 6.2 for single PBL shear connector.

$$q_u = 3.14h_{sc}t_{sc}f_c + 1.21A_{tr}f_y + 2.98nD^2 \sqrt{f_c} \quad (6.5)$$

Zhao et al. (2012) also developed an expression for the computation of the shear resistance, included the test results of 168 specimens from the previous studies and is shown in equation 6.6.

$$q_u = 1.38(D^2 - D_s^2)f_c + 1.24D_s^2f_y \quad (6.6)$$

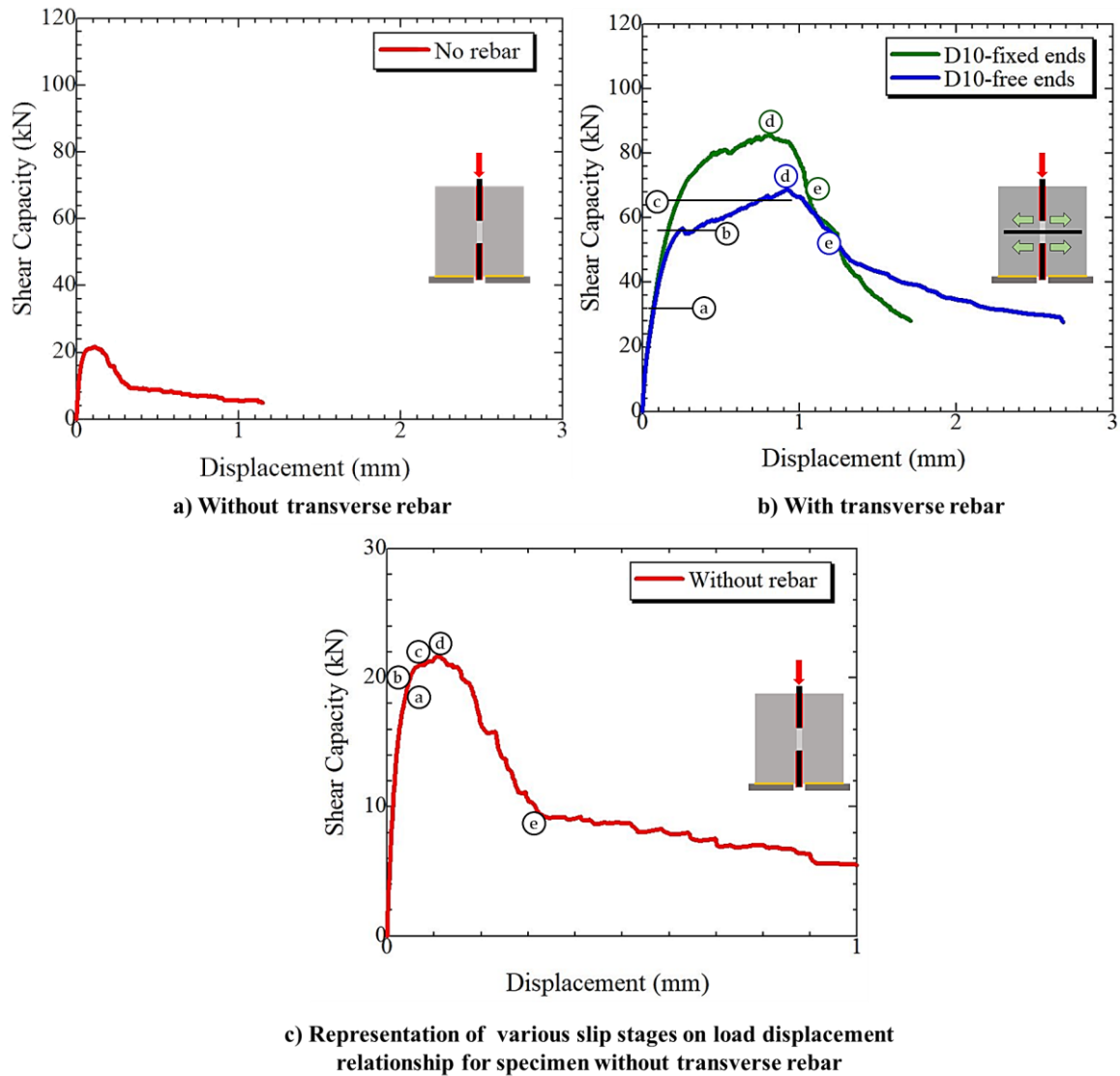
The comparison of the numerical simulation results and the shear capacities calculated using the above empirical equations have been shown in Figure 6.17. Figure 6.17 (a) shows that the numerical model evaluates the underestimation of the shear capacities compared with the empirical shear capacities in specimen without transverse rebar inside the hole of the PBL. While the numerical shear capacity for the specimen with transverse rebar ranges between the empirically calculated shear capacities.



**Figure 6.17 Comparison of the analytical and the empirical shear capacities**

Figure 6.17 (b) and Figure 6.17 (c) shows that the numerical simulation results are close to Oguejiofor and Hosain et al. 1(994, 1997) and Ahn et al. (2010), whereas underestimation has been observed while comparing with the result of JSCE (2009) and Zhao et al. (2012).

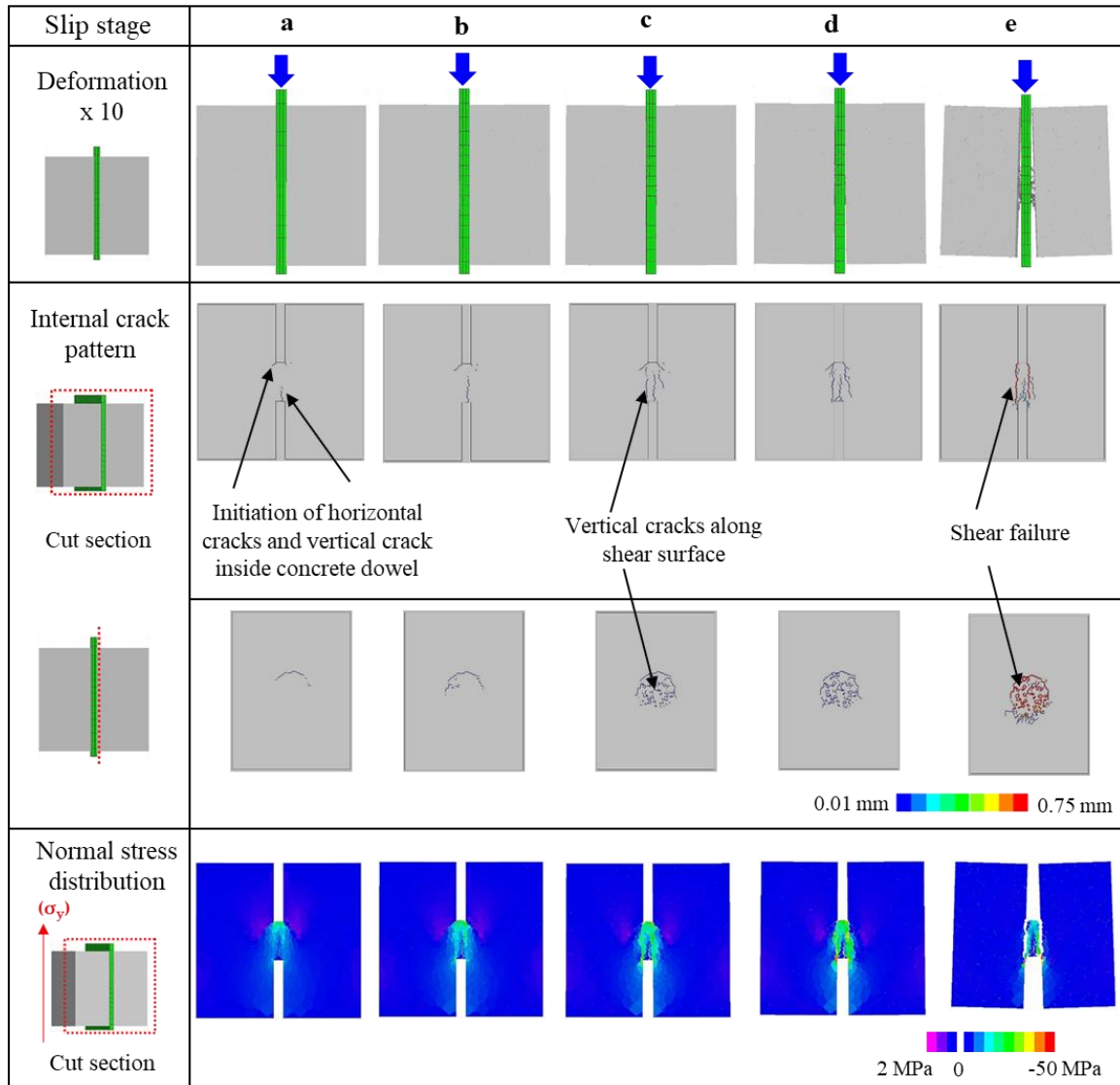
The underestimation of the numerical results may occur because of the reduced and the minimal bonding effects (consideration for presence of grease) on the concrete-steel boundary interface as well as very less frictional effects at the bottom of the specimens i.e. between the concrete blocks and the testing bed (consideration for presence of Teflon sheet) incorporated in numerical models as mentioned earlier in section 6.2.1 and Figure 6.13. Similarly, the model test performed to develop the above equations may have different boundary conditions, geometrical dimensions of the side concrete blocks, configuration and the number of holes in the steel plate, and the transverse rebars in the side concrete blocks. Furthermore, the past researcher; Cândido-Martins et al. 2010, reported that the above equations highly overestimate the results and also provide the unsafe predictions of the shear capacities especially for the specimens with fewer holes in the steel plate and for unreinforced PBL shear connectors.



**Figure 6.18 Representation of various stages for shear response of transverse rebar effect**

The internal failure process of specimen with and without transverse rebar inside the hole of the PBL shear connector are discussed here. In order to highlight the mechanism, various load displacement stages have been selected as marked in the Figure 6.18. The points a, b, c, d, and e in Figure 6.18(c) are corresponding to 17.8 kN, 20 kN, 21 kN, the peak and the post-peak, respectively. Similarly, the points a, b, c, d, and e in Figure 6.18(b) are corresponding to 32 kN, 56 kN, 66 kN, the peak and the post-peak, respectively. To evaluate the shear contribution of the transverse rebar

against applied vertical shear load in the simple push-out test, firstly the failure process in specimen without the transverse rebar is investigated. The failure process of the specimen without transverse rebar is shown in Figure 6.19.



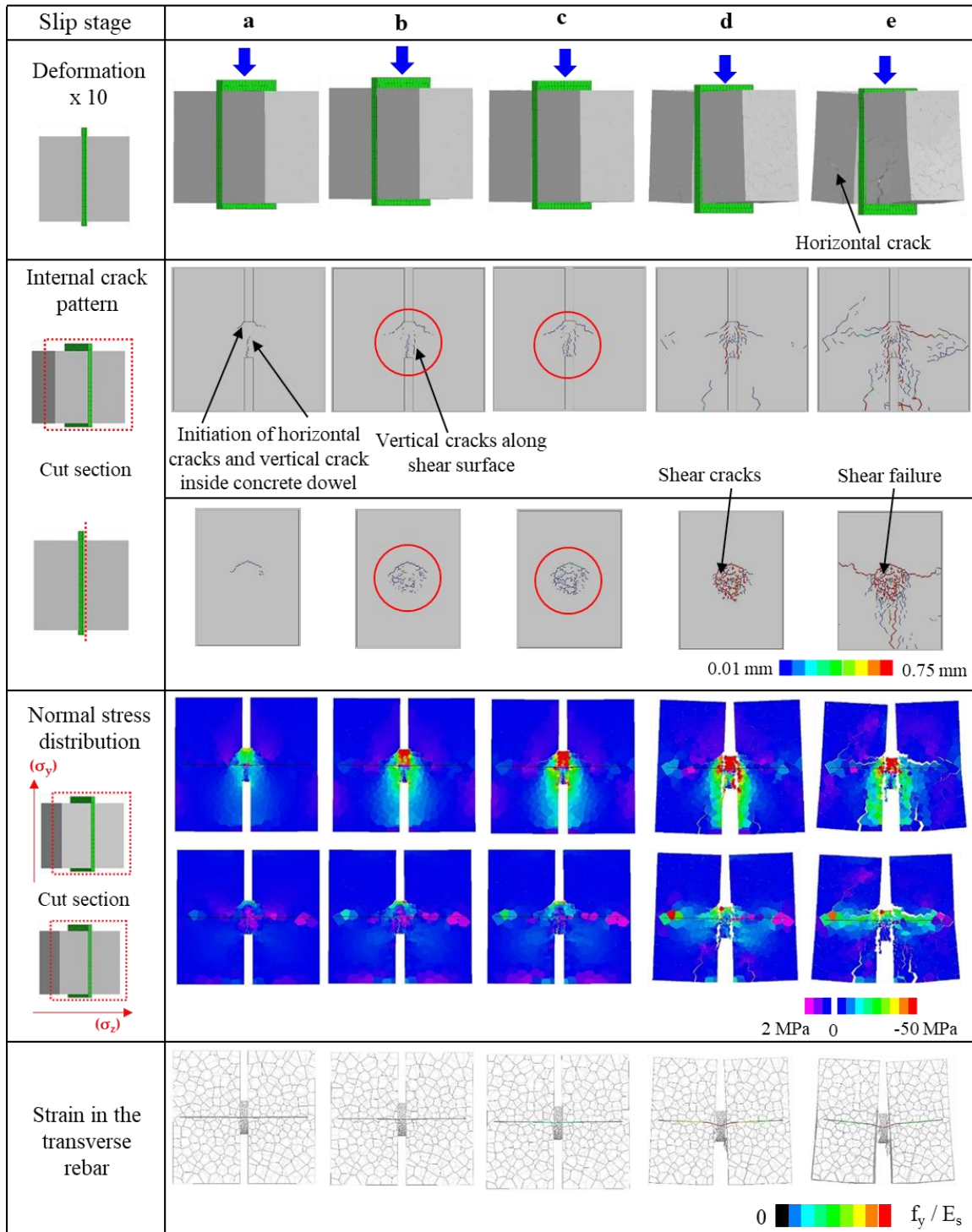
**Figure 6.19 Failure process of the specimen without transverse rebar**

Figure 6.19 shows that at the slip stage (a), firstly two horizontal cracks on the top of the concrete dowel and one vertical crack occurs inside the concrete dowel originating from the bottom of the concrete dowel. At slip stages (b) and (c), the horizontal cracks progress more and the vertical cracks also propagate along the shear surface and the normal stress along the y-axis ( $\sigma_y$ ) also transfer from top to the bottom

of the dowel. Figure 6.19 shows that at slip stages (d), the vertical completely propagate to the shear surface and the load becomes to decrease on the load-displacement curve afterward as shown in Figure 6.18. In the post-peak stage, the vertical crack propagation along the shear surface causes the shear failure and the stress concentration has only been observed in the region of the concrete dowel. Figure 6.19 shows that in the case of the specimen without transverse, the concrete dowel mainly resists the applied vertical shear load in a simple push-out and reproduces the shear failure along the shear surfaces.

The failure process of the specimens with transverse rebar inside the hole of the PBL with fixed end and free ends of the rebar has been shown in Figure 6.20 and Figure 6.21, respectively. In order to investigate the shear resistance contributed by the transverse rebar, the discussion regarding the comparison of the failure process is presented for specimens without and with transverse rebar (fixed ends) inside the hole of the PBL as shown in Figure 6.19 and Figure 6.20, respectively.

Figure 6.20 corresponding to slip stages (a) and (b) show that the initial internal failure process such that; initiation and propagation of the two horizontal cracks on the top of the concrete dowel and one vertical inside the concrete dowel originating from the bottom of the concrete dowel as well as the initiation of the vertical cracks along the shear surface, are same as that of the specimens without transverse rebar as shown in Figure 6.19 at slip from (a) to (c). In specimen without transverse rebar, once the vertical cracks along the shear surface start to propagate and these vertical cracks cause the shear failure along the shear surface as shown in Figure 6.19 at slip stages (d) and (e), whereas in specimens with transverse rebar, the vertical crack propagation is restrained by the transverse rebar inside the concrete dowel as shown in Figure 6.20 (c) and the shear strength of the PBL tends to improve as shown in Figure 6.18 (b).



**Figure 6.20 Failure process of the specimen with transverse rebar of fixed ends**

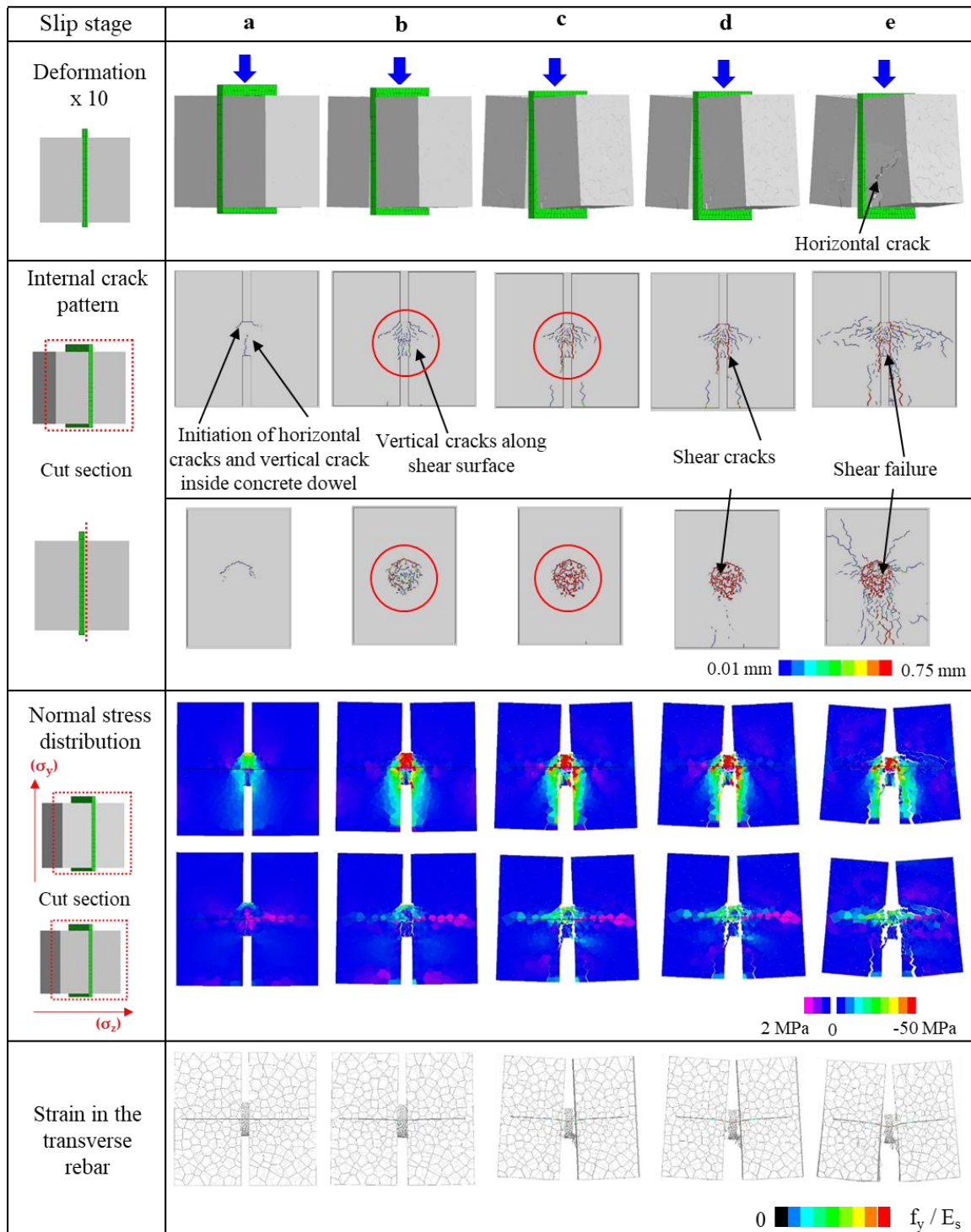


**Figure 6.21 Failure process of the specimen with transverse rebar of free ends**

The normal stress distribution along the y-axis ( $\sigma_y$ ) in Figure 6.20 at slip stage (c) shows that the large compressive stresses are resisted by the concrete on the upper side of the dowel because of the presence of the transverse rebar and are the large

compressive stresses are also concentrated up to rebar depth (mid-depth of the dowel). However, at slip stage (d) in Figure 6.20, the vertical cracks along the shear surface completely progress to the shear surface and the large compressive stresses ( $\sigma_y$ ) also transfer to the bottom side of the rebar and cause the shear failure of the concrete dowel, as well as the horizontal cracks, also propagate to the surface of the specimen in the post-peak region. The normal stress distribution along the y-axis ( $\sigma_y$ ) and along the z-axis ( $\sigma_z$ ) as shown in Figure 6.20 show that the compressive stresses are generated in the concrete dowel region as well as in the some portion of the side concrete blocks because of the presence of the transverse rebar, in contrast with specimen without transverse rebar inside the hole as shown in Figure 6.18.

The presence of the transverse rebar inside the hole of the PBL provides confinement to the concrete dowel due to bond behavior characteristics between the transverse rebar and the concrete inside the hole and causes the improvement of shear resistance contributed by the concrete dowel. In case of specimens with transverse rebar, the applied shear force in a simple push-out test is resisted by; concrete dowel as well as tensile force of the transverse rebar.

The discussion is highlighted here regarding the difference of internal failure process for the specimens with fixed and free end conditions of the transverse rebar inside the hole as shown in Figure 6.20 and Figure 6.21, respectively. Figure 6.20 and Figure 6.21 show that initial internal failure corresponding to slip stages (a) and (b) as mentioned earlier is same, however, the internal crack pattern of fixed ends rebar in Figure 6.20 at slip (b) stage shows that the vertical crack propagation along the shear surface is less as compared to free ends in Figure 6.21 as highlighted by red circles around the concrete dowel region. The same difference of the crack propagation has been observed at slip stage (c) in Figure 6.20 and Figure 6.21. Because of this difference of the less crack propagation along the shear surface, the load tends to increase up to the peak in fixed ends case and reproduces more shear capacity compared with free ends case. Figure 6.21 shows that the internal crack propagation and the occurrence of the large compressive stresses in concrete dowel region are more in free ends case compared with the fixed ends case as shown in Figure 6.20, therefore the contribution of the concrete dowel is also less in free ends case against the applied shear load although

both specimens reproduce the shear failure along the shear surfaces and the horizontal cracks also propagate to surfaces of the specimens.

The difference between the normal stress distributions in Figure 6.20 and Figure 6.21 is elaborated here. The large compressive stresses along the y-axis ( $\sigma_y$ ) around the concrete dowel region in fixed ends case are slightly less as shown in Figure 6.20 compared with the free ends as shown in Figure 6.21. Similarly, the compressive stresses distribution along the z-axis ( $\sigma_z$ ) in fixed ends case are distributed along the complete length of the rebar and provides more shear resistance as shown in Figure 6.20 compared with the free ends as shown in Figure 6.21. It can also be confirmed through the strain of the transverse rebar in fixed and free ends specimens as shown in Figure 6.20 and Figure 6.21, respectively. The strain of the transverse rebar in Figure 6.20 and Figure 6.21 shows the yielding of the rebar in concrete dowel region and also reproduce the kinking deformation of the transverse rebar, which is found to be consistent with the observations of the Zhao et al. (2018).

The comparison of the strain distribution and the curvature of the transverse rebar in fixed ends and free ends have been shown in Figure 6.22 and Figure 6.23, respectively.

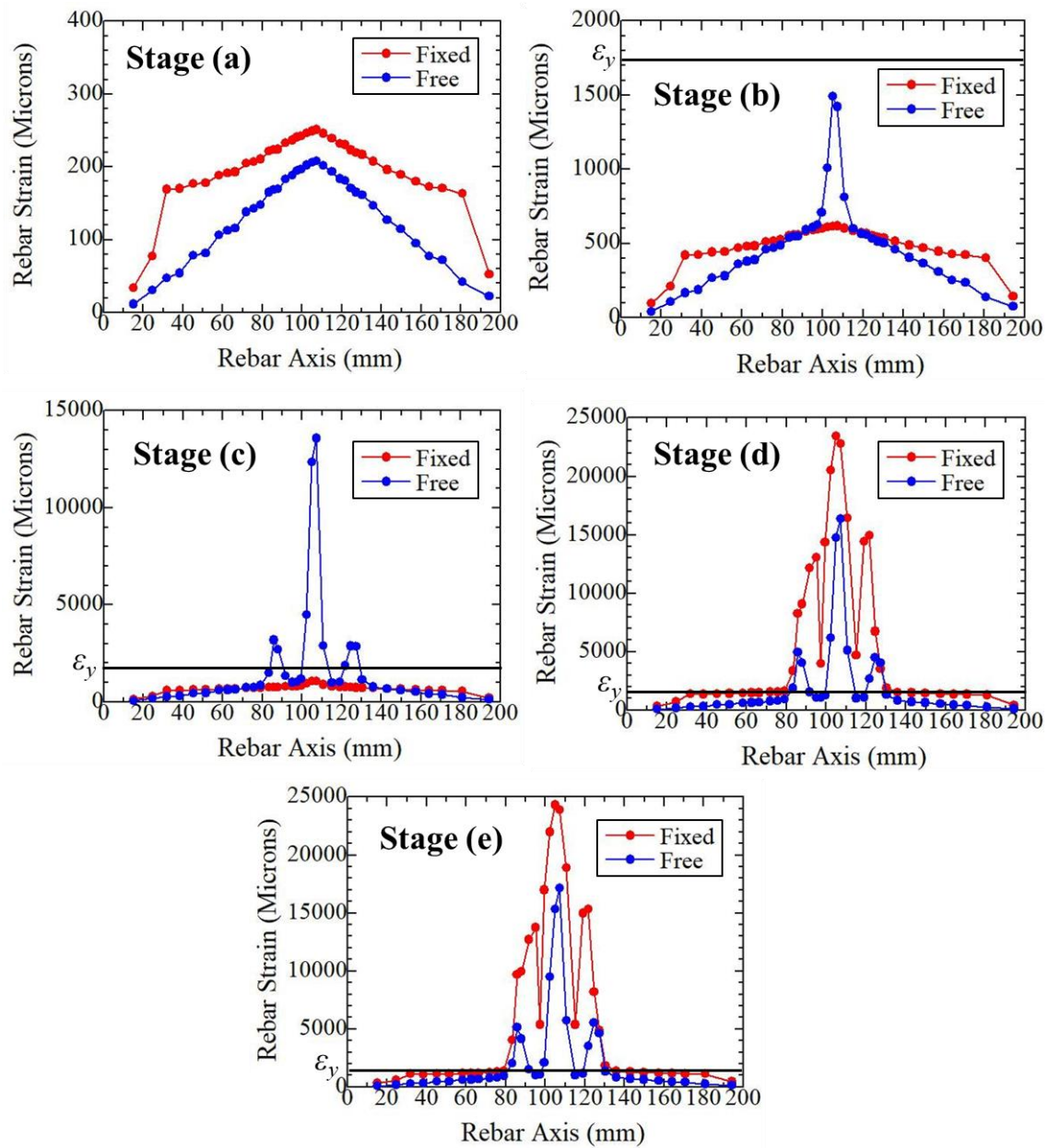


**Figure 6.22 Comparison of strain distribution of transverse rebar for fixed and free ends cases**

Figure 6.22 presents the strain distribution of the transverse rebar along the length of the rebar corresponding to various stages marked on the load-displacement curve as shown in Figure 6.18 (b). The strain distribution correlates well with the strain along with the transverse rebar as shown in Figure 6.22 and Figure 6.21 to show the yielded part of the rebar. Figure 6.22 shows that the rebar with free ends yields earlier compared with the fixed end case as shown at the slip stage (c). Figure 6.22 also shows

that in both cases the large strain values of the transverse rebar are observed in the central region between two side concrete blocks.

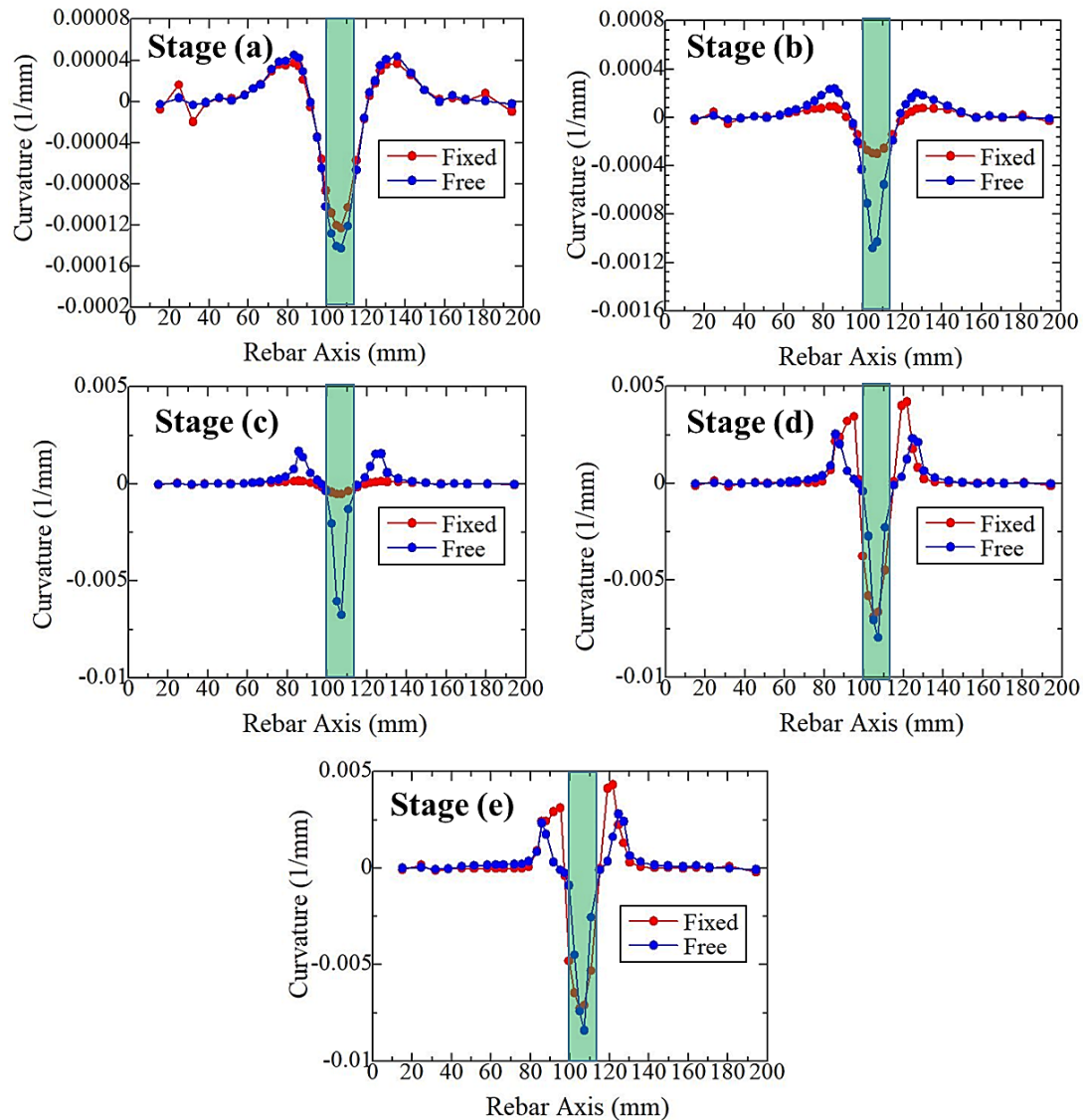


**Figure 6.23 Comparison of curvature distribution of transverse rebar for fixed and free ends cases**

Figure 6.23 shows the curvature distribution of the transverse rebar along the length of the rebar against various stages on the load-displacement curve. Figure 6.23 shows that in pre-peak; slip stages (a), (b), and (c), the curvature of the transverse rebar with free ends is more compared with fixed end whereas the magnitude of the curvature at the peak and the post-peak are almost same. Figure 6.23 also shows that region along with the length of the rebar experiencing the larger magnitudes of the curvature around

the edges of the steel plate is more in free ends case compared with fixed ends. The curvature distribution in Figure 6.23 also shows that in both cases the large curvature magnitude of the transverse rebar is concentrated in the central region of the concrete dowel.

#### 6.4.2 Effect of the rebar diameter

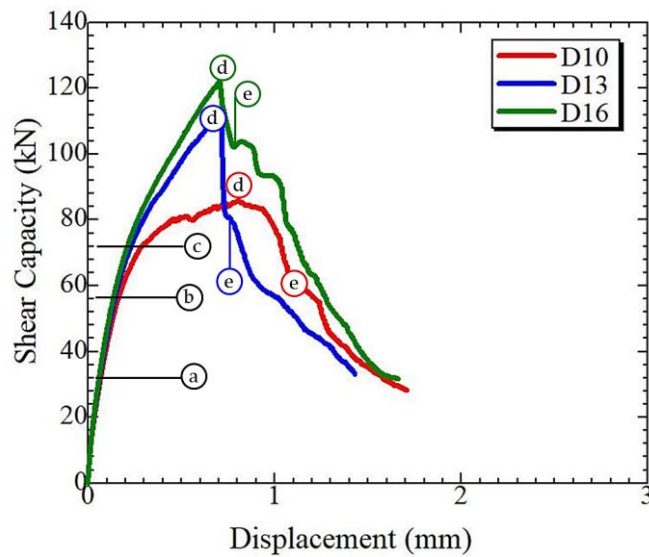


**Figure 6.24 Effect of the rebar diameter on the shear capacity**

The numerical investigations have also been performed for the diameter effect of the transverse rebar inside the hole with rebars of D10, D13, and D16 as shown in Table 6.1, employing the same specimens as shown in Figure 6.10 (b) with the fixed end conditions of the rebars as most of the real structures usually have fixed ends conditions. The numerically simulated load-displacement relationships are shown in Figure 6.24. Figure 6.24 shows that as the diameter of the transverse rebar increases the numerical model also reproduces an increasing trend of the shear capacities which is found to be consistent with the findings of the previous researchers. Figure 6.24 also highlights that the specimen embedded with rebar of D10 reproduce relatively better ductile behavior whereas in specimens embedded with D13 and D16, the load suddenly decreases after peak. The points a, b, c, d, and e in Figure 6.24 are corresponding to 32 kN, 56 kN, 72 kN, the peak and the post-peak, respectively. The numerically determined shear

capacities are also compared with the shear capacities calculated by using the empirical equations as mentioned earlier in section 6.3.1.

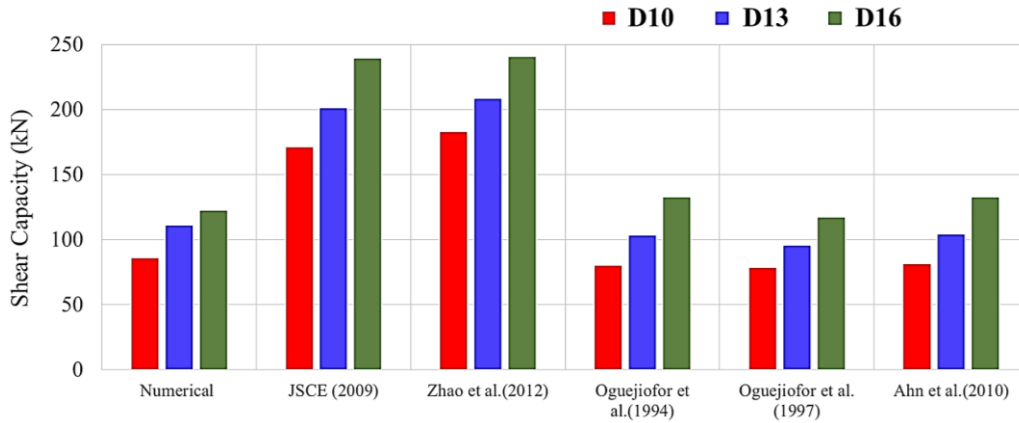


**Figure 6.25 Comparison of the analytical and the empirical shear capacities for rebar diameter effect**

The comparison of the analytical results and the shear capacities calculated by using the empirical equations is shown in Figure 6.25. Figure 6.25 shows that analytical results are found to be reasonable compared with the empirical results. Figure 6.25 shows that the analytical results lie between the maximum and minimum range of the empirical shear capacities as well as capture the tendency of the increasing shear capacities against the increased diameters of the transverse rebars as also produced by the empirical equations. Figure 6.25 also highlights that the analytical results are very close to Oguejiofor and Hosain et al. (1994, 1997) and Ahn et al. (2010), whereas underestimation has been observed while comparing with the result of JSCE (2009) and Zhao et al. (2012). The underestimation may be due to the reasons as mentioned earlier in section 6.3.1. The reasons behind an increasing trend of the shear capacities against the increased diameter of the transverse rebar can be explained through the internal failure process of the specimens. The detailed failure process of the specimens embedded with D10, D13, and D16 have been in Figure 6.26, Figure 6.27, and Figure 6.28, respectively.

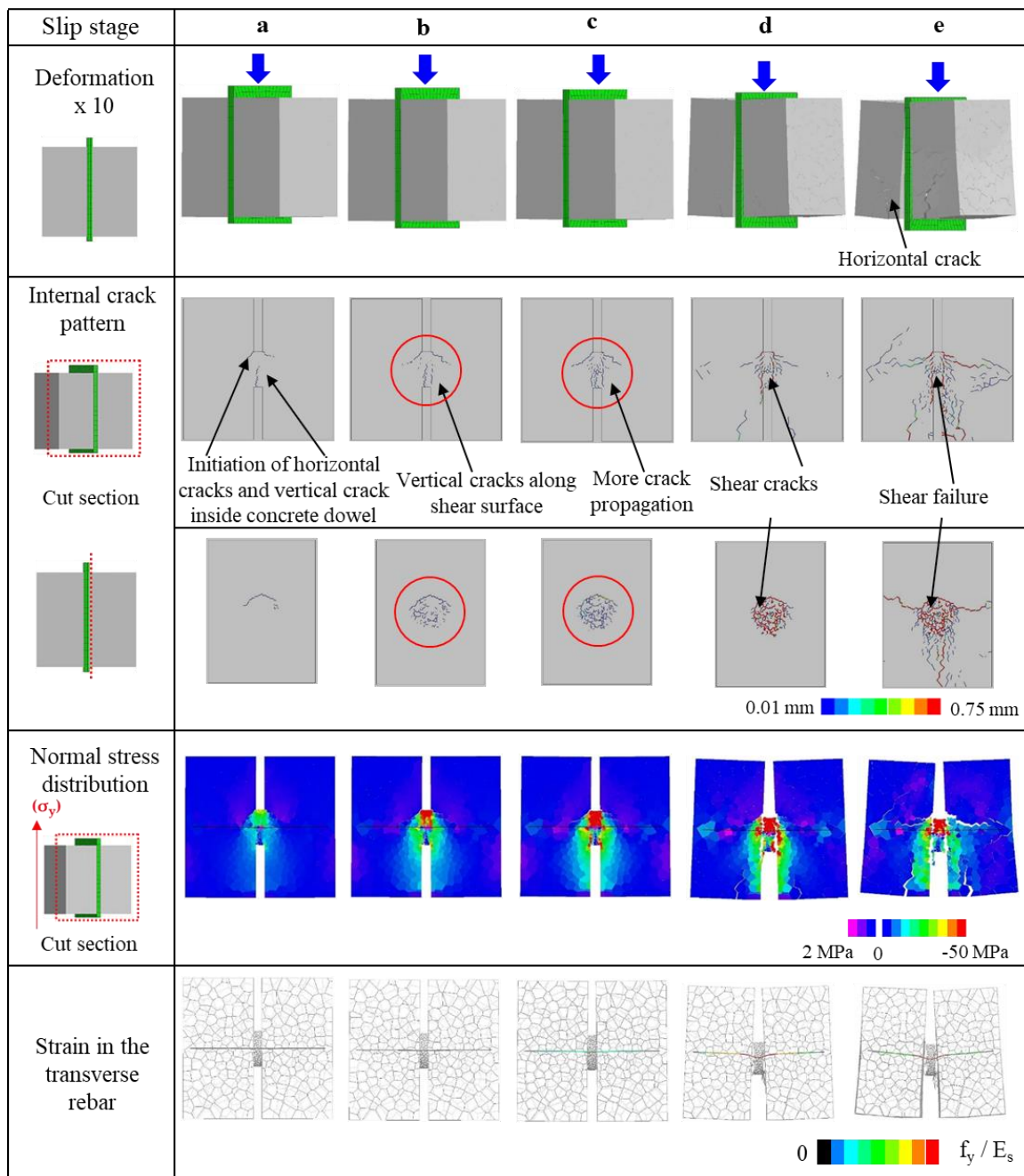


**Figure 6.26 Failure process of the specimen embedded with transverse rebar of D10**

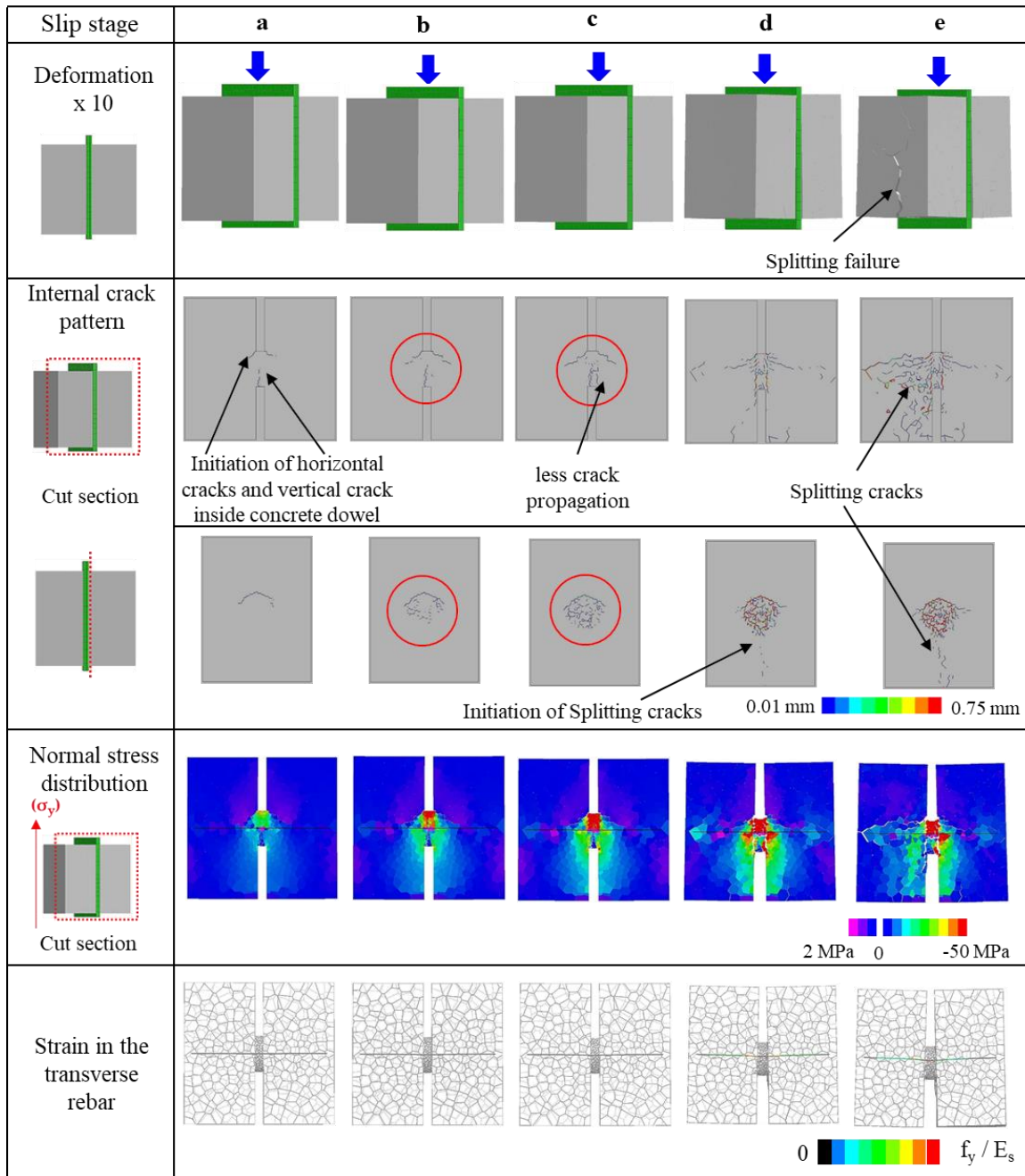


**Figure 6.27 Failure process of the specimen embedded with transverse rebar of D13**

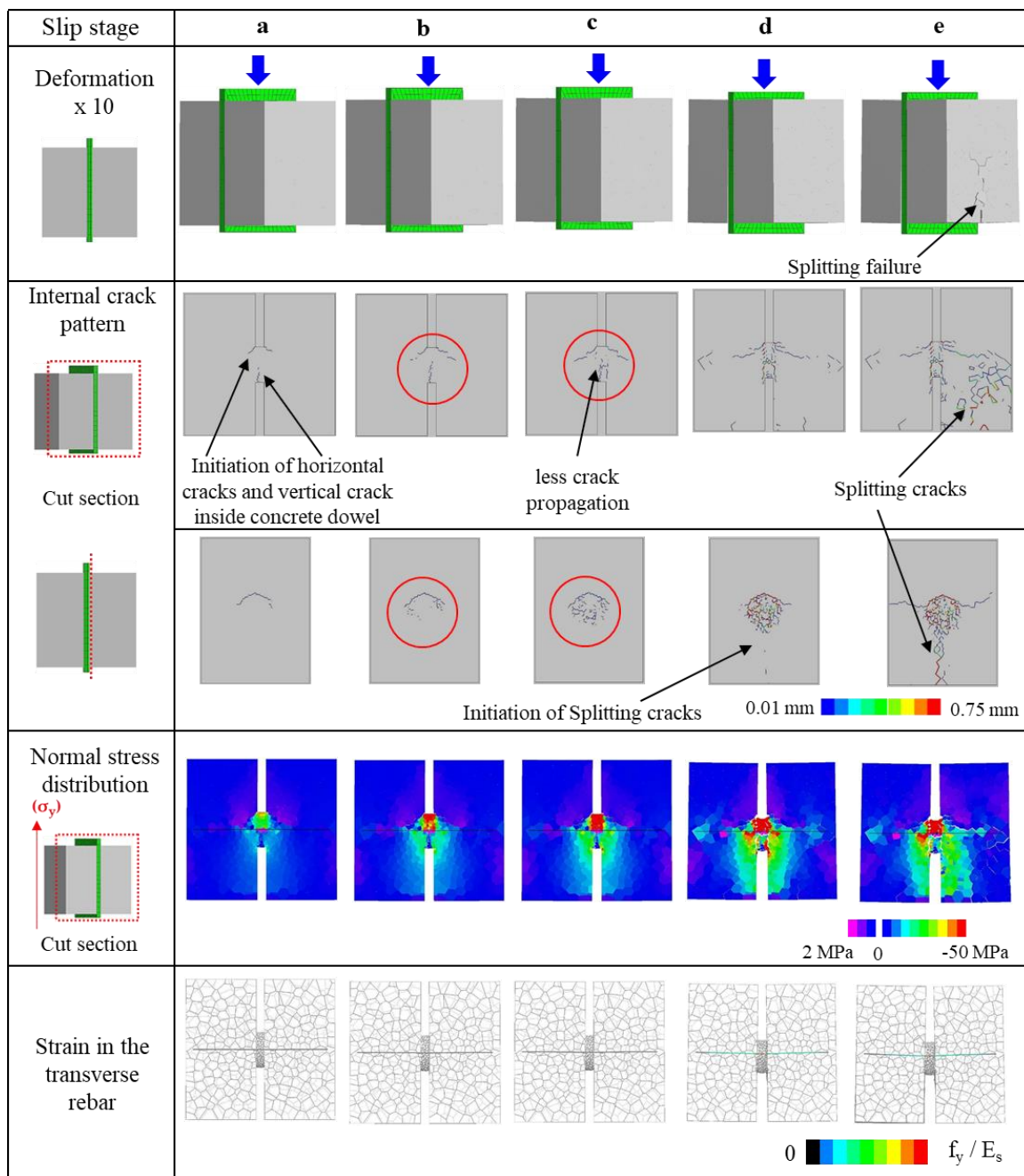


**Figure 6.28 Failure process of the specimen embedded with transverse rebar of D16**

The comparison of the internal failure process of the specimens embedded with the transverse rebar of diameters D10, D13, and D16 is elaborated here. The initial failure process at slip stage (a) is almost the same in all diameters cases as shown in Figure 6.26, Figure 6.27, and Figure 6.28. The internal crack patterns in at slip stages (b)

and (c) in Figure 6.26, Figure 6.27, and Figure 6.28 are found to be different as highlighted by a red circle around the concrete dowel regions. Figure 6.26 shows that the internal crack propagation at slip stages (b) and (c) are more compared with the specimens embedded with D13 and D16 as shown in Figure 6.27 and Figure 6.28. Figure 6.26 shows that after the occurrence of the vertical along the shear surface, the shear failure occurs at the slip stages (d), and (e) and horizontal cracks also propagate to the surface of the specimen.

While the specimens embedded with rebar of diameters D13 and D16 highlight the initiation of the splitting cracks under the concrete dowel on the inner sides of the side concrete blocks at slip stage (d) as shown in Figure 6.27 and Figure 6.28. The initiation of the splitting crack in specimens embedded with rebar of diameters D13 and D16 as shown in Figure 6.27 and Figure 6.28 is because of the improvement of the shear resistance contributed by the concrete dowel against the applied shear load. As the diameter of the rebar increases, the more surface area of the rebar provides the more bond strength and hence the more confinement to the concrete inside the hole. After initiation of the splitting crack in specimens embedded with rebar of diameters D13 and D16 at slip stage (d), the splitting failure has been observed in the post-peak region. Figure 6.26 and Figure 6.28 show that as the diameter of the transverse rebar inside the concrete dowel increases the shear capacity also increases and the deformed behaviors changes from the shear failure mode to the splitting failure mode and load decreases abruptly on the load-displacement curve after peak as shown in Figure 6.2. The difference between the normal stress distributions in Figure 6.26, Figure 6.27, and Figure 6.28 is elaborated here. Figure 6.26, Figure 6.27, and Figure 6.28 show that at slip stages (a), (b), and (c) the large compressive stresses along the y-axis ( $\sigma_y$ ) occur on the top of the concrete dowel, while the difference of the compression envelope in the side concrete blocks in specimens embedded with D10, D13 and D16 is found to be different. The specimens embedded with D13 and D16 experience the more envelope of the compressive stresses at slip stages (d) and (e) because of the splitting crack propagation as shown in Figure 6.27, and Figure 6.28, respectively compared with the specimen embedded with rebar of D10 as shown in Figure 6.26. Similarly, the difference of the strain in the transverse rebar has also been revealed for the specimens embedded with rebars of D10, D13, and D16 as shown in Figure 6.26, Figure 6.27, and

Figure 6.28, respectively. The yielding of the rebar has been observed in all the cases. Figure 6.26 shows that the specimen embedded with rebar of D10 experiences the maximum kinking deformation and the yielded parts along the length of the rebar because of its less bending resistance compared with the specimens embedded with rebars of D13 and D16 as shown in Figure 6.27, and Figure 6.28, respectively.

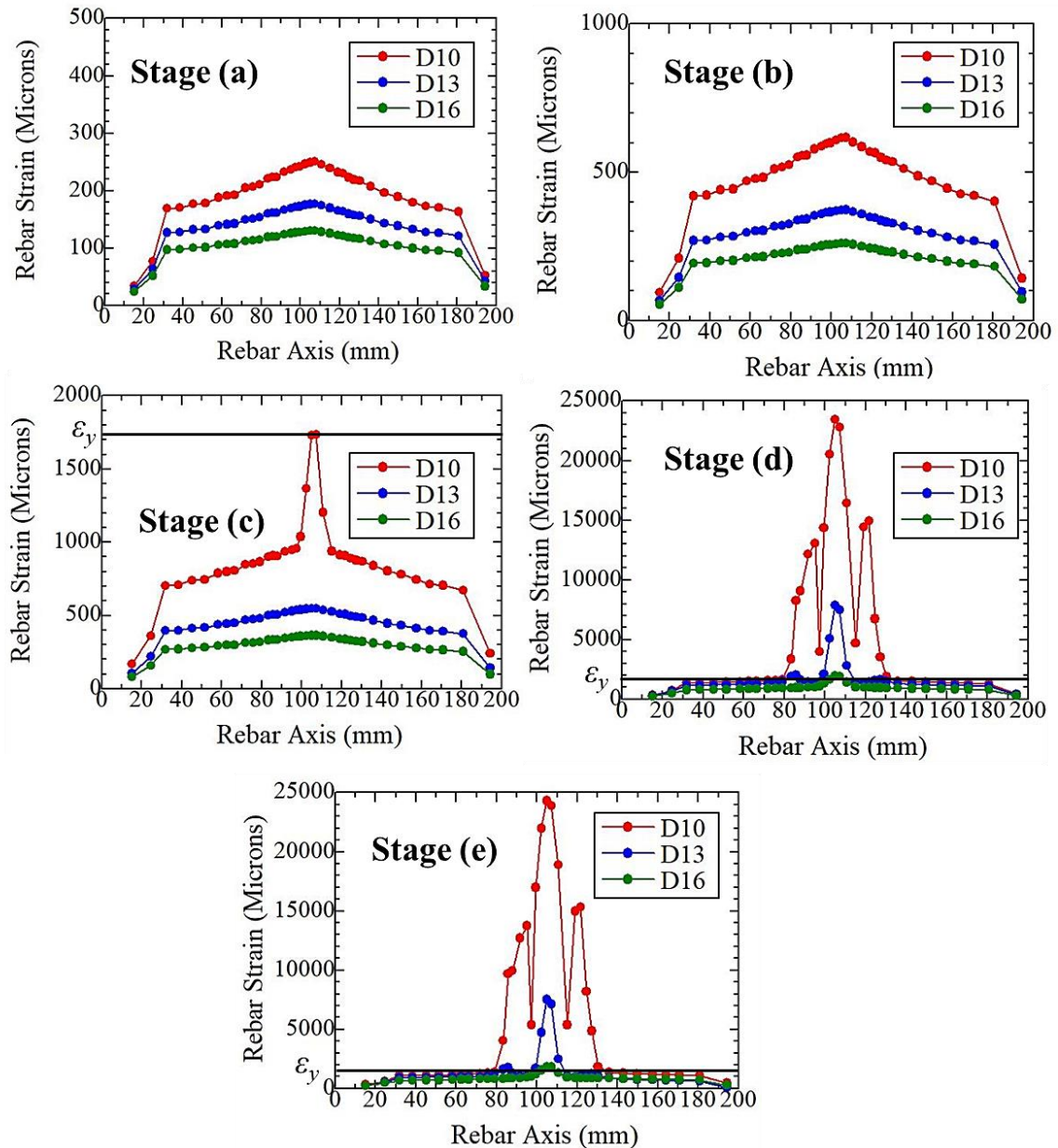


**Figure 6.29 Comparison of strain distribution for different diameters of the transverse rebars**

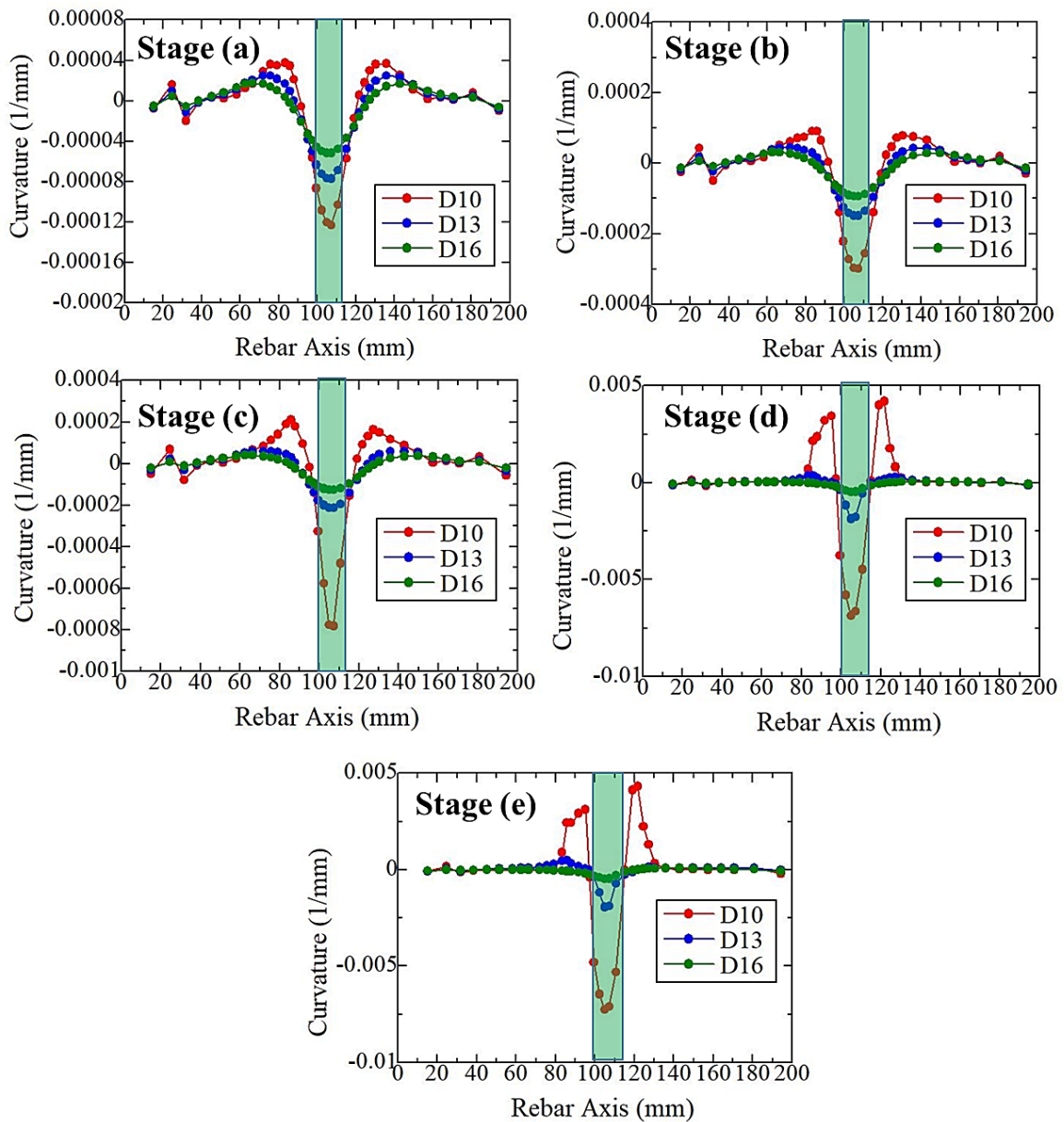


**Figure 6.30 Comparison of curvature distribution for different diameters of the transverse rebars**

The comparison of the strain and the curvature distribution along the rebar axis against various stages on the load-displacement in the simple push-out test have been shown in Figure 6.29 and 6.30, respectively. The strain distribution along with the rebar also supports the previous discussion. The yielding of the rebar starts from the slip stage (c) for rebar of D10, while at the peak and the post-peak the rebars of D13 and D16 also show the yielding phenomenon. Figure 6.29 also illustrates that the rebar of D10

reproduces the maximum strain magnitude in contrast with rebars of D13 and D16. Figure 6.30 shows that damage or the deformation region is more for rebar of D10 around the steel plate corresponding to all the stages compared with the rebars of D13 and D16. Figure 6.29 and Figure 6.30, show that because of the maximum curvature and the strain of the rebar of D10, the failure behaviors reproduce the better ductility of the specimen compared with the specimens embedded with rebars of D13 and D16 as shown in Figure 6.24.

#### ***6.4.3 Effect of the rebar position inside hole***

After the parametric evaluation of the transverse rebar corresponding to rebar end conditions and the rebar diameters, the numerical evaluation has also been performed for the rebar positions inside the hole of the PBL shear connector. The effect of the rebar position inside the hole has been considered as an important parameter at the construction site as the rebar position inside the hole of the PBL may be changed during placement at the site. Keeping in view, the construction errors at the site, the current parametric analyses have been adopted as there are no experimental and analytical studies yet, aimed at to investigate the failure process for different positions of the rebar inside the hole of the PBL shear connector. In this regard, three rebar positions have been selected i.e. top, middle, and bottom considering the same specimen as shown in Figure 6.14 (b). These three rebar positions inside the concrete dowel are considered keeping in mind that the specimens are purely subjected to vertical shear loading applied on the top of the perforated steel plate in simple push-out test.

The 10 mm concrete cover has been provided from the top and from the bottom for the rebars located at the top and the bottom positions inside the concrete dowel, respectively. The analytical models (all dimensions are in mm) of the specimens have shown in Figure 6.31.

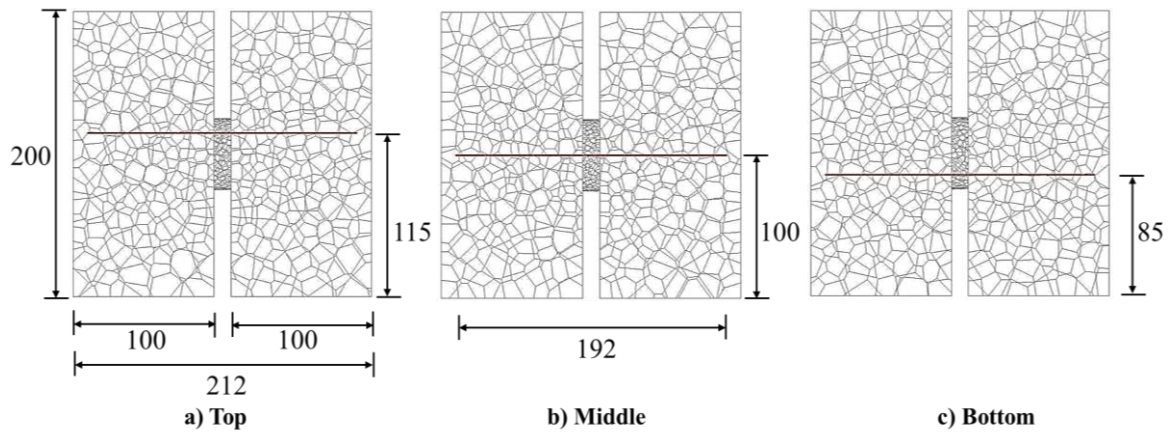


**Figure 6.31 Analytical models with different rebar positions inside hole**

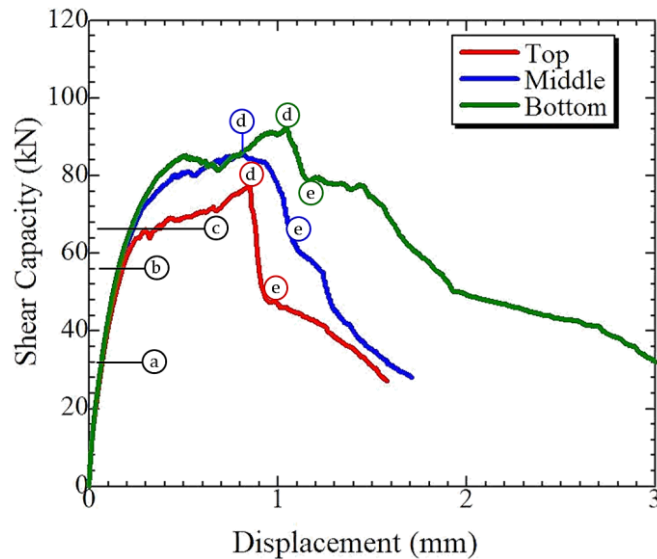


**Figure 6.32 Load-displacement relationships with different rebar positions inside hole**

The load-displacement relationships against the different positions of the rebar are shown in Figure 6.32. Figure 6.32 shows that the shear capacity of the PBL increase from top to bottom position of the rebar, keeping all other parameters constant. Approximately 20 % increase of the shear capacity has been observed as the rebar position is changed from the top to the bottom position inside the hole. The increment of the shear capacity can be investigated through the internal failure process against these three positions of the rebar. The failure processes for the top, the middle and the bottom positions of the rebar have been shown in Figure 6.33, Figure 6.34, and Figure

6.35, respectively. The points a, b, c, d, and e in Figure 6.32 are corresponding to 32 kN, 56 kN, 66 kN, the peak and the post-peak, respectively

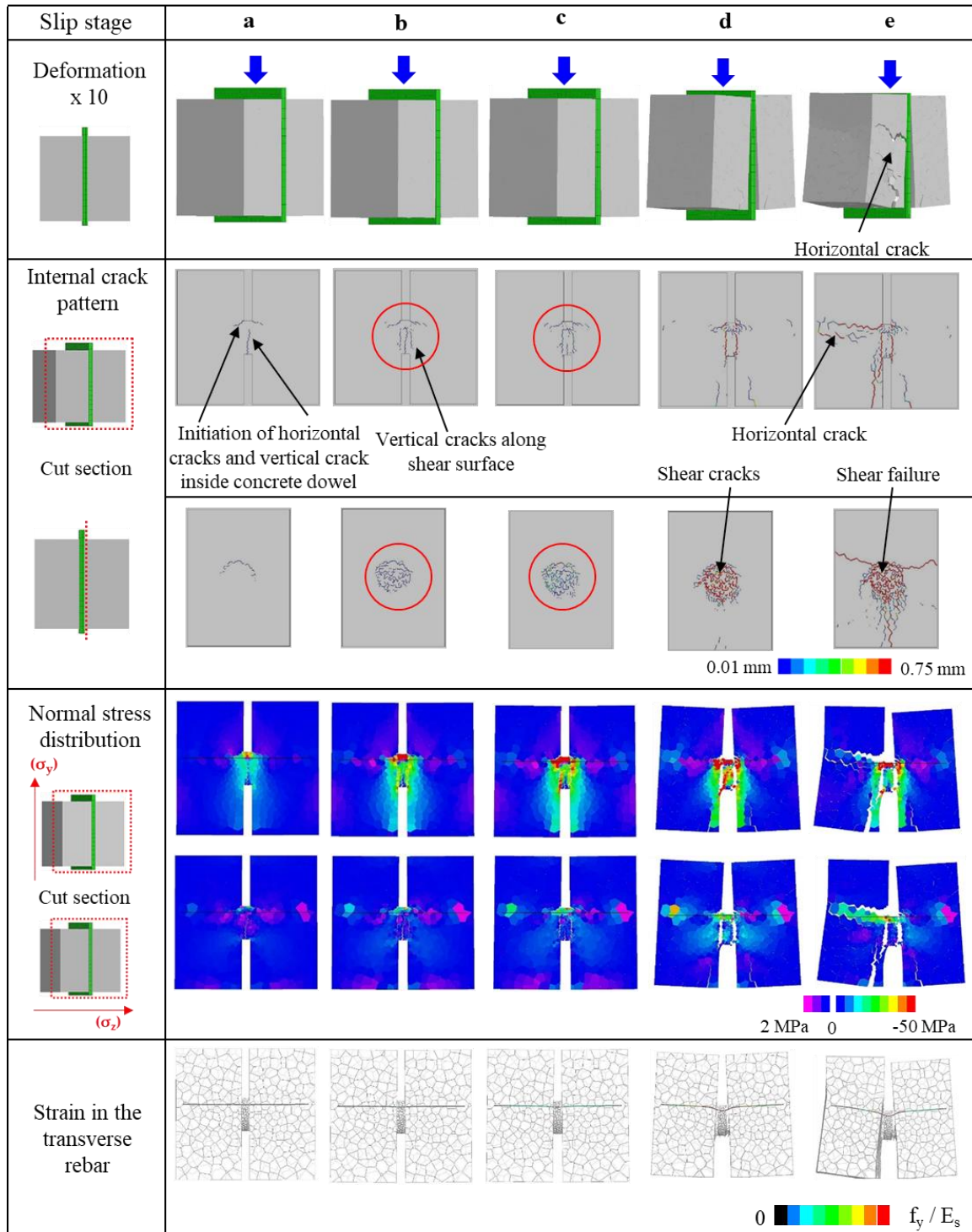


**Figure 6.33 Failure process of the specimen with transverse rebar at a top position**

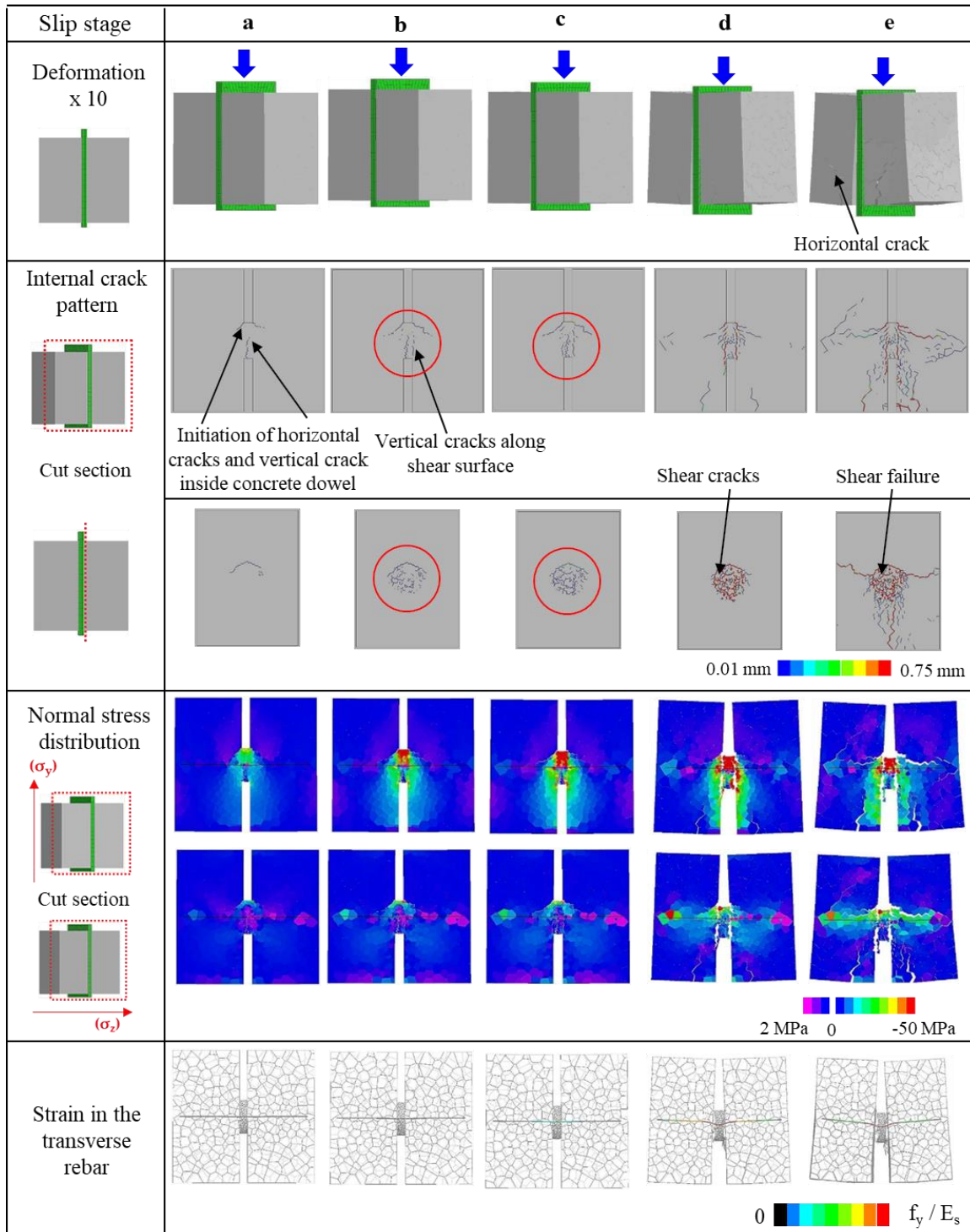


**Figure 6.34 Failure process of the specimen with transverse rebar at a middle position**

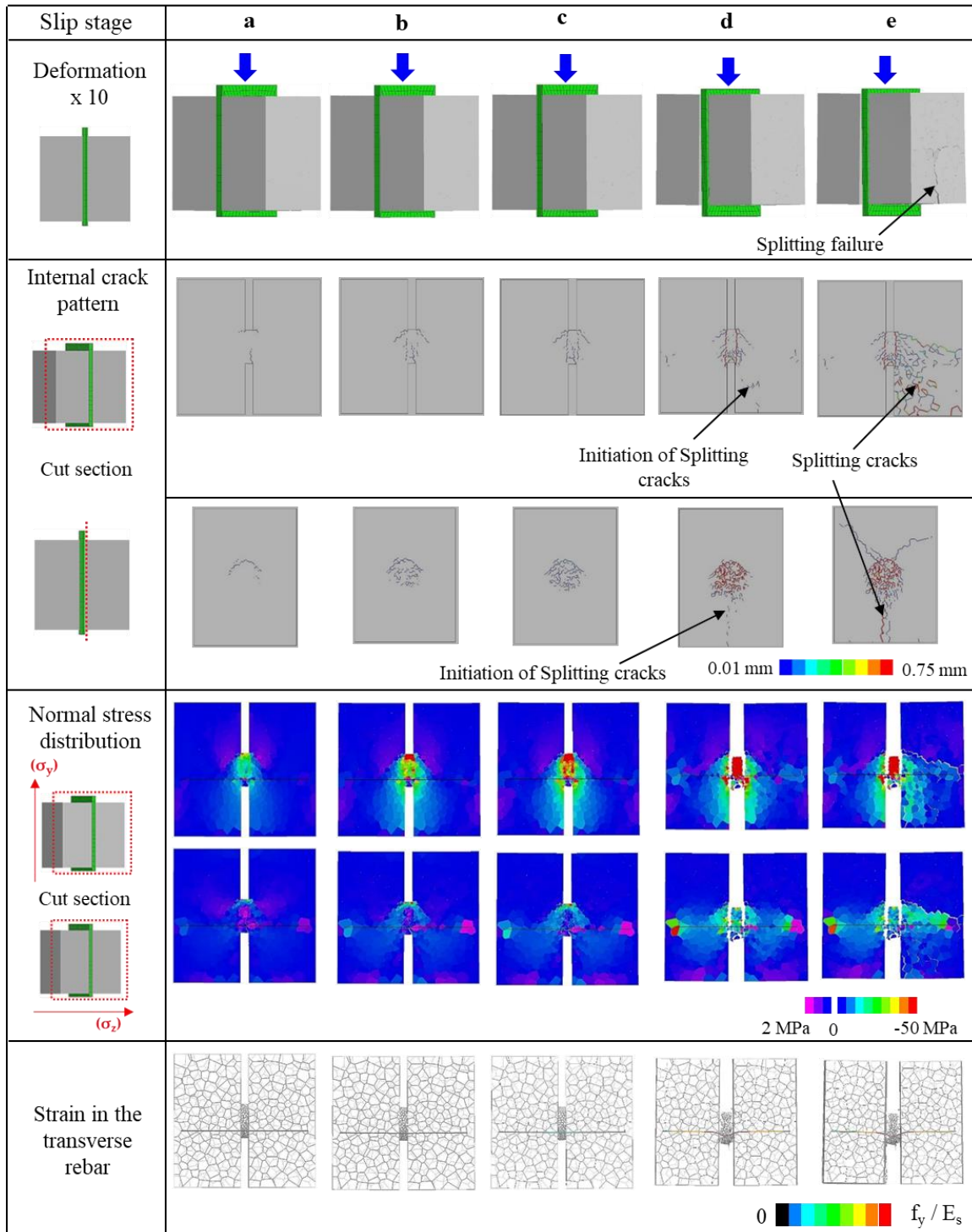


**Figure 6.35 Failure process of the specimen with transverse rebar at a bottom position**

The comparison of the internal failure process of the specimens with the transverse rebar located at the top, middle and the bottom positions is elaborated here.

The internal crack patterns in Figure 6.33, Figure 6.34, and Figure 6.35 corresponding to slip stages (a), (b), and (c) show that the initial failure process at these slip stages is almost the same for all the three positions of the transverse rebar. The internal crack patterns in Figure 6.33 and Figure 6.34 show that after the occurrence of the vertical crack along the shear surface at slip stages (b) and (c), the shear failure occurs at the slip stages (d), and (e) and the horizontal cracks also propagate to the surface of the specimen.

While the specimens embedded with rebar at the bottom position of a hole highlight the initiation of the splitting cracks under the concrete dowel on the inner sides of the side concrete blocks at slip stage (d) as shown in Figure 6.35. The initiation of the splitting crack in specimens embedded with rebar at the bottom position of a hole as shown in Figure 6.35 is because of the improvement of the shear resistance contributed by the concrete dowel against the applied shear load. As the concrete region above the rebar increases inside the hole, the ability of the concrete dowel to resist the applied vertical shear load in a simple push-out test also increases. After the initiation of the splitting crack in specimens embedded with rebar at the bottom position of a hole at slip stage (d), the splitting failure has been observed in the post-peak region. Figure 6.33, Figure 6.34, and Figure 6.35 show that as the concrete region above the rebar increases inside the hole the shear capacity also increases and the deformed behaviors change from the shear failure mode to the splitting failure mode and load decreases on the load-displacement curve after the peak as shown in Figure 6.32.

The difference between the normal stress distributions in Figure 6.33, Figure 6.34, and Figure 6.35 is elaborated here. Figure 6.33, Figure 6.34, and Figure 6.35 show that at slip stages (a), (b), and (c) the large compressive stresses along the y-axis ( $\sigma_y$ ) occur on the top of the concrete dowel, while the difference of the compression envelope in the side concrete blocks in specimens embedded with rebar at the top, the middle and the bottom positions of a hole are found to be different. The specimen embedded with rebar at the bottom position of a hole experiences the more envelope of the compressive stresses at slip stages (d) and (e) because of the splitting crack propagation as shown in Figure 6.35 compared with the specimen embedded with rebar at the top and the middle positions of a hole as shown in Figure 6.33 and Figure 6.34, respectively. Furthermore, the normal stresses along the z-axis ( $\sigma_z$ ) as shown in Figure

6.33, Figure 6.34, and Figure 6.35 demonstrate the difference of the internal resistance mechanism. Figure 6.35 shows that as the concrete region above the rebar increases, the more compressive stresses in a trapezoidal manner are being produced for the rebar at the bottom position inside the hole and hence more resistance is being provided against the applied shear load and causes the increase of shear capacity.

Similarly, the difference of the strain in the transverse rebar has also been revealed for the specimens embedded with rebar at the top, the middle and the bottom positions of a hole as shown in Figure 6.33, Figure 6.34, and Figure 6.35, respectively. The yielding of the rebar has been observed in all the cases. Figure 6.33 shows that the specimen embedded with rebar at the top position experiences the maximum kinking deformation and the yielded parts along the length of the rebar because of the less concrete over the rebar compared with the specimens embedded with rebars at the middle and the bottom positions as shown in Figure 6.34, and Figure 6.35, respectively.

The comparison of the strain and the curvature distribution along the rebar axis against various stages on the load-displacement have been shown in Figure 6.36 and Figure 6.37, respectively. Figure 6.36 shows that the yielding of the rebar starts from the slip stage (c) for the rebar located at the top position inside the hole of the PBL, while at the peak and the post-peak all the rebars positioned at the top, the middle and the bottom show the yielding. Figure 6.36 also illustrates that the rebar positioned at the top reproduces the maximum strain magnitude before the peak, while almost same magnitude of the strain for all the rebars positioned at the top, the middle and the bottom inside the hole. Figure 6.37 shows that damage or the deformation region is more for the rebar positioned at the top around the steel plate corresponding to all the stages compared with the rebars positioned at the middle and the bottom. Figure 6.36 and Figure 6.37, show that because of the maximum curvature and the strain of the rebar positioned at the top, the peak slip is more of this specimen compared with the specimens embedded with rebars positioned at the middle and the bottom as shown in Figure 6.32.

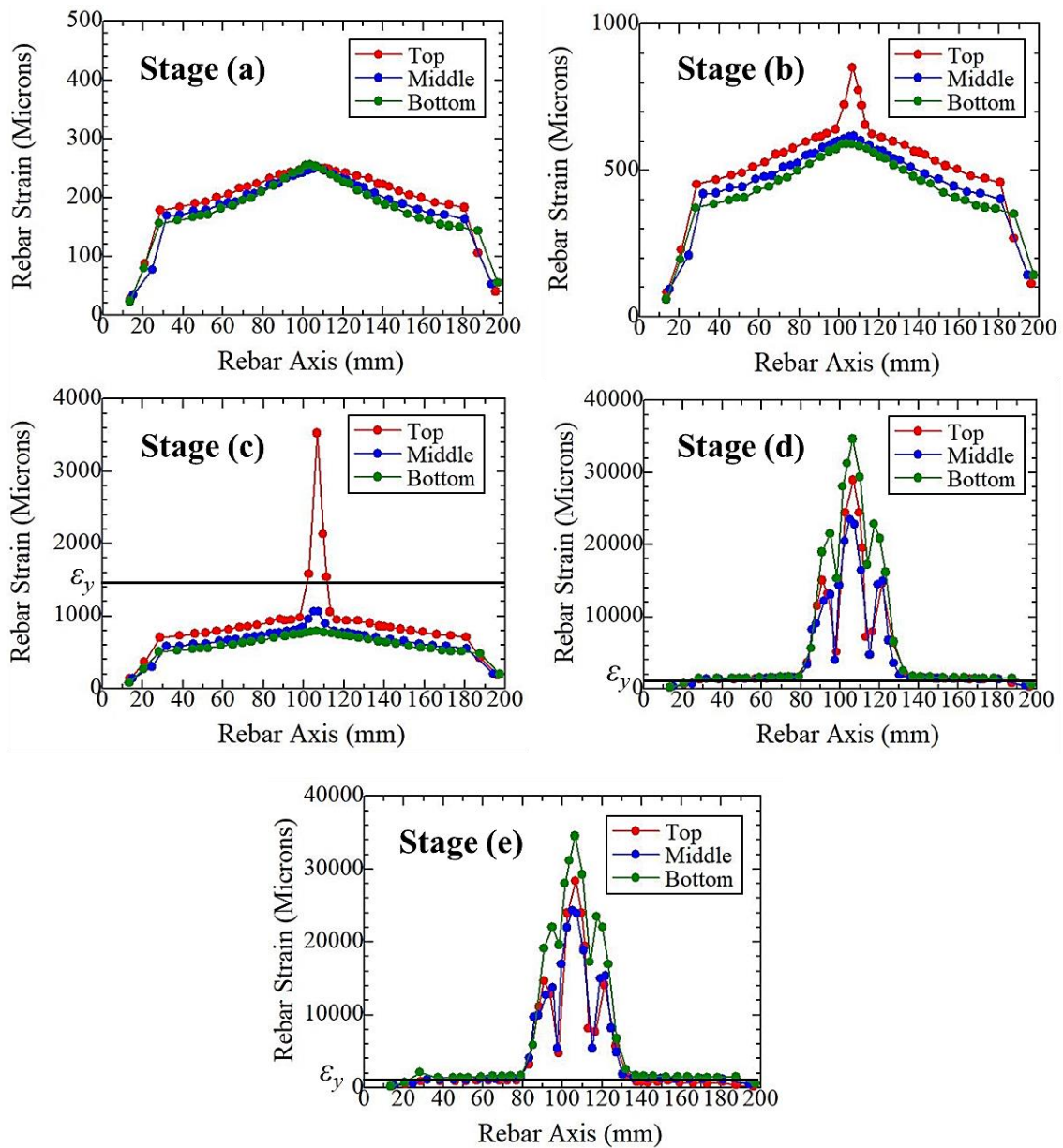


**Figure 6.36 Comparison of strain distribution for the different positions of the transverse rebars inside hole**

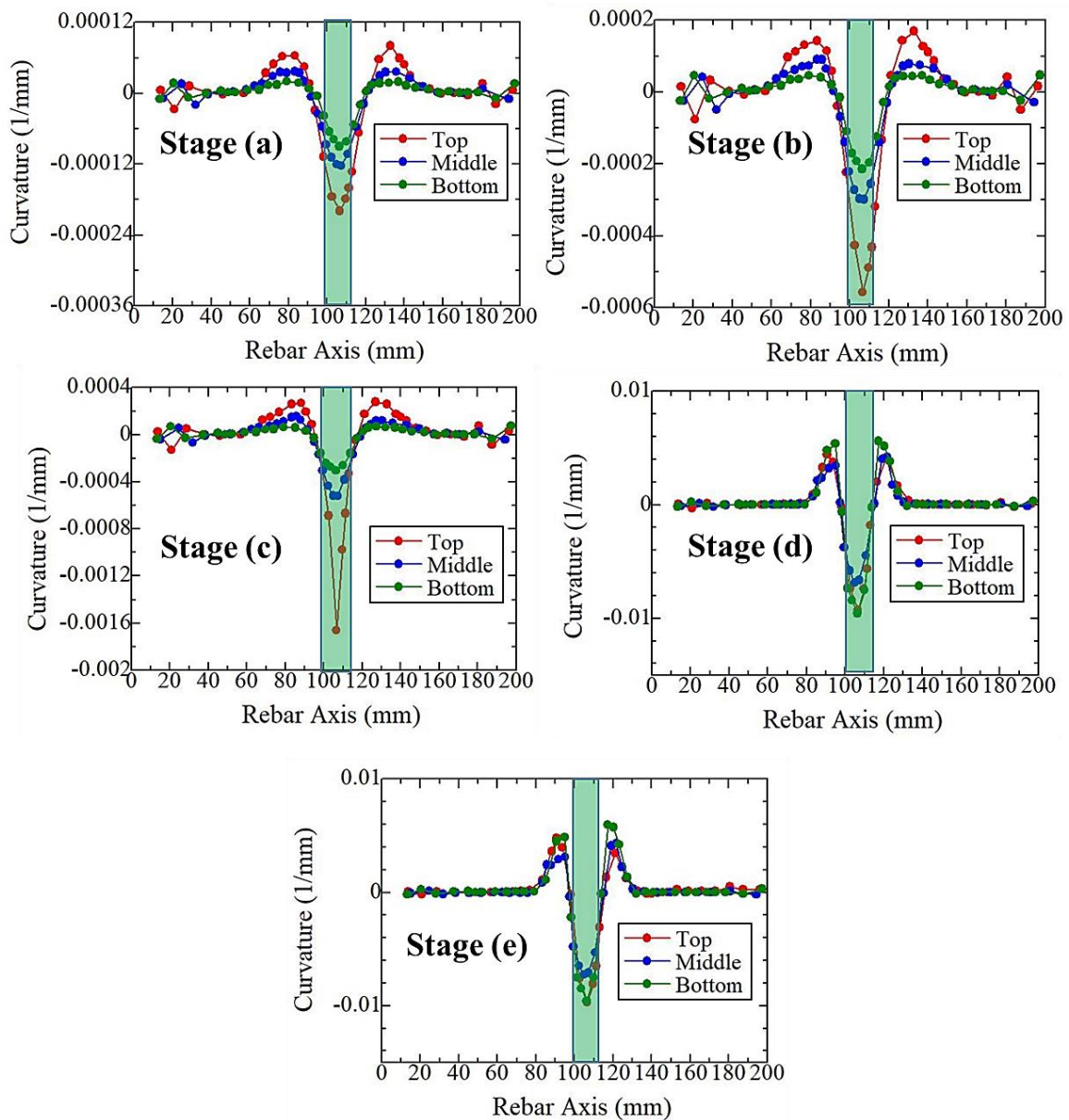


**Figure 6.37 Comparison of curvature distribution for the different positions of the transverse rebar inside hole**

#### **6.4.4 Effect of the yield strength ( $f_y$ ) of the rebar**

After the numerical evaluation of the transverse rebar corresponding to rebar end conditions, the rebar diameters, and the position of the rebar inside the hole the numerical evaluation has also been performed for the yield strength of the transverse rebar as a parameter of the design equations of the PBL shear connector as shown earlier in section 6.3.1.

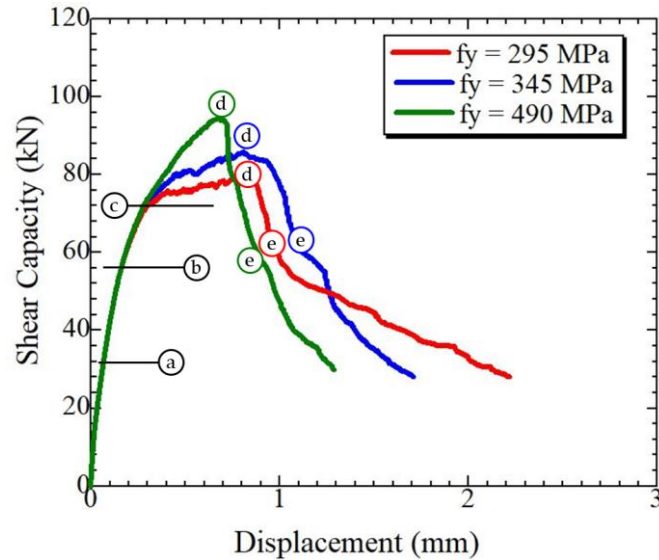


**Figure 6.38 Load-displacement relationships with different yield strengths of the transverse rebar**

The effect of the yield strength of the transverse rebar has been carried by selecting three yield strengths of the transverse rebar; 295 MPa, 345 MPa, and 490 MPa for rebar of D10, as shown in Table 6.1. Similarly, there are no experimental and analytical studies yet, aimed at investigating the failure process for different yield strengths of the transverse rebar inside the hole of the PBL shear connector.

The load-displacement relationships against the different yield strengths of the rebar are shown in Figure 6.38. Figure 6.38 shows that the shear capacity of the PBL increases from 295 MPa to 490 MPa while keeping the diameter of the rebar constant (D10). Approximately 19 % increase of the shear capacity has been observed as the rebar yield strength is increased from the 295 MPa to the 490 MPa. The increment of the shear capacity can be investigated through the internal failure process against these yield strengths of the rebar. The failure processes for the 295 MPa, 345 MPa, and 490 MPa for rebar of D10 of the rebar have been shown in Figure 6.39, Figure 6.40, and Figure 6.41, respectively. The points a, b, c, d, and e in Figure 6.38 are corresponding to 32 kN, 56 kN, 72 kN, the peak and the post-peak, respectively

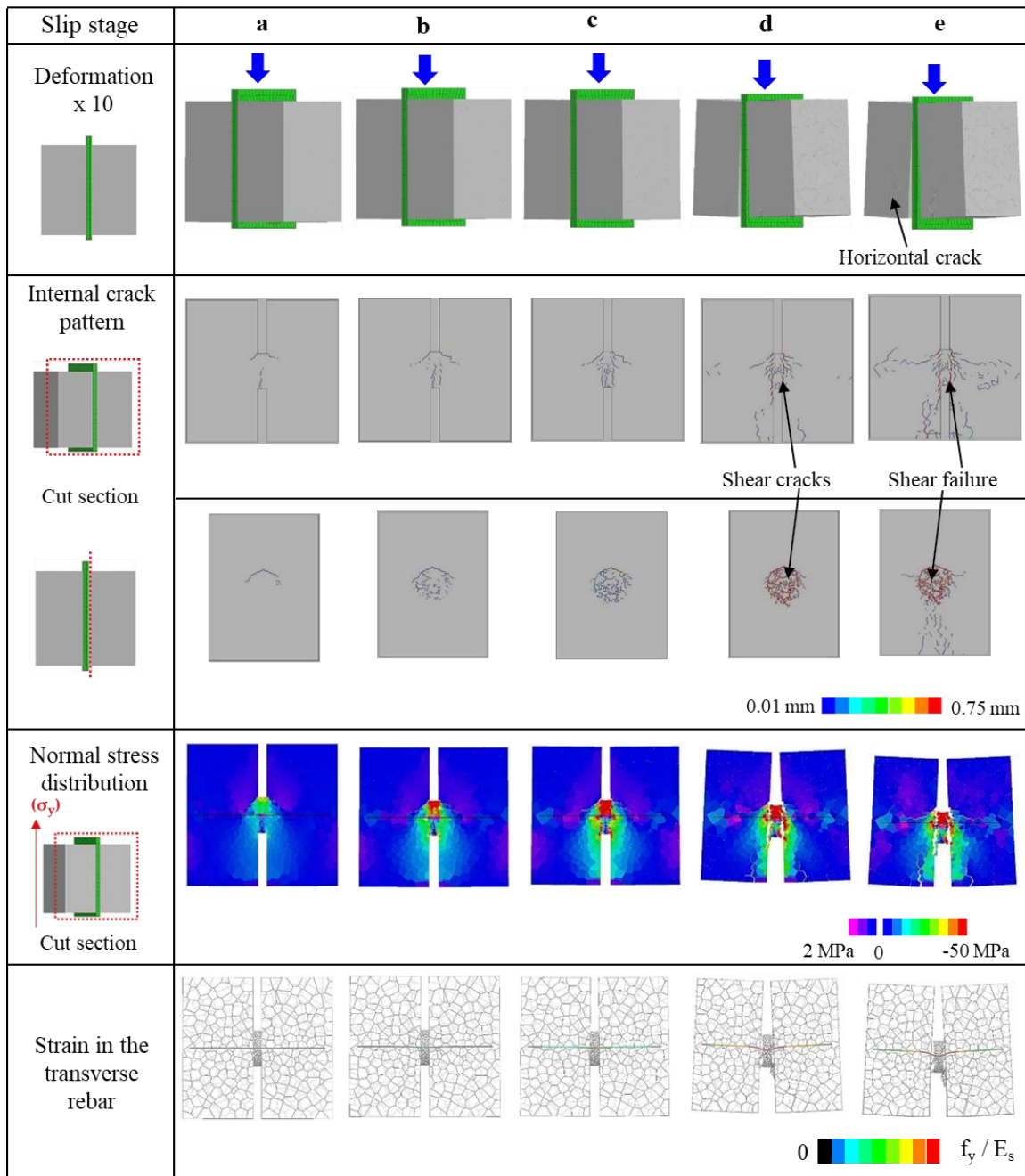


**Figure 6.39 Failure process of the specimen with transverse rebar of yield strength 295 MPa**

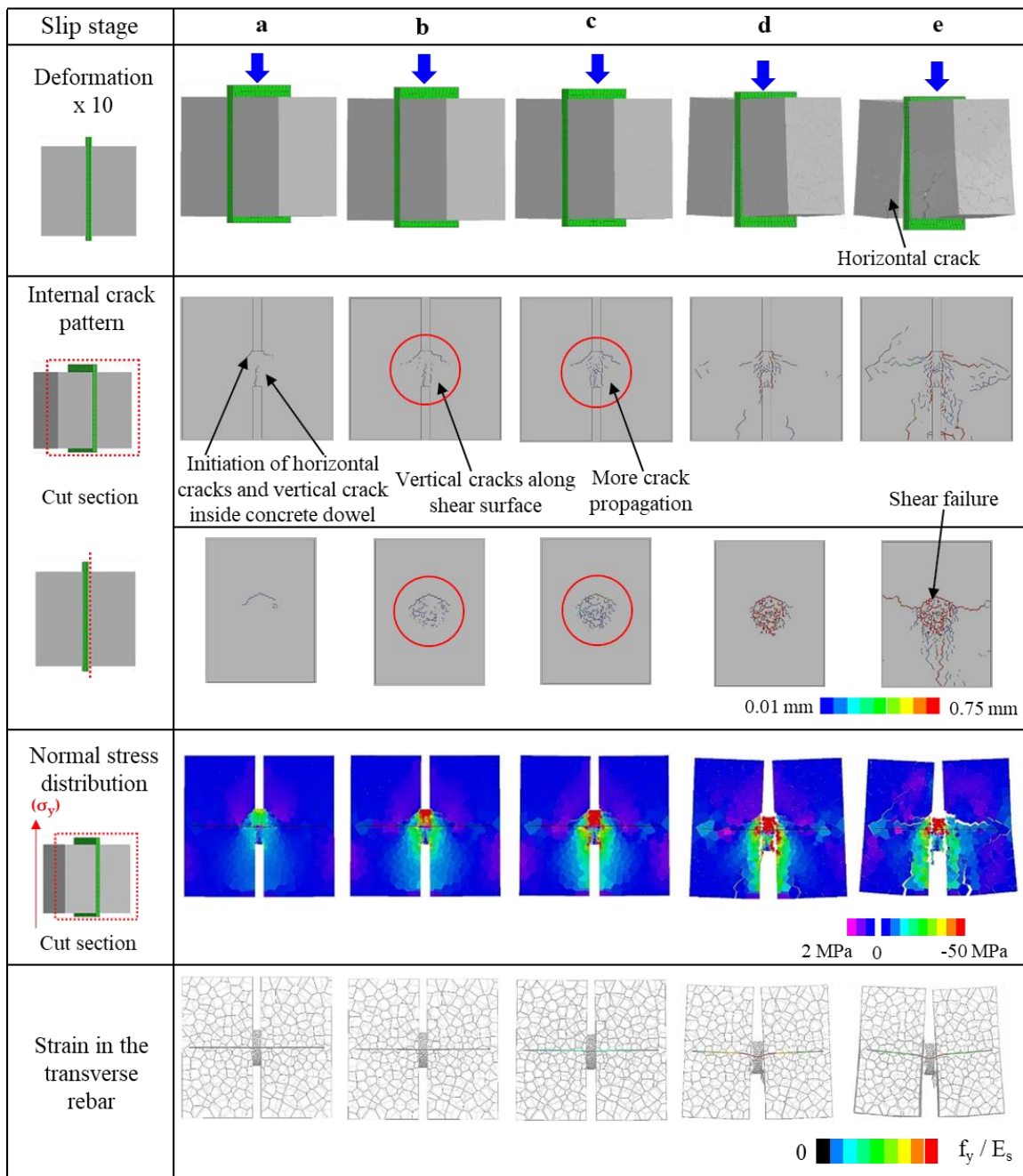


**Figure 6.40 Failure process of the specimen with transverse rebar of yield strength 345 MPa**

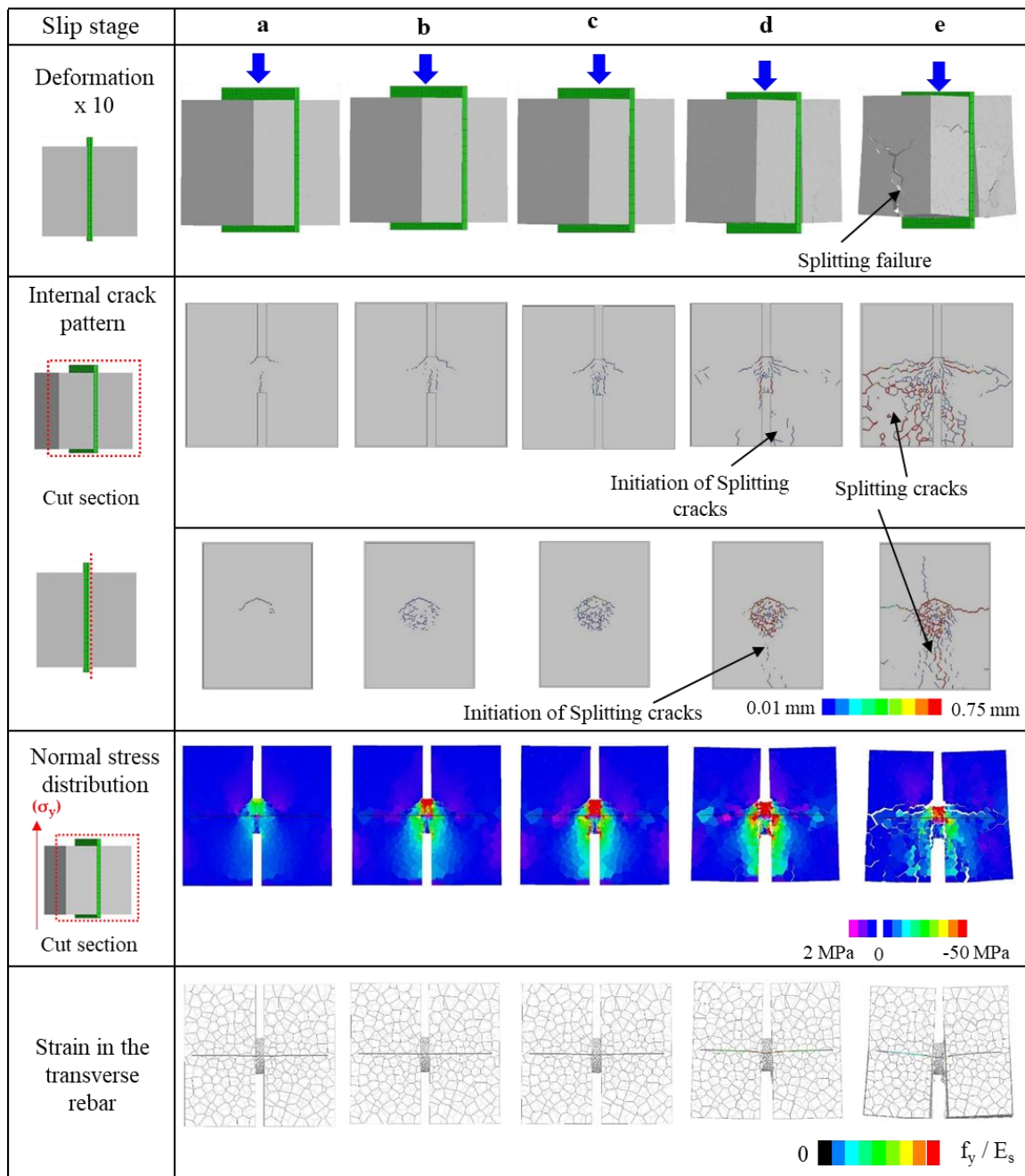


**Figure 6.41 Failure process of the specimen with transverse rebar of yield strength 490 MPa**

The comparison of the internal failure process of the specimens with the transverse rebar of D10 having yield strengths of; 295 MPa, 345 MPa, and 490 MPa is discussed here. The corresponding failure patterns are shown in Figure 6.39, Figure 6.40, and Figure 6.41, respectively. The internal crack patterns in Figure 6.39, Figure 6.40,

and Figure 6.41 corresponding to slip stages (a), (b), and (c) show that the initial failure process at these slip stages is almost the same for the all the three yield strengths of the transverse rebar and the crack propagation is also almost of same magnitude. The internal crack patterns in Figure 6.39 and Figure 6.40 shows that after the occurrence of the vertical along the shear surface at slip stages (b) and (c), the shear failure occurs at the slip stages (d), and (e) and the horizontal cracks also propagate to the surface of the specimen.

While the specimens embedded with rebar of yield strength 490 MPa shows the initiation of the splitting cracks under the concrete dowel on the inner sides of the side concrete blocks at slip stage (d) as shown in Figure 6.41. The initiation of the splitting crack in specimens embedded with rebar of yield strength 490 MPa as shown in Figure 6.41 is because of the improvement of the shear resistance contributed by the concrete dowel against the applied shear load. As the yield strength of the rebar increases inside the hole, the ability of the concrete dowel to resist the applied vertical shear load in a simple push-out test also increases. After the initiation of the splitting crack in specimen embedded with rebar of yield strength 490 MPa, at slip stage (d), the splitting failure has been observed in the post-peak region. Figure 6.39, Figure 6.40, and Figure 6.41 show that as the yield strength of the transverse rebar is increased from 295 MPa to 490 MPa the shear capacity also increases and the deformed behaviors changes from the shear failure mode to the splitting failure mode.

The difference between the normal stress distribution in y direction ( $\sigma_y$ ) as shown in Figure 6.39, Figure 6.40, and Figure 6.41 is presented here. Figure 6.39, Figure 6.40, and Figure 6.41 show that at slip stages (a), (b), and (c) the large compressive stresses along the y-axis ( $\sigma_y$ ) occur on the top of the concrete dowel and the region of the large compressive forces is almost the same. The specimen embedded with rebar of yield strength 490 MPa experiences slightly more envelope of the compressive stresses at slip stages (d) and (e) because of the splitting crack propagation as shown in Figure 6.41 compared with the specimens embedded with yield strength 295 MPa and 345 MPa of the transverse rebar as shown in Figure 6.39 and Figure 6.40, respectively.

Similarly, the difference of the strain in the transverse rebar has also been revealed for the specimens embedded with rebar yield strengths of 295 MPa, 345 MPa, and 490 MPa as shown in Figure 6.39, Figure 6.40, and Figure 6.41, respectively. The

yielding of the rebar has been observed in all the cases. Figure 6.39 shows that the specimen embedded with a rebar yield strength of 295 MPa exhibits the maximum kinking deformation and the yielded parts along the length of the rebar because of the lesser yield strength compared with the specimens embedded with rebars yield strengths of 345 MPa and 490 MPa as shown in Figure 6.40, and Figure 6.41, respectively.

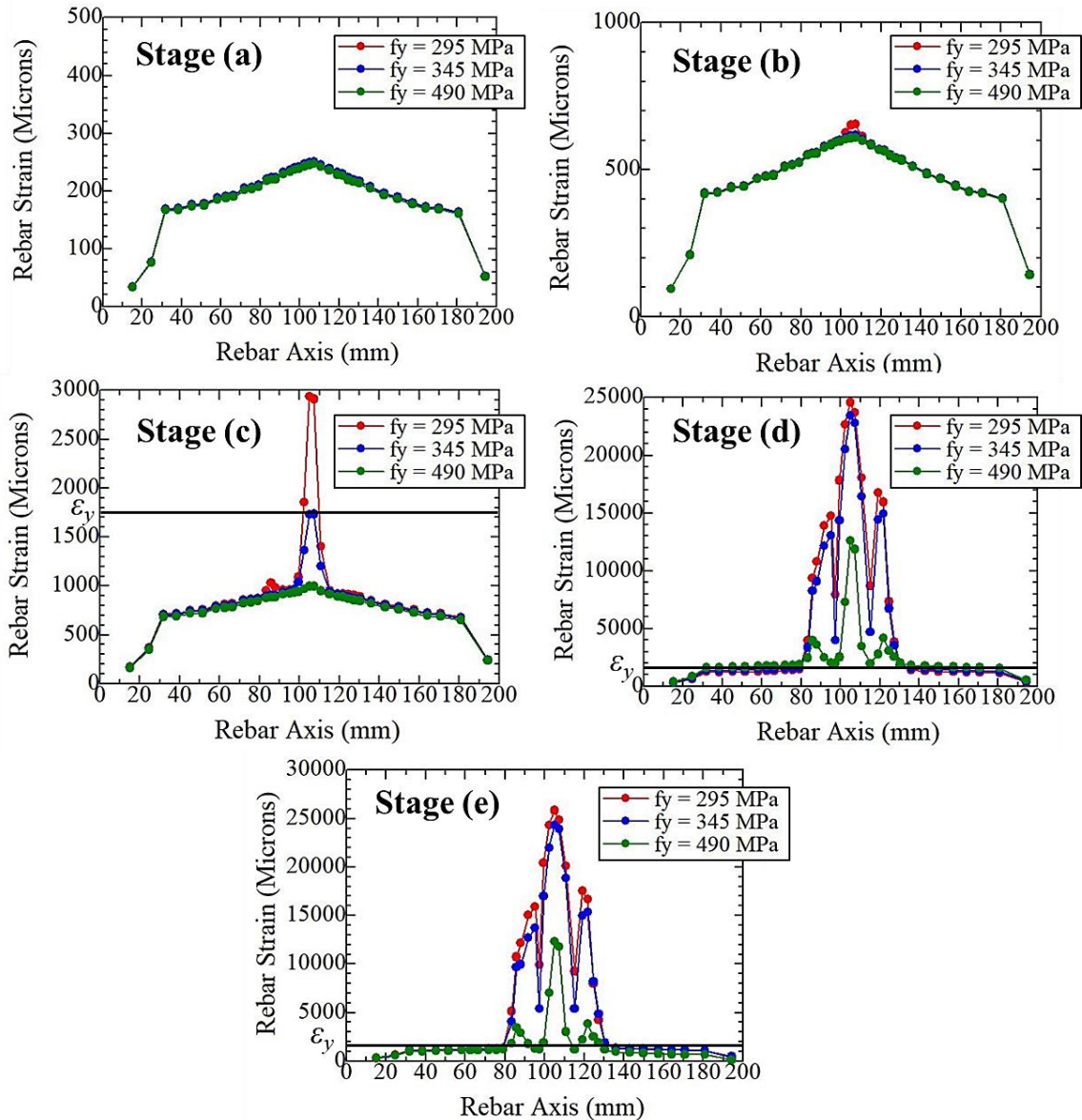


**Figure 6.42 Comparison of the strain distribution with different yield strengths of the transverse rebar**

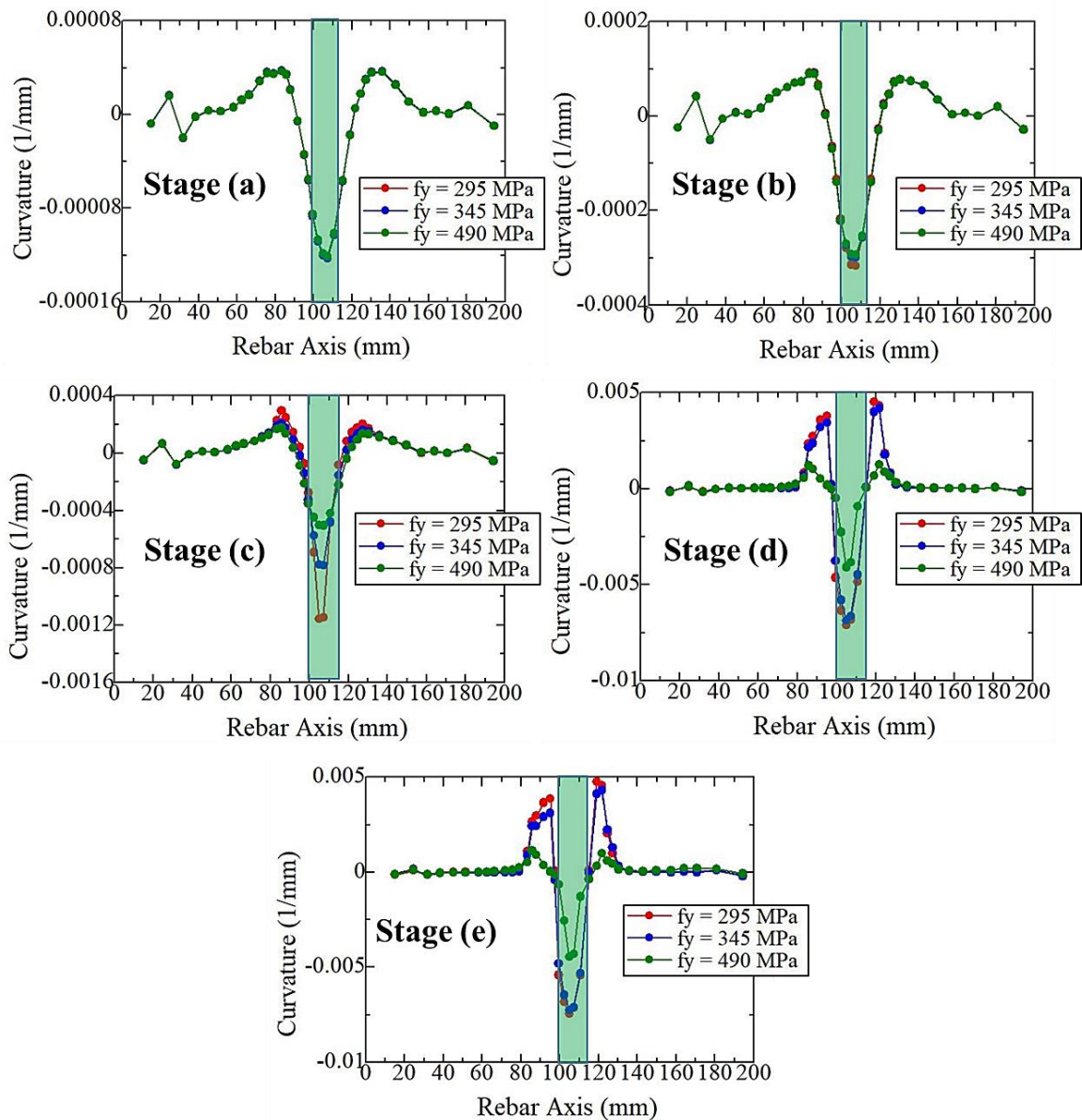


**Figure 6.43 Comparison of the curvature distribution with different yield strengths of the transverse rebar**

The comparison of the strain and the curvature distribution along the rebar axis against various stages on the load-displacement have been shown in Figure 6.42 and Figure 6.43, respectively. Figure 6.42 shows that the yielding of the rebar starts from the slip stage (c) for the rebar having a yield strength of 295 MPa, while at the peak and the post-peak all the rebars with yield strengths of 295, 345, and 490 MPa show the yielding. Figure 6.42 also illustrates that the rebar having a yield strength of 295 MPa reproduces the maximum strain magnitude before the peak, while the almost same

magnitude of the strain for all the rebars with yield strengths of 295, 345, and 490 MPa has been observed at the peak and the post-peak. Figure 6.43 shows that damage or the deformation region is more for the rebars with yield strengths of 295, and 345 MPa. Figure 6.42 and Figure 6.43, show that because of the maximum curvature and the strain of the rebars with yield strengths of 295, and 345 MPa, the peak slips are more of these specimens compared with the specimens embedded with rebar of yield strength of 490 MPa as shown in Figure 6.38.

## 6.5 Summary

The current chapter presented the numerical evaluation of shear resistance of the PBL shear connector under the influence of the varying amounts of the lateral pressures applied to the side concrete blocks and effect of the transverse rebar employing a coupled RBSM and solid FEM model, emphasized on the damage progress (internal crack propagation behavior and stress distribution) of the concrete. Additionally, the combined effects of the various lateral pressures and the diameters of the holes on the shear capacity of the PBL shear connector were also highlighted. Furthermore, the detailed internal failure mechanism of a single PBL shear connector in the simple push-out test was also revealed quantitatively. Based on the outcomes of the current research, the conclusions enumerated hereafter are drawn.

- 1) The numerical evaluation of the PBL shear connector using a coupled RBSM and solid FEM model under a simple push-out test was carried out. The evaluation was performed considering the numerical simulations for quantitative shear strength evaluation and the failure modes of concrete under the influence of the varying amounts of lateral pressures.

It was confirmed numerically that the shear capacity of the PBL increased and the failure mode changed from shear failure to splitting failure with the increased amounts of lateral pressure, which was the same as the behavior shown with the test investigations.

In the low lateral pressure case, the vertical cracks propagated along with the shear surface, the large compressive stresses ( $\sigma_y$  and  $\sigma_z$ ) were concentrated only around the concrete dowel region, and the shear strength of the PBL shear

connector was determined by the shear failure of two cracked surfaces around the edge of the hole in the steel plate.

While in the high lateral pressure application case, as the amount of the applied lateral pressure was increased, the shear strength of the two vertical cracked surfaces along with the shear surfaces was also enhanced, the splitting cracks propagated in the side concrete blocks perpendicular to the thickness of the perforated steel plate, and the large compressive stresses ( $\sigma_y$  and  $\sigma_z$ ) were also observed in the concrete dowel region as well as in the side concrete blocks. In the high lateral pressure application case, the shear strength of the PBL shear connector was characterized by the occurrence of the splitting cracks in the surrounding concrete blocks.

- 2) Numerical evaluation of the combined effects of the lateral pressures and the diameters of the holes revealed that there existed a clear combined effect and the increase in the shear strength was more in the large diameter case subjected to high lateral pressure because of the wide compressive regions generated around the concrete dowel region as well as in the side concrete blocks.
- 3) The numerical evaluation was performed for the transverse rebar effect, considering the influential varying parameters; the end conditions (free and fixed), the diameter of the rebar (D10, D13, and D16), the position of the transverse rebar inside the hole (top, middle, and bottom) and the yield strength (295 MPa, 345 MPa, and 490 MPa). The effect of these parameters is summarized as;

The presence of the transverse rebar inside the hole of the PBL provided confinement to the concrete dowel due to bond behavior characteristics between the transverse rebar and the concrete inside the hole and caused the improvement of shear resistance contributed by the concrete dowel. In the case of specimens with transverse rebar, the applied shear force in a simple push-out test was resisted by; concrete dowel as well as the tensile force of the transverse rebar. The effect of the rebar diameter is explained here. As the diameter of the rebar was increased, the more surface area of the rebar provided the more bond strength and hence the more confinement to the concrete inside the hole. The

splitting failure was observed in the post-peak region for the largest rebar diameter.

The effect of the rebar position is discussed here. The specimens embedded with rebar at the bottom position of a hole highlighted the initiation of the splitting cracks under the concrete dowel on the inner sides of the side concrete blocks at peak. The initiation of the splitting crack in specimens embedded with rebar at the bottom position of a hole was because of the improvement of the shear resistance contributed by the concrete dowel against the applied shear load. As the concrete region above the rebar increased inside the hole, the ability of the concrete dowel to resist the applied vertical shear load in a simple push-out test got increased. After the initiation of the splitting crack in specimens embedded with rebar at the bottom position of a hole at the peak, the splitting failure has been observed in the post-peak region.

The effect of the rebar yield strength is addressed here. The specimens embedded with rebar of maximum yield strength showed the initiation of the splitting cracks under the concrete dowel on the inner sides of the side concrete blocks at the peak slip stage while all remaining specimens reproduced the shear failure behavior.

# 7 Conclusions

## 7.1 Conclusions

The dissertation presented investigated the performance evaluation of the RC joint of the concrete structures. The mesoscale model of 3D-RBSM was employed to evaluate the complicated mechanical phenomena of RC joint such as the internal failure process and the stress bearing mechanism between concrete and steel. The numerical evaluations to investigate the internal cracking behavior specifically the normal stress distribution of the concrete for various structural behaviors (evaluation of the macroscopic bond behavior between the concrete and the deformed rebar) using the mesoscale numerical investigations through 3D-RBSM were performed.

Similarly, the evaluation of the RC joints (loop joints in precast beams and the Perfobond shear connector in steel-concrete composite construction) were simulate to clarify the internal failure mechanism and to demonstrate the reasons behind the occurrence of any particular failure behaviors of concrete, comprehensively. The conclusions are presented against the bond behavior between concrete and deformed rebar and the performance evaluation of the horizontal type loop joints in precast beams and the PBL shear connector in concrete-steel composite construction.

(1) The performance evaluation of the horizontal type loop joints using 3D-RBSM discussed in chapter 3 is concluded as the failure of the loop joint without inner reinforcing rebars inside the loop was by the occurrence of diagonal cracks in the tensile loop region and showed brittle failure behavior. The presence and the bond strength of the inner reinforcing bars inside the loop joint played the vital role in suppressing the diagonal crack occurrence and propagation, thus restrained the loop type failure and reproduced the compression failure having ductile failure characteristics. The numerical

investigation against increased the loop interval between loop rebars also highlighted that the deformation capacity of the loop. The peak decreased with the increased of loop interval due to increase in diagonal crack propagation between two tensile loop rebars at the joint region. The varying steel amount of the inner reinforcing rebars inside the loop did not show any significant change in the loop failure mode. However, the surface area of the inner reinforcing rebars inside the loop showed more influence on the deformation performance and the failure modes of the loop joint. It was observed that more surface of the inner reinforcing rebar inside the loop provided the more bond resistance capacity and hence produced more confinement to the concrete inside the loop due to bond behavior and thus prevented diagonal crack propagation and reproduced the compression failure mode rather than loop type failure.

(2) The numerical evaluation of the macroscopic bond behavior the deformed rebar and concrete as highlighted in chapter 5, is concluded here. In two ends pull-out test, the coupled RBSM and solid FEM model effectively simulates the macroscopic bond characteristics between steel rebars and concrete including the effect of the varying concrete cover thicknesses and the rebar diameters. The stress slip relationships highlighted that the concrete cover thickness reproduced relatively more influence on the macroscopic bond strength characteristics and the deformation capacity than the rebar diameter while keeping the compressive strength of concrete constant. Moreover, the numerical model also adequately captured the deformed behaviors of the reinforced concrete specimens subjected to the varying concrete cover thicknesses. The transformation of the deformed behaviors from splitting failure to the pull-out failure showed the dependency as well as the correlation of the bond strength with the degree of passive confinement i.e. through the concrete cover. In one end pull-out test under the influence of the laterally applied pressures to the concrete, the unconfined RC specimens expressed lower bond strength compared with actively confined specimens. Whereas, the confined specimens showed the increased bond strength and slip at ultimate. The unconfined concrete specimens showed longitudinal radial crack development from reinforcing bar, caused the splitting type failure. Whereas, the confined concrete specimens demonstrate the splitting as well as the pull-out. The internal fracture mechanism was highlighted by the numerical simulations using axially loaded tensile reinforced concrete prisms. The coupled RBSM and solid FEM model not

only quantitatively demonstrated the formation and propagation of different types of cracks (primary, secondary and longitudinal) but also remarkably differentiated them against the increased stress stage of steel reinforcement. Moreover, the mesoscale numerical simulation also presented the effect of rebar geometrical features on the bonding behavior and the internal fracture process in the concrete.

(3) The conclusions are made for the performance evaluation of the PBL shear connector as discussed in chapter 6, under the influence of the varying amounts of the lateral pressures applied to the side concrete blocks and effect of the transverse rebar. It was confirmed that the shear capacity of the PBL increased and the failure mode changed from shear failure to splitting failure with the increased amounts of lateral pressure, which was the same as the behavior shown with the test investigations. In the low lateral pressure case, the vertical cracks propagated along with the shear surface, the large compressive stresses ( $\sigma_y$  and  $\sigma_z$ ) were concentrated only around the concrete dowel region, and the shear strength of the PBL shear connector was determined by the shear failure of two cracked surfaces around the edge of the hole in the steel plate. While in the high lateral pressure application case, as the amount of the applied lateral pressure was increased, the shear strength of the two vertical cracked surfaces along with the shear surfaces was also enhanced, the splitting cracks propagated in the side concrete blocks perpendicular to the thickness of the perforated steel plate, and the large compressive stresses ( $\sigma_y$  and  $\sigma_z$ ) were also observed in the concrete dowel region as well as in the side concrete blocks. In the high lateral pressure application case, the shear strength of the PBL shear connector was characterized by the occurrence of the splitting cracks in the surrounding concrete blocks. Similarly, the evaluation of the combined effects of the lateral pressures and the diameters of the holes revealed that there existed a clear combined effect and the increase in the shear strength was more in the large diameter case subjected to high lateral pressure because of the wide compressive regions generated around the concrete dowel region as well as in the side concrete blocks.

The presence of the transverse rebar inside the hole of the PBL provided confinement to the concrete dowel due to bond behavior characteristics between the transverse rebar and the concrete inside the hole and caused the improvement of shear resistance contributed by the concrete dowel. In the case of specimens with transverse

rebar, the applied shear force in a simple push-out test was resisted by; concrete dowel as well as the tensile force of the transverse rebar. The effect of the rebar diameter is explained here. As the diameter of the rebar was increased, the more surface area of the rebar provided the more bond strength and hence the more confinement to the concrete inside the hole. The splitting failure was observed in the post-peak region for the largest rebar diameter. Furthermore, the specimens embedded with rebar at the bottom position of a hole highlighted the initiation of the splitting cracks under the concrete dowel and reproduced the splitting failure mode. Moreover, the specimens embedded with rebar of maximum yield strength also showed the splitting failure mode while all remaining specimens reproduced the shear failure behavior.

## **7.2 Recommendations for future study**

Regarding the numerical evaluation included in this dissertation was related to specimens embedded with single deformed rebar. The numerical evaluation of the reinforced concrete can also be performed considering multiple rebars inside the concrete. Similarly, the study evaluated the active confinement due to application of the lateral pressures applied to the concrete surface, the effect of the passive confinement due to transverse rebars and the stirrups on the bond behavior can also be evaluated to investigate the internal failure mechanism. Furthermore, the dowel action of the beam can also be an interesting application to investigate using numerical simulation analyses.

The mesoscale simulations using 3D-RBSM can also be useful for evaluating the structural performance and failure mechanism of the different types of reinforced concrete anchorages e.g. standard hooks ( $90^\circ$  and  $180^\circ$ ), headed bars and so on. The internal failure mechanism for the development lengths of RC anchorages provided based on the guidelines of the design codes is not yet explained, deeply. Based on the knowledge obtained internal failure mechanism

The performance evaluation of the other cast in situ RC joints can also be investigated such as the headed rebar joints, cast in situ anchors, etc. directly modeling the shape of steel (headed rebars and anchors, etc.).

In this study, the most fundamental type PBL shear connector with a single hole was used for the numerical evaluation. The numerical analyses can also be performed

considering the multiple holes inside the perforated steel plate. Furthermore, in the current PBL shear connector, the side concrete blocks don not have any stirrups. The performance evaluation can also be performed considering the restrains provided through the stirrups in the side concrete blocks. Additionally, in the current PBL shear connector there is no concrete end bearing zone, for future study, the effect of the concrete end bearing zone can also be adopted. The parametric evaluation can also be performed considering different diameters of the holes, shape of the holes as well as the thickness of the perforated steel plate. The internal resistance mechanism of the PBL shear connector can also be evaluated considering concrete size effect of the adjoining concrete blocks.

Similarly, the other interesting aspect for future study can be the performance evaluation of the shear studs by modeling the actual geometrical features of the shear studs, as they are also one of the most commonly employed shear connectors in concrete-steel composite construction. The comparison of the performance evaluation of PBL and the stud shear connector can be highlighted based on the shear resistance mechanism and the internal failure mechanism. This information can contribute towards the rationalization of the joints in concrete steel composite construction.

## References

- Hayashi, D., and Nagai, K., (2013). “Mesoscopic simulation of RC anchorage in multidirectional reinforcements by 3D discrete analysis.” *J. JSCE*, 69, 241-257. [in Japanese].
- Hayashi, D., Nagai, K., and Eddy, L., (2017). “Mesoscale analysis of RC anchorage performance in multidirectional reinforcement using a three-dimensional discrete model.” *J. Struct. Eng.*, 143(7), 1-13.
- Matsumoto, K., Wang, T., Hayashi, D., and Nagai, K., (2016). “Investigation on the pull-out behavior of deformed bars in cracked reinforced concrete.” *Journal of Advanced Concrete Technology. Eng.*, 14, 573-589.
- Eddy, L., and Nagai, K., (2016). “Numerical simulation of beam-column knee joints with mechanical anchorages by 3D rigid body spring model.” *Engineering Structures*, 126, 547-558.
- Eddy, L., Matsumoto, K., and Nagai, K., (2016). “Effect of perpendicular beams on failure of beam-column knee joints with mechanical anchorages by 3D RBSM.” *Journal of Asian Concrete Federation*, 2, 56-66.
- Daniel, D., Marina, C., and Paulo, F., (2014). “Loop connection with fibre-reinforced precast concrete components in tension.” *Engineering Structures*, 140-151.
- Ryu, H., Kim, Y., and Chang, S., (2007). “Loop connection with fibre-reinforced precast concrete components in tension.” *Engineering Structures*, 29, 145–162.
- K.C.G. Ong., J.B. Hao., and P. Paramasivam., (2006). “Flexural behavior of precast joints with horizontal loop connections.” *ACI structural Journal*, 103, 664-671.
- K.C.G. Ong., J.B. Hao., and P. Paramasivam., (2006). “A strut-and-tie model for ultimate loads of precast concrete joints with loop connections in tension.” *Construction and Building Materials*, 20, 169-176.

- Joergensen, H., and Hoang, L., (2013). “Tests and limit analysis of loop connections between precast concrete elements loaded in tension.” *Engineering Structures*, 52, 558-569.
- Yamamoto, Y., Iwata, M., Kuroda, I., and Furuya, F., (2010). “Analytical evaluation of the failure mechanism of loop-shaped re-bar joint using RBSM.” *Kouzou Kougaku Ronbunshu*, 56A, 915-927. [in Japanese].
- Junbao, H., (2004). “Structural behavior of precast component joints with loop connection.” Doctoral dissertation, Department of civil engineering, National university of Singapore.
- Appa Rao, G., Pandurangan, K., Sultana, F., and Eligehausen, R., (2006). “Studies on the pull-out strength of ribbed bars in high-strength concrete.” *Proc. of the 6th Inter. Conf. on Fract. Mech. of Conc. & Conc. Struct (FraMCoS-6)*, Catania, Italy.
- Lemnitzer, L., Schröder, S., Lindorf, A., and Curbach, M., (2009). “Bond behaviour between reinforcing steel and concrete under multiaxial loading conditions in concrete containments.” *SMiRT 20*, Espoo, Finland.
- Kankam, C.K., (1997). “Relationship of bond stress, steel stress, and slip in reinforced concrete.” *J. Struct. Eng.*, 123(1), 79-85.
- Metelli, G. and Plizzari, G.A., (2014). “Influence of the relative rib area on bond behaviour.” *Institute of Civil Engineering*, 66(6), 274-294.
- Raymond, E., Untrauer., and Henry, R.L., (1965). “Influence of normal pressure on bond strength.” *Journal of the American Concrete Institute*, 62(5), 577-586.
- Torre-Casanova, A., Jason, L., Davenne, L., and Pinelli, L., (2013). “Confinement effects on the steel–concrete bond strength and pull-out failure.” *Engineering Fracture Mechanics*, 97, 92-104.
- Robins, P.J., and Standish, I.G., (1982). “The effect of lateral pressure on the bond of round reinforcing bars in concrete.” *Int. J. Adhesion and Adhesives*, 2(2), 129-133.
- Soroushian, P., Choi, K., Park, G., and Aslani, F., (1991). “Bond of deformed bars to concrete: effects of confinement and strength of concrete.” *ACI Materials Journal*, 88, 227-232.
- Iizuka, K., Higai, T., Saito, S., and Takahashi, R., (2011). “Bond stress-slip-strain relationship of deformed bars including the effect of concrete cover thickness.” *Doboku Gakkai Ronbunshuu*, 67, 280-296. [in Japanese].

- Xu, F., Wu, Z., Zheng, J., Hu, Y., and Li, Q., (2014). "Bond behavior of plain round bars in concrete under complex lateral pressures." *ACI Structural Journal*, 111, 15-25.
- Dawood, N., and Marzouk, H., (2012). "Estimate of cracking and bond splitting stresses of reinforced concrete plates under uniaxial and biaxial tension." *ACI Structural Journal*, 109, 857-866.
- Chu, S.H., and Kwan, A.K.H., (2018). "A new method for pull out test of reinforcing bars in plain and fibre reinforced concrete." *Engineering Structures*, 164, 82-91.
- Goto, Y., (1971). "Cracks Formed in Concrete around Deformed Tension Bars." *ACI Journal*, 68, 244-251.
- Goto, Y., and Otsuka, K., (1980). "Experimental Studies on Cracks Formed in Concrete around Deformed Tension Bars." *J. JSCE*, 85-100. [in Japanese].
- Kim, S.H., Lee, C.G., Ahn, J.H., and Won, J.H., (2011). "Experimental study on joint of spliced steel-PSC hybrid girder, Part I: proposed parallel-perfobond-rib-type joint." *Eng. Struct.*, 33(8), 2382-2397.
- He, J., Liu, Y., and Pei, B., (2013). "Experimental study of the steel-concrete connection in hybrid cable-stayed bridges." *J. Perform. Constr. Facil.*, 28(3), 559-570.
- Liu, Y., Xin, H., He, J., Xue, D., Ma, B., and Mosallam, A.S., (2013). "Experimental and analytical study on fatigue behavior of composite truss joints." *J. Constr. Steel Res.*, 83, 21-36.
- Li, Y., Liu, Y., Wang, F., and Yang, F., (2018). "Load transfer mechanism of hybrid pylon joint with cells and bearing plates." *Adv. Civ. Eng.*
- Liu, Y., Xin, H., and Liu, Y., (2018). "Load transfer mechanism and fatigue performance evaluation of suspender-girder composite anchorage joints at serviceability stage." *J. Constr. Steel Res.*, 145, 82-96.
- Veldanda, M.R., and Hosain, M.U., (1992). "Behaviour of perfobond rib shear connectors: push-out tests." *Can. J. Civ. Eng.*, 19(1).
- Machacek, J., and Studnicka, J., (2002). "Perforated shear connectors." *Steel Compos. Struct.*, 2(1), 51-66.
- Yang, Y., and Chen, Y., (2018). "Experimental study on mechanical behavior of PBL shear connectors." *J. Bridge Eng.*, 23(9).

- Wang, X., Zhu, B., Cui, S., and Liu, E.M., (2018). "Experimental research on PBL connectors considering the effects of concrete stress state and other connection parameters." *J. Bridge Eng.*, 23(1), 1-13.
- Taira, Y., Asanuma, T., Ichimiya, T., and Furuichi, K., (2013). "Strength evaluation of perforated steel plate shear connector considering restrain effect." *Proceedings of JCI annual convention*, 35, 1225-1230. [in Japanese].
- Zhao, C., Li, Z., Deng, K., and Wang, W., (2018). "Experimental investigation on the bearing mechanism of Perfobond rib shear connectors." *Eng. Struct.*, 59, 172-184.
- Ahn, J.E., Lee, C.G., Won, J.H., and Kim, S.H., (2010). "Shear resistance of the perfobond-rib shear connector depending on concrete strength and rib arrangement." *J. Constr. Steel Res.*, 66, 1295-1307.
- Vianna, J. da C., Andrade, S.A.L. de., Vellasco, P.C.G. da S., and Costa-Neves, L. F., (2013). "Experimental study of Perfobond shear connectors in composite construction." *J. Constr. Steel Res.*, 81, 62-75.
- Nakajima, A., Koseki, S., Hashimoto, M., Suzuki, Y., and Nguyen, M.H., (2012). "Evaluation of shear resistance of perfobond strip based on simple push-out test." *J. JSCE.*, 68(2), 495-508. [in Japanese].
- Jeong, Y.J.K., Kim, H.Y., and Koo, H.B., (2009). "Longitudinal shear resistance of steel-concrete composite slabs with perfobond shear connectors." *J. Constr. Steel Res.*, 65, 81-88.
- Hosseinpour, E., Baharom, S., and Badaruzzaman, W.H.W., (2018). "Push-out test on the web opening shear connector for a slim-floor steel beam: Experimental and analytical study." *Eng. Struct.*, 163, 137-152.
- Chen, J.J., Wang, J.H., Qiao, P., Hou, Y.M., and Gu, Q.Y., (2016). "Shear bearing of cross-plate joints between diaphragm wall panels - I: model tests and shear behaviour." *Mag. Concr. Res.*
- Al-Darzi, S. Y. K., Chen, A. R., and Liu, Y. Q., (2007). "Finite element simulation and parametric studies of perfobond rib connector." *Am. J. Appl. Sci.*, 4(3), 122-127.
- Yu, Z., Zhu, B., Dou, S., and Liu, W., (2012). "3D FEM simulation analysis for PBL shear connectors." *Appl. Mech. Mater.*, 170-173, 3449-3453.
- Liu, Y., Xin, H., and Liu, Y., (2019). "Experimental and analytical study on shear mechanism of rubber-ring perfobond connector." *Eng. Struct.*, 197.

- Liu, J., Yang, J., Chen, B., and Zhou, Z., (2020). “Mechanical performance of concrete-filled square steel tube stiffened with PBL subjected to eccentric compressive loads: Experimental study and numerical simulation.” *Thin-Walled Structures*, 149.
- Li, Z., Zhao, C., Shu, Y., Deng, K., Cui, B., and Su, Y., (2019). “Full-scale test and simulation of a PBL anchorage system for suspension bridges: Experimental study and numerical simulation.” *Struct. Infrastruct. Eng.*
- Liu, Y., Wang, S., Xin, H., and Liu, Y., (2020). “Evaluation on out-of-plane shear stiffness and ultimate capacity of perfobond connector.” *J. Constr. Steel Res.*
- Fan, L., and Zhou, Z., (2014). “Study on the shear capacity of PBH shear connector basing on PBL shear connector.” *Computer Modelling & New Technologies*, 18(12D), 174-180.
- Munemoto, S., and Sonoda, Y., (2014). “A fundamental study on the evaluation method of load bearing capacity of PBL jointing area.” *J. Struct. Eng.*, 60A. [in Japanese].
- Munemoto, O., Sonoda, Y., and Koshiishi, M., (2013). “A study on the strength evaluation of perforated steel plate shear connector using 3D elastic-plastic FEM.” *Proceedings of JCI annual convention*, 35, 1243-1248. [in Japanese].
- Ikuma, K., Yamamoto, Y., Nakamura, H., and Miura, T., (2018). “Mesoscale simulation of bond behavior of deformed rebar based on coupled RBSM-FEM method.” *Proceedings of JCI annual convention*, 40, 541-546. [in Japanese].
- Karam, M.S., Yamamoto, Y., Nakamura, H., and Miura, T., (2019). “Mesoscale analysis for the bond behavior of concrete under active confinement using coupled RBSM and solid FEM.” *Proceedings of the 10th International Conference on Fracture Mechanics of Concrete and Concrete Structures (FramCoS-X)*, Bayonne, France.
- Yamamoto, Y., Nakamura, H., Kuroda, I., and Furuya, N., (2008). “Analysis of compression failure of concrete by three-dimensional Rigid Body Spring Model.” *Doboku Gakkai Ronbunshuu*, 64, 612-630. [in Japanese].
- Yamamoto, Y., (2013). “Evaluation of failure behaviors under static and dynamic loadings of concrete members with mesoscopic scale modeling.” Doctoral dissertation, Department of Civil Engineering, Nagoya University. 2008. [in Japanese].
- Thomure J., Bolander J. Jr., and Kunieda M., (2001). “Reducing mesh bias on fracture within Rigid-Body-Spring Networks, Structural Eng./Earthquake Eng.” *JSCE*, 18(2), 95-103.

- Yamamoto, Y., Nakamura, H., and Kuroda, I., (2014). "Crack propagation analysis of reinforced concrete wall under cyclic loading using RBSM." *Eur. J. Environ. Civ. Eng.*, 18, 780-792.
- Gedik, Y. H., Nakamura, H., Yamamoto, Y., and Kunieda, M., (2011). "Evaluation of three-dimensional effects in short deep beams using a Rigid-Body-Spring-Model." *Cem. Concr. Compos.*, 33(9), 978-991.
- Japan Society of Civil Engineers (JSCE): Standard specifications for concrete structures-2012.
- Kawai, T., (1978). "New Discrete Models and their Application to Seismic Response Analysis of Structures." *Nuclear Engineering and Design*, 48, 207-229.
- Toi, Y., and Kawai, T., (1984). "Discrete Limit Analysis of Plate and Shell structures." *Computers & Structures*, 19, 251-261.
- Jr, R.M., Yamamoto, Y., Nakamura, H., and Miura, T., (2018). "Numerical evaluation of localization and softening behavior of concrete confined by steel tubes." *Struct. Concr.*, 19, 1956-1970.
- Jr, R.M., Yamamoto, Y., Nakamura, H., and Miura, T., (2017). "Modeling of composite action in concrete-filled steel tubes using coupled RBSM and Shell FEM." *Proceedings of JCI annual convention*, 39 (2), 991-996.
- Salem, H. M., and Maekawa, K., (2004). "Pre-and Post-Yield Finite Element Method Simulations of Bond of Ribbed Reinforcing Bars." *J. Struct. Eng.*, 671, 671-680.
- Fuji, K., Iwasaki, H., Fukada, K., and Toyota, T., (2008). "Crack restraint factors in ultimate slip behavior of Perfobond strip." *Doboku Gakkai Ronbunshuu*, 64, 502-512. [in Japanese].
- Farooq, U., Nakamura, H., Miura, T., and Yamamoto, Y., (2020). "Proposal of bond behavior simulation model by using discretized Voronoi mesh for concrete and beam element for reinforcement." *Cem. Concr. Compos.*, 110, online version.
- Oguejiofor, E. C., and Hosain, M. U., (1997). "Numerical analysis of pushout specimens with perfobond rib connectors." *Computers and Structures*, 62(4), 617-624.
- Oguejiofor, E. C., and Hosain, M. U., (1994). "A parametric study of perfobond rib shear connectors." *Can. J. Civ. Eng.*, 21(4), 614-625.
- Hosaka, T., Mitsuki, K., Hiragi, H., Ushijima, Y., Tachibana, Y., and Watanabe, H., (2000). "An experimental study on shear characteristics of perfobond strip and its rational strength equations." *JSCE. J. Struct. Eng.*, 46A, 1593-1604. [in Japanese].

Yoshitaka, U., Tetsuya, H., and Kaoru, M., (2001). “An experimental study on shear characteristics of perfobond strip and its rational strength equations.” *Proc., Int. Symp. on Connections between Steel and Concrete*, Rilem, Paris, 1066-1075.

Japan Society of Civil Engineers (JSCE): Standard specifications for hybrid structures 2009.

Zhao, C., and Liu, Y.Q., (2012). “Experimental study of shear capacity of perfobond connector.” *Engineering Mechanics*, 29(12), 349–354. [in Chinese].

Cândido-Martins, J., Costa-Neves, L., and Vellasco, P., (2010). “Experimental evaluation of the structural response of Perfobond shear connectors.” *Engineering Structures*, 1976-1985.